

PHD THESIS

**TOPOLOGICAL WAVEGUIDES AND
SYMMETRICAL DROPLET QUANTUM DOTS
FOR SCALABLE PHOTONIC QUANTUM
TECHNOLOGY**

NILS VALENTIN HAUFF

APRIL 19, 2023

BEYOND A CRITICAL POINT WITHIN A FINITE SPACE, FREEDOM DIMINISHES AS NUMBERS INCREASE. THIS IS AS TRUE OF HUMANS IN THE FINITE SPACE OF A PLANETARY ECOSYSTEM AS IT IS OF GAS MOLECULES IN A SEALED FLASK. THE HUMAN QUESTION IS NOT HOW MANY CAN POSSIBLY SURVIVE WITHIN THE SYSTEM, BUT WHAT KIND OF EXISTENCE IS POSSIBLE FOR THOSE WHO DO SURVIVE.

DUNE (HERBERT, 1965 : 559)

COLOPHON

This thesis was set with \LaTeX 2 ϵ using the memoir class.

The font is Libertine 11, on normal A4 paper

Graphics created using Matlab R2022b, Matplotlib under Python 3.6, TikZ, as well as Inkscape.

Chapterstyles courtesy CP3.

TOPOLOGICAL WAVEGUIDES AND SYMMETRICAL DROPLET QUANTUM DOTS FOR SCALABLE PHOTONIC QUANTUM TECHNOLOGY

Author Nils Valentin Hauff
Advisor Prof. Peter Lodahl
Niels Bohr Institute
University of Copenhagen, Denmark



UNIVERSITY OF
COPENHAGEN

This thesis has been submitted to
The PhD School of The Faculty of Science
University of Copenhagen
April 19, 2023

ABSTRACT

Deterministic quantum emitters able to generate multiphoton entangled states are essential building blocks for a plethora of quantum information applications. Solid-state spin-photon interfaces integrated into nanophotonic structures show great potential as they can form basic elements of scalable photonic circuits that enable on-chip quantum operations. Particularly, InGaAs (indium gallium arsenide) quantum dots (QDs) integrated into planar nanophotonic circuits have made significant technological achievements. An essential component is the interface of a QD and a photonic crystal waveguide (PhCW), as it enables engineering the interaction between the QD and guided light. This thesis explores topologically non-trivial PhCW and a novel type of QDs for advancing scalable photonic quantum technology.

Advances such as the design of broken-symmetry PhCWs have led to chiral light-matter interfaces and non-reciprocal devices, which are essential for proposed quantum gates. However, chiral interfaces have yet to achieve as high interaction enhancements as conventional PhCWs and are limited in their performance by backscattering losses. The first part of this thesis explores the potential of a topological PhCW for chiral interfaces with QDs.

Specifically, planar nanophotonic circuits with embedded topological PhCWs with InGaAs QDs are designed and analyzed. Although the devices show adequate transmission in the spectral region of InGaAs QDs, the capabilities of the utilized nanofabrication method limit their practical application as chiral interfaces. The potential of topological PhCWs to support and enhance chiral interactions while suppressing backscattering losses is examined by finite-element calculations and backscattering theory. It is shown that topological PhCW can outperform dispersion-engineered conventional waveguides due to reduced backscattering on fabrication-induced imperfections for high interaction enhancements. The integration of topological PhCWs into nanophotonic circuits of the state-of-the-art InGaAs QD platform and the numerical performance benchmark promise high-performance designs of efficient, on-chip non-reciprocal devices and scalable circuits based on topological PhCWs and may enable the design of optical isolators, circulators, and quantum gates.

Technological developments of planar nanophotonic circuits are confronted with intrinsic limitations of InGaAs QDs in their coherence properties, fine-structure splitting, and spin-photon entanglement fidelity. The second part of this thesis explores the potential of planar nanophotonic circuits with a novel type of QDs: local droplet-etched GaAs QDs.

More concretely, planar nanophotonic circuits are presented that feature interfaces of PhCWs and GaAs QDs, fabricated from an ultra-thin semiconductor heterojunction. The demonstration of charge-state control and optical transition energy tuning of QDs in planar nanophotonic circuits marks an essential step for realizing scalable spin-photon interfaces with GaAs QDs. Embedded QDs are characterized as a source of single photons for quantum information by resonant

excitation and using time-resolved, high-resolution, and phonon-sideband resolved spectroscopy. Hanbury Brown and Twiss interferometry confirms the single-photon nature of the QDs' photoemission and low blinking probability in timescales up to 25 μ s. The single photon purity, the demonstration of mutual coherence between photons created, and coherent optical driving promise prospects for realizing a scalable deterministic source of indistinguishable single photons with GaAs QDs.

Advancing topological nanostructures for chiral light-matter interaction and developing low-decoherence emitters integrated into planar nanostructures are promising avenues for developing a scalable quantum photonic platform for generating entangled states on-chip.

SAMMENFATNING

Deterministiske kvanteemittere istandtil at generere multifotons sammenfildrede tilstande er essentielle byggesten for en overflod af anvendelsesmuligheder til kvanteinformation. Faststofs spin-foton grænseflader integrerede ind i nanofotoniske strukturer viser stort potentiale da de kan udgøre basale elementer af skalerbare fotoniske kredsløb som muliggør on-chip interaktioner. Navnlig InGaAs (Indium Gallium Arsenid) quantum dots (QD) integreret ind i plane nanofotoniske kredsløb har lavet signifikante teknologiske præstationer. En essentiel komponent er grænsefladen mellem en QD og en fotonisk krystal bølgeleder (PhCW, photonic crystal waveguide), da den tillader kontrol af interaktionen mellem QD'en og det ledede lys. Denne afhandling udforsker topologisk non-trivielle PhCW'er og en ny type QD'er for at fremme skalerbar fotonisk kvanteteknologi.

Fremskridt såsom designet af PhCW'er med brudt symmetri har ledt til chirale interaktioner mellem lys og stof, samt ikke-reciprokke enheder, hvilke er essentielle for foreslåede kvantegates. Imidlertid har chirale grænseflader endnu ikke opnået så høje interaktionsforbedringer som konventionelle PhCW'er, og er begrænsede i deres præsentation af tab via backscattering. Den første del af denne afhandling udforsker potentialet i en topologisk PhCW for chirale grænseflader med QD'er.

Plane nanofotoniske kredsløb med indlejrede topologiske PhCW'er med InGaAs QD'er er designet og analyseret. Selvom enhederne udviser tilstrækkelig transmission i det spektrale område af InGaAs QD'er begrænser kapaciteterne af de anvendte nanofabrikationsmetoderne deres praktiske applikation som chirale grænseflader. Potentialet for topologiske PhCW'er til at støtte og forbedre chirale interaktioner samtidig med at undertrykke backscattering interaktioner er undersøgt via finite-element beregninger og backscattering teori. Det vises, at topologiske PhCW'er kan udkonkurrere dispersion-engineered konventionelle bølgeledere grundet reduceret backscattering på de nanofabrikations-inducerede uperfektheder for høj interaktionsforbedring. Integrationen af topologiske PhCW'er i nanofotoniske kredsløb med en state-of-the-art InGaAs QD-platform og de numeriske ydeevne benchmarks lover høj-ydeevne designs af effektive, integrerede nonreciprokke enheder og skalerbare kredsløb baserede på topologiske PhCW'er og kan muliggøre designet af optiske isolatorer, cirkulatorer og kvantegates.

Teknologisk udvikling af plane nanofotoniske kredsløb bliver konfronteret med iboende begrænsninger af InGaAs QD's i deres kohærente egenskaber, finstruktur splitning og spin-foton sammenfiltringsfidelitet. Den anden del af denne afhandling udforsker potentialet i plane nanofotoniske kredsløb med en ny type QD'er: lokalt dråbeætsede GaAs QD'er.

Plane nanofotoniske kredsløb med grænseflader mellem PhCW'er og GaAs QD'er, fabrikerede fra en ultra-tynd halvleder heterojunction, bliver præsenteret. Demonstrationen af ladningstilstandskontrol samt tuning af den optiske transitionsenergi af QD'er i plane nanofotoniske kredsløb markerer et essentielt skridt for at realisere skalerbare spin-fotons grænseflader med GaAs QD'er. Indlejrede QD'er er

karakteriseret som en kilde til enkeltfotoner for kvanteinformation via resonant excitation og via tidsopløst, højopløsning og fononsidebåndsløst spektroskopi. Hanbury-Brown-Twiss-interferometri bekræfter enkeltfotonsnaturen af QD'ernes fotoemission samt lav sandsynlighed for blink over tidsskalaer op til 25 μ s. Enkeltfotonsrenheden, demonstrationen af gensidig kohærens mellem de skabte fotoner og den koherente optiske drivningsegenskaber lover muligheder for at realisere en skalerbar deterministisk kilde af uskelnelige enkeltfotoner via GaAs QD'er.

Fremme af topologiske nanostrukturer for chiral interaktion mellem lys og stof og udvikling af emittere med lav dekohærens integrerede ind i plane nanostrukturer er lovende retninger for at udvikle en skalerbar kvantefotonisk platform til at generere sammenfildrede tilstande on-chip.

PREFACE

This thesis presents the results of the research carried out in the Quantum Photonics group led by Professor Peter Lodahl, at the Niels Bohr Institute, University of Copenhagen, Denmark, from August 2019 to April 2023. During this period, I was enrolled as a Ph.D. student under the supervision of Professor Peter Lodahl and co-supervision of Assistant Professor Nir Rotenberg until his leave to the Centre for Nanophotonics, Queen's University, Kingston.

I want to use the opportunity to thank my colleagues who helped me and inspired me and acknowledge their contributions to my research: *Peter Lodahl*, who has formed the Quantum Photonics group, for welcoming me to become part of his group and giving me the opportunity to get involved in and contribute to the field of quantum photonics. *Nir Rotenberg* for his supervision during his time at the institute and for his support, guidance, and advice throughout my Ph.D. *Leonardo Midolo* for introducing and advising me on topics of photonics, nanofabrication, and scientific approaches and for providing valuable feedback to this thesis. *Alexey Tiranov* deserves my sincerest gratitude for his advice and contributions to experimental lab work, analyzing data in the field of quantum optics, and data modeling, and for his extraordinary support in writing this thesis. *Camille Papon* for sharing her experience on experimental techniques, providing scientific and non-scientific insights, sharing optimism, introducing me to key persons, and proofreading. *Freja T. Østfeldt* for discussions on chiral nanophotonics, spectroscopy, optical setups, and proofreading. *Ying Wang* for discussion of nanofabrication topics, characterization of photonic devices, and wire bonding. *Zhe Liu*, for sample nanofabrication of all sorts of structures which is the foundation of this thesis. *Xiaoyan Zhou*, for discussions and advice on numerical calculations. The Master students and interns *Hania Salamon*, *Adam Knorr*, *Mathias J. R. Staunstrup*, and *Lucie Tournier*, whom I have enjoyed working with and would like to thank for helping me carry out experiments. *Ravitej Uppu*, *Martin H. Appel*, *Ming Lai Chan*, *Sjaak van Diepen*, *Vasiliki Angelopoulou*, *Hanna Le Jeannic*, *Xiao-Liu Chu*, *Aslı Uğurlu*, *Celeste Qvotrup*, and others, for lab work and scientific discussions.

Furthermore, I want to thank my collaborators: The research group led by *Prof. Andreas D. Wieck* at the Ruhr-Universität Bochum, Germany, who have grown the wafers I have studied. My particular thanks to *Arne Ludwig* and *Hans-Georg Babin* for sample growth, scientific discussions, exchange of research data, and sharing insights. It has been a pleasure working with you. The research group led by *Prof. Richard Warburton* at the University of Basel, Germany, Switzerland, for the fruitful discussions and for sharing insights. I particularly thank *Clemens Spinnler*, *Liang Zhai*, *Giang Nam Ba Nguyen*, *Marcel Erbe*, and *Alisa Javadi*. *Prof. Stephen Hughes* and *Eric Nussbaum* at Queens University, Kingston, Canada, for their collaboration and discussions about topological photonic crystal waveguides, numerical methods in nanophotonics, and photonic transport. *Ryan C. Ng* and *Omar Florez* at the Institut Català de Nanociència i Nanotecnologia (ICN²), Barcelona, Spain, and *Pedro David*

García at the Material Science Institute of Madrid, Spain, for the discussion of topology in phononics and nanophotonics, sharing experiences, and collaboration in design and investigation of devices. The collaborators of the TOCHA project, particularly Prof. *Clivia Sotomayor*, Prof. *Sergio O. Valenzuela*, and Prof. *Daniel Lanzillotti Kimura*, for inspiring discussions.

Furthermore, I would like to thank *Benjamin* for discussing scientific challenges and *Daniel, Rizwan, Gertrud, Luleå, Hetty, Grýla*, and *Mairéad* for their extraordinary support. However, this list is incomplete and cannot represent the support I have experienced. Finally, I thank those who do not find themselves on this list.

LIST OF PUBLICATIONS

PUBLISHED

- Hauff, N. V., Le Jeannic, H., Lodahl, P., Hughes, S., & Rotenberg, N. (2022). Chiral quantum optics in broken-symmetry and topological photonic crystal waveguides. *Physical Review Research*, 4(2), 023082.
- Østfeldt, F. T., González-Ruiz, E. M., Hauff, N., Wang, Y., Wieck, A. D., Ludwig, A., ... & Lodahl, P. (2022). On-demand source of dual-rail photon pairs based on chiral interaction in a nanophotonic waveguide. *PRX Quantum*, 3(2), 020363.
- Nosan, Ž., Märki, P., Hauff, N., Knaut, C., & Eichler, A. (2019). Gate-controlled phase switching in a parametron. *Physical Review E*, 99(6), 062205.

IN PREPARATION

- Hauff, N. V., Tiranov, A., Wieck, A. D., Ludwig, A., ... & Lodahl, P. A Planar Nanophotonic interface for droplet GaAs quantum dots. *In Preperation*.

CONTENTS

Abstract v

Sammenfatning vii

Preface ix

List of publications xi

1 Introduction 1

2 Semiconductor Quantum Dots as Single Photon Sources 5

Introduction to InGaAs and GaAs semiconductor quantum dots as emitters and how their discretized electronic states can be employed as a single-photon source

2.1 Electronic Structure and Excitations in Quantum Dots 7

2.2 Optical Properties of Exciton- and Multiexciton Transitions 12

2.3 Excitation Schemes and Tuning 14

3 Planar Nanophotonic Devices and Waveguide QED 17

Introduction to planar nanophotonic devices and the basic theoretical framework of photon emission and light-matter interaction.

3.1 Planar Photonic Nanostructures 18

3.2 Quantum Dots as Two-Level Emitter 22

4 Topological Photonic Crystal Waveguides for Chiral Interfaces with Quantum Dots 31

This chapter presented the design, fabrication, and photonic characterization of topological photonic crystal waveguides for chiral light-matter interfaces based on a photonic analog of the Quantum Valley-Hall effect and InGaAs quantum dots.

4.1 Design and Fabrication 32

4.2 Photonic Characterization 35

4.3 Numerical Analysis by Finite Element Calculations 39

4.4 Potential of Topological Photonic Crystal Waveguides 41

5 Chiral Quantum Optics in Broken-Symmetry and Topological Waveguides 43

This chapter presents full-wave three-dimensional calculations to quantify the performance of conventional and topological photonic crystal waveguides as chiral emitter-photon interfaces. These results are important to the understanding of light-matter interactions in topological photonic crystal and design of efficient, on-chip chiral quantum devices.

This chapter and its appendix presents data, figures, and parts of text that have been published [1].

- 5.1 Photonic Crystal Waveguides as Quantum Chiral Interfaces 44
- 5.2 Photonic Band Diagrams and Dispersion 45
- 5.3 Directionality, Purcell Enhancement and Disorder-Induced Scattering 46
- 5.4 Overall performance of the chiral interfaces 50
- 5.5 Conclusions 52

6 A Platform for Planar Quantum Photonics with GaAs Droplet Epitaxy Quantum Dots 55

This chapter presents the layout of the first generation of planar photonic circuits with droplet-epitaxy-grown GaAs quantum dots embedded in a heterojunction membrane for charge-state control and tuning of the QD emission wavelength. Analyzing the photonic and accompanying electronic properties grants valuable insights into the performance and further development of this novel quantum photonic platform.

- 6.1 Design and Fabrication of Photonic Circuitry 56
- 6.2 Scanning Electron Microscope Characterization 60
- 6.3 Electric Characterization 64
- 6.4 Photonic Characterization 66
- 6.5 Considerations for Next-Generation Platforms 77

7 Spectroscopy of Droplet-Etched GaAs Quantum Dots in Planar Photonic Devices 79

This chapter presents the first planar platform for quantum photonics with droplet-etched GaAs quantum dots. Its properties, such as the quantum dot density, inhomogenous broadening, the viability of various quantum dot excitation methods, the ability of quantum dot charge-state and stark shift tuning, and the single-photon character of the quantum dot photoluminescence are examined based on a characteristic quantum dot in a line defect waveguide.

- 7.1 Above-Band Excitation and Spatial Mapping of Quantum Dots 80
- 7.2 Quasi-Resonant Excitation 85
- 7.3 Charge-State and Stark-Shift Control 86
- 7.4 Time-Resolved Spectroscopy 89

- 8 Resonant Excitation and Phonon-Sideband-Resolved Spectroscopy of Integrated Droplet-Etched GaAs Quantum Dot 95**
A thorough characterization of quantum dots is crucial for their application in quantum networks. This section characterizes essential properties of droplet-etched GaAs quantum dots integrated into nanophotonic devices, such as the linewidth and the pure dephasing rate under resonant excitation. Phonon-sideband-resolved spectroscopy reveals an elevated phonon-bath temperature to limit the quantum dots in their linewidth and the pure dephasing rate.
- 8.1 Spectroscopy with Resonant Excitation 96
 8.2 Phonon-Sideband-Resolved Spectroscopy 103
- 9 Droplet-Etched GaAs Quantum Dots in Planar Photonic Devices as Single Photon Source 111**
For the application in scalable quantum networks, quantum dots must (i) allow coherent manipulation, (ii) provide pure photoemission of single photons, and (iii) show high indistinguishability of subsequent emitted single photons. This chapter successfully demonstrates the operation of a droplet-etched GaAs quantum dots in a planar photonic device as a single photon source at elevated temperatures. Its high-temperature characterization provides insight into the platform's potential performance at low temperatures.
- 9.1 Coherent State Manipulation 112
 9.2 Single Photon Purity 113
 9.3 Two-Photon Interference 115
- 10 Conclusion and Outlook 121**
Conclusions and summary of the work carried out in this thesis, and an outlook towards future work for single photons from GaAs quantum dots in photonic crystal waveguides and topological waveguides for chiral light-matter interfaces.
- 10.1 Chiral Light-Matter Interfaces with Topological Photonic Crystal Waveguides 121
 10.2 Local Droplet Etched Gallium Arsenide Quantum Dots for Planar Quantum Photonics 122
- A Appendix 125**
- A.I Supportive Information and Theory for the Numerical Study on Chiral Light-Matter Interfaces in Photonic Waveguides 125
 A.II Wafers, Samples and Fabrication Recipe 135
 A.III Characterization of Topological Photonic Waveguides 146
 A.IV Experimental Setups and Equipment 150
 A.V Photonic Characterization of Concentric Waveguides 159
 A.VI Electronics 161
 A.VII Time Resolved Spectroscopy 162
 A.VIII Experimental Details for Continuous-Wave Resonance Fluorescence 171

A.IX Band Gap Temperature Tuning	179
A.X π -Pulse Characterization	180
A.XI Hong–Ou–Mandel Interferometry	181

List of Figures	185
------------------------	------------

List of Tables	204
-----------------------	------------

Bibliography	207
---------------------	------------

CHAPTER
1

INTRODUCTION

Deterministic quantum emitters able to generate multiphoton entangled states are essential building blocks for a plethora of quantum information applications [2–4], including quantum communication and measurement-based quantum computing. Solid-state spin-photon interfaces integrated into nanophotonic structures [5, 6] are especially promising as they can form a basic element of scalable photonic circuits [7] that enable on-chip quantum operations [8–10]. InGaAs quantum dots (QDs) [6, 11] integrated into planar nanophotonic circuits demonstrated significant technological achievements [12]. A critical component is the interface of a QD and a photonic crystal waveguide. The properties of both are vital in order to realize scalable photonic circuits [5].

However, several unavoidable mesoscopic and material constraints exist in the class of InGaAs QDs. Examples are the growth-induced strain, island-like asymmetric shapes [13, 14] and strain-enhanced material intermixing occurring during growth [15]. These constraints attribute to electron-spin decoherence and set limits to the fine-structure splitting and spin-photon entanglement fidelity.

Photonic crystal waveguides enable engineering the interaction of the light field of a guided mode and an embedded QD [5]. Enhancing the interaction strength has been key in demonstrating deterministic spin-photon interfaces [16]. Moreover, the design of broken-symmetry photonic crystal waveguides [17] has led to non-reciprocal devices [18] that are the foundation for quantum gates [19–21] and several protocols for quantum networks [22]. However, photonic crystal waveguides for non-reciprocal devices have yet not achieved as high interaction enhancements as conventional designs [23].

This thesis explores the potential of planar nanophotonic circuits with a novel type of QDs to overcome the limits of InGaAs QDs and the prospect of a new class of photonic crystal waveguides for efficient planar non-reciprocal devices.

Droplet Epitaxial-Grown GaAs Quantum Dots for Planar Quantum Photonics

Local droplet-etched GaAs QDs [24] integrated into photonic nanostructures are especially promising as spin-photon interface for quantum information technologies [25]. Their exceptional properties paved the way for the recent demonstration of two-photon interference between two completely separate GaAs QDs with an exceptional visibility of 93% [8].

The high degree of mutual coherence stems from high-quality pure materials and integration into a semiconductor heterojunction, achieving near-perfect charge control [26, 27]. GaAs QDs are of intrinsic low-strain [28–34] due to a lattice-matching growth method, dramatically lowering nuclear spectral inhomogeneities [35] contrasted by Stranski–Krastanov-grown InGaAs QDs. This makes it possible to bring electron spin coherences beyond 100 μs [36]. Moreover, GaAs QDs are larger in size (typically ≈ 100 nm in diameter and 5–8 nm in height), increasing the radiative rate and reducing the sensitivity to environmental fluctuations. Owing to their intrinsic pronounced spherical symmetry, the GaAs QDs exhibit near-zero fine-structure splitting [37]. Due to the low fine-structure splitting, polarization-entanglement fidelities of photons from the biexciton-exciton cascade [38–41] close to the most prominent sources based on spontaneous parametric down-conversion [42] are possible. All these properties of GaAs QDs are vital to realizing deterministic spin-photon interfaces, directly useful for cluster state generation [43], and non-reciprocal photonic devices [44].

To achieve deterministic spin-photon interfaces, the integration into photonic nanostructures is crucial. Previously GaAs QDs integration into Fabry-Perot cavities based on distributed Bragg reflectors (DBR) [28, 30], circular Bragg gratings [38], and parabolic optical cavities [45] have been demonstrated. Despite the strong interest, integration into planar photonic nanostructures compatible with efficient charge control has yet to be demonstrated. However, the practical implementation of photonic crystal waveguides for GaAs QDs with emission wavelength 780 nm sandwiched between AlGaAs barriers is challenging, due to structural feature sizes between 40–50 nm, below the state-of-the-art nanofabrication limit of 56 nm [46].

This thesis demonstrates the charge state and optical transition energy control of local droplet-etched GaAs QDs [26] integrated into photonic crystal waveguides.

Topological Photonic Crystal Waveguides for Chiral Quantum Optics

Maxwell's equations that describe light propagation in all-dielectric media, as in QD-based scalable photonic devices, obey time-reversal symmetry. This symmetry demands that the electric field in the forward direction is the complex conjugate of the electric field in the backward direction. However, light-scattering and photoemission from a QD are described by a Hamiltonian that is not time-reversal symmetric [47]. In a one-dimensional waveguide, the symmetry between the interaction of a QD's dipole with right- and left-propagating modes can be broken. The condition referred to as chiral interaction corresponds to forward and backward

propagating modes scattering with different strengths [44]. In extreme cases, this interaction can also become unidirectional, or in other words, the QD's dipole couples only to a single direction. In this situation, the dipole radiation will be directional, referred to as chiral emission.

Chiral light-matter interactions enable non-reciprocal devices and circuits, such as optical isolators [18], circulators [48–50] and quantum gates [19–21] and are the foundation for several protocols for quantum networks [22]. In photonic-crystal waveguides, this directionality arises from the interaction of elliptical dipoles with finely structured light fields of the guided mode [18, 20, 23, 51]. An essential requirement to realizing scalable chiral quantum devices is the development of optical waveguides exhibiting slow light, circular polarization, low loss, and negligible backscattering [7, 44, 52].

A concurrent development has been expanding the concept of topological order, particularly robust transport, in condensed matter [53–55] to the field of optics and nanophotonics [56–58]. Topological photonic interfaces are formed at the boundary between topologically distinct photonic crystals and support light guidance in counterpropagating modes, forming a photonic crystal waveguide of topological nature. Recently, a number of topological photonic crystal waveguides have been proposed and demonstrated, ranging from the microwave region to the near-infrared region [59–72]. The helical character of the guided modes naturally suggests the possibility of a chiral topological photonic interface.

Notable developments in the field of topological waveguides are the demonstration of low-loss guiding of light around tight corners [65, 73–75], robust transport despite the presence of defects [76], integration with passive photonic elements [75], and fiber-to-chip couplers [73, 75]. The robustness against tight bends, is attractive for forming low-loss, compact-footprint photonic devices [77, 78].

Principal compatibility with embedded QDs has been demonstrated and has been employed to probe the waveguide transmission [73, 74]. Recently, chiral coupling of QDs to topological waveguides has been demonstrated [73, 77, 78]. All-dielectric topological photonic systems, compatible with QD-based photonic devices, are time-reversal symmetric and therefore do not feature genuine topological protection [79]. Nevertheless, all-dielectric topological photonic crystal waveguides can outperform conventional waveguides [1] for realizing integrated non-reciprocal single-photon devices for scalable complex quantum circuits and networks. However, topological waveguides have not been implemented in quantum photonic platforms which feature electronic charge state control and dipole transition frequency tuning. These features are essential for realizing non-reciprocal devices for scalable quantum networks and their exploitation in non-reciprocal photonic devices.

This thesis demonstrates topological photonic crystal waveguides for chiral light-matter interface with InGaAs QDs. Furthermore, the performance of topological waveguides as chiral light-matter interface is explored, using full vectorial three-dimensional finite-element calculations and rigorous disorder-induced incoherent backscattering theory.

Outline of the Thesis

Chapter 2 and 3 introduce the basic theoretical framework of photo emission, light-matter interaction, and planar nanophotonic devices and highlight important aspects of InGaAs and GaAs quantum dots relevant to this thesis.

Topological photonic crystal waveguides for chiral light-matter interface with state-of-the-art InGaAs QDs are presented in chapter 4. The numerical analysis of the performance of topological waveguides as chiral light-matter interface is presented in chapter 5.

The design, fabrication, and characterization of the electronic and photonic properties of the planar nanophotonic platform are presented in chapter 6. Chapter 7 presents the spectroscopy of QDs in planar devices, charge state, and optical transition energy control. Chapter 8 presents resonant excitation and phonon-sideband-resolved spectroscopy of a QD in a photonic crystal waveguide. The operation of a GaAs droplet epitaxy quantum dots in a planar photonic device as a single photon source is demonstrated in chapter 9.

A final discussion of the work carried out in this thesis and an outlook toward future work are presented in chapter 10.

SEMICONDUCTOR QDs AS SINGLE PHOTON SOURCES

Introduction to InGaAs and GaAs semiconductor quantum dots as emitters and how their discretized electronic states can be employed as a single-photon source

For many quantum-optics experiments, having a discrete and anharmonic electronic spectrum is necessary since it allows the generation of single photons by having an electron move between two levels. Creating and modifying atom-like electronic states in quantum dots (QDs) provides numerous possibilities for integrated quantum-photonics devices.

QDs in the family of InAs/GaAs/AlAs III-V semiconductors form excellent sources of indistinguishable single-photons and host single electronic spins. In comparison with other single-photon emitters, QDs have been demonstrated to surpass a combination of metrics of performance [7, 80] as a resource in scalable quantum networks [2, 5]. Among these metrics are brightness, single-photon purity, coherence, and repetition rate [6, 38, 81–84]. These excellent photonic properties can be extended further by trapping electrons and holes to the QD, enabling photon-photon [20], spin-photon [85], and spin-spin [86] entanglement. These developments are underpinned by, 1) a self-assembly process to create nano-scale QDs, 2) a heterostructure design, and 3) high-quality material.

The established platform consists of Stranski-Krastanov grown InGaAs QDs [89] embedded in GaAs, achieving a bright, fully deterministic source of indistinguishable photons of long coherence time and narrow linewidths [7, 18, 90–94], integrated into a planar photonic chip. Figure 2.1a) shows a scanning tunnelling microscope image of a Stranski-Krastanov grown InGaAs QD. Spin coherence times have been achieved that allow for the emission of multiple photons within the spin coherence

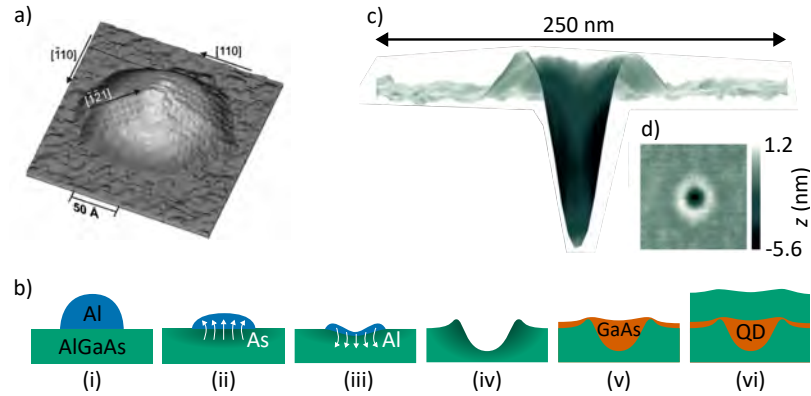


Figure 2.1: Figure a) shows a scanning tunneling microscope image of a Stranski-Krastanov InGaAs QD, grown on GaAs. Image from [87]. Figure b) shows schematics of the growth process of droplet-epitaxy grown GaAs QDs, adapted from [88]: (i) Al is deposited under low arsenic pressure, forming droplets on the surface of the AlGaAs substrate; (ii) dissolution of As from the substrate and concurrent (iii) diffusion of Al into the substrate; (iv) high in-plane symmetry nanoholes etched into the AlGaAs substrate; (v) overgrown with GaAs; (vi) capping with AlGaAs. Figures c) and d) show the cross-section and top view of an AFM image of a droplet-epitaxy-grown GaAs QD. These images are from [40]. In figure c), the color scale reflects the local surface inclination (white for flat areas and black for maximal inclination). The aspect ratio is set to 17 to highlight the shape of the etched hole.

time, which is essential for the scalability of advanced multi-photon entanglement sources [95]. However, the InGaAs QDs emit at wavelengths between 900 nm and 1200 nm, a spectral regime lying inconveniently between the telecom wavelengths (1300 nm and 1550 nm) and the wavelength where silicon detectors have a high efficiency (600 nm to 800 nm) [96]. It is therefore important to develop QD quantum photonics to extend the wavelength range toward shorter and longer wavelengths.

Droplet-epitaxy-grown GaAs QDs embedded in AlGaAs [25, 29, 97, 98] emission contains the wavelengths of the D_1 and D_2 of rubidium vapor-based quantum-memory [99] and are within the peak quantum efficiency of silicon detectors. Furthermore, GaAs QDs typically have more symmetric shapes [29, 37], facilitating the creation of polarisation-entangled photon pairs from the biexciton cascade [38, 100, 101].

Figure 2.1b) shows schematics of the growth steps. Al is deposited on the AlGaAs substrate under low As pressure, which leads to the formation of Al nano-droplets. The concurrent dissolution of As from the substrate and diffusion of Al into the substrate leads to the formation of nanoholes. Figure 2.1c) and d) show atomic force microscope images of droplet-etched nanohole with high in-plane symmetry. The hole is epitaxially filled with GaAs. Due to the weak intermixing between the two materials, the final GaAs QD takes the symmetric shape of the etched hole. The filled holes are then capped off with AlGaAs to obtain isolated QD with three-dimensional carrier confinement. The growth process of the QDs presented in this thesis is further described in [26].

While previous GaAs QDs suffered from the population of optical active DX centers [102] in the conduction band, GaAs QDs with sufficient low Al-concentration in the barrier material AlGaAs have been achieved meeting the challenge of unpopulated DX centers at cryogenic temperatures [26]. Blinking-free, single-photon emission [27, 103] and optical linewidths close to the transform limit [27] have been demonstrated. The recent demonstration of two-photon interference with near-unity visibility (93.0%) using photons from two completely separate GaAs QDs [8] shows a route to the realization of generation of coherent single photons in a scalable way.

The high level of strain in the widely used InGaAs QDs complicates the interaction of an electron spin with the nuclear spins on account of the atomic site-specific quadrupolar interaction [32, 104–106]. In contrast, GaAs QDs have improved electron spin coherence [27, 32, 36, 105, 107] due to lower strain [25, 31–34]. Recently, prolonging of the spin dephasing time has been demonstrated, achieving lifetimes $T_2 = 113 \mu\text{s}$, several orders of magnitude above the radiative lifetime [36]. In this case, in combination with optical cavities [108] and photonic crystal waveguides [16], droplet GaAs QDs can potentially serve as fast, high-fidelity sources of spin-photon pairs and cluster states [109].

In this chapter the electrical and optical properties of droplet-epitaxial-grown GaAs and Stranski-Krastanov InGaAs QDs are described. Stranski-Krastanov InGaAs QDs are implemented into the topological photonic waveguides presented in the chapter 4. Droplet-epitaxy grown GaAs QDs, are extensively studied in the chapters 6, 7, 8, and 9.

2.1 ELECTRONIC STRUCTURE AND EXCITATIONS IN QUANTUM DOTS

The fundamental optical excitation in a QD consists of an electron in the conduction band and a hole in the valence band. The exciton, is a correlated electron-hole pair bound by direct and exchange Coulomb interaction. In small QDs, the motion of electrons and holes is dominated by quantum confinement, which implies that they are mutually independent, but exciton effects are required to explain the fine structure of the optically active states [5].

The unfilled orbital shells of atomic Al, Ga, In, and As show a $\bar{F}43m$ configuration in GaAs and in the other relevant binary and ternary alloys. Spin-orbit effects break the 3-fold degeneracy and shift the valence band to lower energy. The invariance of the spin-orbit interaction with respect to the time-reverse operation leads to the Kramers degeneracy of the light- and heavy-hole bands [110, 111]. The heterojunctions of InGaAs in GaAs and GaAs in AlGaAs have type-I energy-band alignment. This is essential for efficient interaction with light and allows for quantized states for electrons and holes.

Typically, the aspect ratio of QDs is larger than unity and the dominant quantization axis is the growth direction. This lifts Kramer's degeneracy of the heavy-hole and light-hole bands, shifting the heavy-hole upwards. Consequently, the transitions from the conduction band to the heavy-hole band have the lowest energy.

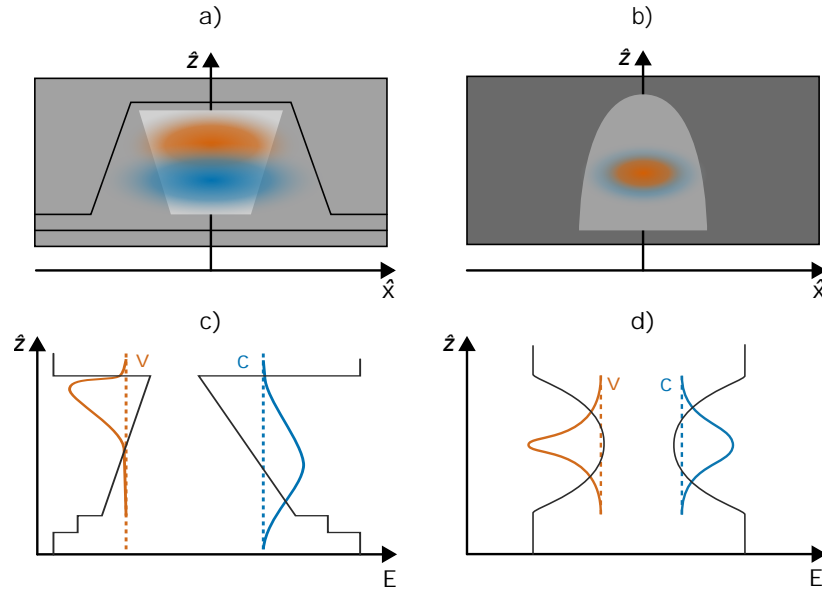


Figure 2.2: Schematics of the structural properties of Stranski-Krastanov-grown InGaAs QDs and drop-epitaxy grown GaAs QDs. The confinement potentials, where dark, neutral, and bright gray indicate AlGaAs, GaAs, and InAs are shown in figure a) for Stranski-Krastanov-grown InGaAs QDs and b) for drop-epitaxy grown GaAs QDs. Schematics of the electron and hole wave functions are shaded blue and red oval. The wave functions along the growth axis \hat{z} are shown in figure c) for Stranski-Krastanov-grown InGaAs QDs and d) for drop-epitaxy grown GaAs QDs. For Stranski-Krastanov QDs, the electron and hole wavefunctions have a significant offset in their center of mass, due to an asymmetric confinement potential a pyramidal shape [112]. In contrast to unstrained GaAs QDs, the materials intermix significantly during growth, leading to strain that varies throughout the QD.

For InGaAs QDs, the intrinsic strain lifts the degeneracy further. Neglecting the light-hole band is often a good approximation. However, in QDs with a pronounced structural asymmetry, the hole-masses are no longer a good quantum number resulting in substantial band mixing [113, 114]. In contrast, for the highly symmetric GaAs QDs, the light- and heavy-hole mixing is minimal [115, 116] and the character of the hole ground state is easily controllable by application of external stress [115, 117].

The full theoretical description and its experimental verification remains challenging. For the conditions relevant for quantum-optics experiments, i.e., QDs at low temperatures, and small carrier populations, many features of QDs can be described remarkably well by using a simple two-band effective-mass model, where only the heavy-hole valence band and the conduction band are included [5].

2.1.1 The Transition Matrix Element

The interaction strength of a QD with light is described by the transition matrix between the ground and excited states. This may also be expressed as a transition dipole moment. For QDs, the transition dipole moment can be controlled by modifying the exciton's wave function. The quantum state of an electron in the conduction

band (index c) or heavy-hole valence band (index v) consists of three parts,

$$|\Psi_{c/v}\rangle = |F_{c/v}\rangle |u_{c/v}\rangle |\alpha_{u/c}\rangle, \quad (2.1)$$

where $|F_{c/v}\rangle$, $|u_{c/v}\rangle$, and $\alpha_{u/c}$ is the envelope wave function, the electronic Bloch function evaluated at the Γ point of the band structure, and the spin state, respectively. The envelope wave function is obtained from the effective-mass Schrödinger equation. The relevant quantity derived from equation 2.1 describing spontaneous emission is, therefore, the momentum matrix element $\mathbf{P} = \langle \Psi_u | \mathbf{p} | \Psi_c \rangle$ [5, 118]:

$$\mathbf{P} = \langle F_u | F_c \rangle \langle u_u | \mathbf{p} | u_c \rangle \langle \alpha_u | \alpha_c \rangle, \quad (2.2)$$

where $\mathbf{p} = -i\hbar\nabla$ is the momentum operator. In the electron-hole picture, the decay of an electron from the conduction band to the valence band is viewed as the recombination of an electron and a hole [119]. Here, the electron and hole pseudospin states are introduced (keeping the envelope wave function implicit), which describe the total angular momentum of the Bloch functions and the spin,

$$\begin{aligned} |\uparrow\rangle &= |u_c\rangle |\uparrow_e\rangle, \\ |\downarrow\rangle &= |u_c\rangle |\downarrow_e\rangle, \\ |\uparrow\rangle &= |u_h\rangle |\uparrow_h\rangle, \\ |\downarrow\rangle &= |u_h\rangle |\downarrow_h\rangle, \end{aligned} \quad (2.3)$$

where the arrows denote the projected spin of an electron (hole) \uparrow (\uparrow) onto the \hat{z} -axis along the semiconductor growth direction. In experiments transitions obeying for optical transitions rules have been observed to be dominant [118]. The conduction and hole Bloch functions inherit the symmetry of the atomic orbitals, determining the polarization of the dipole moment [5]. The magnitude of the dipole moment depends on the wave-function overlap $\langle F_v | F_c \rangle$, which can be controlled by, e.g., external static electric fields, and the bulk semiconductor's Kane energy [120]. QDs are most often grown on (001) substrates where the symmetry leads to in-plane anisotropic confinement potentials even for rotational symmetric QDs [114]. The preferential elongation is along $[11\bar{1}]$ [89].

The exchange interaction breaks the four-fold degeneracy of the excitonic states (a single bound electron-hole pair) completely [121]. The states are commonly denoted in quantum optics literature as [5]

$$\begin{aligned} |X_b\rangle &= \frac{1}{\sqrt{2}} (|\uparrow\downarrow\rangle - |\downarrow\uparrow\rangle), \\ |Y_b\rangle &= \frac{1}{\sqrt{2}} (|\uparrow\downarrow\rangle + |\downarrow\uparrow\rangle), \\ |X_d\rangle &= \frac{1}{\sqrt{2}} (|\uparrow\uparrow\rangle - |\downarrow\downarrow\rangle), \\ |Y_d\rangle &= \frac{1}{\sqrt{2}} (|\uparrow\uparrow\rangle + |\downarrow\downarrow\rangle). \end{aligned} \quad (2.4)$$

The excitonic states' labels indicate allowed dipole transitions into the ground state $|g\rangle$ (bright, b) and transitions involving spin-flip or non-radiative decay processes (dark, d). The dipole moment orientation of $|X_b\rangle$ and $|Y_b\rangle$ is along the \hat{x} - and \hat{y} -axis, perpendicular to the growth direction.

The energy separation between the two bright states $|X_b\rangle$ and $|Y_b\rangle$ is referred to as fine structure splitting E_{fss} in its atomic analogy. For InGaAs, the fine structure splitting is typically on the order of $10\ \mu\text{eV}$ to $100\ \mu\text{eV}$, whereas the splitting E_{db} between the two dark excitons is one to two orders of magnitude smaller [122, 123]. It has been shown that for the highly symmetric droplet-epitaxy grown GaAs QDs, the fine-structure splitting correlates with the shape and size of the QD [37, 124] and much smaller splittings, comparable to the radiative linewidth of the emission lines, have been observed [40].

QDs can contain multiple electrons and/or holes leading to additional transitions with different optical properties than single neutrally charged excitons. Multiple bound states may exist as solutions to the effective-mass equation for both the conduction and valence bands and these eigenstates are commonly denoted as s , p , and d shells, etc., in analogy with atomic physics. The approximate selection rule for the envelope wave functions $|F_{u/c}\rangle$ implies that only transitions between the same shell in the conduction and the valence band need to be considered [5].

2.1.2 Electronic structure of Multiexcitonic s -Shell States

In the s -shell only three types of excitonic quasiparticles exist due to the Pauli exclusion principle beyond the neutral exciton: two trion states of positive (two electrons and one hole) and negative charge (one electron and two holes), and the neutral biexciton (two electrons and two holes). The charge configuration, pseudospin state, and dipole-allowed transitions of these states are displayed in figure 2.3.

Biexcitons have the pseudospin configuration

$$|XX\rangle = |\uparrow\downarrow\uparrow\downarrow\rangle, \quad (2.5)$$

and can relax radiatively to either of the bright excitons. Depending on which exciton the biexciton it decays to, a cascade of either two horizontally polarized or two vertically polarized dipole transition occur. The biexcitons decay cascade can be utilized as a source of polarization-entangled photons [20, 40]. A requirement is a sufficiently small fine-structure splitting, which can be reduced by growth [37, 124, 126, 127] or by applying various tuning schemes, such as electric fields [128] and strain [40].

Due to Kramer's theorem, the positive trion states $|X^+\rangle$ and negative trion states $|X^-\rangle$ are both doubly degenerate in the absence of an external magnetic field that would break time-reversal symmetry. For an electron-spin state $|\alpha_e\rangle$ (hole-spin state $|\alpha_h\rangle$) the trion states are

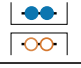
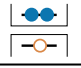
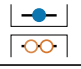


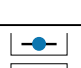

state name	charge config.	state	transitions			
			lin.	circ.	spin flip	non-rad.
biexciton		$ XX\rangle = \uparrow\uparrow\downarrow\downarrow\rangle$				
negative trion		$ X^-\rangle = \frac{1}{2} (\uparrow\downarrow\rangle - \downarrow\uparrow\rangle) u_v\rangle \alpha_h\rangle$				
positive trion		$ X^+\rangle = \frac{1}{2} (\uparrow\uparrow\rangle - \downarrow\downarrow\rangle) u_c\rangle \alpha_e\rangle$				
exciton		$ X_b\rangle = \frac{1}{\sqrt{2}} (\uparrow\downarrow\rangle - \downarrow\uparrow\rangle)$				
		$ Y_b\rangle = \frac{1}{\sqrt{2}} (\uparrow\downarrow\rangle + \downarrow\uparrow\rangle)$				
		$ X_d\rangle = \frac{1}{\sqrt{2}} (\uparrow\uparrow\rangle - \downarrow\downarrow\rangle)$				
		$ Y_d\rangle = \frac{1}{\sqrt{2}} (\uparrow\uparrow\rangle + \downarrow\downarrow\rangle)$				
electron		$ \bar{g}\rangle = u_c\rangle \alpha_e\rangle$				
hole		$ g^+\rangle = u_v\rangle \alpha_h\rangle$				
ground state		$ g\rangle$				

Figure 2.3: The lowest-energy confined states in QDs and their transitions. The full (empty) circles indicate the electron (hole) configuration in the conduction (valence) band s shells of the QD. The pseudospin states are discussed in the main text. The biexciton decays to one of the two bright exciton states by emission of a horizontally (H , green) or vertically (V , yellow) polarized photon. The negative (positive) trion decays to a single electron (hole) by emission of circularly polarized light with the helicity depending on the total electric charge state. Furthermore, spin-flip processes (dashed arrows) are generally present and can for some transitions be dominant [115, 123, 125]. Here, only the non-radiative decays of the bright excitons are indicated explicitly. The ordering of the states in the figure follows the occupancy, while the emission energies of the radiative excitonic complexes depend not only on the occupancy but also on confinement, correlation effects and manipulation Zeeman- and Stark-effect [5]. Figure adapted from [5].

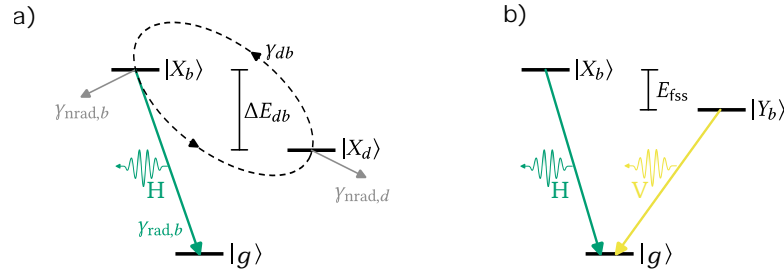


Figure 2.4: Examples of excitonic level schemes in QDs of relevance for quantum-optics experiments. (a) Fundamental three-level optical transition scheme of a single bright exciton, here $|X_b\rangle$, that can emit a photon by decaying radiatively to the ground state $|g\rangle$. Also non-radiative decay processes and coupling to the corresponding dark exciton state $|X_d\rangle$ through spin-flip processes may occur. The dark state can also re-combine nonradiatively. This level scheme leads to a biexponential decay of the emitted intensity. Figure adapted from [5].

$$\begin{aligned}
 |X^+\rangle &= \frac{1}{2} (|\uparrow\downarrow\rangle - |\downarrow\uparrow\rangle) |u_c\rangle |\alpha_e\rangle, \\
 |X^-\rangle &= \frac{1}{2} (|\uparrow\downarrow\rangle + |\downarrow\uparrow\rangle) |u_v\rangle |\alpha_h\rangle.
 \end{aligned} \tag{2.6}$$

The transition matrix elements for the decay of a trion to a single electron or hole are circularly polarized with the helicity depending on the spin of the additional carrier. As opposed to excitons they have no corresponding dark states. This makes them particularly interesting for interfacing spin and photonic degrees of freedom [32, 129].

2.2 OPTICAL PROPERTIES OF EXCITON- AND MULTIEXCITON TRANSITIONS

QDs are reliable sources of photons for quantum optics and various level schemes can be realized by different excitation and detection strategies. Figure 2.4 summarizes the most relevant levels and decay processes. In many applications the two three-level scheme of $|X_b\rangle$ ($|Y_b\rangle$), $|X_d\rangle$ ($|Y_d\rangle$), and $|g\rangle$ is Fig. 2.4 is applied, which suffices for describing single-photon emission. For chiral quantum photonics mainly three schemes are applied. Either the two excitons $|X_b\rangle$, $|Y_b\rangle$ are brought into resonance with external magnetic fields, or chiral dipole transitions of the biexciton or the the trion-cascades are utilized.

In the following, the key figures of merit of the three-level system are discussed and the single-photon-emission properties and coherence are summarized.

2.2.1 Quantum Dot Decay Dynamics

A detailed understanding of the dynamics of QDs is essential in order to exploit them as reliable photon sources in quantum-photonics applications. The various exciton

states can be coupled by spin-flip processes where, e.g., an exchange-mediated process between electron and hole [130] or spin-orbit coupling [131] flips the spin of the exciton, while longitudinal acoustic (LA) phonons provide or remove the energy difference between the two states. Spin-flip processes are generally much slower than the radiative decay processes so it is a good approximation to include only spin flips between $|X_b\rangle$ and $|X_d\rangle$ ($|Y_b\rangle$ and $|Y_d\rangle$). Transitions between $|X_b\rangle$ and $|Y_b\rangle$ require changing the spin of both the electron and the hole and are therefore negligible. This implies that $|X_b\rangle$ and $|X_d\rangle$ are decoupled and lead to two identical three-level schemes relevant for many chiral- and non-chiral quantum-photonics experiments involving a single (neutral) exciton in a QD. For the case of non-resonant excitation where both bright and dark exciton states are populated, the population ρ_b of the bright exciton follows a biexponential decay [132],

$$\rho_b(t) = A_f \exp(-\gamma_f t) + A_s \exp(-\gamma_s t), \quad (2.7)$$

where γ_f and γ_s are the fast and slow decay rates

$$\begin{aligned} \gamma_f &= \gamma_{\text{rad},b}/2 + \gamma_{\text{nrad},b}/2 + \gamma_{db}/2 + \sqrt{\gamma_{\text{rad},b}^2/4 + \gamma_{db}^2}, \\ \gamma_s &= \gamma_{\text{rad},b}/2 + \gamma_{\text{nrad},b}/2 + \gamma_{db}/2 - \sqrt{\gamma_{\text{rad},b}^2/4 + \gamma_{db}^2}, \end{aligned} \quad (2.8)$$

where $\gamma_{\text{rad},b}$ denotes the radiative decay rate for the bright exciton, $\gamma_{\text{nrad},b}$ ($\gamma_{\text{nrad},d}$) denotes the nonradiative decay rate of the bright (dark) exciton, γ_{db} is the bright-dark spin-flip rate, and under the assumption of symmetric non-radiative decays $\gamma_{\text{nrad},d} = \gamma_{\text{nrad},b} = \gamma_{\text{nrad}}$ [125]. The latter is a good approximation in the high temperature limit of phonon number densities in the energy regime comparable with the splitting of the dark and bright states $k_B T > \Delta E_{db}$, which is valid even in liquid helium cryogenics. Determining the population dynamics ρ_b of both states $|X\rangle$ and $|Y\rangle$ then allows for the extraction of the non-radiative decay rate γ_{nrad} , the radiative decay rates and γ_b as well as the rate between dark and bright states γ_{db} via the amplitudes A_f and A_s [5]. With this method, single QDs can be employed for mapping the local light-matter interaction strength [133, 134]. Trions and biexcitons do not have a fine structure and their population dynamics follows a single-exponential decay with no direct access to the non-radiative rates. Considerable variations in the spin-flip and non-radiative rates are generally found across a quantum-dot ensemble and between different growth runs. The described quantitative method of determining these processes is thus required.

For optical emission of InGaAs QDs in most quantum optics experiments, excitons in higher-lying states (p, d , and higher) are not relevant for optical emission because they decay to the s shells on a few-picosecond time scale by emission of phonons. In contrast, for droplet-epitaxy-grown GaAs QDs, reported relaxation times of excitons with an excited hole range from short values as low as ≈ 29 ps [135] to very high values of ≈ 1.8 ns [136]. Recently, the coherent control of high-orbital states of a hole has been demonstrated [137], indicating that the phonon-assisted

relaxation is strongly inhibited due to the mismatch between hole level separations and phonon energies. Thus, in a given experiment incorporating higher-order hole state excitation, the radiative decay may be dominated by the the slow relaxation of the excited hole state [136].

The Quantum Efficiency

The relative strength of the radiative and the non-radiative decays γ_{nrad} is quantified by the quantum efficiency η [5], as the relative fraction of recombination events leading to photon emission in an homogeneous reference medium $\gamma_{\text{hom}}^{\text{rad}}$,

$$\eta = \frac{\gamma_{\text{hom}}^{\text{rad}}}{\gamma_{\text{hom}}^{\text{rad}} + \gamma_{\text{nrad}}}. \quad (2.9)$$

The quantum efficiency typically approaches unity [18, 138], but the exact experimental quantification for both GaAs [139–145] and InGaAs QDs [146] is laborious and the theoretical modeling remains a challenge. Experiments on InGaAs QDs indicate that the non-radiative decay rate scales with the surface-to-volume ratio of the QD [147] and on the coupling strength of the QD to a charge reservoir. Furthermore, the mesoscopic symmetry of the QD and its surrounding lattice can introduce multipolar dipole contributions, which can alter the radiative and non-radiative decay dynamics [148]. Large variation in the non-radiative decay rate can occur and resemble important difference between the Stranski-Krastanov InGaAs with quantum efficiencies $\eta = 30\text{-}60\%$ [146] and Droplet grown GaAs QDs with quantum efficiencies exceeding $\eta > 70\%$ [142]. In photonic nanostructures the projected local density of optical states (LDOS) can be altered, as discussed in chapter 3. By modification of the LDOS the quantum efficiency of the QD can be modified [146] and becomes dependent on the particular location, wavelength, and orientation in a photonic structure [149]. Particularly, the influence of nonradioactive effects may be partially suppressed.

2.3 EXCITATION SCHEMES AND TUNING

A QD can be studied under above-band, quasi-resonant, phonon-assisted, or resonant (resonant fluorescence) excitation. Above-band excitation uses excitation energies above the band gap of the barrier material, and quasi-resonant excitation uses resonances with excited excitonic states, such as p -shell states. In above-band and quasi-resonant excitation, the energy difference between the excitation laser and the emitted photons allows effective filtering of the laser background spectrally, isolating the signal of a QD. However, these excitation methods are associated with the inevitable creation of additional carriers or phonons in the environment of the QD, degrading the QDs performance as a single photon source [28]. Thus, a QD is ideally characterized as a single photon source under phonon-assisted or resonant excitation. Additionally, for droplet-epitaxy-grown GaAs QDs, the slow relaxation of

excited hole states may resemble a bottleneck for the radiative decay dynamics [150], rendering only resonant and quasi-resonant excitation suitable for time-resolved spectroscopy. However, suppressing the laser background in resonant excitation can be challenging, as spectral filtering is not possible.

Integrating the QDs into the intrinsic layer of semiconductor heterostructure with a p-i-n-type of layout brings several advantages [129]. The built-in electric field reduces the current across the heterostructure, providing an effective charge noise reduction [27, 92]. Additionally, the application of an external bias voltage allows charge state control by Coulomb blockade [151–153] and in-situ tuning of the transition energy [27, 83, 107] by the quantum-confined Stark effect [154].

By controlling the charge state and transition energy it is possible to create a qubit with a well-defined spin state and control the interactions between QDs, which are important for the development of scalable quantum networks [2]. For spectroscopical characterization of a QD, charge- and transition energy control allows to effectively turn 'on' and 'off' the QD in a highly convenient manner for reliable excess to laser background measurements. Furthermore, a QD can be tuned conveniently into resonance with an excitation laser with high speed and precision, allowing efficient spectroscopical characterization.

Embedding InGaAs QDs in semiconductor heterojunctions of p-i-n and p-i-n-i-n layouts is an established and reliable method [152]. In contrast, charge noise and charge control has been a challenge in the platform of droplet-epitaxy-grown GaAs quantum dots previously. Recently, near-perfect charge control of charge-tunable GaAs QDs has been demonstrated [26, 27]. Charge stated tuning ranging from the two-times positively charged exciton X^{2+} to the eight-times negatively charged exciton X^{8-} has been achieved. Simultaneously, transition energy tuning of about a factor of four larger than the typical DC Stark shifts of InGaAs QDs has been observed.

PLANAR NANOPHOTONIC DEVICES AND WAVEGUIDE QED

Introduction to planar nanophotonic devices and the basic theoretical framework of photon emission and light-matter interaction.

Developing quantum systems, which are sensitive to decoherence from the environment and losses, demands designing and manufacturing high-quality hardware for quantum information networks poses a formidable challenge. Among the plethora of hardware platforms, photonics has emerged as a key technology in developing scalable quantum networks [4]. Particularly, nanophotonics offers a small footprint, modular architecture, efficient interfaces between individual building blocks, and the potential to incorporate mature photonic integrated circuit technology [2]. Recently, QDs in nanophotonic cavities and waveguides have demonstrated near-deterministic high-quality photon-emitter interfaces [6, 7, 80, 84, 155].

A significant advantage of the light-matter interface of QDs in planar nanostructures fabricated in semiconductor membranes, such as photonic waveguides, is the ability to route photons for further integration with different devices on the same chip, such as photon routers [156, 157], switches [158], phase shifters [159], and filters [160]. Moreover, the signal collection and laser excitation modes can be spatially separated, as seen in the following sections.

The following sections introduce the planar photonic structures and the basic theoretical framework of photon emission and light-matter interaction as relevant for this thesis.

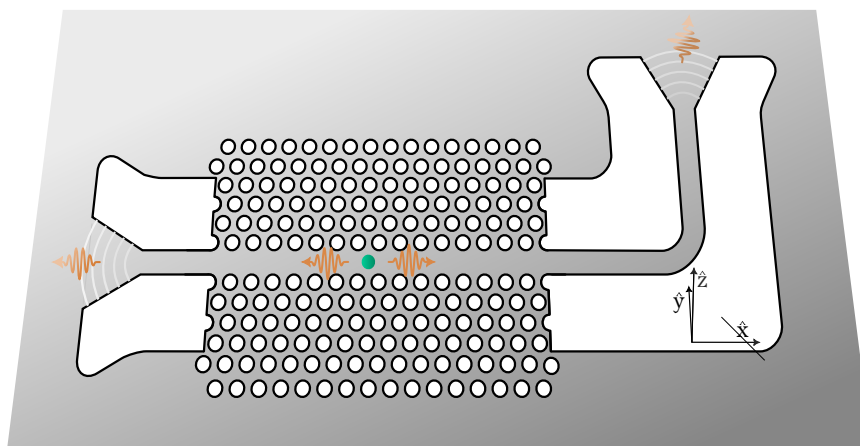


Figure 3.1: Schematic of a planar nanophotonic device often investigated in this thesis. A QD (green dot) embedded in the guided mode region of a line-defect (W_1) photonic crystal waveguide, emits photons into the guided mode. The emitted photons are routed in-plane by nanobeam waveguides (NBWs) towards shallow-etch grating (SEG) chip-to-fiber couplers, where they are scattered quasi-orthogonal out of plane. The photons are collected by a microscope objective and fiber coupled by free-space optics. The devices are aligned to the crystallographic axes of the membrane, such that the dipole orientations are oriented along with x and y . In chapter 4, topological photonic crystal waveguides in place of the W_1 waveguide are investigated.

3.1 PLANAR PHOTONIC NANOSTRUCTURES

In planar nanophotonics, QDs are located at the center of the semiconductor membrane. Embedding QDs into guided modes of photonic waveguide enables to engineer their light-matter interactions, as discussed in the following sections. Furthermore, interfacing QDs with nanophotonic waveguides enables in-plane routing of emitted photons to other nanophotonic structures [5, 7].

3.1.1 Elements of Nanophotonic Circuits

In this thesis, a modular architecture of planar nanophotonics devices is adopted, where photonic crystal waveguides implement the light-matter interaction with QDs and nanobeam waveguides (NBWs) [161] are employed for low-loss routing [157] of single photons to high efficiency shallow-etch gratings (SEG) [162]. A typical device of this thesis, a line-defect (W_1) photonic crystal waveguide [163] is shown in figure 3.1. The SEG chip-to-fiber couplers [162] are an adaptation from silicon-on-insulator photonics [164], replacing traditional circular gratings [16]. SEG are superior in their efficiency and back reflections into the NBW are strongly reduced. Moreover, the SEG couplers allow to suppress laser background by preferentially coupling one linear polarization and enable to spatially separate the excitation laser and the signal collection.

For GaAs QDs the, operating near 780 nm, the photonic circuit elements are adapted from the platform of InGaAs, operating near 930 nm. Their performance is examined in chapter 6.

3.1.2 Photonic Crystals

Photonic crystal waveguides are based on photonic crystals. A photonic crystal is a metamaterial that exhibits a periodic variation in its dielectric permittivity $\epsilon(\mathbf{r})$, allowing it to control the flow of light. Here, the periodic variation is achieved by creating a structure of periodically arranged holes in the semiconductor membrane, with periodicity on the order of the wavelength of light.

Bragg scattering is the key phenomenon in photonic crystals, similar to how X-rays are diffracted by the crystal lattice in a crystallography experiment. It arises from the periodicity of the structure, which allows the crystal to act as a natural diffraction grating for light waves. When a light wave is incident on the photonic crystal at a certain angle, the periodic structure of the crystal causes the wave to be reflected back in the opposite direction.

A photonic band gap opens if Bragg scattering is so pronounced that no modes exist for a range of frequencies. A complete photonic band gap inhibiting all modes for any propagation direction and polarization can be obtained only in photonic crystals with periodicity in all three dimensions. Importantly, for two-dimensional photonic crystals in high refractive-index contrast semiconductor membranes, pronounced pseudogaps exist that modify major parts of the optical modes. In these structures, the in-plane propagation of light is suppressed due to a two-dimensional photonic band gap, while out-of-plane leakage is limited to a narrow cone (light cone) of wave vectors.

For a through review on photonic crystals, see for example reference [161].

3.1.3 Conventional Photonic Crystal Waveguides

In planar quantum photonics with QDs, conventional and topological photonic crystal waveguides find application. Conventional photonic crystal waveguides operate on the principle of confining light spatially in-between photonic crystals. In quantum photonics, the line-defect (W_1) photonic crystal waveguide is frequently utilized, where a spatial confinement of a propagating mode is achieved by leaving out a line of holes in a photonic crystal with triangular lattice, that is, in the photonic crystallographic Γ - K direction. Despite its basic design, the W_1 enables to suppress a QD's coupling to non-guided modes due to the band gap of the photonic crystal and to simultaneously enhance the light-emitter coupling with the guided mode. The operation of QDs as an effective one-dimensional "artificial" atom has been demonstrated, where the QD interacts almost exclusively with just a single propagating optical mode [16].

The coupling of a QD with a guided mode, as discussed in section 3.2.1, depends on the local properties of the finely structured mode profile. The mode profile

of a system composed of mixed dielectric media are the steady-state solutions of Maxwell's equations, which resemble linear Hermitian eigenvalue problems [165]

$$\nabla \times \frac{1}{\epsilon(\mathbf{r})} \nabla \times \mathbf{H}(\mathbf{r}) = \left(\frac{\omega}{c}\right)^2 \mathbf{H}(\mathbf{r}), \quad (3.1)$$

where \mathbf{H} is the magnetic field, ω is the frequency, and c is the speed of light. The solutions are the electric $\mathbf{e}_{n,k}(\mathbf{r})$ Bloch modes (with magnetic field $\mathbf{h}_{n,k}(\mathbf{r})$) and eigenfrequencies $\omega_{n,k}$ of wavenumber k and mode index n , that satisfy the normalization by $\int d^3\mathbf{r} \mathbf{e}_{n,k}(\mathbf{r}) \mathbf{e}_{n,k}^*(\mathbf{r}) \epsilon(\mathbf{r}) = 1$. A band diagram, examples of mode profiles and the dispersion relation of a W1 are discussed in chapter 5.

The properties of a guided mode can be controlled by varying the parameters of the photonic crystal, such as the lattice constant and the radius of the holes. Moreover, dispersion engineering [161, 166] can be employed to design waveguides with specific properties, such as low dispersion and high confinement, and thereby engineer the light-emitter interaction. Band engineering the W1 towards high local circular polarization in the vicinity of high field regions and concurrent slow light for efficient chiral light-matter interfaces with QDs [18, 20, 23] has led to the glide-plane waveguide (GPW) design [17], examined in chapter 5.

3.1.4 Topological Photonic Crystal Waveguides

In conventional photonic waveguides, back-reflection on fabrication defects is a major source of unwanted feedback [167]. Scattering losses limit the experimental achievable light-matter interaction enhancements and hinders large-scale optical integration for photonic quantum information processing [44].

Recently, topological ideas for nanophotonic platforms branched off from exciting developments in the field of topological quantum matter of solid state physics [53, 54]. In the center of attention is the discovery of new phases of matter called topological insulators [55]. Topological insulators, being insulating in the bulk, conduct electricity on their surface without dissipation and backscattering, even in the presence of large impurities [58].

The underlying concept of topological effects in various fields is the geometric phase, which arises when a system parameter undergoes a closed cycle. First introduced to explain the behavior of light passing through a series of polarizers, this geometric phase plays a role in numerous physical phenomena, ranging from Foucault pendulums [168] to polarization in helical waveguides [169].

It has been proposed [60, 63] and demonstrated [62, 170] that the corresponding key mechanisms and features can be transferred to nanophotonic systems. Among these systems are waveguides based on edge states of topological photonic insulators of time-reversal symmetric (TRS) and non-symmetric nature [56, 57]. Unidirectional edge state waveguides transmitting electromagnetic waves without back-reflection even in the presence of arbitrarily large disorder have been demonstrated based on breaking TRS [59, 64, 171, 172]. However, breaking TRS can only be achieved by system modification which interfere with other functionalities of light-matter interfaces for

quantum information processing. For example, the typical approach of employing gyromagnetic materials obstructs the utilization of the magnetic fields as a degree of freedom to tune QDs of quantum networks to resonance [173].

Topological edge states of two-dimensional all-dielectric photonic crystals maintaining TRS have been proposed [56, 61, 68] and demonstrated [174]. Among them are edge states of topological photonic insulators mimicking the Quantum Spin-Hall effect and the Quantum Valley-Hall effect. The first only inhibits quasi-guided edge states and as such shows high loss [73] and strong coupling of QDs with non-guided modes [175]. In stark contrast, edge states of interfaces of topological photonic insulators mimicking the Quantum Valley-Hall effect show band edge states below the light line.

topological Photonic Valley-Chern Insulators

topological photonic Valley-Chern insulators, that is, triangular photonic crystals with broken inversion symmetry of non-zero Valley-Chern number, can be interfaced to form topological edge states localized along the interface in real space. A photonic crystal's insulator valley-Chern number $C_{v,n}^{K/K'}$ is derived for the K and K' symmetry points from the Bloch modes $\mathbf{e}_{n,\mathbf{k}}(\mathbf{r})$ of the photonic crystal by

$$C_{v,n}^{K/K'} = \frac{1}{2\pi} \int_{K/K'} d\mathbf{k} \Omega_n(k_x, k_y), \quad (3.2)$$

where n denotes the Bloch mode index, K or K' denotes the integral over halves of the Brillouin zone containing the high-symmetry points K or K' of the photonic crystal, $\mathbf{k} = (k_x, k_y, k_z)$ is the wavevector, and Ω_n is the two-dimensional Berry curvature, defined by

$$\Omega_n(k_x, k_y) = \frac{\partial A_{n,k_y}}{\partial k_x} - \frac{\partial A_{n,k_x}}{\partial k_y}, \quad (3.3)$$

where $A_n = (A_{n,k_x}, A_{n,k_y})$ is the Berry connection defined by

$$\begin{aligned} A_{n,k_x} &= i \int d^2\mathbf{r} \frac{\partial \mathbf{e}_{n,\mathbf{k}}(\mathbf{r})}{\partial k_x} \cdot \mathbf{e}_{n,\mathbf{k}}^*(\mathbf{r}) \epsilon(\mathbf{r}) \\ A_{n,k_y} &= i \int d^2\mathbf{r} \frac{\partial \mathbf{e}_{n,\mathbf{k}}(\mathbf{r})}{\partial k_y} \cdot \mathbf{e}_{n,\mathbf{k}}^*(\mathbf{r}) \epsilon(\mathbf{r}) \end{aligned} \quad (3.4)$$

At an interface, an edge state emerges⁽ⁱ⁾ if the difference of the valley-Chern numbers of the band above and the band below the bandgap (index n and n') of the photonic crystal $\left| C_{v,n'}^K - C_{v,n}^K \right| = \left| C_{v,n'}^{K'} - C_{v,n}^{K'} \right|$ is non-zero.

In this thesis, the waveguides formed by an edge states of an interface of a bearded and in a zigzag-type configuration are referred to as the bearded interface waveguide (BIW) and the zigzag interface waveguide (ZIW). Both have been experimentally

(i) In accordance with the bulk-edge correspondence.

demonstrated and feature highly confined light, transverse-electric-like modes of slow light, points of high local circular polarization, allow for sharp-edge bending, and show indications of high β factors [65, 68, 74, 75, 78, 174, 176, 177].

The ZIW and BIW and their application for chiral light-matter interactions are subjects of chapter 4 and 5.

3.2 QUANTUM DOTS AS TWO-LEVEL EMITTER

The model of a two-level emitter is useful to describe the light-matter interactions of a QD embedded in a photonic waveguide. This section briefly introduces some concepts of the textbook description of a two-level emitter [5, 178, 179] in the context of a QD in a photonic waveguide, covering spontaneous emission, interaction enhancement, directional coupling, dephasing, and line-broadening mechanisms.

3.2.1 Equations of Motion for Spontaneous Emission

The Hamiltonian for a two-level system with an excited state $|e\rangle$, ground state $|g\rangle$, transition energy $\hbar\omega_0$, coupled to a continuum of radiation modes of frequency $\omega_{\mathbf{k}}$ of wavevector \mathbf{k} via an electric dipole \mathbf{d} in the rotating wave approximation is

$$\mathcal{H} = \frac{1}{2}\hbar\omega_0\sigma_z + \hbar \sum_{\mathbf{k}} \omega_{\mathbf{k}} \left(a_{\mathbf{k}}^\dagger a_{\mathbf{k}} + \frac{1}{2} \right) + \left(g_{\mathbf{k}}\sigma_+ a_{\mathbf{k}} e^{i(\omega_0 - \omega_{\mathbf{k}})t} + \text{H.c.} \right), \quad (3.5)$$

where $a_{\mathbf{k}}$ and $a_{\mathbf{k}}^\dagger$ are the quantized field operators, $\sigma_z = |e\rangle\langle e| - |g\rangle\langle g|$ is the inversion operator, $\sigma_+ = |e\rangle\langle g|$ and $\sigma_- = |g\rangle\langle e|$ are the inversion and transition operators, and $g_{\mathbf{k}}$ is the electric dipole matrix element, i.e., the light-matter coupling strength, H.c. denotes the Hermitian conjugate. The coupling strength contains the electric field strength of the quantized electromagnetic radiation mode $\mathbf{E}_{\mathbf{k}}$

$$g_{\mathbf{k}}(\mathbf{r}_0) = i\mathbf{d}\mathbf{E}_{\mathbf{k}}^*(\mathbf{r}_0)/\hbar, \quad (3.6)$$

where the QD position is denoted by \mathbf{r}_0 and with two polarization components for each wave vector \mathbf{k} .

In the case of coupling to a one-dimensional photonic waveguide, the electric field strength of the quantized electromagnetic radiation mode $\mathbf{E}_{\mathbf{k}}(\mathbf{r})$ can be expressed by the Bloch functions $\mathbf{e}_{n,k}(\mathbf{r})$,

$$\mathbf{E}_{\mathbf{k}}(\mathbf{r}) = \sqrt{\frac{\hbar\omega_{\mathbf{k}}}{2\epsilon_0}} \sum_{n,k} \left(a_{\mathbf{k}} e^{-i\omega_{\mathbf{k}}t} \mathbf{e}_{n,k}(\mathbf{r}) \right), \quad (3.7)$$

where n is the waveguide mode index, ϵ_0 is the vacuum permittivity, and where indexing over the wavenumber k and mode index n has replaced indexing over the wavevector \mathbf{k} . Discussing single-mode waveguides, the photonic waveguide mode index n is omitted in the following for simplicity.

Spontaneous Emission

The formalism above is suitable for describing spontaneous emission or single-photon absorption. The equation of motion for the ansatz $|\Psi(t)\rangle = c_e(t) |e, \{0\}\rangle + \sum_k c_{g,k}(t) |g, \{1_k\}\rangle$ in the interaction picture is

$$\begin{aligned} \frac{\partial}{\partial t} c_e(t) = & - \sum_k |g_k(\mathbf{r}_0)|^2 \int_0^t dt' c_e(t') e^{i(\omega_0 - \omega_k)(t-t')} \\ & - i \sum_n g_k^*(\mathbf{r}_0) c_{g,k}(0) e^{i(\omega_0 - \omega_k)t}, \end{aligned} \quad (3.8)$$

where $\{0\}$ denotes all continuum radiation modes in the vacuum state and $\{1_k\}$ denotes a single photon in the radiation mode with wavenumber k .

The equation of motion can be expressed in terms of the Green's tensor \mathbf{G} , which solves Maxwell's wave equations for a point-like source at position \mathbf{r}' and of frequency ω

$$\nabla \times \nabla \mathbf{G}(\mathbf{r}, \mathbf{r}', \omega) - \frac{\omega^2}{c^2} \epsilon(\mathbf{r}) \mathbf{G}(\mathbf{r}, \mathbf{r}', \omega) = \frac{\omega^2}{c^2} \mathbf{I} \delta(\mathbf{r} - \mathbf{r}'), \quad (3.9)$$

where ϵ is the permittivity, c is the speed of light, \mathbf{I} the unity tensor and δ the Dirac delta function. Expansion of the Green's function in photonic waveguide's Bloch modes yield

$$\mathbf{G}(\mathbf{r}, \mathbf{r}', \omega) = \sum_k \omega^2 \frac{\mathbf{e}_k(\mathbf{r}) \odot \mathbf{e}_k^*(\mathbf{r}')}{\omega_k^2 - \omega^2}, \quad (3.10)$$

where the " \odot " symbol denotes the outer product. Inserting equation 3.10 into the of the equation of motion, equation 3.8, yields

$$\frac{\partial}{\partial t} c_e = - \frac{d^2}{2\epsilon_0 \hbar} \int_0^\infty d\omega \omega \rho_{\text{LDOS}}(\mathbf{r}_0, \omega, \hat{\mathbf{e}}_d) \int_0^t dt' c_e(t') e^{i(\omega_0 - \omega_k)(t-t')}, \quad (3.11)$$

where $\rho_{\text{LDOS}}(\mathbf{r}_0, \omega, \hat{\mathbf{e}}_d)$ is the projected local density of optical states (LDOS) [180] for a dipole orientation described by the unity vector $\hat{\mathbf{e}}_d$. The LDOS is defined by

$$\rho_{\text{LDOS}}(\mathbf{r}, \omega, \hat{\mathbf{e}}_d) = \frac{2}{\pi \omega} \text{Im} \left(\hat{\mathbf{e}}_d^* \cdot \mathbf{G}(\mathbf{r}, \mathbf{r}, \omega) \cdot \hat{\mathbf{e}}_d \right) \quad (3.12)$$

which describes the nanophotonic environment of the photonic waveguide. The LDOS specifies the number of optical states at the frequency ω per frequency bandwidth and volume as experienced by the QD at its position r_0 .

Under the Markov approximation, that is, back-action from the radiation reservoir is neglected and the product $\omega \rho_{\text{LDOS}}$ is constant over the frequency contained in the QD's linewidth. As a result, the decay rate of the excited state is [5]

$$\gamma_{\text{rad}}(\mathbf{r}_0, \omega_0, \mathbf{d}) = \frac{\pi d^2}{\epsilon_0 \hbar} \omega_0 \rho_{\text{LDOS}}(\mathbf{r}_0, \omega, \hat{\mathbf{e}}_d) \quad (3.13)$$

The decay rate is directly proportional to LDOS.

The Purcell Effect in Photonic Crystal Waveguides

The ratio of the decay rate of a QD coupled to a photonic waveguide mode γ_{rad} (equation 3.13) the decay rate, located in a homogeneous medium $\gamma_{\text{rad}}^{\text{hom}}$ defines the Purcell factor [181]

$$F_{\text{P}}(\mathbf{r}_0, \omega, \hat{\mathbf{e}}_{\text{d}}) = \frac{\gamma_{\text{rad}}}{\gamma_{\text{rad}}^{\text{hom}}}. \quad (3.14)$$

In a photonic crystal waveguide, suppression and enhancement of the decay rate can occur. Assuming that the emission of a QD is completely into the photonic crystal waveguide, the Green's function can be derived analytically [182] and related to the Green's function of the homogeneous medium, allowing to express the Purcell factor as

$$F_{\text{P}}(\mathbf{r}_0, \omega_0, \hat{\mathbf{e}}_{\text{d}}) = \frac{3\pi c^2 a n_g(\omega_k)}{2\omega_k^2 \sqrt{\epsilon(\mathbf{r}_0)}} \left| \hat{\mathbf{e}}_{\text{d}}^* \cdot \mathbf{e}_k(\mathbf{r}_0) \right|^2, \quad (3.15)$$

where a is the lattice constant of the photonic crystal, $n_g(\omega_k) = c/v_g(\omega_k)$ is the group index and $\omega_k = \omega_0$ is the eigenfrequency of the Bloch mode of wavenumber k . Equation 3.15 expresses the dependence of the light-matter interaction on the projection of the dipole onto the finely structured electric field of the waveguide's Bloch mode at the QD location \mathbf{r}_0 . Moreover, the group velocity (slow light) and the mode confinement (large Bloch mode amplitude) can be utilized to achieve high enhancement [5].

Waveguide Coupling Efficiency: The β -factor

The probability that the preparation of a bright exciton state leads to the emission of a photon in the desired photonic waveguide mode is described by the β -factor [5]

$$\beta = \frac{\gamma_{\text{wg}}}{\gamma_{\text{wg}} + \gamma_{\text{ng}} + \gamma_{\text{nrad}}}, \quad (3.16)$$

where γ_{ng} is the loss rate of coupling to all non-guided modes, such as photonic crystal bulk modes or modes of the light cone, γ_{nrad} is the rate of intrinsic nonradiative recombination, as discussed in chapter 2, and γ_{wg} is the rate of spontaneous photon-emission into the waveguide mode. In photonic crystal waveguides, the two-dimensional photonic bandgap suppresses γ_{ng} , while enhancement of the LDOS can partially suppress nonradiative (γ_{nrad}) effects by enhancing γ_{ng} . Experimentally, near-unity waveguide coupling with $\beta \approx 98\%$ has been demonstrated [16]. However, the β -factor is highly spatially dependent on the LDOS [134].

Directional Coupling in Photonic Crystal Waveguides

Maxwell's equations in all-dielectric media, such as a photonic waveguide, obey time-reversal symmetry (TRS). TRS demands that the electric field in the forward direction

(wavenumber k) is the complex conjugate of the electric field in the backward direction (wavenumber $-k$)

$$\mathbf{e}_k(\mathbf{r}) = \mathbf{e}_{-k}^*(\mathbf{r}). \quad (3.17)$$

However, light-scattering and photoemission from a QD are described by a Hamiltonian that is not time-reversal [47]. In a one-dimensional waveguide, the symmetry between the interaction of a QD's dipole with right- and left-propagating modes can be broken. The condition referred to as chiral interaction corresponds to forward and backward propagating modes scattering with different strengths [44]. An ideal chiral interface for quantum light-matter interactions, as discussed in chapter 5, is characterized by several properties. First and foremost, emission or scattering of photons by a QD into the counter-propagating modes left (L) or right (R) should be highly asymmetric with radiative decay rates $\gamma_{\text{wg},L} \gg \gamma_{\text{wg},R}$, or vice versa. This directionality occurs when the overlap of circular (or elliptical) transition dipoles with the two counter-propagating modes differs and is quantified by the directionality,

$$D = \frac{\gamma_{\text{wg},L} - \gamma_{\text{wg},R}}{\gamma_{\text{wg},L} + \gamma_{\text{wg},R}}, \quad (3.18)$$

which indicates left-handed ($D > 0$), right handed ($D < 0$) or balanced emission or scattering of photons. In extreme cases, $D = \pm 1$, the QD's coupling is unidirectional, referred to as chiral emission and scattering. To quantify the directionality, it is useful to introduce the directional Purcell factor of a left- (subscript $-$) or right-handed (subscript $+$) circular point-like dipole $\hat{\mathbf{e}}_d = \boldsymbol{\sigma}_{\pm} = 1/\sqrt{2}(\hat{\mathbf{x}} \pm i\hat{\mathbf{y}})$ for left- and rightwards propagating modes [182, 183]

$$F_{\text{P},\text{R}/\text{L}}(\mathbf{r}_0, \omega_0, \boldsymbol{\sigma}_{\pm}) = \frac{3\pi c^2 a n_g(\omega_k)}{2\omega_k^2 \sqrt{\epsilon(\mathbf{r}_0)}} |\boldsymbol{\sigma}_{\pm}^* \cdot \mathbf{e}_k(\mathbf{r}_0)|^2. \quad (3.19)$$

The directionality D can be expressed by the directional Purcell factor $F_{\text{P},\text{R}/\text{L}}$

$$D_k(\mathbf{r}_0, \omega_0, \boldsymbol{\sigma}_{\pm}) = \frac{F_{\text{P},\text{L}} - F_{\text{P},\text{R}}}{F_{\text{P},\text{L}} + F_{\text{P},\text{R}}} = \frac{|\boldsymbol{\sigma}_{-}^* \cdot \mathbf{e}_k(\mathbf{r}_0)|^2 - |\boldsymbol{\sigma}_{+}^* \cdot \mathbf{e}_k(\mathbf{r}_0)|^2}{\|\mathbf{e}_k\|}, \quad (3.20)$$

indicating that chiral light-matter interactions between a QD and photonic waveguide modes is obtained with an exciton state with circular dipole located in a waveguide region with locally circular polarized Bloch mode.

3.2.2 Resonant Fluorescence from a Quantum Dot

The formalism above described spontaneous emission of a QD in the excited state into a continuum of reservoir modes. This section describes resonant fluorescence from a quantum dot, where a coherent state drives the QD into the excited states, from where it spontaneously emits. The formalism below describes resonance fluorescence with density-operator theory and the master equation formalism [179].

The coherent drive of a QD by a laser is described by the Hamiltonian [179]

$$\mathcal{H}_{\text{coh}} = \hbar\Delta\sigma_+\sigma_- + \hbar(\Omega^*\sigma_- + \Omega\sigma_+), \quad (3.21)$$

where Ω is the Rabi frequency of the driving field, and $\Delta = \omega_L - \omega_0$ is the detuning between the excitation field frequency ω_L and the QD transition frequency ω_0 .

The state of the system (S) and its reservoir (R) is described by a density operator $\rho_{S\otimes R}(t) = |\Psi(t)\rangle\langle\Psi(t)|$ in the interaction picture. The equation of motion of the system is obtained by tracing out the information about the reservoir $\rho(t) = \text{Tr}_R(\rho_{S\otimes R}(t))$. Under the Markov approximation and the assumption of the continuum radiation modes in the vacuum state, the equation of motion reads

$$\frac{\partial}{\partial t}\rho(t) = \frac{i}{\hbar} [\mathcal{H}_{\text{coh}}, \rho(t)] + \mathcal{L}_\Gamma(\rho(t)) + \mathcal{L}_{\Gamma_{\text{dp}}}(\rho(t)), \quad (3.22)$$

where the Lindblad terms $\mathcal{L}_\Gamma(\rho(t))$ and $\mathcal{L}_{\Gamma_{\text{dp}}}(\rho(t))$ account separately for the spontaneous emission with rate Γ and loss of coherence due to interaction with the environment with pure dephasing rate Γ_{dp} , respectively.

The Maxwell-Bloch Equations

The equations of motion, referred to as optical Bloch equations, are obtained from the projections $\rho_{ij} = \langle i|\rho|j\rangle$, where $i, j = \{g, e\}$ and read:

$$\begin{bmatrix} \frac{\partial}{\partial t}\rho_{gg}(t) \\ \frac{\partial}{\partial t}\rho_{ge}(t) \\ \frac{\partial}{\partial t}\rho_{eg}(t) \\ \frac{\partial}{\partial t}\rho_{ee}(t) \end{bmatrix} = \begin{bmatrix} 0 & i\Omega/2 & -i\Omega^*/2 & \Gamma \\ i\Omega/2 & -\Gamma/2 - \Gamma_{\text{dp}} + i\Delta & 0 & -i\Omega/2 \\ -i\Omega/2 & 0 & -\Gamma/2 - \Gamma_{\text{dp}} - i\Delta & i\Omega^*/2 \\ 0 & -i\Omega/2 & i\Omega^*/2 & -\Gamma \end{bmatrix} \begin{bmatrix} \rho_{gg}(t) \\ \rho_{ge}(t) \\ \rho_{eg}(t) \\ \rho_{ee}(t) \end{bmatrix} \quad (3.23)$$

Pure dephasing only affect the coherence terms ρ_{ge} and ρ_{eg} , and does not affect the ground state and excited state population ρ_{gg} and ρ_{ee} .

Continuous-Wave Excitation

For continuous-wave excitation, studied in chapter 8, steady-state solution ($d\rho_{ee}/dt = 0$) of the excited state population is [179]

$$\lim_{t \rightarrow \infty} \rho_{ee}(t) = \frac{\Omega^2}{\Gamma} \frac{\Gamma + 2\Gamma_{\text{dp}}}{4\Delta^2 + (\Gamma + 2\Gamma_{\text{dp}})(\Gamma + 2\Gamma_{\text{dp}} + 2\Omega^2/\Gamma)}, \quad (3.24)$$

where the total decay rate $\Gamma_2 = \Gamma/2 + \Gamma_{\text{dp}}$ has been introduced. Figure 3.2 shows the steady-state solution of equation 3.24 for various pure dephasing rates Γ_{dp} . The excited state population as a function of the detuning Δ , shown in figure 3.2a), describes a Lorentzian lineshape. The excited state population asymptotically reaches 1/2 in steady-state, shown in figure 3.2b) as the Rabi frequency increases. The

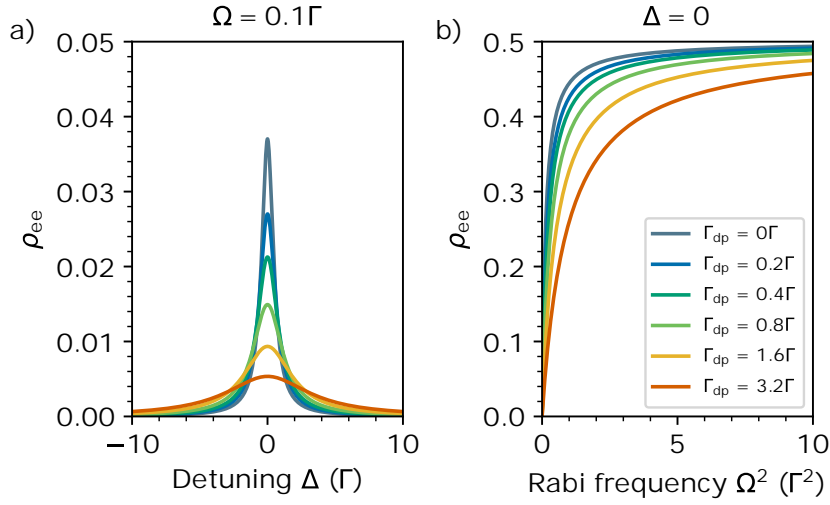


Figure 3.2: The excited state population ρ_{ee} of the steady state solutions of the Maxwell-Bloch equations for continuous-wave excitation for various pure dephasing rate Γ_{dp} . a) The dependence of the laser frequency detuning $\Delta = \omega_L - \omega_0$ for weak excitation $\Omega \ll \Gamma$, showing a Lorentzian lineshape. b) The Rabi frequency area dependence Ω^2 (normalized excitation intensity) of the steady state solutions for zero detuning ($\Delta = 0$).

presence of pure dephasing broadens the line shape. The full-width-half-maximum (FWHM) linewidth as a function of the saturation parameter S is

$$\Delta_{\text{FWHM}} = 2\Gamma_2 \sqrt{S + 1}, \quad (3.25)$$

where the saturation parameter S is defined as

$$S = \frac{\Gamma_2 \Omega^2}{\Gamma(\Gamma_2^2 + \Delta^2)}. \quad (3.26)$$

The steady-state population of the excited state for resonant excitation is

$$\lim_{t \rightarrow \infty} \rho_{ee}(t) = \frac{1}{2} \frac{S}{S + 1}. \quad (3.27)$$

The saturation parameter S as function of the Rabi frequency area Ω^2 and the FWHM linewidth Δ_{FWHM} as function of the saturation power are shown in figure 3.3.

For increasing pure dephasing rate, stronger excitation fields are required to saturate the QD as shown in figure 3.3a). In the weak excitation field limit, that is, in the low saturation parameter limit ($S \ll 1$), the linewidth is $\Gamma + 2\Gamma_{dp}$ as shown in figure 3.3b). For negligible pure dephasing, the linewidth is given by the decay rate Γ (life-time-limit).

The temporal dynamics of the excited state population, leading to Rabi oscillations, and the derivation of the second-order correlation function under resonant excitation can be found in the references [178] and [179].

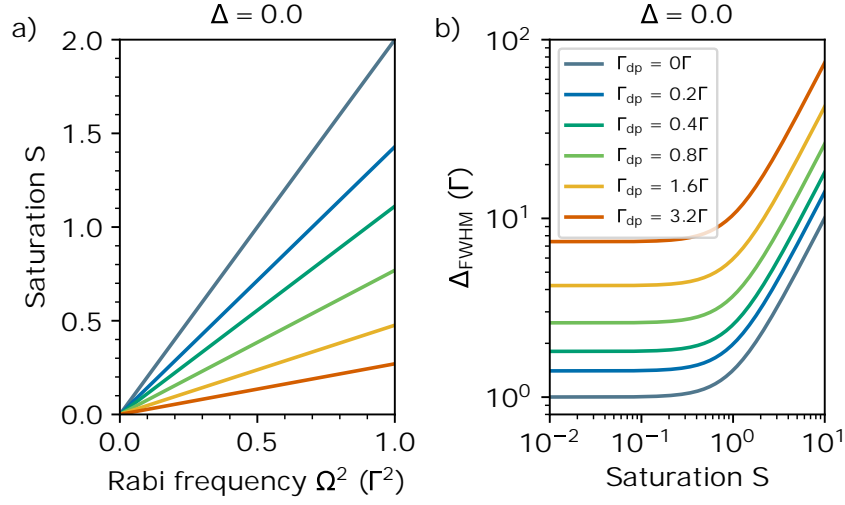


Figure 3.3: The saturation parameter S and the full-width-half-maximum linewidth (FWHM) Δ_{FWHM} of the steady state solutions of the Maxwell-Bloch equations for continuous-wave excitation for various pure dephasing rate Γ_{dp} for zero detuning ($\Delta = 0$). a) The saturation parameter S as a function of the Rabi frequency area Ω^2 . b) The FWHM linewidth Δ_{FWHM} as function of the saturation parameter.

3.2.3 Contributions to the Spectral Linewidth

QDs are mesoscopic emitters embedded in a solid-state environment, where interactions with phonons, charge fluctuations associated with lattice defects or impurities, and spin fluctuations in the ensemble of nuclei occur [5]. These interactions give rise to a number of processes, among them broadening of the spectral linewidth by spectral diffusion and dephasing. These processes make it challenging to achieve lifetime-limited linewidths [$\Delta_{\text{FWHM}} = \Gamma$] for high indistinguishability of emitted photons.

Pure dephasing is a fast process in the ps timescale [186, 187] and is mainly caused by phonons. By cooling down the QD to close to zero absolute temperature, the influence of phonons can be strongly suppressed [186–189]. However, the phonon density of states is highly dependent on the geometry of the nanophotonic structures. In low-dimensional nanostructures, the density of states at relevant frequencies can strongly differ to homogeneous media, potentially enhancing the pure dephasing [190]. Soft-clamping of photonic crystal waveguides [191] and Purcell enhancement [83] can be utilized to reduce the effect of pure dephasing.

Spectral diffusion originates in charge fluctuations associated with lattice defects or impurities and is not considered by the Maxwell-Bloch equations, but can be modeled as a random process by assuming a Gaussian distributed detuning Δ . The charge fluctuations affect the quantum dot resonance frequency due to the Stark effect. These charge fluctuations are typically on the μs to ms timescale [106], which is much slower than a QD's lifetime. Charge fluctuations can be significantly

reduced [27, 92] by by integrating the QD into the intrinsic layer of semiconductor heterostructure with a p-i-n-type heterojunction [129].

Numerical Solution of the Bloch Equations

To investigate the QD dynamics under pulsed resonant excitation, the Maxwell-Bloch equations can be solved numerically. To model the excitation by a pulsed laser, a Gaussian time-envelope is assumed, which modifies the Rabi frequency that enters the Bloch equations

$$\Omega \longrightarrow \Omega(t) = \frac{\Omega_p}{\sqrt{2\pi}\sigma_p} \exp\left(-\frac{(t-t_p)^2}{\sigma_p^2}\right) \quad (3.28)$$

where Ω_p is the pulse area, σ_p represents the bandwidth of the laser pulse and t_p is the temporal center of the laser pulse.

TOPOLOGICAL PHOTONIC CRYSTAL WAVEGUIDES FOR CHIRAL INTERFACES WITH QUANTUM DOTS

This chapter presented the design, fabrication, and photonic characterization of topological photonic crystal waveguides for chiral light-matter interfaces based on a photonic analog of the Quantum Valley-Hall effect and InGaAs quantum dots.

Originating from the studies of two-dimensional condensed-matter states, the concept of topological order [192] has been expanded to the field of optics and photonics [56–58]. Analogous to the dissipation-free and impurity immune transport of electrons, topologically protected photonic surface states⁽¹⁾ have demonstrated to enable robust control and unidirectional transport of light [62]. Unfortunately, all-dielectric topological photonic systems, compatible with quantum dot (QD) based scalable photonic devices [5, 7], are time-reversal symmetric and therefore lack topological protection [79]. However, despite this lack of topological protection, all-dielectric topological photonic crystal waveguides (PhCWs) can outperform conventional PhCWs⁽²⁾ for realizing integrated non-reciprocal single-photon devices for constructing scalable complex quantum circuits and networks [44].

Recently, a number of topological waveguides have been proposed and demonstrated, ranging from the microwave region to the near-infrared region [59–72]. Notable developments in the field of topological waveguides are the demonstration of low-loss guiding of light around tight corners [65, 73–75], robust transport despite

(1) In systems of broken time-reversal symmetry.

(2) See chapter 5, published as an article [1].

the presence of defects [76], and integration with passive photonic elements such as nanobeam waveguides (NBW) [75] and fiber-to-chip couplers [73, 75].

Principal compatibility with embedded QDs has been demonstrated and has been employed to probe the waveguide transmission [73, 74]. Recently, chiral coupling of QDs to topological waveguides has been demonstrated [73, 77, 78, 193]. However, topological waveguide have not been implemented in quantum photonic architectures which feature electronic charge state control and dipole transition frequency tuning. These features are essential for realizing non-reciprocal devices for scalable quantum networks [7].

This chapter presents the integration of topological PhCWs into efficient planar nanophotonic circuits and the embedment of InGaAs QDs.

4.1 DESIGN AND FABRICATION

For the application in quantum photonic circuits, topological waveguides based on a photonic analog of the Quantum Valley-Hall effect (QVH) [60, 78] are favorable as their guided modes are known to lie below the light lines and hence do not couple to the free-space continuum. In contrast, modes of topological waveguides based on the photonic analog of the Quantum Spin-Hall effect lie above the light line and are therefore leaky [175, 194]. PhCWs based on the QVH are formed by interfacing two photonic topological insulators [60, 78]. The photonic topological insulator base on a point group of C_{3v} symmetry⁽³⁾ with a broken inversion symmetry. Figure 4.1(a), b), and c) show schematics of possible unit cells.

The photonic topological insulators can be interfaced in a bearded-type or zig-zag-type configuration [195] to obtain a topological interface mode and guide light. Both interface types can be achieved regardless of the unit cell designs, which reflects the potential of topological waveguides for band-engineering [196].

However, a waveguide based on the zig-zag-type of an interface (ZIW), shown in the schematics of figure 4.1e), has guided modes that differ drastically from modes of a waveguide formed by a bearded-type of an interface (BIW), shown in the schematics of figure 4.1d). The modes of a ZIW are predominantly linearly polarized in regions of high field strength, whereas the modes of a BIW are circularly polarized in regions of high field strength. The contrast in the polarization of the guided modes reflects the symmetry of the waveguides. The ZIW possesses an inversion symmetry, whereas the BIW has a broken inversion symmetry and features a glide-plane symmetry instead. Due to their mode profile, the BIW supports directional coupling and Purcell enhancement of a circular dipole better [1, 197]. Consequently, the BIW outperforms the ZIW as a chiral light-matter interface, as discussed in chapter 5.

The unit cell determines the dispersion of the guided interface mode. The most simple design, a unit cell consisting of two unequal circular holes, shown in figure

(3) Schönflies notation C_{3v} : 3-fold rotational symmetry with the addition of 3 mirror planes containing the axis of rotation (vertical planes).

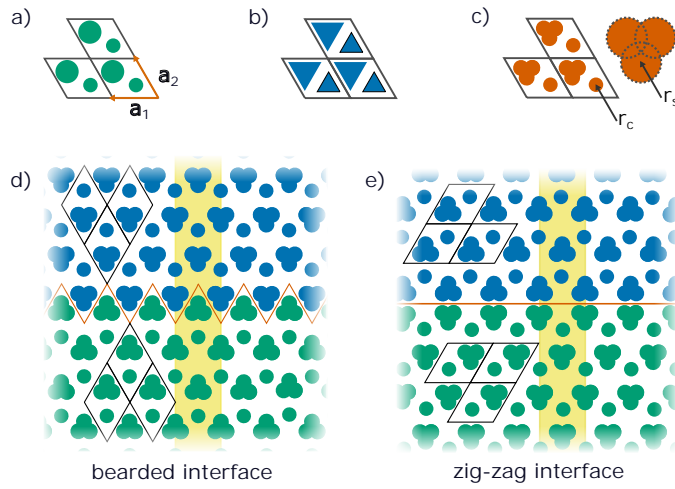


Figure 4.1: Schematic of a topological photonic insulator and crystal waveguides based on a photonic Quantum Valley-Hall effect analogon. Figure a) shows three unit cells (with lattice constants a_1, a_2) of a photonic insulator of non-trivial Valley-Chern number. The inversion symmetry of the unit cells is broken due to non-identical circular hole radii within the unit cell. Figure b) shows non-identical equilateral triangles as an alternative for elements in the unit cell. Figure c) shows the unit cell of a shamrock pattern, consisting of three overlapping holes of radii r_s , and a single circular hole of radius r_c . The photonic topological insulators' configuration as a bearded-type interface and zig-zag-type interfaces are shown in Figures d) and e). Three unit cells of each distinct photonic topological insulator (blue/green) are highlighted in black, whereas the interface is highlighted in red. The one-dimensional supercell of the waveguides is highlighted in yellow. The zig-zag-type interface features an inversion symmetry at the interface. The bearded-type interface has a glide-plane-like symmetry [17].

4.1a), is not ideal, as a BIW of such photonic topological crystals is not single-moded [175]. Additionally, the smaller hole is difficult to fabricate [46]. BIW of photonic topological insulators with unit-cells of equilateral triangles, as shown in figure 4.1b), feature single-moded slow light. However, the nanofabrication of such small and sharp features is also challenging.

For the implementation into the platform of InGaAs quantum dots, a unit cell is designed to consist of a shamrock pattern and a single circular hole as shown in figure 4.1c). Strong inversion asymmetry, that is, a larger waveguide operation bandwidth, is achieved already with comparable large circular hole due to the significantly larger shamrock pattern. By finite element calculation, an ideal air hole radius of approximately 50 nm, just within the limits of the nanofabrication capabilities, is estimated. Thus, the design is about a factor two less demanding on the nanofabrication in the minimal feature size compared to a unit-cell consisting of two holes. Shamrock patterns also allow simultaneously for wave-guiding of phonons in the GHz-regime [198,199] enabling phonon-photonic hybrid waveguides and hybrid devices [199,200].

4.1.1 Design of a Photonic Device with a Topological Interface Mode

For integration into a scalable platform, the BIW requires mode-adapters to NBW are adapted from literature [75], which allow for on-chip routing and interfacing with highly efficient shallow etch grating (SEG) fiber-to-chip couplers [162]. Figure 4.2 shows a schematic of the BIW design with a shamrock unit-cell and mode adapters to a NBW.

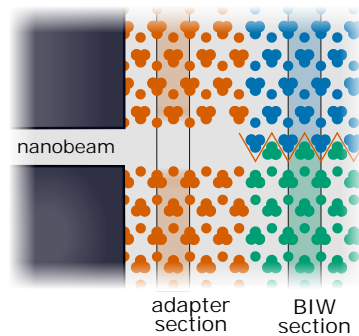


Figure 4.2: Schematic of a BIW device with mode adapter to a nanobeam waveguide (NBW) [75]. The two distinct photonic topological insulators are highlighted in blue and green, and their interface is highlighted as a solid red line. Two solid black lines and blue/green shading marks a single supercell of the one-dimensional waveguide. For mode adaptation to a NBW, the first row of shamrocks is removed in the adapter section (over eight supercell columns), highlighted in red. The NBW routes the guided mode to shallow etch grating (SEG) fiber-to-chip couplers [162].

The BIW devices, as displayed in the schematic in figure 4.2 are patterned into a suspended state-of-the-art p-i-n-type heterojunction membrane, improving the charge environment and allowing active electrical control of the charge state and manipulation of the dipole transition frequency of the embedded quantum dots. The semiconductor heterojunction layout is provided in the appendix⁽⁴⁾. The nanophotonic device fabrication combines soft-mask electron-beam lithography, reactive-ion etching (RIE), inductively coupled plasma RIE (ICP-RIE), and wet etching with hydrogen fluoride [46, 162]. Scanning electron microscope images of a BIW device are shown in figure 4.3.

The photonic properties of the topological waveguide can be directly compared to the properties of an NBW by studying an adjacent photonic reference device. The reference device features the same layout (i.e., the exact same SEG fiber-to-chip couplers position and orientation) but replaces the PhCW section with an NBW section. Devices without a topological interface (i.e., a single photonic topological insulator) allow the discrimination of the magnitude of scattered light and bulk modes from significant transmission through a PhCW. Additional devices with the same photonic crystal parameters but differing PhCW section lengths allow discriminating variations of the device properties due to different parameters and nanofabrication imperfections.

(4) Wafer B14769. See appendix A.II.

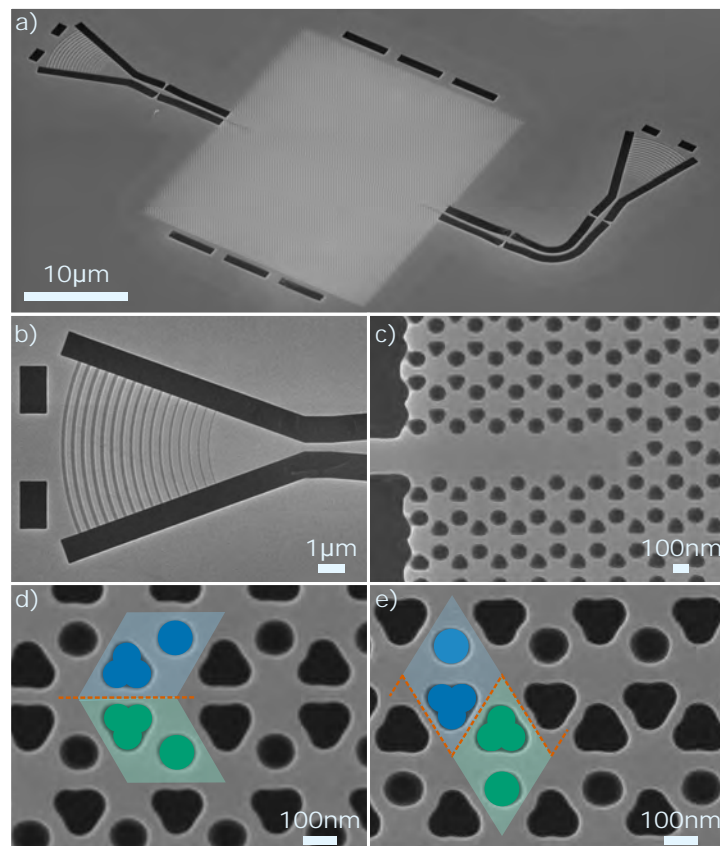


Figure 4.3: Scanning electron microscope images of a photonic device with a topological PhCW. Figure a) shows a bird-eye image of a full photonic device. The device consists of two polarizing SEG fiber-to-chip couplers (shown in b), NBWs to connect the couplers with mode adapters (shown in c), and a topological PhCW. Figures d) and e) show a zoom into the topological interface of a bearded and a zig-zag-type. The interface is highlighted as a dashed red line, and a unit cell of each distinct topological insulator is highlighted in blue and green.

4.2 PHOTONIC CHARACTERIZATION

For photonic characterization, the sample is placed in a closed-cycle cryostat⁽⁵⁾. The base temperature of the sample mounting platform is about 5 K. The microscope objective⁽⁶⁾ ($NA = 0.6$) for optical access is outside the cryostat. All free-space optics and the microscope objective are mounted onto an open-loop X - Y stage⁽⁷⁾. The optical setup is positioned such that a device's two SEG fiber-to-chip couplers are accessible simultaneously for injection and analysis of transmitted light. Figure 4.4 displays a schematic of the optical setup.

(5) Advanced Research System CS210SF-GMX-20-QM.

(6) Nikon CFI S Plan Fluor ELWD ADM 40XC.

(7) Newport ESP stage and XPS-Q motion controller.

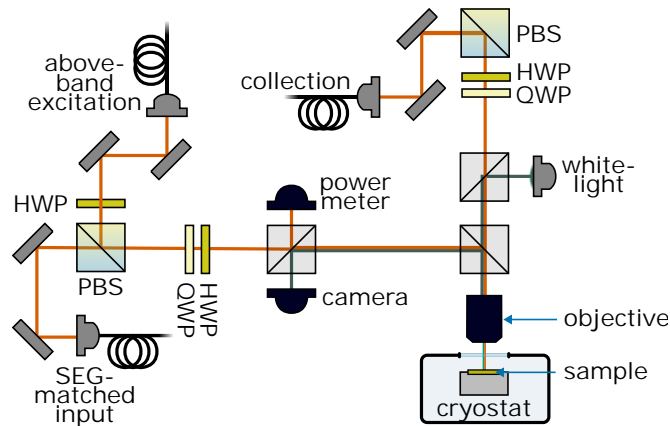


Figure 4.4: Schematic of the optical setup. The sample is installed in the cryostat. All free-space optics and the microscope objective are mounted onto an open-loop X-Y stage to characterize and compare different photonic devices without requiring optical realignment. Polarizing beam splitters (PBS), half-wave plates (HWP), and quarter-wave plates (QWP) control the input polarization and filter the excitation laser from the collected signal. The optical collection and photonic characterization input path match the output mode diameter from an SEG fiber-to-chip coupler.

A beam-splitter before the cryostat separates the optical input paths (in reflection) from the optical collection path (in transmission). The free-space optical setup images the collimated laser-input path to the back focal plane of the microscope objective. A polarizing beam splitter as a linear polarizer, a half-wave plate, and a quarter-wave plate control the laser-input polarization. The laser-input and optical collection paths are matched in their mode diameter to the SEG for maximal fiber-to-chip coupling efficiency. The collected light is polarization filtered for filtering out the cross-polarized laser input. For photonic characterization, a narrow line single mode diode laser⁽⁸⁾ (900-980 nm) is injected into the device. The collected light is analyzed with an avalanche photodiode⁽⁹⁾ and a spectrometer⁽¹⁰⁾. The setup features a CMOS camera for optical imaging and laser beam alignment.

4.2.1 Transmission Measurements

As a reference signal, the optical setup is aligned for the photonic reference device, where an NBW section replaces the topological PhCW section such that the spectral features in transmission are directly comparable. Figure 4.5 shows the transmission of a reference device. The transmission spectrum is governed by the transmission of the SEG fiber-to-chip coupler [162]. Overall, the transmission follows approximately a Gaussian envelope [162].

For the characterization of a topological PhCW, the optical setup is moved such that laser injection and collection spot align with a topological device without

(8) Toptica CTL.

(9) Excelitas Technologies Inc. SPCM-AQRH-14-FC.

(10) Princeton Instruments SpectraPro 2500i.

optical alignment modifications. As an example, the transmission of a topological device with a BIW and a ZIW section with the photonic crystal parameters of $a = 280$ nm, $r_s = 35$ nm, and $r_c = 55$ nm are shown in figure 4.5. The device's

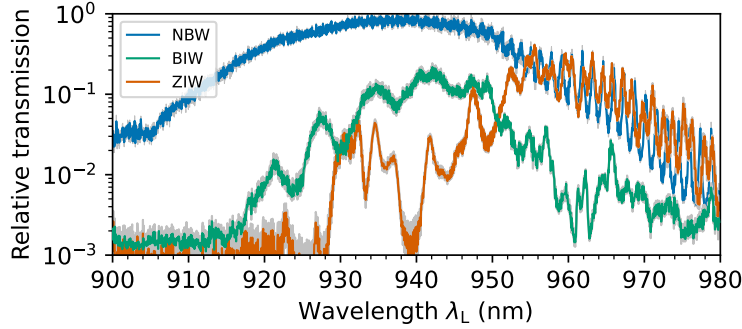


Figure 4.5: Laser transmission of three photonic devices. Green (red) shows the transmission of a device with a $L \approx 13 \mu\text{m}$ long topological PhCW section based on a bearded-type (zig-zag-type) interface. The photonic crystal parameters are $a = 280$ nm, $r_s = 35$ nm, and $r_c = 55$ nm. Blue shows the transmission of the photonic reference device where the topological waveguide section is replaced with a nanobeam waveguide (NBW). The transmission of the topological PhCW is normalized to the maximal transmission of the NBW. The gray shades indicate the uncertainty of the transmission measurements based on photon counting statistics. The NBW shows characteristic fringes for long wavelengths, which are attributable to reflections at the interface of the NBW to the SEG fiber-to-chip couplers [162].

transmission with a ZIW section in the long wavelength region is comparable to the NBW, indicating a highly efficient mode adapter. The effectiveness of the mode adapter is demonstrated for both interface types in figure A.11 in appendix A.III.

The BIW shows satisfactory transmission in a comparable wavelength range. The slightly lower transmission compared to the ZIW is likely limited by the mode adapter design. The BIW and its mode are asymmetric, whereas the NBW and its mode are inversion symmetric. For trivial topological waveguides, like the glide-plane waveguide [17], it has been shown that modes of asymmetric PhCWs require careful mode adaptation with the adiabatic introduction of the asymmetry.

The BIW fulfills the requirement of a chiral light-matter interface of adequate transmission in the operation wavelength of InGaAs QDs near 930 nm. However, for the efficient operation of the interface, it is essential to have access to a high group index. Access to slow light allows Purcell enhancement of the light-matter coupling, thereby suppressing leaky modes [5]. Furthermore, Purcell enhancement increases the potential photon flux through the interface, which determines the operation speed of proposed quantum networks [19, 22].

4.2.2 Group Index Estimation

The photonic reference devices reveal the group index of the NBWs by the emergence of the characteristic Fabry-Pérot fringes at long wavelengths. The SEG fiber-to-chip

couplers have a finite reflectivity at long wavelengths [162] by design, such that the NBW reference devices operate as low-quality factor cavities. The fringes' free spectral range (FSR) $\Delta\lambda_{\text{FSR}}$ scales with the group index n_g and the device length L [201]:

$$n_g = \frac{\lambda^2}{2\Delta\lambda_{\text{FSR}}L}, \quad (4.1)$$

where λ is the probed wavelength. The fringes of the photonic reference device are well visible in figure 4.5, revealing the finite reflectivity of the SEG couplers for $\lambda > 950$ nm. The analysis of the FSR indicates the NBW's group index of $n_g \approx 4$, in agreement with the literature [165].

For shorter wavelengths $\lambda < 950$ nm, the SEG fiber-to-chip couplers have near-ideal transmission [162], and the transmission of the photonic reference devices is smooth. In contrast, slow light inside the topological PhCW and reflection at the topological waveguide's mode adapters manifest in the emergence of fringes at all wavelengths. However, the transmission fringes of a photonic device with a topological waveguide section are challenging to interpret. Next to reflections within the topological PhCW, reflections within the two shorter NBW sections, the interference of the laser on optical elements in the input path, and the interference with scattered light complicate the transmission spectrum. Particularly for high group indices, examining fringes in transmission spectra for a group index estimation poses the risk of misinterpretation [202].

Group Index Characterization with Quantum Dots

Investigating the group index by illuminating the guided mode with QDs inside a waveguide [203] instead of the analysis of the laser transmission can reduce the misinterpretation risk. For sufficiently high excitation power and sufficient QD density, the embedded QDs illuminate the guided mode like a white-light source, i.e., as an internal light probe with low spectral modulation. The mode adapters reflect the photoemission of the QDs within the topological waveguide. Farby-Pérot fringes arise in the photoluminescence spectrum collected from the fiber-to-chip couplers and provide an estimate of the group index.

By the use of non-resonant p -shell excitation⁽¹¹⁾ and signal analysis with a spectrometer, the laser background is not contaminating the spectrum. The laser's potential reflection on optical elements does not alter the fringe pattern. The photoluminescence spectra are low-pass filtered digitally⁽¹²⁾ to reject high-frequency modulations that the spectrometer's resolution cannot resolve well, corresponding to a group index exceeding $n_g \geq 30$. The reliability of this method is demonstrated for an NBW reference device in appendix A.III.

(11) PicoQuant PDL 800-B, excitation wavelength $\lambda_L = 781$ nm.

(12) Using a digital Butterworth filter of 3rd order, with a cut-off wavelength (-3 dB) of ≈ 1 nm (5 pixels of the spectrometer's CCD camera). This rejects fringes corresponding to approximately $n_g \geq 30$ for the shorter PhCW, and $n_g \geq 15$ for the longer PhCW in figure 4.6.

Figure 4.6 shows the photoluminescence spectra and estimated group $n_g(\lambda)$ index for two devices of the same photonic crystal parameters but of different waveguide lengths $L_1 = 13.02 \mu\text{m}$ and $L_2 = 23.10 \mu\text{m}$.

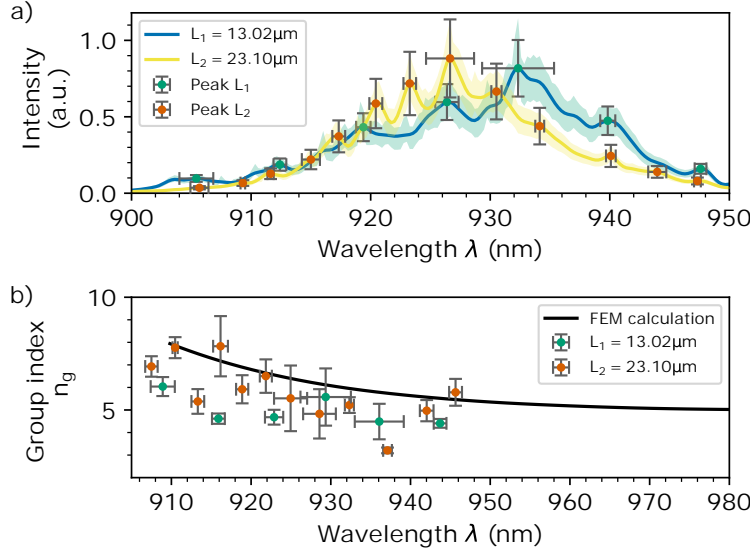


Figure 4.6: a) The low-pass filtered photoluminescence spectra of two devices with a BIW length of $L_1 = 13.02 \mu\text{m}$ (blue) and $L_2 = 23.10 \mu\text{m}$ (yellow) and their fringes (green and red), probed by illumination with QDs as an internal probe. The shaded areas represent the statistical uncertainties of the spectrometer signal. b) Group index of the BIW of length $L_1 = 13.02 \mu\text{m}$ (green) and $L_2 = 23.10 \mu\text{m}$ (red) determined with the photoluminescence of embedded quantum dots as internal light probe and the prediction of finite-element (FEM) calculations based on scanning electron microscope images of the unit cell (black). The wavelength uncertainties represent the half-width-half-maximum fringe width. The device parameters $a = 280 \text{ nm}$, $r_s = 35 \text{ nm}$, and $r_c = 55 \text{ nm}$.

The group index estimates, displayed in Figure 4.6b), do not indicate the presence of slow light. Within the evaluated wavelength range of 900 nm to 950 nm, the group index shows only a slight increase towards shorter wavelengths. The values range between $n_g(\lambda = 937.11 \text{ nm}) = 3.21(13)$ to $n_g(\lambda = 916.2 \text{ nm}) = 7.8(13)$. The estimates of both devices overlap well.

4.3 NUMERICAL ANALYSIS BY FINITE ELEMENT CALCULATIONS

Examining the Farby-Pérot fringes of the topological waveguides reveals only small group indices. The slow light region of the waveguide may be located outside the bandgap.

The nanofabrication process's pattern infidelity can modify the waveguide's dispersion relation significantly. A slow light region inside the bandgap is associated with a pronounced inversion asymmetry in the unit cell [78]. Thus, the absence of slow light suggests that the fabricated photonic crystals lack sufficient inversion asymmetry.

The dispersion relation of the BIW can be approximated numerically by finite element (FEM) calculations of the PhCWs supercell. For the highest accuracy, the FEM calculation assumes a supercell hole pattern based on scanning electron microscope images of the PhCW. A scanning electron microscope image of a single unit cell of the examined BIW is shown in figure 4.7.

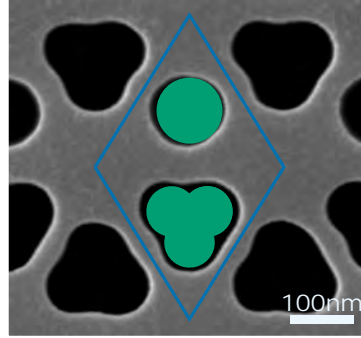


Figure 4.7: Scanning electron microscope image of a unit cell of a photonic topological photonic insulator of $a = 280$ nm, $r_s = 35$ nm, and $r_c = 55$ nm. The blue line marks the unit cell border. The green area indicates the pattern of the electron-beam lithography soft mask. Due to feature sizes below the resolution limit of the soft mask fabrication method, the shamrocks emerge similar to the pattern of blunt triangles. The circular hole and the shamrocks experience significant over-etching and visible random deformation.

The shamrock pattern and the radii of the circular holes are near the resolution limit of the soft mask nanofabrication method [46]. The delicate features of the shamrock patterns are not resolved well in the fabrication process. In consequence, the shamrock pattern emerges closer to a blunt triangle. Moreover, the shamrock patterns and the circular holes are etched as significantly larger features.

The etching process is susceptible to spatial inhomogeneities, e.g., due to soft mask resist thickness variations, close to the soft mask fabrication resolution limit. As a consequence, the shamrock pattern varies among different unit cells slightly. For the FEM calculation of the band diagram of the BIW, the averaged shamrock pattern of 10 unit cells is extracted from a scanning electron microscope image of the PhCW⁽¹³⁾. Figure 4.8a) shows the band diagram of the approximated unit cells.

The BIW and the ZIW are predicted to be single-moded and have a low group index within the bandgap, as shown in figure 4.8b). The ZIW's group index of $n_g = 6$ inside the bandgap explains the observation of the Farby-Pérot fringes similar to those of a NBW for wavelengths above 950 nm as visible in figure 4.5.

The BIW's group index is predicted to decrease slightly for increasing wavelengths from $n_g \approx 8$ to $n_g \approx 5$. The monotonous decrease in group index with increasing

(13) The scanning electron microscope images show that the shamrock pattern does not have an ideal C_{3v} symmetry, as required for a FEM calculation of the band diagram based on a single supercell. To approximate a shamrock pattern for finite-element calculations, the shamrock holes are evaluated after symmetrization by averaging the patterns after performing a 0° , 120° , and 240° rotation around their center.

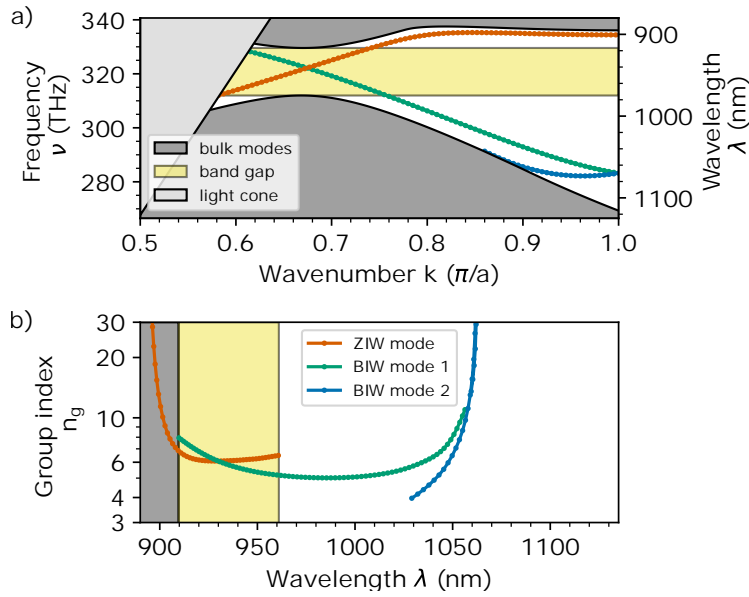


Figure 4.8: Band diagram (a) and dispersion of the group index (b) of the BIW and ZIW from FEM calculations based on the scanning electron microscope image of the PhCW. The lattice constant is $a = 280$ nm. Dark gray areas indicate bulk modes. The light gray area indicates the light cone. The light yellow shading indicates the bandgap. Red indicates the ZIW mode. Blue and green indicate the two modes of the BIW.

wavelength agrees with the experimental observation shown in figure 4.6. The values of the two different PhCW lengths and the FEM calculation are of comparable magnitude.

However, the transmission curves of the PhCWs of figure 4.5 show a difference in the wavelength region of efficient transmission, i.e., the bandgap location and width. The FEM calculation indicates a band gap between 910 nm and 961 nm. Above 961 nm, the FEM calculations expect bulk modes to couple with the guided mode and introduce additional losses. However, the transmission spectra in figure 4.5 show low loss transmission for wavelengths as large as 980 nm.

This discrepancy may arise from the approximation of the unit cell. For example, the scanning electron images reveal the shape of the patterns on the surface and do not account for conical etching, which may be significant due to the small feature size.

In conclusion, the FEM calculations confirm the experimental observations of only a low group index $n_g < 8$. Due to the low group index and the wide mode volume of topological waveguides [1, 204] no significant Purcell can be expected.

4.4 POTENTIAL OF TOPOLOGICAL PHOTONIC CRYSTAL WAVEGUIDES

Numerical studies have shown that topological waveguide can be utilized to design efficient, on-chip chiral quantum devices [1]. However, the utilization of topological

waveguide for chiral light-matter interfaces relies on the fabrication of non-trivial shapes, such as (blunt) triangles or shamrocks. Resist reflow techniques [205] could be incorporated into the fabrication process to reduce the spatial rest inhomogeneity, improve fabrication reliability, and achieve a higher pattern fidelity. Ultimately, higher etching selectivity and improved control over the fabrication process can be achieved using intermediate hard masks [206] and modeling and optimization of the electron-beam scattering process [207–209].

By increasing the pattern fidelity and the etching selectivity, single-moded slow light and significant Purcell enhancement inside the band gap can be achieved [78, 210]. Additionally, dispersion engineering can be utilized to increase the wavelength region of slow light and move the region into the bandgap [211].

The transmission measurements reveal decently efficient mode adapters. Comparison with the NBW reference shows that the mode adapters of the BIW have a transmission of $\approx 25\%$ ($\approx 50\%$ for each adapter), overlapping well with the wavelength range relevant for QD emissions. By designing a mode adapter that adiabatically converts the inversion-symmetric NBW mode to the asymmetric BIW mode, similar to the design of the topologically trivial glide-plane waveguide [17], the transmission of the BIW can be further improved.

CHAPTER
5**CHIRAL QUANTUM OPTICS IN
BROKEN-SYMMETRY AND TOPOLOGICAL
WAVEGUIDES**

This chapter presents full-wave three-dimensional calculations to quantify the performance of conventional and topological photonic crystal waveguides as chiral emitter-photon interfaces. These results are important to the understanding of light-matter interactions in topological photonic crystal and design of efficient, on-chip chiral quantum devices.

This chapter and its appendix presents data, figures, and parts of text that have been published [1].

Chiral single-photon emission has been demonstrated in conventional PhCWs [18,20,23] and topological photonic crystal waveguides (PhCW)s [73,74,78]. However, only few works [210, 212, 213] have considered scattering losses beyond 60° bends that constitute inherent symmetry directions of the structure [214–216]. The studies are limited to effective disorder models in two-dimensional crystals [213], are only semi-analytical models [212], or do not contextualize the losses with the overall performance of the PhCW as a light-matter interface [210].

This chapter explores how well different photonic crystal waveguides, specifically their guided modes, can act as quantum chiral-light matter interfaces using full vectorial three-dimensional finite-element simulations and rigorous scattering theory.

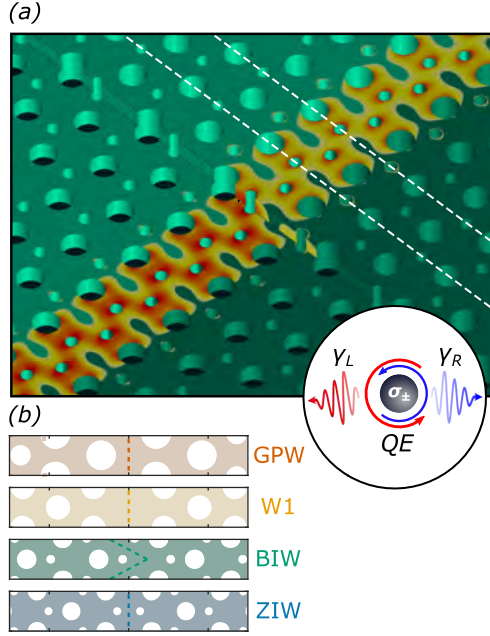


Figure 5.1: (a) Schematic of a chiral light-matter interface utilizing an edge mode between two topological photonic insulators (dark and bright green). The field norm for the guided edge-mode is shown (yellow to red) and an embedded quantum emitter indicated. The quantum emitter's transition dipoles are left- or right-handed circular (σ_{\pm}), resulting in directional emission (left and right as shown in the inset) when it is placed at a position where the polarization of the guided mode is circular. The white-dashed line highlights a single supercell of the waveguide. (b) Schematics of the supercells of the glide-plane waveguide (GPW), line-defect waveguide (W1), bearded-type interface waveguide (BIW), and zig-zag-type interface waveguide (ZIW) with the interface or center of each waveguide highlighted with a dashed line.

5.1 PHOTONIC CRYSTAL WAVEGUIDES AS QUANTUM CHIRAL INTERFACES

An ideal chiral interface for quantum light-matter interactions, such as the one shown in the schematic of figure 5.1a), is characterized by several properties. First and foremost, emission or scattering of photons by a quantum emitter (QE) into the counter-propagating modes left (L) or right (R) should be highly asymmetric with decay rates $\gamma_L \gg \gamma_R$, or vice versa. This directionality occurs when the overlap of circular (or elliptical) transition dipoles with the two counter-propagating modes differs and is quantified by,

$$D = \frac{\gamma_L - \gamma_R}{\gamma_L + \gamma_R}. \quad (5.1)$$

In the following, it is shown how this directionality factor can be calculated for any electric field profile.

Second, an efficient quantum light-matter interface typically enhances photonic interactions and minimizes subsequent losses as photons solely propagate to and from the emitter. Emission enhancement into a selected, guided mode is quantified by the Purcell Factor F [181], which for PhCWs scales linearly with the group index n_g [182]. Consequently, PhCWs are often used in the slow-light regime [217], where $n_g \approx 58$ [218] has been measured and $F \approx 20$ has been observed [23]. Unfortunately, in-plane backscattering between the counter-propagating modes scales as n_g^2 [219], resulting in prohibitively large losses at high n_g 's. As discussed below, the backscattering loss also depends on how the electric field is distributed within the PhCW unit cell, opening up a route towards realistic slow-light interfaces.

In this chapter, four different PhCWs are examined in their performance in each of the three areas identified above: D , F , and the minimization of backscattering losses. The corresponding unit cell of each structure is shown in figure 5.1b), with the interface (center) of each waveguide marked. These have been designed and experimentally implemented [78] to guide light near $\lambda = 930 \text{ nm}$ ⁽¹⁾ for use with high-quality self-assembled InAs quantum dots in a GaAs membrane [5]. For this study, their lattice constants are fixed to $a = 266 \text{ nm}$, but their design can readily be scaled [165] for use with any other quantum photonic platform. Similarly, the considered designs are limited to circular holes. However, in practice, more complex and fabricationally-challenging shapes such as triangles [175] or shamrocks [18] are possible.

Two of the examined PhCWs are topological and two are conventional PhCW designs. The conventional waveguides are standard photonic crystal line-defect waveguide (W_1) [16], and a broken-symmetry glide-plane waveguide GPW that has been optimized to work as a chiral interface [17]. The two conventional PhCWs are compared to topological PhCWs based on a photonic analog of the Quantum Valley-Hall effect (QVH) of two photonic topological insulators [78]. In analogy with the electronic QVH insulators [220], the difference between topological invariants, the Valley-Chern number, denotes the number of expected topological interface modes (here 1) that span the bandgap, although recent experiments suggest the existence of spectral regions where the mode does not afford protection to sharp bends [78]. Regardless, the QVH insulators are preferable as their guided modes are known to lie below the light lines and hence do not couple to the free-space continuum, in contrast to topological waveguides based on the photonic analog of the Quantum Spin-Hall effect, whose modes lie above the light line and are therefore leaky [175, 194]. Here, QVH waveguide designs formed by bearded-type interface (BIW) and zig-zag-type (ZIW) interfaces [195] are considered as shown in figure 5.1b).

5.2 PHOTONIC BAND DIAGRAMS AND DISPERSION

The photonic band diagrams and corresponding electromagnetic field distributions are calculated for all four PhCWs, using commercially available finite element software⁽²⁾. Details of the numerical simulations can be found in appendix A.I.2.

The guided TE-like bands for the topological and conventional PhCWs are displayed in figure 5.2a) and b), respectively. In each case, the solid regions give the bulk continuum modes, while solid curves give the guided modes. The dashed curves show additional modes close to the continuum and would therefore be leaky or the higher-order mode of the W_1 and GPW. An exemplary Bloch normalized mode-profile of the electric field $\|e_{n,k}\|$ is shown for each well-coupled mode of index n , taken for a group index $n_g(\omega_{n,k}) = c/(d\omega_{n,k}/dk) \approx 15$ (cf. circles in figure

(1) See appendix A.I.1 for further design parameters.

(2) COMSOL Multiphysics.

5.2c)), where c is the speed of light, $\omega_{n,k} = 2\pi\nu_{n,k}$ is the eigenfrequency, and k is the wavenumber.

Several interesting similarities emerge between the dispersion relations of the topologically conventional and topological waveguide. First, the W₁ and the ZIW waveguides support one well-coupled mode and others that are poor choices for a quantum interface. The W₁ dispersion contains an odd mode (dashed yellow curve in figure 5.2a)) and the ZIW dispersion contains two modes in close proximity to the bulk modes (dashed blue curves in figure 5.2b)) that in practice are expected to leak into the continuum. Furthermore, these two modes have a very large mode volume, as discussed in appendix A.I.2, rendering them unsuitable for efficient light-matter coupling. The W₁'s fundamental mode is highly confined throughout the entire k -space, while the mode volume of the ZIW mode has a more complex frequency dependence. As discussed in appendix A.I.2, the ZIW mode-width can be either large or small in regions of high n_g .

Likewise, there exist several similarities between the guided modes of the GPW and those of the BIW, as expected, since both share the same broken transverse symmetry. The BIW topological edge mode is comprised of two separate bands, each of which covers a large frequency interval, in much the same way as the guided modes of the GPW [17]. However, the two bands differ in their backscattering losses around bends as demonstrated in measurements and supported by finite-difference time-domain calculations [78]. For 60° bends, the upper mode shows little transmission, while near-unity transmission was observed over a large bandwidth of the lower band, making it suitable for creating triangular resonators. The two BIW bands cross at $ka/2\pi \approx 0.42$ and are degenerate at the band edge. Both GPW and BIW modes are tightly confined across the entire k -space, with the mode-width of the BIW being significantly larger than that of the GPW and smaller than that of the ZIW⁽³⁾. Nevertheless, highly confined, slow light can be found at the band edge of the lower branch of the BIW, indicating that large Purcell enhancement is possible with this structure.

5.3 DIRECTIONALITY, PURCELL ENHANCEMENT AND DISORDER-INDUCED SCATTERING

Having determined the guided modes of each structure, it can now be quantified how well each functions as a bright, highly directional, and low-loss interface. First, the directional Purcell enhancement $F_{\sigma_{\pm},n,k}$ is calculated for a left- (subscript -) or right-handed (subscript +) circular point-like dipole $\sigma_{\pm} = 1/\sqrt{2} (\hat{x} \pm i\hat{y})$ for each PChW according to [183]

$$F_{\sigma_{\pm},n,k}(\mathbf{r}) = \frac{3\pi c^2 a n_g(\omega_{n,k})}{2\omega_{n,k}^2 \sqrt{\epsilon(\mathbf{r})}} |\sigma_{\pm}^* \cdot \mathbf{e}_{n,k}(\mathbf{r})|^2. \quad (5.2)$$

Although this quantity and others are mode-dependent, the subscript n is omitted for clarity. Exemplary maps of a unit cell of each structure are displayed in figure

(3) Cf. appendix A.I.2.

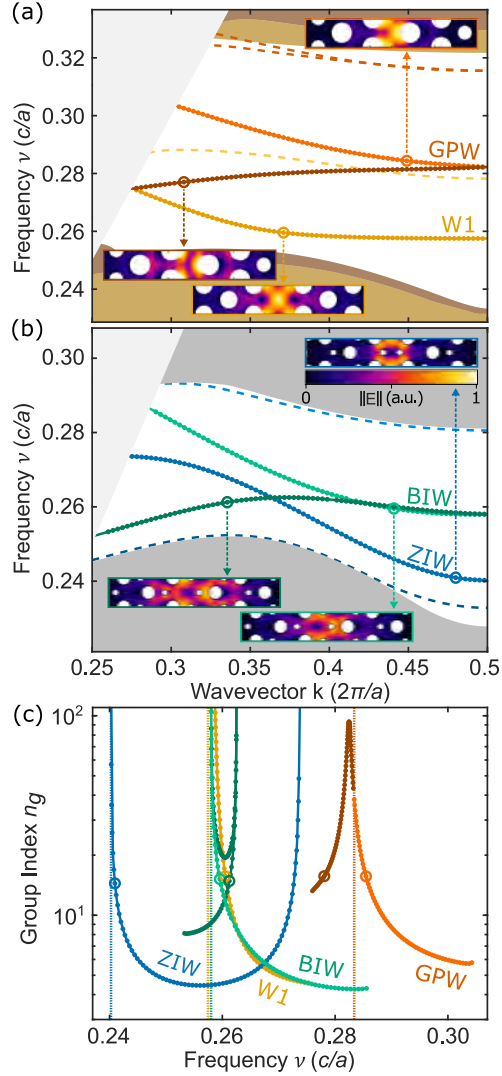


Figure 5.2: a) Photonic band diagram of the GPW (orange) and W1 (yellow) waveguides. Shaded regions correspond to the bulk modes of the GPW (brown) and W1 (yellow), while the grey region represents the light cone. The solid and dashed curves represent guided modes that are considered or excluded in this work, as discussed in the main text. Insets show exemplary mode profiles at $n_g \approx 15$. (b) Same as (a) but for topological BIW (green) and ZIW (blue) waveguides, noting that both topological waveguides share the same bulk modes. (c) Group index of the guided modes denoted by solid curves in (a) and (b) as a function of frequency for all four structures, with circles representing the modes whose profiles are shown above. The band-edges are indicated by a dotted line.

5.3a), taken again for modes with $n_{g,n} \approx 15$. From these, it can be observed that for both the GPW and BIW there is little overlap between $F_{\sigma_+,k}$ and $F_{\sigma_-,k}$. In contrast, these maps differ only near the holes for the W1 structure and are nearly identical for the ZIW, foreshadowing that these two structures fare poorly as chiral interfaces.

As noted above, the chirality of the interaction is quantified by the directionality,

$$D_k(\mathbf{r}) = \frac{F_{\sigma_-,k}(\mathbf{r}) - F_{\sigma_+,k}(\mathbf{r})}{F_{\sigma_+,k}(\mathbf{r}) + F_{\sigma_-,k}(\mathbf{r})}, \quad (5.3)$$

examples of which are also present in figure 5.3a). Here, it can be observed that while highly directional interactions are possible with all four structures, there is only a high degree of overlap between regions of high Purcell enhancement and directional interactions for the GPW and BIW. For the W1 and ZIW, in contrast, relatively

high Purcell factors are found in regions of linear electric field polarization, largely precluding efficient chiral light-matter interactions and showing the importance of breaking inversion symmetry in the waveguides.

The maximal Purcell enhancement factor $F_{\sigma_{\pm},k}^{\max} = \max_{\mathbf{r} \in S_c} \{F_{\sigma_{\pm},k}(\mathbf{r})\}$ within each map (where S_c denotes the area corresponding to the regions of high-index material), is determined. These values are plotted as a function of frequency in figure 5.3b) for all structures. It can be observed that all structures predict Purcell factors of upwards of 15 away from the band-edge, where both n_g and $F_{\sigma_{\pm},k}$ may diverge. In practice, the range of accessible factors is limited by several effects, among them scattering due to structural imperfections [221] and disordered-induced mode broadening [222]. Experimentally, a Purcell enhancement factor of $F \approx 20$ has been observed [218], and PhCW systems with significantly higher enhancements have been proposed [223].

A good chiral interface must not only enhance interactions but must also allow for subsequent low-loss transport. Transport losses are taken into account by calculating the ensemble-averaged mean-free path (or backscatter loss length) $L_{\text{back},k} = \langle \alpha_{\text{back},k} \rangle^{-1}$, limiting the analysis to the single-mode and single-event backscattering regime as is typical for relatively short waveguides [224]. Here, $\langle \alpha_{\text{back},k} \rangle$ is the power-loss factor per unit cell which is the ensemble average over disorder-induced imperfections⁽⁴⁾ for non-uniform air-hole size R_α , where α is the index of the individual holes⁽⁵⁾.

Multi-mode scattering from degenerate modes of the BIW are neglected, since their degeneracy can be lifted without significantly altering their mode profile [204, 211], as was done with the GPW [17], resulting in

$$\begin{aligned} \langle \alpha_{\text{back},k} \rangle &= \sum_{\alpha} \frac{a^2 \omega_k^2 n_g^2 \sigma^2}{4} (\epsilon_2 - \epsilon_1)^2 \\ &\times \iint \text{d}\mathbf{r} \text{d}\mathbf{r}' \Theta\left(\frac{h}{2} - |z|\right) \Theta\left(\frac{h}{2} - |z'|\right) \\ &\times \delta(R_\alpha - |\boldsymbol{\rho} - \boldsymbol{\rho}_\alpha|) \exp\left(\frac{-R_\alpha |\tilde{\phi} - \tilde{\phi}'|}{l_p} + i2k(x - x')\right) \\ &\times [\mathbf{e}_k^*(\mathbf{r}) \cdot \mathbf{p}_k^*(\mathbf{r})] [\mathbf{e}_k(\mathbf{r}') \cdot \mathbf{p}_k(\mathbf{r}')], \end{aligned}$$

where σ is the statistical surface roughness factor, Θ denotes the Heaviside function, h is the membrane height, z is the vertical Cartesian coordinate, δ is the Kronecker delta function, ρ (ρ_α) denotes the in-plane projection of the position vector (the individual hole center axis); also, \mathbf{p}_k is the polarizability, l_p is the surface roughness correlation length, and $\tilde{\phi}$ is the azimuth angle of the position vector in the cylindrical coordinate system which is centered in the hole α . In principle, multi-mode back-

(4) See appendix A.1.3 for details and discussion of the scattering mechanisms.

(5) Adapted from ref. [225] for non-uniform hole sizes R_α .

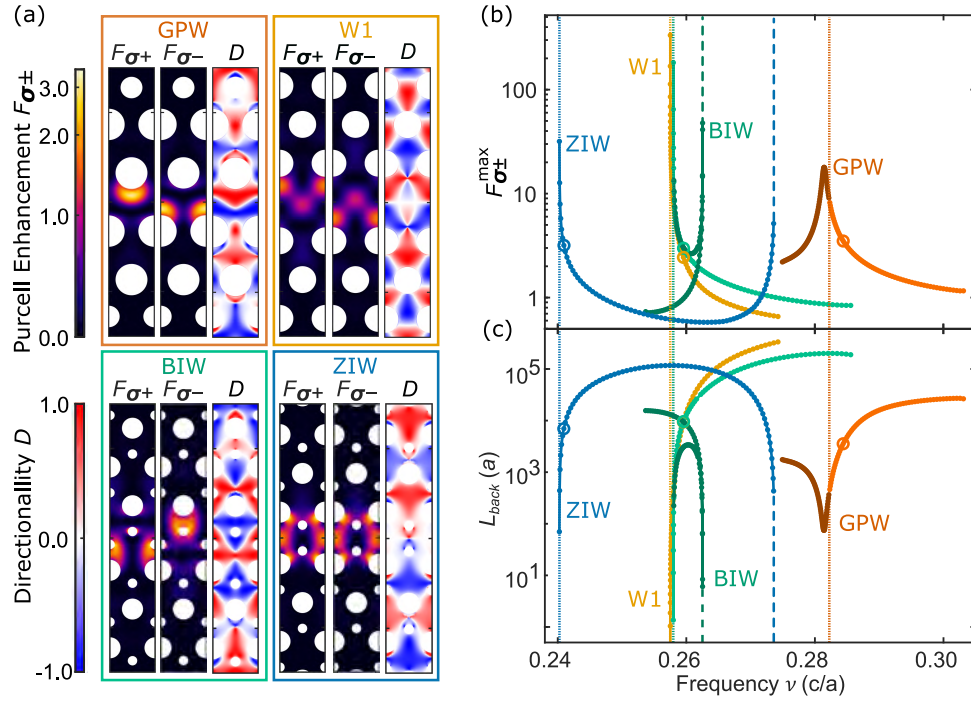


Figure 5.3: a) Mode maps of the directional Purcell factor $F_{\sigma_{\pm},k}(\mathbf{r})$ and directionality $D_k(\mathbf{r})$ for a unit cell of each PhCW, taken at $n_g \approx 15$ as shown in figure 5.2c). b) Maximal $F_{\sigma_{\pm},k}^{\max}$ for each mode as a function of frequency, with dashed curves representing the divergence predicted in the slow-light regions. c) Corresponding backscattering length $L_{\text{back},n,k}$ in units of the lattice constant a as a function of frequency. Note that both the backscattering losses and interaction enhancement diverge as the group index diverges. The band-edges are indicated by dotted lines, where the group index of all PhCWs except for the GPW diverge. Dashed lines indicate group-index divergences of the band-edge. Circles in b) and c) represent the modes whose profiles are shown in a).

PhCW	$F_{\sigma_{\pm}}^{\max}$	L_{back}
W1	2.4	$9.4 \times 10^3 a$
GPW	3.5	$3.6 \times 10^3 a$
ZIW	3.2	$7.0 \times 10^3 a$
BIW	3.0	$9.6 \times 10^3 a$

Table 5.1: Purcell factors $F_{\sigma_{\pm}}^{\max}$ and mean-free paths L_{back} for the highlighted modes with a group index of $n_g = 15$.

scattering can be explicitly included [221]. Yet is not expected to significantly contribute to losses other than for slow, small k (leaky) modes [221, 226].

Considering state-of-the-art soft mask nanofabrication methods [224, 227], a surface roughness for each hole of $\sigma = 3$ nm and a correlation length for this disorder within each hole of $l_p = 40$ nm (Cf. figure A.1.3b) is assumed. The resulting mean-free path $L_{\text{back},k} = \langle \alpha_{\text{back},k}^{-1} \rangle$ for all structures is presented in figure 5.3c). Interestingly, and as shown in appendix A.1.3, the relative performance of the different structures,

with respect to backscattering losses is relatively insensitive to the absolute value of l_p . As expected, scattering losses increase with the group index, yet the absolute scattering length can significantly differ for the different structures (and in general does not scale quadratically with n_g [224], as also shown in appendix A.I.4). As an example, the Purcell factors and mean-free paths are listed in table 5.1 for $n_g = 15$.

That is, for this moderate group index all PhCWs show Purcell factors and mean-free paths varying by more than a factor of 2. The W₁ and BIW PhCWs show the least losses, while the GPW provides the strongest enhancement factor. As can be seen in the mode distributions (cf. figure 5.2a)), the field of the W₁ PhCW is mainly located in the line defect center, away from the holes⁽⁶⁾, yet is only weakly circularly polarized (cf. figure 5.3a)). The GPW mode is more strongly localized near the hole edges, leading to higher scattering losses, yet it is also circularly polarized at these areas of high field intensity. In contrast, while the field distribution of the BIW is also highest at points of circular polarization, these are located more separated from the holes, reducing backscattering due to imperfections.

While the BIW's performance according to table 5.1 may seem similar to the W₁, the mode profile shown in figure 5.3 is very alike the GPW's. The relatively lower Purcell factors and the lower losses stem from a wider Bloch mode with relatively lower field strength at the hole interfaces⁽⁷⁾. Analogously, the ZIW's mode profile is similar to the W₁'s, but the wider Bloch mode with significant field strength at the hole interface results in a performance reduction.

5.4 OVERALL PERFORMANCE OF THE CHIRAL INTERFACES

A real quantum chiral light-matter interface must not only simultaneously enhance the interactions with circular transition dipoles and limit subsequent transport losses but also be designed such that high-quality quantum emitters can be readily embedded in regions where the coupling is effective. This places two constraints: (i) the emitters cannot be located too close to the air-dielectric interfaces of the holes so as to avoid interactions with surface states, and (ii) the area of the region where the emitters can be located should be large enough to ensure a high yield of successful couplings⁽⁸⁾. Condition (i) can typically be met with a distance $\delta_{\min} = 40$ nm [228–230]. At the same time, state-of-the-art nanofabrication protocols allow for the deterministic solid-state emitter-photonic structure integration with an accuracy of around $\delta_{\text{acc}} \approx 40$ nm [231–233].

Figure 5.4 show the maximal propagation length $L_{\text{back}}^{\max}(F_{\sigma_{\pm}}, |D|)$ that is possible, for a minimum desired directionality amplitude $|D|$ ⁽⁹⁾ and Purcell enhancement $F_{\sigma_{\pm}}$

(6) See appendix A.I.4.

(7) See appendix A.I.2.

(8) For details on the spatial constraints see appendix A.I.5.

(9) In all-dielectric media light propagation is described by Maxwell's equations obeying time-reversal symmetry. In that regard, the overall performance of the discussed chiral interfaces for a given directionality D is identical to a directionality $-D$.

for each structure with free choice of the mode and wavenumber $k^{(10)}$, but with the condition that a quantum emitter fits within an area $A_k(F_{\sigma_{\pm}}, |D|, \delta_{\min})$ of minimum size $A_{\min} = \pi \delta_{\text{acc}}^2$ while all points within this area are at least δ_{\min} away from the edge of an air hole⁽¹¹⁾. From this figure, it is evident that only the GPW and BIW will realistically make good chiral light-matter interfaces, as there essentially does not exist a sufficiently large enough area to couple an emitter to either a W1 or ZIW structure with high directionality and even a moderate $F_{\sigma_{\pm}} = 5$ ($F_{\sigma_{\pm}} = 3$) for the ZIW (W1) (although, for a ZIW, these points do exist within δ_{\min} of the air holes). In contrast, sufficiently large areas can be found within unit cells of the GPW and BIW where both near-perfect directionality ($|D| \geq 0.99$) and enhancements up to $F = 14$ and beyond are possible.

Where the topological BIW distinguishes itself from the GPW is both in the size of the area that can be used to efficiently and chirally interface to emitters and in its performance at enhancement factors exceeding 14. For fixed $|D| = 0.99$ and $F_{\sigma_{\pm}} \leq 10$ areas of at least $7.6 \times 10^5 \text{ nm}^2$ ⁽¹²⁾ can be found within a GPW unit cell, while for this area a BIW is limited to $4.4 \times 10^4 \text{ nm}^2$ (corresponding to a circle of radius $R_{|D|=0.99} \approx 118 \text{ nm}$). This can be seen in appendix A.I.5, where it is discussed how this area is determined.

Figure 5.4 shows that for high directionality $|D| = 0.99$ the GPW outperforms the BIW as a chiral interface by about 30 % higher propagation lengths if low interaction enhancements $F_{\sigma_{\pm}} \leq 4$ are desired. For intermediate Purcell enhancements ($4 \leq F_{\sigma_{\pm}} \leq 12$), the GPW and the BIW show similar losses, while for higher interaction enhancements ($F_{\sigma_{\pm}} > 12$) the propagation length of the BIW is longer than that of the GPW. The highest achievable Purcell enhancement for the GPW is $F_{\sigma_{\pm}} = 17.5$ (14) for a minimal directionality amplitude $|D| = 0.5$ ($|D| = 0.99$). It is important to recognize that this limit arises due to the dispersion engineering of the GPW, which causes its group index to remain finite in the entire reciprocal space, in contrast to an unoptimized GPW whose dispersion relation diverges at the lower band edge [17].

The difference between the losses of the GPW and BIW can be understood by considering their respective mode profiles (cf. appendix A.I.2), and realizing that in general the light is better confined in the GPW compared to the BIW. Particularly for low to intermediate group indices, the mode width of the GPW is half, or less, than that of the BIW (cf. appendix A.I.2). In the GPW, the same enhancement can be found as in the BIW for lower n_g 's, and hence fewer scattering losses. However, for large group indices, the Bloch mode profile of the GPW's shows high intensity near the first air-hole row leading to a strong relative increase of the backscattering losses (cf. appendix A.I.4). In other words, for low Purcell enhancements, the GPW's disadvantage of high backscattering losses are compensated by tighter mode confinement. For example, for $|D| = 0.99$ the propagation length is $20880a$ ($51330a$)

(10) For photonic crystals there is no fundamental constant with the dimension of length since the master equation in dielectric media is scale invariant. A quantum emitter can be brought in resonance with a mode of wavenumber k by scaling the lattice constant a .

(11) For details on the numerical implementation, see appendix A.I.5.

(12) Corresponding to a circle of radius $R_{|D|=0.99} \approx 491 \text{ nm}$.

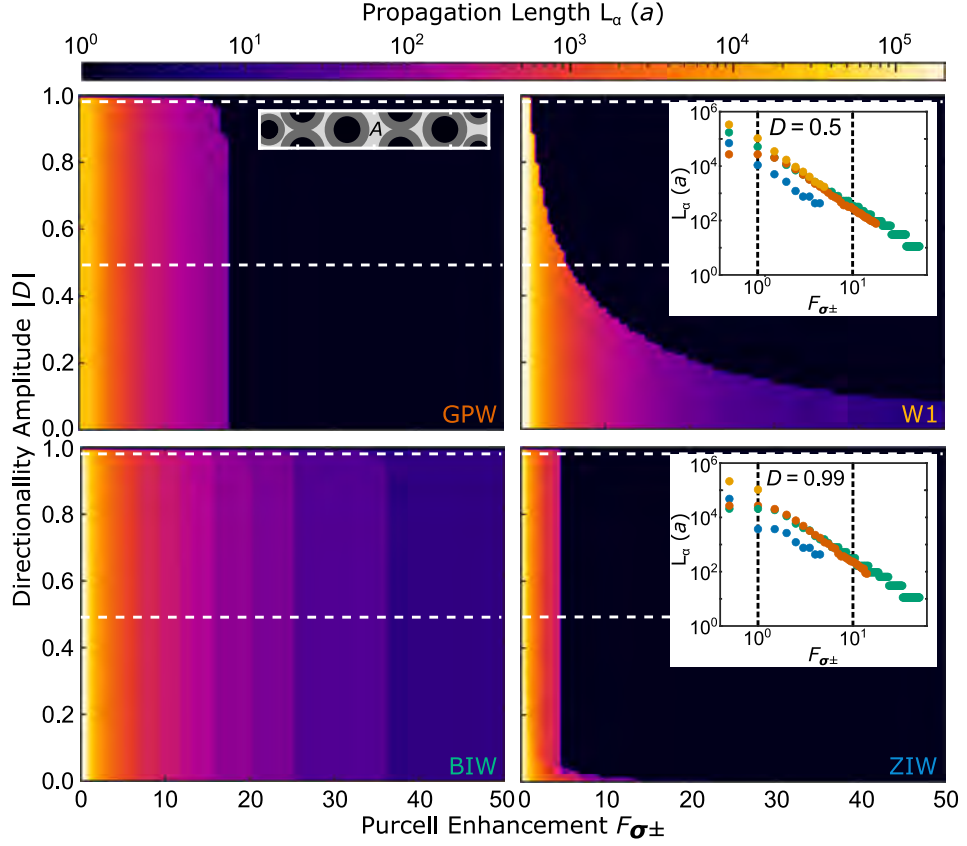


Figure 5.4: A summary of PhCW parameters for use as practical quantum chiral-light matter interfaces. Maps of the maximal achievable propagation length (in units of the lattice constant a) as a function of the minimum desired directionality or Purcell Enhancement factor (structure marked in each panel). This combination of D and F must be found in an area $A \geq A_{\min}$, which is sufficiently distant δ_{\min} from a hole, as sketched in the inset of the first panel and explained in the main text. The bright grey area indicates the area A as an example for the W_1 , while the dark and black areas indicate the excluded regions given by δ_{\min} . Insets in the W_1 and ZIW panels show line cuts showing the propagation length as a function of F for $|D| = 0.5$ and $|D| = 0.99$, respectively (cuts taken along the white dashed lines).

for a Purcell enhancement of $F = 1$, and $318a$ ($240a$) for a Purcell enhancement of $F = 10$ for the BIW (GPW). This means less than 4% (5%) backscattering losses for a 10 unit cell long waveguide and out-of-plane scattering dominating for low Purcell enhancements [234].

5.5 CONCLUSIONS

From the selected photonic crystal waveguides studied, only the GPW and the topological BIW are suitable platforms for chiral quantum optics. Both of these designs can enhance highly directional interactions for emitters located in relatively

large regions. Both designs suffer from backscattering due to fabrication impurities, although the topological waveguide offers protection to 60-degree bends [74, 75, 213, 235], enabling sharp-edge microresonators that do not suffer from bending losses [68, 77, 78, 236, 237].

The ability of these structures to act as elements in viable quantum chiral light-matter interfaces is perhaps easier to visualize using a concrete example. As an demonstration, the performance of a single quantum emitter chirally interfaced with a PhCW is considered. This fundamental element enables the realization of integrated non-reciprocal single-photon devices for constructing of scalable complex quantum circuits and networks [5]. Examples are loss-tolerant two-qubit measurements [22], optical isolators and circulators [18, 48], photon number dependent routing [238–240], $\sqrt{\text{SWAP}}$ [241] and CNOT gates [242].

Specifically, the setting is assessed where single photons are injected into the PhCW in which the chirally coupled quantum emitter coherently (and asymmetrically) scatters the injected photon forward or backwards [44]. The forward propagating photons are single-sidedly collected after transmission through the PhCW of N_α unit cells.

The speed with which such an element ideally operates is set by the characteristic rate of the emitters, namely, their decay rates: $\gamma_{R/L} = \gamma_{R/L}^0 F_{\sigma_\pm}$, where $\gamma_{R/L}^0$ is the quantum emitter's directional emission rate in a homogeneous medium. In reality, the circuit operation rate (and fidelity) will be further decreased as photons are lost to scattering due to imperfections or imperfect directionality. Assuming backscattering only, the intensity, or accessible photon flux $\Phi_{R/L}$, is thus given by,

$$\Phi_{R/L} = \gamma_{R/L}^0 F_{\sigma_\pm} \exp\left(-\frac{N_\alpha}{L_{\text{back}}^{\max}(F_{\sigma_\pm}, |D|)}\right), \quad (5.4)$$

where the maximum propagation length (in units of a) is an explicit function of the desired enhancement and directionality.

A directionality of $|D| = 0.99$ is set for near-ideal chiral coupling. Two limiting cases are considered: a 10 unit cell PhCW ($\approx 2.7 \mu\text{m}$ for our structures), which is the shortest length to act as a proper interface [223] and a 100 unit cell waveguide ($\approx 27 \mu\text{m}$) which is a more typical length in current circuits [18], and plot $\Phi_{R/L}/\gamma_{R/L}^0$ as a function of F_{σ_\pm} in figure 5.5a) and b), respectively. The performance of the shorter structures is limited by the maximum achievable Purcell Factor (cf. figure 5.4), and losses of less than 1% for both GPW and BIW for $F \leq 2$ are observed, which increase to 10% at around $F = 13$. For higher values of F , an operation is only possible with the BIW, and 15% losses are expected at $F = 20$. That is, for the shorter interfaces, a low-loss operation is compatible with moderate interaction enhancement. Here, $\Phi_{R/L}$ can directly quantify device performance, with the exact dependence determined by how many chiral elements are needed and the specific protocol (e.g., whether it depends on emission or transmission). For example, the operation speeds of quantum networks for all-optical routing of single photons [19] and loss-tolerant two-qubit

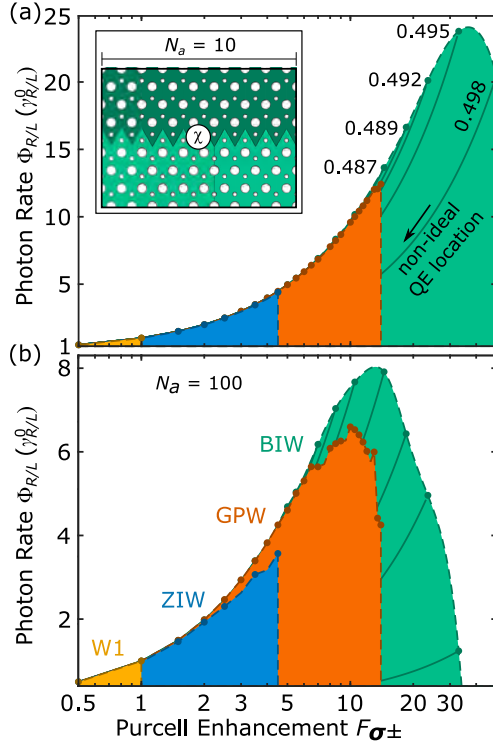


Figure 5.5: Calculated detectable photon flux, in units of the homogeneous decay rate, as a function of the Purcell enhancement for a quantum emitter χ chiral coupled to a PhCW as shown in the inset to a) [22]. The photon rate is shown for (a) short, 10-unit cell structures and b), the more typical 100-unit cell waveguides in solid circles resolution limited by the k -space sampling, which are labeled as an example for the BIW for the data points of highest Purcell enhancements, (cf. appendix A.1.6). The dashed lines represent a guide to the eye, while the solid curves represent a sub-optimal positioning of the QE. In both a) and b), the performance of all 4 structures is shown, with the topological BIW supporting the highest-rate operation. This is true both for the shorter systems, where losses are low in all cases, as well as for the longer structures, where the high n_g (enhancement) operation is limited by the scattering.

measurements capable of universal quantum computation [22] is determined by the accessible photon flux directly, $\Phi_{R/L}$, showing that GHz rate operation is possible.

For the longer devices, about 1% losses occur for the BIW and GPW, respectively, at $F = 2$, which increase to 27% and 34% at $F = 10$. At $F = 20$, where only the BIW can be used, upwards of 79% losses are expected, resulting in characteristic photon rates of $\Phi_{R/L}/\gamma_{R/L}^0 \approx 4$. Thus while even the longer waveguides can serve as chiral elements in quantum photonic circuits, for the most efficient operation, one should opt for a short, topologically protected waveguide.

Finally, it is to be considered that the topological waveguides considered here have yet to be optimized, in contrast with the GPW [17]. Several methods can be used to optimize their directionality and losses [204, 211, 243, 244]. All rely on dispersion engineering, where changing the size, shape, or position of the holes modifies both the band structure and field distributions, enabling slow light single-mode operation away from the bulk modes or pushing the electric field distribution away from the holes [65, 74, 175, 211, 245, 246], Doing so will reduce both backscattering and out-of-plane scattering while allowing for efficient and directional interactions.

A PLATFORM FOR PLANAR QUANTUM PHOTONICS WITH GAAS DROPLET EPITAXY QUANTUM DOTS

This chapter presents the layout of the first generation of planar photonic circuits with droplet-epitaxy-grown GaAs quantum dots embedded in a heterojunction membrane for charge-state control and tuning of the QD emission wavelength. Analyzing the photonic and accompanying electronic properties grants valuable insights into the performance and further development of this novel quantum photonic platform.

An ambitious goal in photonic quantum technologies is to scale up integrated nanophotonic circuits for efficiently generating, routing, and detecting single photons [4,7]. However, the architecture of planar quantum nanophotonic platforms is of high complexity [5]. A deep understanding and control over the properties of a platform are essential for its future applications in nanophotonic quantum technologies. This chapter discusses the layout and presents the electronic and photonic properties of the first generation of planar nanophotonic circuits with embedded droplet-epitaxy-grown GaAs quantum dots (QDs).

The material that hosts the QDs defines their electric environment. For InGaAs QDs, it is common to embed the emitters in a p-i-n-type of semi-conductor heterostructure [247]. Integrating the QDs into the intrinsic layer provides electric noise reduction [92], while allowing for the control of charge state by applying a bias voltage by Coulomb blockade [152] and tuning of the QD emission wavelength [107] by the quantum-confined Stark effect [154].

The host material constitutes a membrane of sub-wavelength thickness that enables in-plane light confinement by the design of engineered nanostructures [165].

On a microscopic scale, nanophotonic devices patterned into this membrane mold the flow of light [161] and engineer the light-matter interaction of the confined light with the QD's transition dipoles [5]. On a macroscopic scale, the nanophotonic devices guide and process the QD emission, allowing light extraction from the membrane [2]. Thus, the nanophotonic devices' properties and performance define a planar platform's capabilities to utilize embedded QDs as a single photon source and form larger-scale integrated quantum circuits.

6.1 DESIGN AND FABRICATION OF PHOTONIC CIRCUITRY

The presented planar photonic circuits⁽¹⁾ feature embedded GaAs droplet epitaxy QDs, an electronic interface for electric control of the QDs, nanophotonic devices, and nanostructures for interfacing guided light with QDs and extracting their emission from the chip.

Both the electronic interface and the nanostructures are based on adaptations from the previously reported work on InGaAs QDs [5, 7]. The InGaAs platform has made substantial progress towards quantum-dot-based deterministic photon-emitter interfaces for scalable photonic quantum networks [2]. Adapting the InGaAs platform's technologies provides leverage towards the fast development of the planar platform of GaAs droplet epitaxy QDs. However, this chapter reveals the limitations of the technological conversion from the InGaAs platform into the GaAs platform and identifies the challenges and opportunities in transitioning towards GaAs droplet epitaxy QDs.

6.1.1 A Heterojunction for Electric Control of Quantum Dots in Nanophotonic Circuits

Recently, the first generation of p-i-n-type heterojunctions for GaAs droplet epitaxy QDs in non-planar platforms achieved reduction of the charge noise, charge-state control via the Coulomb blockade, and tuning of the QDs' energy levels [26, 27]. However, the layout of a planar quantum photonic platform poses additional challenges due to additional system restrictions. The heterojunction's thickness must remain well below the wavelength of the QD emission to allow for the in-plane confinement of light by planar photonic devices such as nanobeam waveguides (NBW) and photonic crystal waveguides (PhCW). Furthermore, a waveguide-based light-matter interface limits the QD location in the heterojunction layout to the heterojunction's center region due to the electromagnetic field distribution of guided transverse electric modes [5].

The QDs of the presented nanophotonic circuits are embedded in a semiconductor heterostructure membrane with a thin p-i-n layout on top of a sacrificial layer. The sacrificial layer underneath the membrane can be removed chemically to suspend nanophotonic devices⁽²⁾. Underneath the sacrificial layer is a distributed Bragg

(1) This chapter presents the circuits of the sample B15459-A. See appendix A.II.

(2) More on the fabrication process in section 6.1.3.

mirror. The distributed Bragg mirror reduces the QD emission from the suspended membrane into the wafer below [248].

The semiconductor heterostructure membrane is 158.2 nm thick and constitutes an $p^+p-i-n-n^+$ junction based on $Al_{0.15}Ga_{0.85}As$ and GaAs. The QDs are grown in the intrinsic layer close to the membrane center by local droplet-etching [37]. The n-type back gate is silicon-doped, and the p-type top gate is carbon-doped. The outer layers of higher acceptor p^+ and higher donor n^+ doping levels serve as charge carrier reservoirs. These reservoirs counter the charge depletion of the p- and n-layers without drastically increasing the built-in electric field experienced by the QD in the center of the membrane. The heterostructure layout, doping levels, and intrinsic field are provided in appendix A.II in more detail.

Figure 6.1 displays the band structure of the diode using a one-dimensional Poisson equation solver [249] assuming ohmic contacts and neglecting Fermi-level pinning effects [250, 251] for the case of zero bias and a forward bias.

At zero bias, the conduction band of the QD and hence the lowest excitonic state is well above the Fermi level. A significant forward bias of approximately $U_B = 1.4$ V is required to lower excitonic states into the Fermi level and allow their population by electrons by tunneling through the potential barrier. The flat-band voltage, where the heterojunction operates similarly to a light-emitting diode [119], is around $U_B = 1.6$ V. Thus, the QDs' lowest excited states get populated at a bias voltage close to the flat-band voltage, and a significant tunneling current is expectable even at cryogenic temperatures.

The low Al-concentration in the heterojunction layout is crucial, since it prevents the occupation DX-centers [102], defects in doped AlGaAs, which affect the charge distribution and are optically active [102, 252]. Furthermore, an overall low Al-concentration is essential for the processing of the membrane into nanostructures without the risk of oxidation [46]. Additionally, the heterostructure features GaAs capping layers on both membrane surfaces to prevent the risk from oxidation post-fabrication.

6.1.2 The Nanophotonic Platform Layout

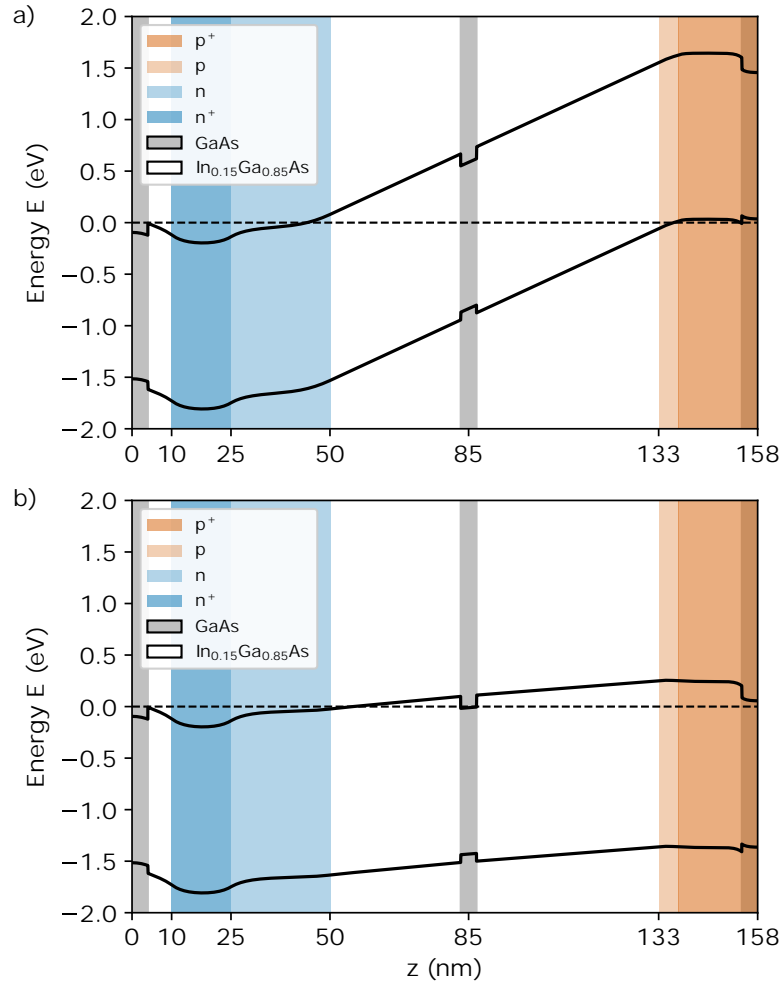


Figure 6.1: Band structure of the heterojunction, calculated using a one-dimensional Poisson equation solver, assuming perfect ohmic contacts to the p-type and n-type layers for a bias voltage of a) $U_B = 0$ V and b) $T = U_B = 1.4$ V at 30 K. GaAs layers are shaded as gray and $\text{Al}_{15}\text{Ga}_{0.85}\text{As}$ layers are shaded as white backgrounds. Overlaid colored shading indicates the doping levels with acceptors (red) and donors (blue). The black lines indicate the calculated conduction and valance band. In a more realistic scenario, the waveguide surfaces have been exposed to air and have oxidized [25].

The nanophotonic devices, such as PhCWs, NBW, and grating couplers, are fabricated by etching into the heterojunction. The semiconductor heterojunction sections of nanophotonic devices are subsequently suspended into a membrane by chemical removal of the sacrificial layer. The schematic cross-section of the semiconductor heterostructure is displayed in figure 6.2.

The top-gate and back-gate of the heterojunction are contacted for the electrical control of the QDs by applying an external bias voltage. First, an ohmic contact with the back gate is fabricated by etching through the heterojunction towards the donor-doped layers, the deposition of the metals nickel, germanium, and gold, and

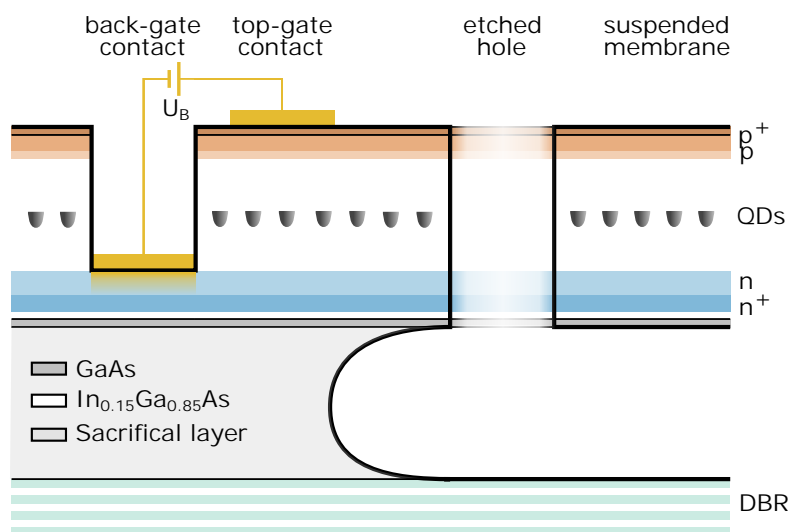


Figure 6.2: Schematic cross-section of the planar quantum photonics platform of GaAs droplet epitaxy QDs. The sample is processed out of a wafer on top of which a distributed Bragg mirror (DBR), a sacrificial layer (shaded light-gray), and the semiconductor heterojunction are grown. The junction is made out of $\text{Al}_{15}\text{Ga}_{85}\text{As}$ (shaded white), and its lowest and uppermost layers are made out of GaAs (shaded dark gray). Blue and red shaded overlays indicate the donor and acceptor levels in the heterojunction. The centered intrinsic layer hosts the QDs. The sacrificial layer is removed chemically to suspend nanophotonic structures above the DBR. Nanophotonic devices are formed by etching into the heterojunction. The top and back-gate are electrically contacted from the surface.

subsequent rapid thermal annealing. The annealing process allows the deposited metal alloys to diffuse and form an ohmic contact with the donor-doped layer of low contact resistivity. Subsequently, the highly-doped top gate is contacted by the deposition of chromium and gold onto the heterojunctions surface.

For nanophotonics in dielectric media, there is no fundamental constant with the dimension of length since the Maxwell equations in dielectric media⁽³⁾ are scale invariant. For example, the guided modes of a waveguide can be brought into resonance with a QD of any frequency by scaling the physical dimensions accordingly to the wavelength of the QD. The nanophotonic devices from the InGaAs quantum platform [7], operating near 930 nm, require a down-scaling of approximately 15% for their application in photonic circuits with GaAs droplet epitaxy QD, operating near at around 800 nm.

The presented platform features all principal elements of a quantum-dot-based photon-emitter interface of the scalable InGaAs platform [7]. NBWs [165] interface light from PhCWs and route it towards high-efficiency grating couplers [162] for chip-to-fiber coupling and access by free-space optics. The sample contains standard line-defect (W1) PhCWs [16] of high coupling efficiency of light emitted by the QDs into waveguide modes and glide-plane (GPW) PhCWs for chiral light-matter interfaces [17].

(3) Assuming identical refractive index.

The fabricated sample contains redundant copies of each nanophotonic device with separate electric contacts to account for random QD positions. A schematic of the arrangement of nanophotonic devices of the sample is shown in appendix A.II.

6.1.3 Nanofabrication

Nanofabrication processes the semiconductor heterojunction wafer that hosts the QDs into structures for electronic control and the photonic nanostructures. The nanophotonic device fabrication combines soft-mask electron-beam lithography, reactive-ion etching (RIE), inductively coupled plasma RIE (ICP-RIE), and wet etching with hydrogen fluoride. ICP-RIE etches the photonic devices. For the suspension of the photonic devices, the wafer⁽⁴⁾ features a layer of AlGaAs with high Al content as the sacrificial layer between the distributed Bragg mirror layers and the semiconductor heterostructure membrane layers. The wet etching step dissolves the sacrificial layer selectively.

To achieve resonance of the GaAs QDs near 800 nm with the slow-light wavelength region of the fundamental mode of PhCWs, small photonic crystal hole radii between 45 nm and 55 nm are required. In comparison, the well-developed fabrication process of the InGaAs platform achieves the etching of holes of a minimum radius of 56 nm through the heterojunction membrane of comparable thickness [46, 253]. The minimal hole size is limited by the etching selectivity of soft-mask nanofabrication, i.e., the etch-rate contrast between the lithographically exposed and unexposed soft-mask regions.

The fabrication of nanophotonic devices for GaAs QDs followed the characterization and optimization of the electron-beam resist deposition, electron-beam exposure dosage, and ICP-RIE etching process for a higher etching selectivity. The best results are achieved with a reduced resist thickness and increased electron-beam exposure dosages compared with the fabrication procedure of nanophotonic devices of the InGaAs platform. The fabrication recipe is provided in appendix A.II.3. Finite-element calculations of the band diagram of PhCWs within the parameter space accessible by the fabrication procedure and photonic characterization of test devices⁽⁵⁾ allow for the fabrication of single-moded PhCWs.

6.2 SCANNING ELECTRON MICROSCOPE CHARACTERIZATION

Along with higher etching selectivity, the amount of over-etching of features, i.e., the difference between the electron-beam mask and the feature size post-fabrication, increases. Furthermore, the minimal feature size is position dependent due to high sensitivity to inevitable spatial variations in the electron-beam resist deposition thickness. Therefore, examining the nanophotonic devices by scanning electron microscopy is essential to explain the photonic properties of the platform.

(4) Wafer B15459, see appendix A.II.

(5) See section 6.4.

Figure 6.3 shows scanning electron microscope images of the most basic nanophotonic device consisting of a nanobeam with shallow etch grating (SEG) couplers.

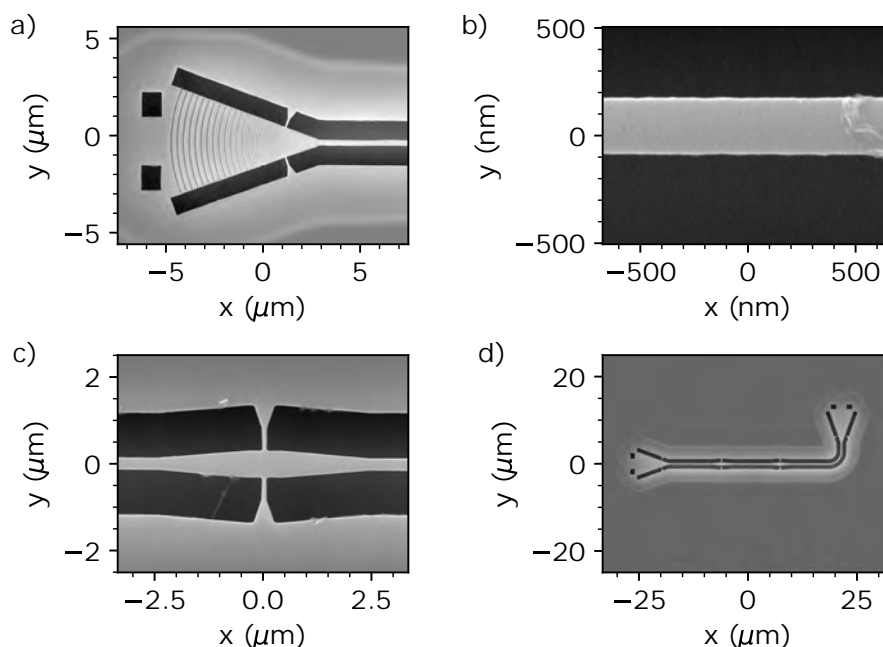


Figure 6.3: Scanning Electron Microscope of a nanobeam waveguide (NBW) with shallow etch grating (SEG) couplers with embedded GaAs droplet epitaxy QDs. Figure a) shows one of the two SEG couplers for coupling light into the waveguide mode and collecting the light from the waveguide mode. Figure b) shows a zoom into a NBW section with high resolution. Figure c) shows a tether supporting the NBW in its suspension. Figure d) shows the entire device.

The scanning electron microscope image of the SEG, displayed in figure 6.3a), is fully under-etched. A full suspension is critical for the efficient refraction of light from the waveguide mode out-of-plane by the grating.

The NBW, displayed in figure 6.3b), is fully suspended and supported by tethers but shows excess over-etching. The difference between the width of the NBW on the electron beam mask and the post-fabrication width is between 40 nm and 65 nm and varies within the different locations of the sample. Compared to the desired width of 245 nm, the variation in the amount of over-etching can be significant and need to be considered for assessment of their photonic properties [165]. Furthermore, the NBW images indicate a high sidewall roughness.

According to waveguide scattering theory, such as the Payne–Lacey model [254], sidewall roughness causes unwanted coupling between the fundamental guided and the radiation modes. Scattering due to sidewall roughness is a primary source of intrinsic loss for the planar InGaAs platform [46]. Moreover, the Payne–Lacey model predicts increased loss rates for reduced ratios of wavelengths over sidewall roughness. Hence, the sidewall roughness can be a limiting factor for its scalability

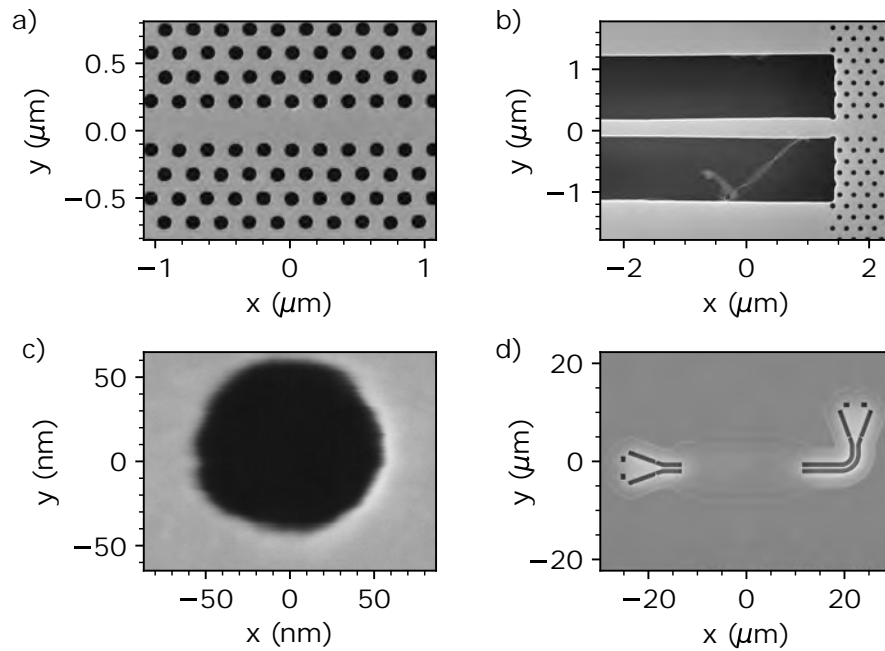


Figure 6.4: Scanning Electron Microscope of a nanophotonic device consisting of a line-defect photonic crystal waveguide (W_1 PhCW) of fast and slow light, mode tapers, and nanobeam waveguides (NBWs) that route light from the PhCW's guided mode to SEG couplers (sample B15459-A). Figure a) shows the waveguide center of the W_1 PhCW in the slow-light section. Figure b) shows the mode adapter from the W_1 PhCW to the NBW. Figure c) shows a zoom into a single hole of the photonic crystals of approximately 53 nm radius. The image is blurred due to the drift of the sample during the image acquisition. Figure d) shows the entire device.

in this platform. However, the photonic waveguide - QD interfaces of the fabricated circuits are short, and associated losses do not limit this first generations platform's functionality.

Persistently, scanning electron microscope images of the sample show sub- μm flake-like contaminations scattered over the whole sample. Examples are visible in figure 6.3b) and c). These contaminants seem to adhere to the surface and sidewalls. Their shape and occurrence are evidence for their identification as residuals from incomplete electron-beam resist removal [46]. Electron-beam resists residuals must be considered in the platform's performance since these carbon-rich residuals [255] could contribute to a fluorescent background, as discussed in section 7.1.

The presented sample features the first PhCWs with embedded GaAs droplet epitaxy QDs in a p-i-n-type heterojunction membrane. PhCWs are an essential building block in high-performance photonic platforms of QDs because they allow engineering QDs' light-matter interaction [5,256]. Figure 6.4 shows scanning electron microscope images of a nanophotonic device with a W_1 PhCW.

For chip-to-fiber coupling of QD emission, W_1 PhCWs on the sample are embedded

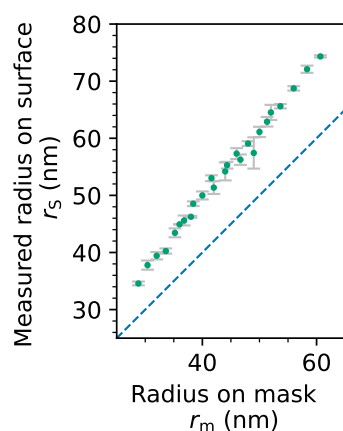


Figure 6.5: The radius of the etched holes on the surface post fabrication r_s as a function of the radius on the electron beam exposure mask r_m (sample B15459-A). Each data point is the average and standard deviation of the characterization of 3 holes of a photonic crystal. While the hole radius on the surface varied little between photonic crystals of the same parameters, holes with a radius $r_s < 40$ nm did not etch through the heterojunction reliably. The dashed blue line is the identity function and resembles the absence of over-etching.

in a photonic device that carefully adapts the photonic modes and routes the light towards SEG couplers. The W1 PhCWs consist of a slow and a fast light section which are interfaced by adiabatically stretching the photonic crystal along the propagation axis [257, 258]. The fast-light sections are subsequently interfaced to NBWs via adiabatic tapers [259], shown in figure 6.4b), for low-loss routing of the photons towards SEG couplers. Similarly to the scanning electron microscope images of figure 6.3, the images of figure 6.4 show electron-beam resists residuals that remain on the surface of the devices and may cause an enhanced background fluorescence for highly energetic laser excitation.

As a consequence of optimizing the fabrication method for high selectivity, the etch rate is fast. One consequence is the trade of a decreased minimal hole radius required for PhCW for GaAs droplet epitaxy QDs for a higher sidewall roughness, potentially increasing the out-of-plane and backscattering rate [234]. Figure 6.4c) indicates that in-plane sidewall deformation of about 3 nm on the length of about 20 nm are common.

In addition, over-etching must be considered for designing the PhCWs and requires calibration to match the guided mode frequency with the QD. The etched hole radii of photonic crystal holes are characterized by scanning electron microscopy. The radius of the etched holes on the surface of the sample post fabrication r_s as a function of the radius on the electron beam exposure mask r_m is displayed in figure 6.5.

For the functionality of a photonic crystal as a photonic insulator, it is vital that all holes are etched through to avoid mode-mixing and closing of the bandgap [165].

In regions of the thinnest deposition of electron-beam resist hole with a radius of $r_s = 33.6(3)$ nm are fabricated. However, these smallest holes are unreliable and likely of pronounced conical shape. Based on optical inspection, only holes with a radius of approximately $r_s \approx 40$ nm are reliably etched through the heterojunction membrane⁽⁶⁾. Thus, only photonic crystals waveguides consisting of holes with a radius larger than 40 nm can be assumed to operate reliably and be reproducible.

The pattern infidelity, i.e., the difference between electron-beam exposure mask radius r_m and surface hole radius on the sample post fabrication r_s , monotonously increases with the hole radii. For the smallest holes the over etching amounts 11.5(6) nm, were for the larges holes the over-etching increased toward 27.3(4) nm.

6.3 ELECTRIC CHARACTERIZATION

Probing the current-voltage characteristics of the heterostructures gives insight into the electromagnetic environment of the QD. Ideally, no leakage and tunneling currents disturb the QDs' electromagnetic environment. A pronounced p-i-n-like current-voltage characteristic with a low shunt-resistance indicates successful fabrication of high-quality ohmic contacts [260].

The current-voltage characteristic of the heterojunction is shown in figure 6.6⁽⁷⁾. As shown in figure 6.6c), the current-voltage curve shifts toward higher voltages from high temperatures (300 K) toward cryogenic temperatures (approximately 30 K).

Figure 6.6a) shows the sensed current J_S along with the statistical error of 30 samples and the systematic error of the source measure unit at cryogenic temperatures. At cryogenic temperatures, no significant current is sensed in the bias voltage range of approximately 0.6 V within the statistical error and the systematic error of the source measure unit. At a bias voltage above $U_B = 1.0$ V, a steep incline of the forward current is sensed. The forward current follows an exponential law qualitatively, as expected for an ideal p-i-n diode described by the Sah–Noyce–Shockley model [261]:

$$J_{SNS} = J_0 \left(\exp \left(\frac{U_B}{\eta_d U_T} \right) - 1 \right), \quad (6.1)$$

where J_0 is the scale current, η_d is the ideality factor, U_T is a measure of the thermal energy $qU_T = k_B T$, q is the elementary charge, k_B the Boltzmann constant and T the temperature. However, the Sah–Noyce–Shockley model fails to describe the observed forward current quantitatively. Better accuracy for modeling the forward current is achieved when taking a non-negligible ohmic shunt resistance R_S , a finite internal ohmic resistance $R_{||,1}$, and a finite parallel resistance to the circuit $R_{||,2}$ into account. For such a electronic circuit, the total current J_S can be analytical expressed

(6) The etching of a hole through the membrane is conditional for the hydrogen fluoride to dissolve the sacrificial layer locally underneath a PhCW. The regions of a suspended heterojunction membrane, i.e., regions of a dissolved sacrificial layer, are well recognizable under optical microscope inspection.

(7) The electronic setup is described in A.VI.

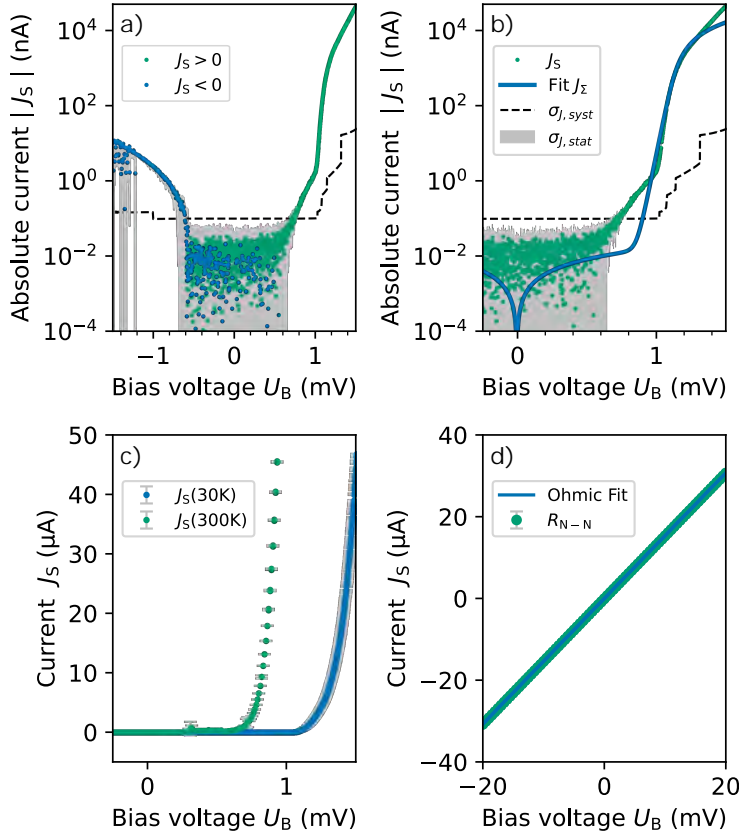


Figure 6.6: The current-voltage characteristic of the p-i-n heterojunction after nanofabrication in cryogenic conditions. Figure a) shows the absolute current of the heterojunction, where the green (blue) indicates forward (backward) currents. The dashed line indicates the source-meters systematic error specifications, and the area shaded in gray indicates the statistical error of 30 samples. Figure b) shows a fit, as discussed in the text. Figure c) shows the current-voltage characteristic at 300 K (green) for comparison with cryogenic conditions (blue). Figure d) shows the current-voltage characteristic through two separate back gate contacts (green) and a fit (blue).

as [262]:

$$J_{\Sigma} = \frac{\eta_d U_T}{R_S} \mathcal{W} \left(\frac{J_0 R_S R_{\parallel,1}}{\eta_d U_T (R_{\parallel,1} + R_S)} \exp \left(\frac{R_{\parallel,1} (U_B + J_0 R_S)}{\eta_d U_T (R_{\parallel,1} + R_S)} \right) \right) + \frac{U_B - J_0 R_{\parallel,1}}{(R_{\parallel,1} + R_S)} + \frac{U_B}{R_{\parallel,2}}, \quad (6.2)$$

where \mathcal{W} is the LambertW function [263]. A qualitative fit of equation 6.2⁽⁸⁾ is displayed in figure 6.6b).

The fit does describe the turn-on region around 1V of the diode and the subsequent saturation and current limitation by the shunt resistance R_S at around

(8) The fit excludes the data between $U_B = 0.5$ V and $U_B = 0.9$ V, as well as the very high bias voltage region $U_B > 1.4$ V, as discussed in the main text. The goodness of fit is $\chi_{\text{red}}^2 = 58$.

$U_B \approx 1.1\text{V}$ well. Equation 6.2 provides a shunt resistance estimate of $R_S \approx 11(5)\text{ k}\Omega$ and a diode ideality factor estimate of $\eta_d = 9.5(18)$. No significant parallel resistances ($R_{\parallel,1}$ and $R_{\parallel,2}$) are present (i.e., $R_{\parallel,1}, R_{\parallel,2} > 1\text{G}\Omega$), and therefore no considerable leakage current is expected.

The shunt resistance R_S is attributed to the complex current flow through the highly non-uniform semiconductor heterostructure. The charge mobility of electrons in the n-doped layers, the hole mobility in the p-doped layers, the ohmic quality of the electric contact of the gates, and the topology of the contacts define the shunt resistance.

Probing the current through a pair of back gate contacts shows that their quality does not limit the shunt resistance R_S . A characterization⁽⁹⁾ of the resistance between separate back gate-contacts is displayed in figure 6.6d). The back gate contacts are purely ohmic with a total resistance of $R_{N-N} = 650.88(23)\ \Omega$, indicating the fabrication of high-quality electronic back-gate contacts.

The sheet resistance of the p-layer is ≈ 20 times higher than the n-layer [157]. For similar heterojunctions, p-layer sheet resistances of the order of $10\text{ k}\Omega/\text{square}$ have been measured [264] Thus, the sheet resistance of the p-layer are likely to limit the shunt resistance, suggesting high-quality top-gate contacts.

The estimated ideal factor well above the Sah–Noyce–Shockley model limit of 2 reflects the heterojunctions complex layout closer to a series of metal-semiconductor, uni-polar, and p-i-n junctions [265, 266].

The forward current's the first knee at $U_B = 0.6\text{V}$ cannot be described by equation 6.2. This feature may indicate the presence of a parallel current flow inside of the heterojunction [267]. However, in the voltage region of around 1.35V where the excitonic state is populated, the electric heterojunctions properties are approximated well by equation 6.2 as a p-i-n diode with high ideality factor. Although the ohmic isolation between the p and the n gate is high ($\text{G}\Omega$) and effective charge noise reduction can be expected at low voltages, the tunneling current in the forward-biased diode is significant in the voltage region of a populated exciton state. Consequently, tunneling-current-induced spectral diffusion is likely to occur. However, the magnitude of spectral diffusion depends on the local current density of the highly heterogeneous structure.

6.4 PHOTONIC CHARACTERIZATION

A fundamental challenge of planar quantum photonics is to allow true scalability of integrated nanophotonic circuits and to keep the overall device loss as low as possible. Simultaneously, the photonic circuits must be reliable in fabrication and reproducible in their properties. In this section, the fabricated photonic circuitry⁽¹⁰⁾ is investigated regarding the reproducibility of nanophotonic devices and their losses.

(9) Ohmic charge-voltage relation fit yields a goodness of fit of $\chi_{\text{rad}}^2 = 1.01$.

(10) Sample B15459-A. See appendix A.II.

The sample is placed in a closed-cycle cryostat on top of a stack of nanopositioners (X,Y,Z). The base temperature of the sample mounting platform is about 7 K⁽¹¹⁾. The nanopositioners can position the sample with respect to a fixed microscope objective inside the cryostat. The sample is positioned such that a device's two SEG fiber-to-chip couplers are accessible simultaneously for injection and analysis of transmitted light. Figure 6.7 displays a schematic of the optical setup.

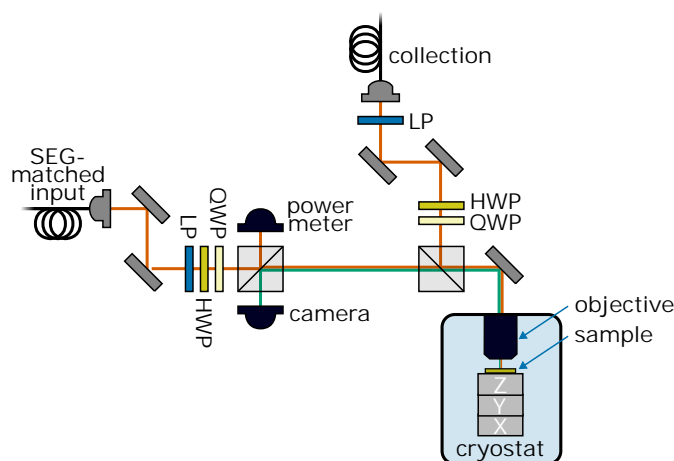


Figure 6.7: Schematic of the optical setup. The sample is installed in the cryostat on top of nanopositioners (XYZ). Linear polarizers (LP), half-wave plates (HWP), and quarter-wave plates (QWP) control the input polarization and filter the excitation laser from the collected signal. The optical collection path is matched to the output mode diameter from a shallow etched grating.

A beam-splitter outside the cryostat separates the optical input paths (in transmission) from the optical collection path (in reflection). The free-space optical setup images the collimated laser-input path to the back focal plane of the microscope objective. A linear polarizer, a half-wave plate, and a quarter-wave plate control the laser-input polarization. The laser-input and optical collection paths are matched in their mode diameter to the shallow etched grating for maximal efficiency. The collected light is polarization filtered for filtering out the cross-polarized laser input.

For photonic characterization, a supercontinuum laser (620 – 850 nm) and a single-mode tunable diode laser (755 – 815 nm) are injected into the device. The collected light is analyzed with an avalanche photodiode and a spectrometer. The setup features a CMOS camera for optical imaging. The schematic of the entire optical setup and its elements, instruments, and functionality can be found in appendix A.IV.1 for reference.

6.4.1 Photonic Routing

A planar photonic platform's most elementary functionality is in-plane routing and coupling light from free-space optics into guided modes. In the planar platform

(11) The sample temperature is approximately 30 K, see chapter 8.

of InGaAs QDs, nanobeam waveguides (NBWs) route light with low loss [46]. For efficient chip-to-fiber coupling, NBWs are interfaced with shallow etch grating (SEG) couplers [162, 268].

Figure 6.8a) shows a CMOS camera image of a $\lambda_L = 795$ nm narrow-band laser injected into the most basic nanophotonic device. The device consists of two orthogonally oriented SEG couplers and an NBW linking routing the light from one coupler to the other.

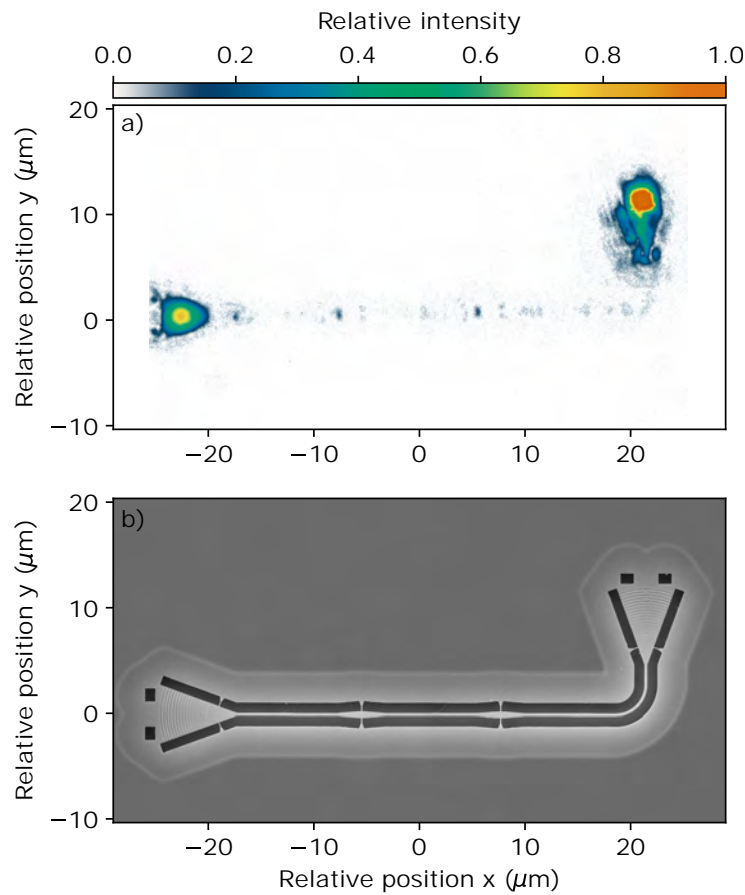


Figure 6.8: Figure a) shows the CMOS camera image of a nanophotonic device of two shallow etch grating (SEG) couplers linked by a nanobeam waveguide (NBW). A laser with $\lambda_L = 795$ nm is injected into the coupler on the top right. The input coupler appears bright due to the direct reflection of the laser on the grating. The injected light is transmitted to the other coupler on the left. The light at the output coupler is of comparable brightness to the light reflected from the input port. Figure b) shows a scanning electron microscope image of the same device.

The CMOS camera image of the nanophotonic device indicates efficient coupling and routing of light. The light transmitted to the output coupler appears of comparable brightness to the light directly reflected from the input coupler. The output coupler's far-field mode profile is approximately gaussian, suggesting a coupling efficiency into a single-mode fiber.

Light in the guided mode of the nanobeam along the device is scattered into the camera imaging path. Comparison with the device's scanning electron microscope image in 6.8b) indicates out-of-plane scattering in confined regions along the waveguide. Most out-of-plane scattering occurs at the interfaces of the NBWs with the SEG couplers and the tethers.

Shallow Etch Grating Couplers

Efficient chip-to-fiber coupling is essential for efficient quantum photonic integrated circuits. In silicon-on-insulator photonics, surface-focused grating couplers achieve moderately high chip-to-fiber coupling efficiency over a large bandwidth, high polarization selectivity, and a decent fiber alignment tolerance [268]. Similar designs, like the SEG coupler, demonstrate high performance in the planar platform of InGaAs QDs [162]. With a coupling efficiency into a single-mode fiber exceeding 60 % [162], SEGs constitute an essential building block of the proposal of scalable quantum photonic networks with InGaAs QDs [7].

The SEG coupler's polarization sensitivity [162] allows the powerful elimination of an excitation laser background from the signal collected from a coupler. By cross-polarizing the laser to the coupler's far field, the subsequent polarization filtering efficiently removes the laser background from the signal. This filtering method is crucial to the platform's performance as a source of highly indistinguishable single photons.

Figure 6.9 shows the normalized transmission through the nanophotonic device of two SEG couplers linked by NBW (shown in figure 6.8) for a laser wavelength of $\lambda_L = 795$ nm as a function of the laser polarization. The linearly polarized input laser passes through a series of half-wave and quarter-wave-plate. The wave-plate angles ϕ_{HWP} and ϕ_{QWP} are swept independently, mapping out the transmission for the entire polarization space.

The normalized transmission shows periodic maxima or minima corresponding to the wave-plate configurations that result in collinear or transverse input polarization relative to the SEG mode. The laser extinction, defined as the ratio of transmitted light for transverse and collinear polarization, is $33.8^{(+1.2)}_{(-1.6)}$ dB. At 795 nm the fiber-coupling efficiency into a single-mode fiber of light emitted from the SEG coupler is 48(1) % without the correction of the non-trivial aspect ratio of the mode profile [162]. The SEG grating couplers' design parameters stem from numerical simulations and can be further improved by adjusting the grating layout for the operation wavelength of 795 nm [162].

6.4.2 Loss Estimations and Nanobeam Waveguide Performance

Understanding the platform's loss mechanisms is crucial for designing and fabricating the next generation of quantum photonic integrated devices with quantum emitters. The platform's propagation losses can be studied conveniently by studying the transmission of a set of concentric nanobeam waveguide (CNBW) devices [251],

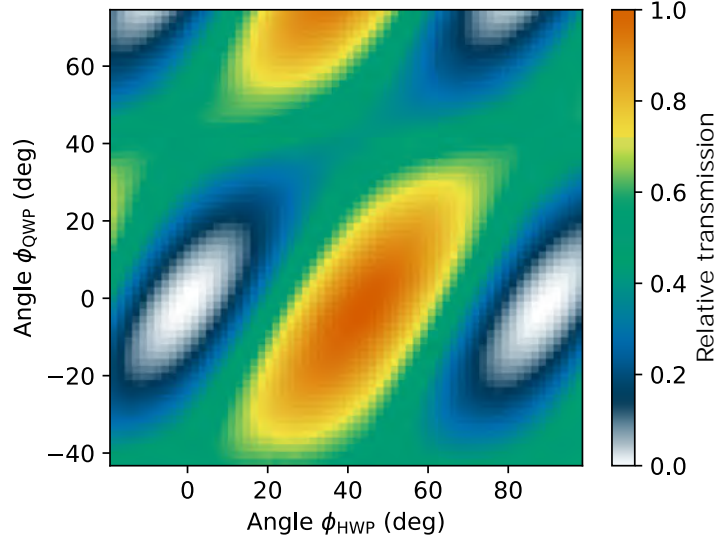


Figure 6.9: Relative laser transmission through a NBW for injection of a laser ($\lambda_L = 795$ nm) and as a function of the half-wave and quarter-wave-plate angles ϕ_{HWP} , ϕ_{QWP} controlling the input laser polarization.

shown in figure 6.10.

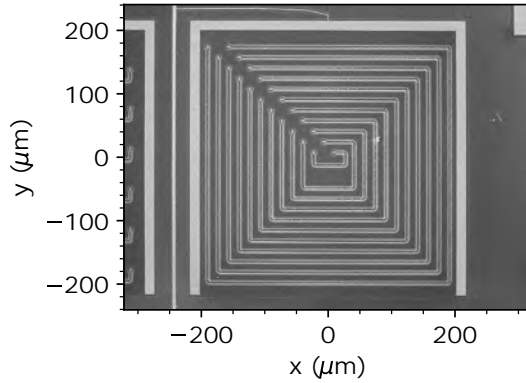


Figure 6.10: A set of concentric devices consisting of two fiber-to-chip couplers and NBWs of various lengths between $L_0 = 60 \mu\text{m}$ and $L_{10} = 1.486$ mm. The gratings are placed at a fixed relative position from each other to avoid re-aligning the position and angle of laser injection and collection beams. The couplers' relative orientation enables laser-background filtering by cross-polarizing the injected laser at the input port and the collected light at the output port.

The total transmission through a CNBW devices $T_{\text{II,CNBW}}$ can be described as product of the transmission of the photonic elements of the device [251]:

$$T_{\text{II,CNBW}}(L, \lambda) = \theta_G^2(\lambda) \theta_B^3 \theta_T^{N_T} T_{\text{NB}}(L, \lambda), \quad (6.3)$$

where L is the NBW length, $\theta_G(\lambda)$ is the fiber-to-chip coupling efficiency of the SEG, θ_B is the loss from a single nanobeam tether N_T , θ_B is the transmission loss in a 90 deg-bend, and $T_{NB}(L, \lambda)$ is the NBWs propagation loss.

For comparable conditions, studies on the InGaAs platform [158, 251] have shown that the bending losses are negligible and that losses on tethers can be described as a minor contribution to the propagation losses⁽¹²⁾. By measuring the transmission, $T_{\Pi, \text{CNBW}}$ for devices of varying NBW length L , the SEG fiber-to-chip coupling efficiency and the propagation losses rate per unit length can be determined.

For examining the propagation loss rate, both the SEG couplers and the NBWs spectral response must be reliable and identical among the different devices. Fabrication-induced imperfections that modify the fiber-to-chip coupling efficiency or defects on the NBW that scatter propagating light are challenging to identify and complicate the spectral analysis.

Figure 6.11 displays examples⁽¹³⁾ of the concentric devices' transmission $T_{\Pi, \text{CNBW}}(L, \lambda)$ probed with the super-continuum laser and the spectrometer relative to the transmission maximum of the shortest waveguide of $L = 60 \mu\text{m}$.

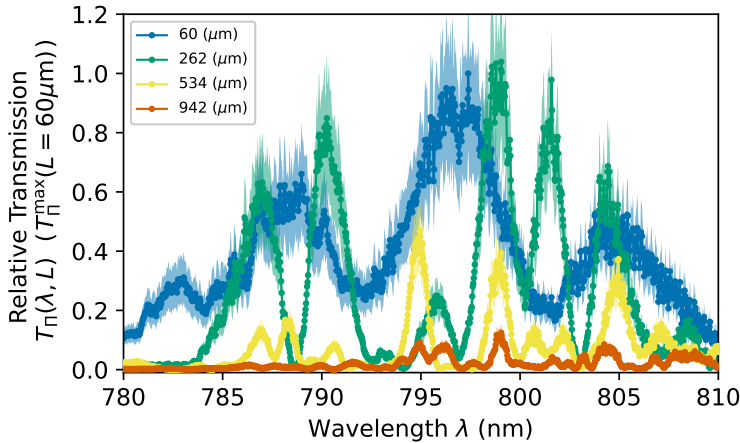


Figure 6.11: Examples of the devices transmission $T_{\Pi, \text{concentric}}(L, \lambda)$ relative to the shortest waveguide of $L = 60 \mu\text{m}$. The devices are probed by injection of a super-continuum laser. The emission band is filtered to the spectral range of 750 nm to 850 nm. The transmission spectra is measured with a spectrometer. The input-path and collection-path are aligned by an initial alignment with the narrow band laser at $\lambda = 795 \text{ nm}$. The transmission spectra are normalized by the spectral power-density of the continuum laser obtained by the direct exposure of the spectrometer. The shaded areas indicate the uncertainty of 3 standard deviations.

The transmission spectra displayed in figure 6.11 follow a Gaussian-shaped envelope as designed [251], but their transmission spectra show additional spectral features, such as periodic modulation fringes. The spectral modulations are regular with a

(12) The propagation losses are insensitive to the number of tethers N_T per unit length L [158].

(13) The transmission spectra of all 11 CNBW devices are displayed in appendix A.V.

periodicity that scales with the inverse of the CNBW length $1/L$. This periodicity reminds of Fabry–Pérot interferometry and indicates reflections within the devices. A possible explanation is a poor alignment of the sample between different nanofabrication steps causing a spatial offset between the NBWs and the SEG couplers. Such an offset would cause out-of-plane scattering and back-reflections at the SEG coupler-to-NBW interfaces.

Even though quantitative propagation loss analysis is hindered by the spectral modulation of the concentric device transmission, the transmission spectra displayed in figure 6.11 give insight into the platform’s loss performance. The relative attenuation of the transmission⁽¹⁴⁾ provides a qualitative propagation loss estimate of about 20 dB/mm to 30 dB/mm. In comparison, the platform of InGaAs QDs typically shows 20 dB/mm [46].

As discussed in section 6.2, increased losses are expected from the increased sidewall roughness of the NBW, displayed in figure 6.3. Additionally, the photonic devices experiences losses arising from the semiconductors heterostructure’s layout of 4 nm thick GaAs layers on both surfaces of the heterojunction. The GaAs layers are absorptive at the platform’s operation wavelength below the bandgap of GaAs 815 nm at cryogenic temperatures [269]. Furthermore, electroabsorption increases in their efficiency for shorter operation wavelengths [270, 271].

However, the waveguide total insertion loss is still small (< 1 dB) for the very short devices of and thus can be neglected for the characterization of the emitters. [223]. The reduction of propagation losses will be addressed in the design and development of the next-generation planar platform for GaAs droplet epitaxy QDs, discussed in section 6.5.

Electroabsorption in gated $\text{Al}_{15}\text{Ga}_{85}\text{As}$ nanophotonic waveguides

Likewise the platform of InGaAs QDs [251], the platform of GaAs droplet epitaxy QDs experiences free carrier absorption [270] and losses due to the Franz–Keldysh effect (FKE) [271]. However, both absorptive effects are of higher efficiency for the shorter operation wavelengths of the GaAs QD platform.

In planar nanophotonic platforms, the FKE originates from the electric fields inside and on the surface of the heterojunctions [251]. The electric fields distort the electron and hole wave functions and enable optical absorption at energies below the bandgap of $\text{Al}_{15}\text{Ga}_{85}\text{As}$. Losses related to the FKE originating from the built-in field⁽¹⁵⁾ can be measured by probing the transmission of a waveguide and variation of the bias voltage U_B .

For high bias voltages close to the flat-band voltage $U_B \approx 1.6$ V, the electric field inside the heterojunction and associated losses arising from the FKE are comparably small. In this regime of high bias voltages, losses due to FKE from surface charges and scattering on the side walls limit the propagation losses [251]. For decreasing

(14) See figure A.24 in appendix A.V.

(15) The electric field inside the heterojunction of sample B15459-A as a function of the bias voltage U_B is displayed in figure A.9 in appendix A.II.

bias voltages, the electric field inside the heterojunction and associated losses arising from the FKE increase.

Experimentally, the waveguide attenuation arising from the FKE of the electric fields F inside the heterojunction $A_{\text{FKE},F}(U_B)$ is estimated⁽¹⁶⁾ from the transmission of a NBW device at bias voltage U_B relative to the transmission at a high bias voltage of $U_B = 1.5 \text{ V}$ by

$$A_{\text{FKE},F}(U_B, \lambda) = 1 - \frac{T_{\text{IL,NBW}}(U_B, \lambda)}{T_{\text{IL,NBW}}(U_B = 1.5 \text{ V}, \lambda)}, \quad (6.4)$$

where $T_{\text{IL,NBW}}(U_B)$ is the transmission of a NBW device for a bias voltage U_B .

Figure 6.12 shows the waveguide attenuation from the FKE of the electric fields inside the heterojunction $A_{\text{FKE},F}(U_B, \lambda)$ for an NBW device of $42.2 \mu\text{m}$ length for the wavelengths of $\lambda_L = 785 \text{ nm}$, $\lambda_L = 795 \text{ nm}$ and $\lambda_L = 805 \text{ nm}$.

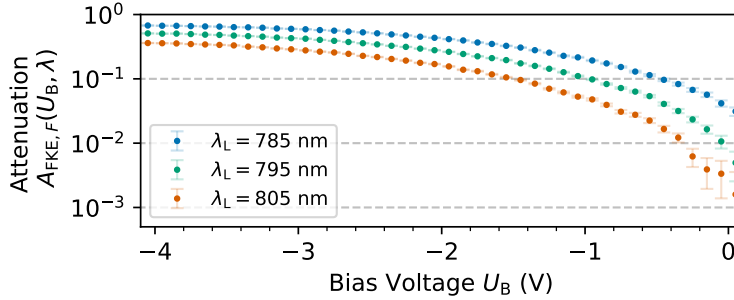


Figure 6.12: Waveguide attenuation from the FKE of the electric fields inside the heterojunction of light transmitted in a $42.2 \mu\text{m}$ long NBW as a function of the applied bias voltage U_B probed with laser wavelengths of $\lambda_L = 785 \text{ nm}$, $\lambda_L = 795 \text{ nm}$ and $\lambda_L = 805 \text{ nm}$. The attenuation is estimated from the waveguide transmissions for a bias voltage of $U_B = 1.5 \text{ V}$.

Figure 6.12 shows that the absorption losses due to the FKE drastically increase when applying a negative bias voltage. For wavelengths near the QD photoemission spectrum, at $\lambda_L = 795 \text{ nm}$, more than 50 % of the light is absorbed for a negative bias of -4 V for a short NBW of only $42.2 \mu\text{m}$ length. As expected from theory, shorter wavelength experience stronger absorption [271], and the platform experience significantly more electroabsorption arising from the FKE than heterojunctions of the InGaAs platform [251]. The increased electroabsorption may be exploitable for realizing FKE-based high-speed, high-efficiency on-chip photodetectors [272].

For zero bias, the built-in field causes $\approx 1\%$ of additional attenuation for $\lambda_L = 795 \text{ nm}$. For higher bias voltages, the FKE of the electric field inside the heterojunction is no longer significant.

(16) The effect of the residual electric field at $U_B = 1.5 \text{ V}$ is neglected. This approximation is sufficient to determine the effect of the FKE effect due to the built-in field at zero or negative bias voltages. However, for a thorough loss estimation at forward bias, the electric field F distribution, material, and guided mode profile inside the waveguide must be taken into account [251].

6.4.3 Line-Defect (W₁) Photonic Crystal Waveguides

The W₁ PhCW are essential for a planar platform of QDs [256] and have demonstrated their high performance in the InGaAs platform [93, 218]. For chip-to-fiber coupling of QD emission, W₁ waveguides are embedded in a photonic device that carefully adapts the photonic modes and routes the light towards SEG couplers. The photonic crystal consists of slow and fast light sections, which are interfaced by adiabatically stretching the photonic crystal along the propagation axis [257, 258]. The slow-light section hosts the quantum dot. The fast-light sections are interfaced to NBW via an adiabatic taper [259] for low-loss routing of the photons towards SEG couplers.

W₁ PhCWs possess higher transmission losses per unit length compared to NBWs. Their higher loss rate arises from sensitivity to fabrication-induced disorder [273–276]. The higher group index of PhCW n_g enhances light-defect coupling [149, 167]. Losses due to out-of-plane scattering scaling with the group index n_g and losses due to in-plane scattering into bulk modes and reverse propagation modes scale with n_g^2 [219]. The scaling of the propagation loss per unit length in the group index can be utilized to identify the slow light region of a W₁ waveguide. In the long-wavelength regime of the fundamental mode of a W₁ PhCW, the group index and, therefore, the propagation losses diverge as displayed for an example in figure 5.2a) and c).

For the identification of slow light, the transmission of a NBW is compared with the transmission of a W₁ PhCWs. A photonic device of a layout as displayed in figure 6.13b) provides the reference. The reference device is identical to the device hosting the PhCW, shown in figure 6.13a), except for the replacement of the mode taper and the PhCW section with an NBW.

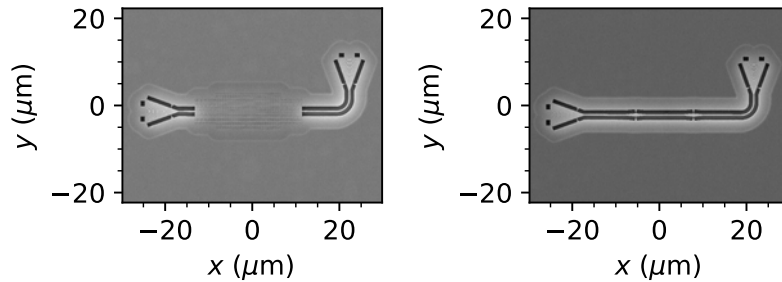


Figure 6.13: Scanning Electron Microscope of nanophotonic devices (sample B15459-A). The device in figure a) consists of a W₁ PhCW section, a mode taper, and NBWs that route light from the PhCW's guided mode to SEG couplers. Figure b) shows a reference device of identical dimensions but where the PhCW is replaced with a nanobeam section.

The transmission of the devices is comparable for wavelengths of the fast-light regime of the W₁ PhCW's guided mode. However, for wavelengths in the slow-light regime of the guided mode, the propagation losses increase, and the transmission

is significantly lower. For wavelengths outside the guided mode, no significant transmission is expected. Hence, the spectral width and the slow light region of the fundamental mode of a W_1 PhCW guided mode can be determined by comparison of the device transmission with a reference.

For the design of the devices with PhCWs, the nanophotonic devices were fabricated and characterized on a wafer with comparable layout⁽¹⁷⁾. Figure 6.14 shows transmission spectra of W_1 PhCW devices for various photonic crystal lattice parameters and for reference from devices with a NBWs replacing the W_1 PhCWs sections.

The reference T_{ref} in figure 6.14 is the envelope of the normalized transmission averaged over 4 reference devices. The spectral shape of the reference reflects the transmission of the fiber-to-chip coupler $\theta_G(\lambda)$ fabricated on the wafer B15280. As expected, the transmission of the PhCWs remains below the transmission of a NBW (T_{ref}). For the smallest lattice constants, ($a = 195$ nm, $a = 197$ nm), the fundamental mode of the PhCW is far blue detuned to the fiber-to-chip coupler transmission window. For the smallest hole radii, r , the long wavelength part of the mode reaches into the transmission window of the coupler. The long wavelength part of the fundamental mode is of slow light, and the transmission is consequently low.

For intermediate lattice constants ($a = 205$ nm, $a = 207$ nm), the hole radii strongly determine the spectral overlap of the fundamental mode and the fiber-to-chip coupler transmission. The transmission of the W_1 PhCWs is comparable with an NBW, indicating highly efficient mode adapters.

For the largest hole radius ($r = 54$ nm), the slow light is approximately in the center of the fiber-to-chip coupler transmission window. For the smallest holes, the PhCWs fundamental mode fully overlaps the fiber-to-chip coupler transmission window. For the longer lattice constants ($a = 215$ nm, $a = 217$ nm), the slow light region is outside the couplers transmission window independent of the hole radius.

The guided modes of the W_1 PhCW are blue-shifted with respect to their design. Finite-element-calculations of the guided mode eigenfrequencies taking the over-etched hole radii into account fails to explain a blue-shift by 20 nm. This may be explained by surface oxidization during the fabrication.

The final sample design takes the blue-shift observed for these test devices into account. To ensure that W_1 PhCW with slow light near the spectral region of GaAs droplet epitaxy quantum dots at 795 nm are available, the parameter space of the W_1 PhCWs is selected to compensate for a blue-shift of up to 30 nm. Figure 6.15 shows the transmission of a W_1 PhCW⁽¹⁸⁾ and a NBW of the final sample. The examination of the W_1 PhCW properties of the final sample is hindered by the abnormal device-dependent modulation of the NBW transmission, as discussed in section 6.4.2. Qualitative comparison of the device transmission of the W_1 PhCW

(17) This and the following chapters discuss the nanophotonic devices and QDs of sample B15459-A, fabricated from wafer B15459. The PhCW were designed by fabrication of test devices on wafer B15280. See appendix A.II.

(18) Device $W_1^{(3,5)}_{206,36}$, see appendix A.II.

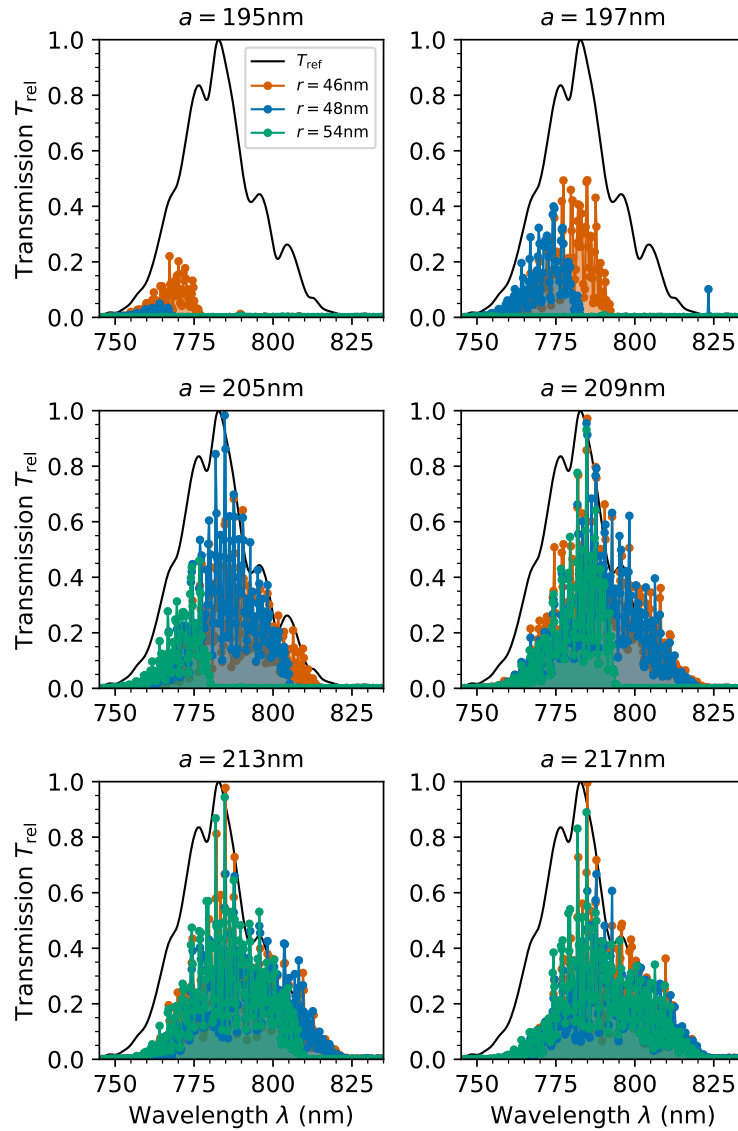


Figure 6.14: The transmission of W_1 PhCW test devices of various lattice constants a and hole radii r and a NBW reference (fabricated on wafer B15280). The hole radii refer to the radius on the electron-beam-resist mask. The hole radius over-etching of these test devices is approximately 5 nm. The reference NBW reference is the normalized transmission envelope of the averaged transmission spectrum 4 reference devices.

of figure 6.15 on the final sample with the W_1 PhCW of similar parameters on the test sample in figure 6.14 indicates a similar blue-shift of the guided mode and the general functionality of the device. As for the NBW, CMOS camera images indicate most losses at the SEG coupler to NBW interface.

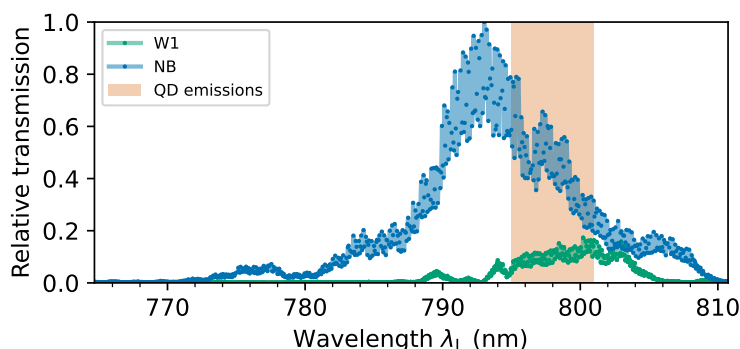


Figure 6.15: Relative transmission of two devices of sample B15459-A with identical waveguide length with a narrow-band diode laser and photo-detection with an avalanche photodiode. Blue shows the device's transmission where a nanobeam links two fiber-to-chip couplers, as shown in figure 6.8. Green shows the transmission of a device with a intermediate W₁ PhCW waveguide section, like the device shown in figure 6.4. The W₁ waveguide consists of holes with a electron-beam mask radius of $r_m = 35$ nm and an etched hole radius of approximately $r_s \approx 45$ nm. The photonic crystal lattice constant is $a = 206$ nm. The red area indicates the wavelength region of the QDs examined in this device in chapter 7, 8, and 9.

6.5 CONSIDERATIONS FOR NEXT-GENERATION PLATFORMS

The photonic and electric characterization and the scanning electron microscope imaging provide insights for designing and developing the architecture of the next-generation planar platform for GaAs droplet epitaxy QDs.

The analysis of the electric bandstructure and the electric characterization showed that the electric field, in combination with the small thickness of the heterojunction, leads to a large potential at the position of the QDs. The large potential shifts the Coulomb plateaus to large forward bias voltages and results in high tunneling currents that contribute to charge noise effects [277] and induce losses due to the Franz-Keldysh effect [271]. Incorporating an additional n-layer, resulting in a p-i-n diode, could be utilized to reduce the electric field at the location of the QDs and operate the QD at close-to-zero bias voltage [260, 278].

The heterostructure of the presented devices features GaAs capping layers on both sides of the membrane to prevent the risk of post-processing oxidation. However, these layers are absorptive for the operation wavelength of the platform. In order to reduce the platform's propagation losses and maintain surface layer protection, an alternative approach may be chemical passivation replacing the GaAs surface layers. Chemical passivation of the surface layers can also reduce surface charge effects and free carrier absorption losses [46, 270]. Recently, sulfur passivation of the GaAs surface followed by a dielectric layer of Al₂O₃ of 6 to 12 nm has been demonstrated to be effective [279].

In heterostructure layouts similar to the one presented in this thesis, the p-doped layer is identified as the largest source of free-carrier absorption [46]. Selectively

etching away the p-doped layer from the surface, the free-carrier absorption can be reduced, and the Franz–Keldysh effect due to built-in fields can be suppressed [46]. However, for future-generation devices, other heterojunction layouts should be considered. Recently, an n-i-n⁺ type of heterojunction has been demonstrated [280]. An n-i-n⁺ heterojunction layout allows for high-speed tunable platforms [280] and may allow re-design of the layout within the limitations of an ultra-thin membrane free of p-doped layers.

The presented heterojunction, as the first generation of ultra-thin membrane heterojunction for GaAs QDs, does not feature a tunnel barrier [107, 260, 281] for deterministic spin-photon interfaces with quantum dots [12]. The functionality of a tunneling barrier has been demonstrated in high performance as GaAs bulk-samples [27] but has yet to be adapted into the ultra-thin membrane layout.

The scanning electron microscopy characterization shows that the soft-mask fabrication method brings with the optimization for high-selectivity a high sidewall and surface roughness. The aggressive etching requires pre-characterization of the fabricated feature sizes and inhibits the reliability and reproducibility of the fabrication. Resist reflow techniques [205] could be incorporated into the fabrication process to reduce the spatial rest inhomogeneity. On a macroscopic scale, a homogenous thickness improves fabrication reliability. On a microscopic scale, resist reflow reduces the surface roughness, potentially reducing the intrinsic waveguide loss. Ultimately, higher etching selectivity and improved control over the fabrication process can be achieved by using intermediate hard masks [206].

* * *

This chapter presented the layout of the first generation of a planar quantum photonic platform for GaAs droplet epitaxy quantum dots. The semiconductor heterojunction membrane, in which the quantum dots are embedded, shows near-ideal current-voltage characteristics. Nanophotonic devices with efficient fiber-to-chip couplers and line-defect and nanobeam waveguides were processed from the membrane. The next chapter performs spectroscopy on the quantum dots embedded in these nanophotonic devices.

SPECTROSCOPY OF DROPLET-ETCHED GaAs QUANTUM DOTS IN PLANAR PHOTONIC DEVICES

This chapter presents the first planar platform for quantum photonics with droplet-etched GaAs quantum dots. Its properties, such as the quantum dot density, inhomogeneous broadening, the viability of various quantum dot excitation methods, the ability of quantum dot charge-state and Stark shift tuning, and the single-photon character of the quantum dot photoluminescence are examined based on a characteristic quantum dot in a line defect waveguide.

The development of scalable sources of non-classical light is fundamental to unlocking the technological potential of quantum photonics. While the planar platform of Stranski–Krastanov InGaAs QDs demonstrates fast progress in developing photonic scalable building blocks [7], the platform has shown non-optimal levels of entanglement and indistinguishability. Platforms of droplet epitaxial-grown GaAs have recently demonstrated superior-quality single-photon sources [8, 27, 40]. However, to date, these QDs have yet to be integrated into planar nanophotonic devices.

This chapter describes the first planar platform of droplet epitaxial-grown GaAs that features charge-state and Stark shift tuning in detail. First, the system properties, such as the QD density, inhomogeneous broadening, and the viability of various QD excitation methods, are examined. Second, the basic functionalities and properties of a QD embedded in a line-defect photonic crystal waveguide are presented. Lastly, the single-photon character of the QD photoluminescence is verified.

The sample⁽ⁱ⁾ is placed in a closed-cycle cryostat on top of nanopositioners (XYZ) with a base temperature of the sample mounting platform of 7 K. With the nanopositioners, the sample can be moved with respect to a fixed microscope objective inside the cryostat. A beam-splitter outside the cryostat separates the optical excitation paths and the imaging path in transmission from the optical collection path in reflection. Figure 7.1 displays a schematic of the optical setup.

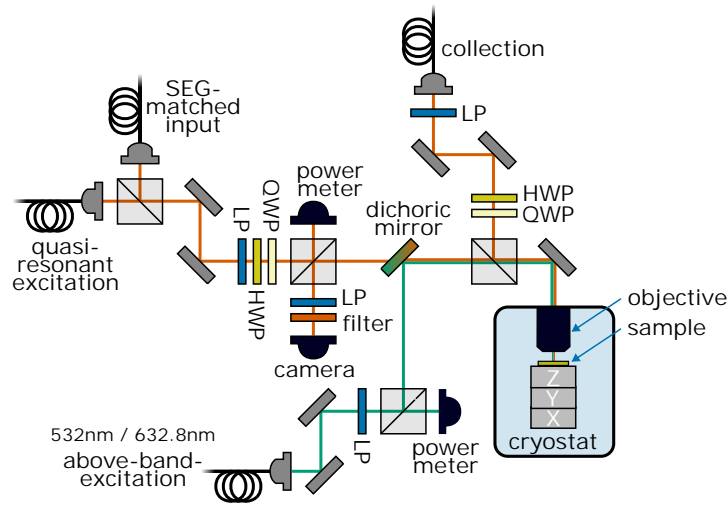


Figure 7.1: Schematic of the optical setup. The sample is installed in the cryostat on top of nanopositioners (XYZ). A dichroic mirror combines the input paths for above-band-excitation (532 nm and 632.8 nm), the path for quasi-resonant excitation, and the path matched with the shallow-etch-grating coupler mode diameter. Linear polarizers (LP), half-wave plates (HWP), and quarter-wave plates (QWP) control the input polarization and filter the excitation laser from the collected signal and from the CMOS camera image. The camera image path can be equipped with a filter. The optical collection path is matched to the output mode diameter from a shallow etched grating.

The optical setup is a confocal microscope for the full spectral range between 535 nm to 850 nm. For above-band and quasi-resonant excitation, the inserted laser fills the objective’s back focal plane, which then focuses the laser to a diffraction-limited laser spot on the sample. This input is used to focus maximal power onto a single QD. The imaging path features a CMOS camera. The optical collection path is matched to the output mode diameter from a shallow etched grating for maximal collection efficiency. A detailed schematic of the optical setup and a description of its elements can be found in appendix A.IV.1.

7.1 ABOVE-BAND EXCITATION AND SPATIAL MAPPING OF QUANTUM DOTS

The band gap energies of GaAs and $\text{Al}_{15}\text{GaAs}_{0.85}$ at cryogenic temperatures are approximately $E_g^{\text{GaAs}} = 1.519$ eV and $E_g^{\text{Al}_{15}\text{GaAs}_{0.85}} = 1.728$ eV [269, 282]. Above-band

(i) Sample B15459-A. See appendix A.II for a wafer and sample layout description.

excitation with a laser wavelength of $\lambda_L = 532$ nm [144] and $\lambda_L = 632.8$ nm [27] of GaAs droplet QDs has been demonstrated. Figure 7.2a) displays CMOS camera images spectrally filtered with a 750 nm long-pass filter of a non-structured section of sample B15459-A excited with a wavelength of $\lambda_L = 632.8$ nm with and without a bias voltage.

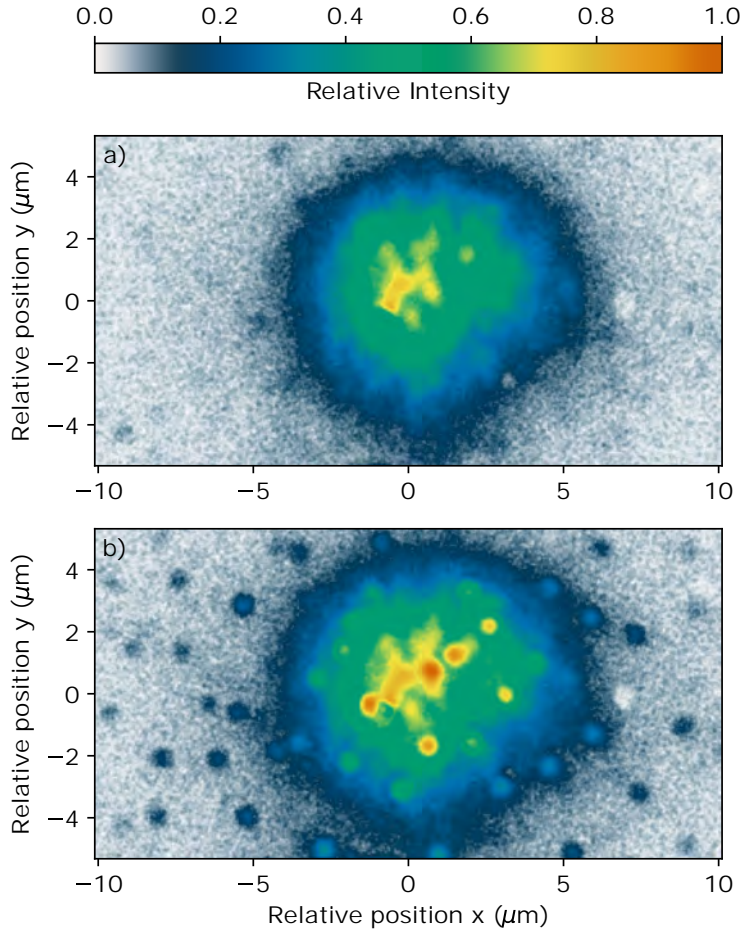


Figure 7.2: Camera images of a non-structured section of sample B15459-A under excitation with a wavelength of $\lambda_L = 632.8$ nm. The camera image is filtered by a 750 nm long-pass filter. The integration time is 5 s, and the excitation power of approximately $P_L \approx 500$ nW. Figure a) shows the image for a bias voltage of $U_B = 0$ V. No QDs are visible, and the fluorescence of impurities on the surface of the sample can be seen. Figure b) shows the same area for a bias voltage of $U_B = 1.5$ V. QDs are clearly visible not only at the center of the near-aberration limited laser focus spot, but also micrometers away from the focus spot.

By spectral filtering, the laser and the background fluorescence are sufficiently suppressed such that QDs are visible on the CMOS camera with a good signal-to-noise ratio. The CMOS camera images indicate the intensity of the optical

background fluorescence in the near-infrared region above 750 nm to be comparable to the QD fluorescence intensity.

However, above-band excitation with either wavelengths $\lambda_L = 532$ nm or $\lambda_L = 632.8$ nm induced a strong background signal. The background signal is likely caused by nanofabrication-induced impurities [46]. Figure 7.3 shows electronic microscope images of typical impurities on the surface of the sidewalls of the photonic devices of sample B15459-A.

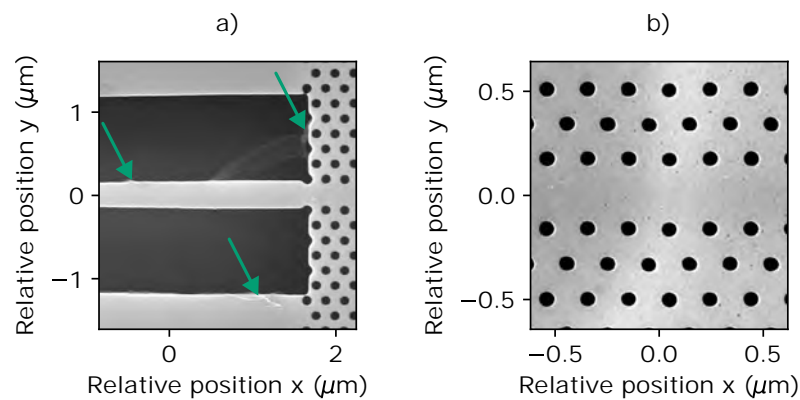


Figure 7.3: Scanning electron microscope images of a) the mode adapter b) the waveguide center of a W₁ PhCW showing typical nanofabrication-induced impurities. The sidewalls of deep trenches show wrapping by μm-sized flakes (Green arrows in figure a). Both the surface of the substrate and the surface of the membrane show nm-sized randomly scattered particles.

Carbon-rich impurities are typical contamination from electron-beam-resist residuals [46] and can be related to exposure to the inductively-coupled plasma during etching [46, 255, 283]. The scanning electron image in figure 7.3a) shows that the sidewalls of deep trenches show wrapping by μm-sized flakes, which likely are electron-beam-resists residuals. The image in figure 7.3b) shows nm-sized particles of unidentified nature scattered on the surface of a W₁ PhCW, which may contribute to the optical background. The signal-to-noise ratio for a excitation with a wavelength of $\lambda_L = 532$ nm is too poor for spectroscopic purposes. Excitation with a wavelength of $\lambda_L = 632.8$ nm showed a significantly lower background.

Better images can be achieved by filtering with a 10 nm-wide band-pass filter with a transmission band centered at 800 nm and a linear polarized cross-polarized to the excitation laser. CMOS camera images taken with this spectral filtering configuration are displayed in figure 7.4.

Figure 7.4a) shows how nano-structured areas, such as the shallow etch grating couplers and the side-walls of the deep trenches, contribute to strong background fluorescence. With the improved background fluorescence rejection, the images in figure 7.4b) reveal that QDs in the full field-of-view, far from the excitation spot, are fluorescent.

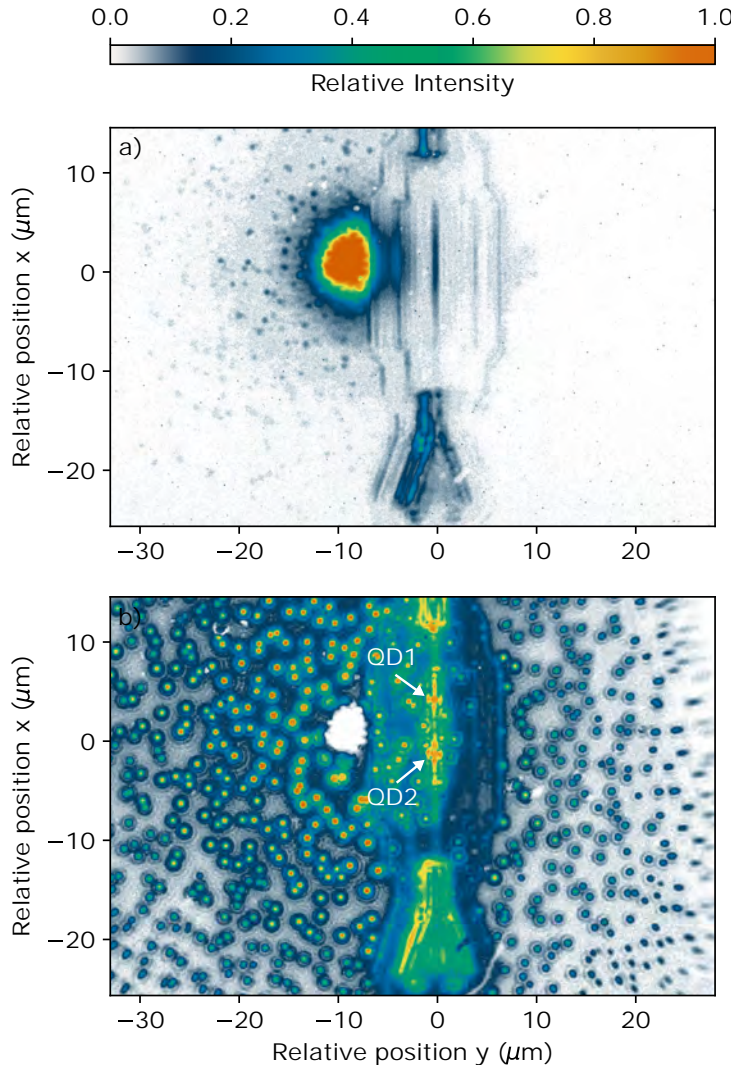


Figure 7.4: Camera images of the sample B15459-A near the W_1 waveguide $W_{1,260,35}^{(3,5)}$ (see appendix A.II) under excitation with a wavelength of $\lambda_L = 632.8$ nm. The laser spot is centered in the microscope objective. The integration time is 5 s, and the excitation power of approximately $P_L \approx 2.5 \mu\text{W}$. The camera image is filtered by a 800 ± 5 nm long-pass filter. Figure a) shows the image for a bias voltage of $U_B = 0$ V. Figure b) shows the same area for a bias voltage of $U_B = 1.5$ V and is background-subtracted. The area where the laser spot saturated the camera has been removed from the image (white area). See discussion in the main text.

The excitation power of approximately $P_L \approx 2.5 \mu\text{W}$ on the sample surface cannot explain the excitation of QDs far outside of the excitation spot. Surprisingly, the QDs appear in comparable brightness regardless of their position on the sample. The only visible reduction of QD brightness appears at the edges of the field-of-view and is likely only due to drop in the collection efficiency. The camera image in figure 7.4b) shows how QDs inside and across the photonic crystal insulator are fluorescent

indicating excitation by an electric charge carrier with a long mean free path. At a bias voltage of 1.5 V, the heterostructure's bands are almost flat, shown in figure 6.1b), similar to the operation of an LED. The laser induces a measurable photocurrent of nA magnitude. A possible explanation for the QDs photoluminescence could be that electrons and holes excited by the laser flatten the band structure locally further and enable an LED-like excitation of the QDs. The effectiveness of this mechanism to excite QDs opposing to tunneling out towards the gate might be explained by observation of hole-state lifetimes of ms-timescales [137]. This would imply that the observed QD excitation mechanism is not possible in a heterostructure with an additional tunneling barrier [152].

The ability to excite QDs spatially well separated from the excitation laser spot provides unique insight into the spatial distribution of the QDs and their coupling efficiency to guided modes. QDs well coupled to a waveguide mode illuminate the shallow etch grating couplers visibly, even for lower bias voltages. For high-bias voltages, the QDs' emission becomes broadband, and photoemission into unguided modes becomes well visible, regardless of their coupling to guided modes, which allows for their localization. This allows mapping all well-coupled QDs in photonic waveguides in a single camera image. In figure 7.4b), two QDs well coupled to the guided mode of the W1 waveguide and their emission into quasi-guided modes at high bias voltages are visible. These two QDs are investigated in the following chapters. For ease of reference, the QDs upper (lower) QD is referred to in chapter 8.1 and this chapter as QD1 (QD2). QDs in their vicinity, inside the photonic crystal insulators, appear dark since their photoemission is strongly suppressed inside the photonic insulator.

Counting all QDs on the left side of the image ($y < -15 \mu\text{m}$) in the camera image of figure 7.4b) provides a QD number density of $\rho_{\text{QD}} = 0.26(3)/\mu\text{m}^2$ for this sample, which matches with the expectation from the sample growth. Moreover, an upper bound for the inhomogenous broadening can be estimated from the camera images and the spectral width of the bandpass filter in the camera imaging path. In the case of spectral filtering with a long-pass filter of 750 nm, QDs are well visible on the camera images, regardless of the inhomogeneous broadening. In the case of spectral filtering with the bandpass filter, an inhomogeneous broadening comparable with the bandpass filter width $800 \pm 5 \text{ nm}$ results in the appearance and disappearance of individual QD on the camera image when sweeping the bias voltage. However, within the signal-to-noise ratio of the camera images, all QDs appear and disappear simultaneously on the camera image. In conclusion, the inhomogenous broadening is significantly smaller than the spectral width of the bandpass filter of 10 nm.

The signal-to-noise ratio (≈ 9) enables us to determine the relative positions of the QDs with high precision without further data processing. Each QD creates an Airy disc pattern as a diffraction-limited image. The fitting of Airy patterns allows for mapping the QD position with high spatial precision. A simple model for the detected CMOS camera counts c_{D} is to assume a monochrome Airy disc

pattern [201] and an spatially homogeneous background

$$c_D(\mathbf{r}, \lambda) = c_0 \left(\frac{2J_1(2\pi NA \|\mathbf{r}\| / \lambda)}{2\pi NA \|\mathbf{r}\| / \lambda} \right)^2 + c_{\text{bgr}}, \quad (7.1)$$

where c_0 is the amplitude, NA is the numerical aperture, λ the wavelength, J_1 is the Bessel function of first kind of first order, and c_{bgr} is the spatially homogeneous background. This is demonstrated in figure 7.5, which displays a region of figure 7.4b) of a single QD and the outcome of an Airy disc fit to the data.

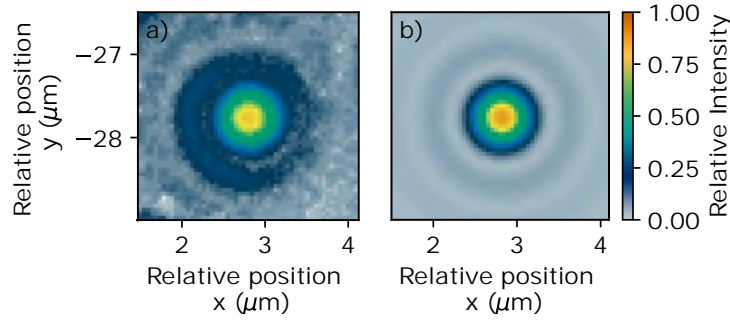


Figure 7.5: a) Zoom onto a single QD in the camera image in figure 7.4. b) Levenberg–Marquardt non-linear least-square fit of a single Airy disc pattern and a homogeneous background.

The Levenberg–Marquardt non-linear least-square fit of equation 7.1 assuming a fixed band-pass center wavelength ($\lambda = 800$ nm) and a fixed microscope numerical aperture $NA = 0.85$ yields a position uncertainty of less than 2.5 nm in each dimension⁽²⁾. The presented approach can be applied for state-of-the-art deterministic nanofabrication of photonic devices with embedded QDs which relies on optical microscopic photoluminescence imaging for spatial localization of QD [233, 284]. Further improvements to the position accuracy are possible by a more spectral filter and a camera of lower noise and higher resolution.

7.2 QUASI-RESONANT EXCITATION

To map out the different charge states populated as a function of the bias voltage, a non-resonant excitation method can be used. Above-band excitation is an efficient method to excite a charge-state independent of its nature and of the bias voltage tuning. On sample B14549-A above band excitation causes a spectrally broad background fluorescence that conceals low-brightness charge states and renders the interpretation of the spectra difficult. An alternative to above-band excitation is quasi-resonant excitation schemes such as p -shell excitation.

⁽²⁾ The goodness of fit $\chi_{\text{red}}^2 = 7.5$ is limited by the simplification of the assumption of monochrome light

7.2.1 Excitation-Emission Fluorescence Map

p -shell excitation has proven to be an efficient method commonly used to characterize QDs of single photon sources [27, 285]. However, the identification of non-resonant excitation schemes is non-trivial. For droplet-etched GaAs QDs, the hole-state energy splitting is small [137], and the optical dipole-allowed recombination of d -state holes and s -state electrons can lie between resonant excitation and p -shell excitation of a QD [135].

Figure 7.6 shows the fluorescence spectra of QD1 for a bias voltage $U_B = 1.4$ V as a function of the excitation laser's wavelength λ_L from 760 nm to 785.5 nm.

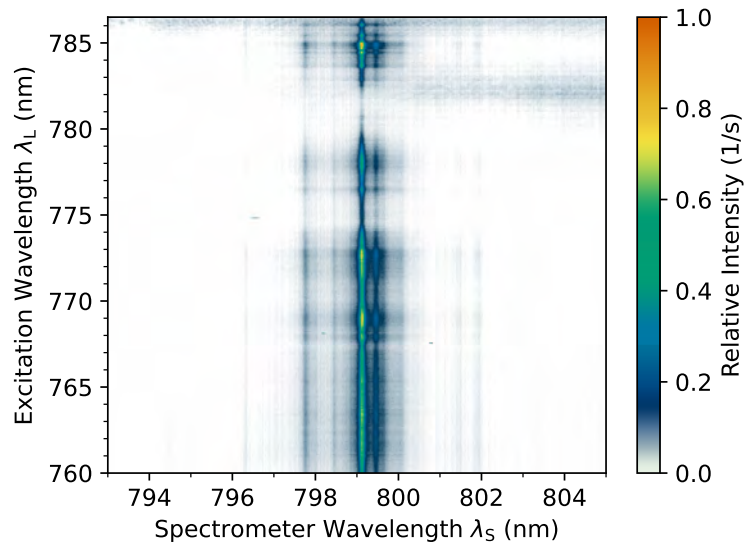


Figure 7.6: Excitation-emission fluorescence map of QD1 for a bias voltage of $U_B = 1.4$ V as a function of the excitation laser's wavelength λ_L from 760 nm to 785.5 nm.

The first plateau of quasi-resonant excitation is 1.4 nm wide and centered at 784.86 nm. This plateau is approximately 28 meV (327 K) separated from the direct transition, which is large compared to the p -shell excitation energy splitting reported for similar platforms [136, 286]. However, excitation with laser wavelengths within this plateau is efficient.

7.3 CHARGE-STATE AND STARK-SHIFT CONTROL

Figure 7.7 shows the photo-emission spectra of QD2 for various bias voltages U_B under quasi-resonant excitation by a laser with a wavelength of $\lambda_L = 784.85$ nm. At low temperatures, voltage sweeps under quasi-resonant excitation allow to distinguish and identify the various charge states of a QD [27]. However, as discussed in section 8.2, the phonon bath temperature is estimated to be approximately 30 K. The identification of the charge states at such elevated temperatures is challenging

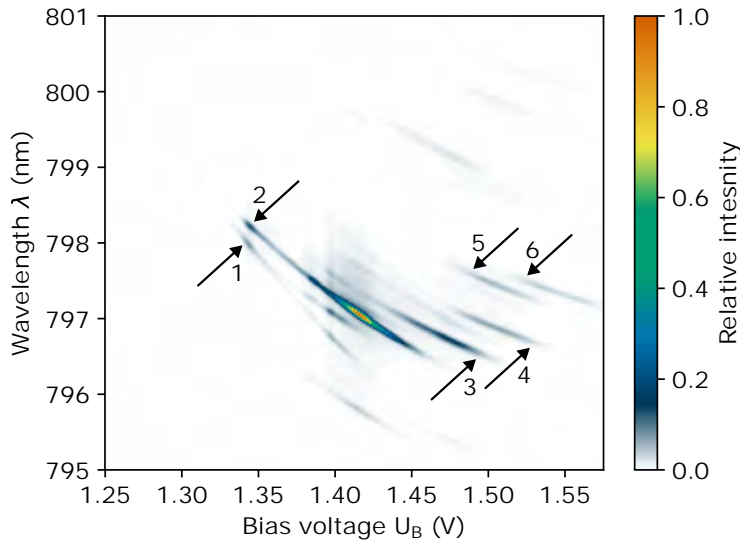


Figure 7.7: The photoluminescence emitted by QD2 as a function of the gate voltage U_B (positive gate voltage indicates a forward bias) under quasi-resonant excitation ($\lambda_L = 784.85$ nm). The wavelength is resolved by a spectrometer, and the intensity is measured on a CCD camera. The emission spectrum shows several plateaus corresponding to different charge states of the quantum dot (lines labeled with numbers). The charge states are discussed in the main text. The spectrally shifted parallel transitions (copies) can be observed (unlabeled lines).

as thermal phonons affect the spectral response [142, 144, 287, 288]. Radiative and non-radiative Auger processes [137, 286, 289] occur, and both higher-order charge states excited by phonon-assisted tunneling and continuum states are potentially occupied [136, 150]. Without applying a magnetic field it is difficult to distinguish these [286]. Indeed, despite only a single QD⁽³⁾, spectrally shifted parallel transitions (copies) can be observed⁽⁴⁾ in the higher bias voltage region. Furthermore, the transmission of the photonic device modulates the spectral response. In a spectral region of poor transmission, some transitions may be concealed from observation, increasing the complexity of charge-state identification.

It has been shown that elevated temperature of the sample affects the mobility of hole states due to scattering events with thermal phonons [288] and makes electron-dominated charge states (e.g. X^-) more likely over positive charge states (e.g. X^+) [144]. Hence, the first charge states are likely the excitation and the next one is the negative trion.

DC-Stark-Tuning Analysis

The QDs photo-emission is tuned in frequency by the electric field in the heterostructure, which can be controlled by the applied bias voltage U_B . The electric field in the

(3) Excitation of a single QD can be verified by observation of the CMOS camera image.

(4) See appendix A.II.4 for a logarithmic colormap.

heterojunction can often be approximated as p-i-n diode [251]. Taking the width of the intrinsic layer $d_i = 83 \text{ nm}$ ⁽⁵⁾, the applied bias voltage U_B and the thermal mobility of the charge carriers near the edges of the depletion region into account [290], the depletion region width of a p-i-n diode is

$$d_{\text{dl}}(U_B) = d_i + \sqrt{\frac{2\epsilon_0\epsilon_r}{q} \frac{N_a + N_d}{N_a N_d} \left(U_0 - U_B - \frac{2k_B T}{q} \right)}, \quad (7.2)$$

where $\epsilon_r = 12.712$ is the relative dielectric permittivity [269], $U_0 = 1.61 \text{ V}$ is the built-in voltage [291], N_a (N_d) is the acceptor (donor) charge density, and T is the sample temperature. The electric field at the QD position is then approximated by:

$$F = \frac{U_0 - U_B}{d_{\text{dl}}(U_B)}. \quad (7.3)$$

However, as shown in figure A.II.4, the p-i-n diode approximation fails to describe the electric field with sufficient precision. The neglect of the higher doping layers overestimates the depletion region width. A good approximation of the electric field inside the junction is obtained [251] from numerical calculations using a one-dimensional Poisson equation solver [249] assuming perfect ohmic contacts and neglecting Fermi-level pinning [250].

The electric field F , depletion length d_{dl} , and their comparison to a p-i-n diode approximation are shown in appendix A.II.4. The temperature is obtained from phonon-sideband resolved spectroscopy (see section 8.2). The diode layout and its doping levels are provided in section A.II.

The DC stark tuning by the electric field F can be described by [27, 292]

$$E_{\text{PL}} = E_0 + \alpha F + \beta F^2, \quad (7.4)$$

where α permanent dipole moment in the growth direction, and β , the polarisability of the QD [293]. Figure 7.8 shows the photoluminescence energy of two selected charge states, as function of the electric field strength F . These two charge states show resonant fluorescence and are thoroughly characterized in chapter 8. For ease of reference is the higher (lower) energy state, labeled with the number 2 (1) in figure 7.7, referred to in the following as $|X_h\rangle$ ($|X_l\rangle$).

The photoluminescence energy is obtained by Levenberg–Marquardt non-linear least-square fitting of Voigt profiles and a constant background⁽⁶⁾ to the spectrum of each bias voltage U_B . Table 7.1 summarizes the result of a subsequent Levenberg–Marquardt non-linear least-square fit of equation 7.4 to the extracted photoluminescence energies in figure 7.8⁽⁷⁾.

(5) Excluding the deposited GaAs and AlAs for QD formation.

(6) Goodness of fits $1 < \chi_{\text{red}}^2 < 3$.

(7) Goodness of fit $\chi_{\text{red}}^2 = 1.55$ for $|X_h\rangle$, $\chi_{\text{red}}^2 = 2.54$ for $|X_l\rangle$.

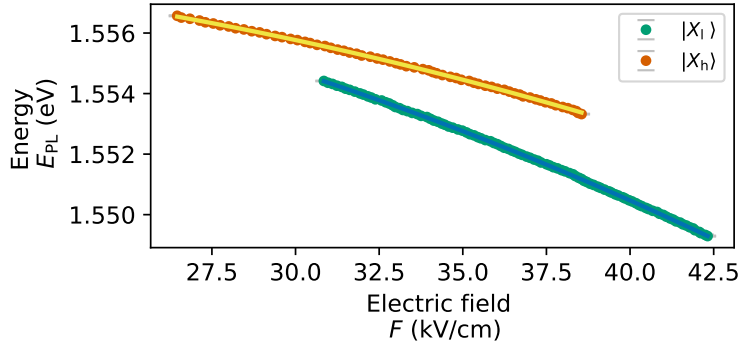


Figure 7.8: Photoluminescence energy E_{PL} as a function of electric field F extracted from the data shown in figure 7.7.

State	Parameter	Value
$ X_h\rangle$	E_0	1.557 97(8) eV
$ X_I\rangle$	E_0	1.558 17(13) eV
$ X_h\rangle$	α	$3.7(8) \times 10^{-5}$ eV/(kV cm)
$ X_I\rangle$	α	$3.5(11) \times 10^{-5}$ eV/(kV cm)
$ X_h\rangle$	β	$-9.27(21) \times 10^{-6}$ eV/(kV ² cm ²)
$ X_I\rangle$	β	$-1.328(25) \times 10^{-5}$ eV/(kV ² cm ²)

Table 7.1: The DC stark tuning parameters of equation 7.4 obtained from Levenberg–Marquardt non-linear least-square fits of the extracted photoluminescence energies in figure 7.8 for both charge states $|X_h\rangle$ and $|X_I\rangle$. Goodness of fit $\chi_{\text{red}}^2 = 1.55$ for $|X_h\rangle$, $\chi_{\text{red}}^2 = 2.54$ for $|X_I\rangle$.

The non-zero value of α represents a permanent dipole moment of $\frac{\alpha|X_h\rangle}{q} = 0.37(8)$ nm and $\frac{\alpha|X_I\rangle}{q} = 0.35(11)$ nm, arising from displacement between the centre-of-mass of the electron and the hole wavefunctions. The sign of the α reflects that the hole wavefunctions are slightly closer to the back gate than the electron wavefunction. The permanent dipole moment of both charge states is identical within the statistical uncertainty. However, the polarizability of the two charge states differs. This indicates that the centers of gravity of the electron and hole wave functions along the vertical direction change significantly when a hole is added to or removed from the QD. Compared to diode layouts in which the intrinsic layer is thicker GaAs QDs [27, 292], the polarizability is about an order of magnitude larger. For both charge states the polarizability contributes a larger Stark-tuning than the permanent dipole moment.

7.4 TIME-RESOLVED SPECTROSCOPY

The single-photon character of the QD photoluminescence examined by time-resolved spectroscopy. Typically, quasi-resonant excitation is a suitable excitation

method since it can be removed from the signal by spectral filtering. However, for above-band and quasi-resonant excitation droplet-etched GaAs quantum dots, the decay can be dominated by the slow relaxation of the p-shell electron or higher-order hole states [136]. Here, we drive the high energy state $|X\rangle_h$ resonantly at a bias voltage $U_B = 1.375$ V.

7.4.1 Lifetime Measurement

The lifetime T_1 of the QDs high energy state $|X\rangle_h$ is determined by time-resolved photon counting under pulsed resonant excitation⁽⁸⁾. The integrated counts are shown in figure 7.9.

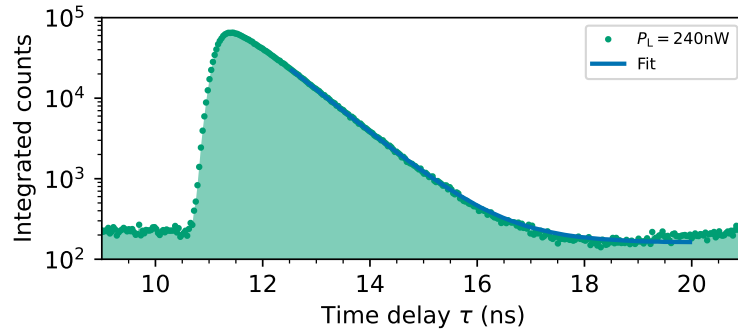


Figure 7.9: Time-bin histogram of a lifetime measurement of QD2 under pulsed resonant excitation with a power of $P_L = 240$ nW, displayed in green. The blue line represents the fit to a single exponential decay convolved with the instrument's response function (IRF).

The decay rate is extracted by fitting the data to an exponential decay convolved with the independently measured instrument's response function (IRF)⁽⁹⁾. A Levenberg–Marquardt non-linear least-square fit of the time-bin histogram shown in figure 7.9 reveals a single exponential decay with a lifetime of $T_1 = 803.7(16)$ ps. In contrast, for GaAs droplet QDs in unstructured heterojunctions of similar layout, a fast radiative decay with a lifetime $T_1 \approx 270$ ps [27] has been reported. The lack of Purcell enhancement of the QD's photoemission is attributable to the spectral position of the QD far from the band-edge of the W_1 PhCW (see figure 6.15). Far from the band-edge, the group index and, consequently, the LDOS is small and only a weak Purcell factor can be expected.

7.4.2 Single-Photon Emission

The single-photon nature of the QD2's photoemission in the charge state $|X_1\rangle$ is probed with a Hanbury Brown and Twiss experiment [294] by time-correlated photon

(8) Tsunami Ti:Sapphire laser, see section A.IV.

(9) The model, fit residuals, and a reference measurement with lower power are presented in appendix A.VII.1.

counting under continuous wave resonant excitation by a narrow-line laser⁽¹⁰⁾. The QD's spectrally unfiltered photoemission into the waveguide is fiber coupled and passed to two photodetectors⁽¹¹⁾, and both detectors' events are time-tagged⁽¹²⁾.

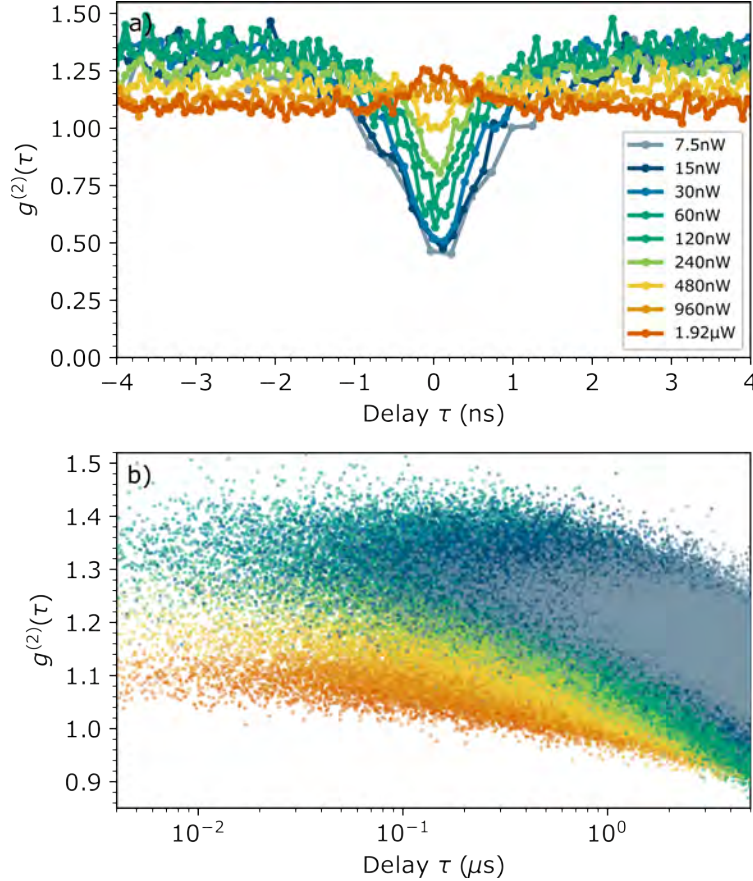


Figure 7.10: Autocorrelation histogram of a Hanbury Brown and Twiss experiment under continuous wave excitation for various excitation laser power P_L settings. The integration time for each excitation power is $t_i = 1$ h. Figure a) shows a close-up of the close-to-zero delay region. For increasing excitation power at zero time-delay, the autocorrelation histogram transitions from pronounced anti-bunching to bunching. Figure b) shows the long delay-time auto-correlation histogram. The QD shows strong blinking in the μ s timescale.

The autocorrelation function $g^{(2)}(\tau)$ is extracted from the time-correlated photon counting histogram. The coherent drive of the excited state, pure dephasing, [94, 185, 295], blinking into dark states [185, 296, 297], and the detector time jitter are taken into account. The model and data evaluation process are described in detail in appendix A.VII.2. The autocorrelation function $g^{(2)}(\tau)$ is shown in figure 7.10 for various excitation laser powers P_L .

(10) DLPro, see A.IV.4.

(11) Avalanche photodetectors APD₁ and APD₂, see section A.IV.

(12) Time-correlated single photon counting module PicoHarp 300, see section A.IV.

Figure 7.10a) shows that, for the lower excitation laser powers, the time-bin histograms show a clear anti-bunching at zero time delay $\tau = 0$. The anti-bunching reflects the single-photon nature of the QD's photoemission. Since the lifetime of the QD is comparable with the time resolution of the detectors, the prominence of the observable bunching feature is reduced. Taking the detectors' time jitters into account, the anti-bunching at zero delay for the lowest power $P_L = 7.5$ nW is $g^{(2)}(0) = 0.26(11)$. The low time resolution of the detector limits the accuracy of the parameter estimation. A more significant estimate is obtained by pulsed resonant excitation in chapter 9.

For increasing excitation power, the autocorrelation function narrows and transitions from pronounced anti-bunching to a slight bunching. The narrowing is owed to the coherent driving of the QD by an increasing Rabi-frequency which induces coherent oscillations of the autocorrelation functions. Yet, no coherent oscillation of the autocorrelation function is observable. This may be explained by the pure dephasing rate which exceeds the QD's optical decay rate. From the fit of the autocorrelation function, a high pure dephasing of $\gamma_{dp} \approx 8\gamma$ is obtained. Additionally, the photodetector's low time resolution limits the observation of high-frequency coherent features. Eventually, when approaching and exceeding the QD's saturation power of approximately $1\mu\text{W}$ ⁽¹³⁾, the anti-bunching turns into a bunching feature due to the scattering of coherent light from the excitation laser into the detectors.

The normalized time-bin histograms in figure 7.10a) show considerable bunching ($g^{(2)} > 1$), and for long time delay dynamics, shown in figure 7.10b), the exponential decay is in the μs timescale. Similar studies of InAs, InGaAs, and GaAs QDs demonstrated that such features are induced by the QD's coupling with dark states, charged states, or impurities in the vicinity the QD [185, 297–299]. The QD's coupling with dark states or its environment causes telegraph-like blinking of the QD [300] into and out of resonance with the narrow-band frequency laser.

The blinking of QD out of resonance with the laser corresponds to the presence of dead times in the QD fluorescence and packets of single photons separated in time [301]. The fraction of average time inside the fluorescence state and the "dark" state β_c and the blinking time constant τ_c can be estimated from the autocorrelation function [185]. Figure 7.11 shows the estimate of the relative time spent in the "dark" state and the blinking time constant for the six lower excitation laser power.

The blinking dynamics are strongly modified as we increase the power of the resonant laser. For GaAs QDs without a semiconductor heterojunction, comparable blinking rates, dead times, and power dependencies of the blinking dynamics have been observed under resonant excitation [185]. For those QDs, it has been shown that the blinking can be reduced by the addition of a weak non-resonant laser to control the charge environment of the QD [185]. In contrast, GaAs QDs in unstructured semiconductor heterojunctions of similar layout to this sample show no blinking even in the ms timescale [27]. This indicates the laser's impact over the QD's en-

(13) The QDs pure-dephasing, saturation power of 934(27) nW, and spectral diffusion are assessed and discussed further in chapter 8.

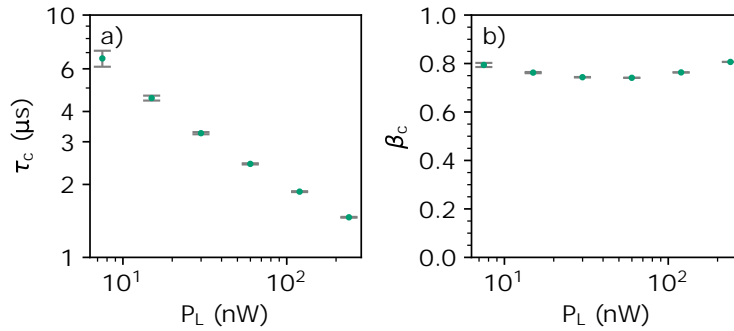


Figure 7.11: The fraction of time in which the QD is in the bright state β_c , and the blinking time constant τ_c of the autocorrelation function g_2 for the lowest six excitation laser power P_L settings.

environment and that the effects of the solid-state environment are not completely suppressed by the semiconductor heterojunction. This may be attributed to a QD's location close to the surface of an hole of the photonic crystal and interactions with surface states [228–230].

However, the autocorrelation function cannot capture the nature of the blinking process. A Hanbury Brown Twiss experiment under pulsed resonant excitation of the same QD presented in chapter 9 shows drastically less blinking. This suggests that the bunching of the autocorrelation function is caused by continuous spectral diffusion driving the QD into and out of resonance with the laser and not telegraph-like blinking. The time constant τ_c agrees with the μ s time-scale of spectral diffusion [106].

* * *

This chapter examined the properties of the first realization of a planar platform for quantum photonics with droplet-etched GaAs QDs. The platform's ability of QD charge-state and stark shift tuning, and the single-photon character of the QD photoluminescence have been demonstrated. The next chapter presents a thorough characterization of QDs for their application in scalable quantum networks.

RESONANT EXCITATION AND PHONON-SIDEBAND-RESOLVED SPECTROSCOPY OF INTEGRATED GaAs DROPLET-ETCHED GaAs QUANTUM DOT

A thorough characterization of quantum dots is crucial for their application in quantum networks. This section characterizes essential properties of droplet-etched GaAs quantum dots integrated into nanophotonic devices, such as the linewidth and the pure dephasing rate under resonant excitation. Phonon-sideband-resolved spectroscopy reveals an elevated phonon-bath temperature to limit the quantum dots in their linewidth and the pure dephasing rate.

Resonant excitation of QDs allows to generate single photons of high indistinguishability and purity for application in photonic quantum-information processing [8, 27, 28]. Spectroscopy with resonant excitation provides insight into the performance and limitations of a QD. Most important, decoherence dynamics, spectral diffusion processes, fine structure interactions, and the indistinguishability of subsequently emitted photons can be revealed [93, 184, 285]. This chapter presents the characterization of a GaAs droplet epitaxy QD⁽ⁱ⁾ by resonant excitation using high-resolution and phonon-sideband-resolved spectroscopy. The QD is integrated into the first-of-its-kind nanophotonic line-defect waveguide fabricated from an ultra-thin semiconductor p-i-n heterojunction membrane that can control its properties and charge environment.

(i) QD2 in the photonic crystal waveguide $W_{1,206,36}^{(3,5)}$ of sample B15459 – A (see appendix A.II).

8.1 SPECTROSCOPY WITH RESONANT EXCITATION

Two excitation configurations are typical for resonant excitation spectroscopy for a QD coupled to a guided mode of a planar photonic waveguide. Either the QD is excited using out-of-plane optical modes [302] or excited through the in-plane waveguide modes [240]. In the case of excitation in-plane, the QD scatters injected photons. The resonant laser's single-photon component is reflected, while two- and higher-photon components are more likely to be transmitted. The transmitted signal is non-linear and highly susceptible to the coherent properties of the light-matter interaction [303]. However, in the presence of substantial decoherence processes, the contrast between the signal and the laser background is low, and suppressing the laser background is paramount. Out-plane excitation allows for probing the linewidths and coherent properties with better suppression of the laser background.

Experimental Setting and the Choice of a Quantum Dot

The experimental findings in this chapter are obtained by out-of-plane excitation since, as shown below, the QDs of the investigated sample show strong decoherence⁽²⁾.

Planar nanophotonic quantum networks depend on the availability of similar QDs and a high yield of QDs in photonic devices. Here, typically 1 to 3 QDs show bright photoluminescence into the guided modes of each nanobeam and photonic crystal waveguide⁽³⁾. These QDs show qualitatively comparable properties under resonant excitation. However, the photonic devices drastically differ in transmission and magnitude of laser scattering due to fabrication imperfections which limits the signal quality. The photonic crystal waveguide that hosts the QD characterized in this chapter has comparably high transmission⁽⁴⁾ and, consequently, the highest signal quality.

8.1.1 Charge-Plateau Identification

The neutral exciton and the two trion charge states can be distinguished from other charge states by their photoluminescence under resonant excitation. Furthermore, spectroscopy with resonant excitation enables the identification of their charge plateaus. Excitation to higher energy can drive continuum states [304, 305] that extend the width of charge plateaus. In contrast, resonant excitation reveals charge plateaus accurately [136, 150].

(2) Excitation via the waveguide mode leads to a signal-to-noise ratio in the sub-percent magnitude. In contrast, in experiments with out-of-plane excitation, the signal-to-noise ratio exceeds 100 using a cross-polarization and polarization-sensitive filtering setup as shown in appendix A.IV.

(3) Column 4 of sample B15459 – A, see appendix A.II.

(4) Nanobeam waveguides show significantly higher transmission, but strong laser scattering at the edges that confine the waveguide decreases the effectiveness of separating laser light from the QD emission. The device transmission is shown in figure 6.15.

The exciton and trions' charge plateaus can be obtained by sweeping the bias voltage of the heterojunction U_B and the excitation laser's frequency λ_L [27, 260]. The resonant fluorescence signal is collected and corrected for the laser background by subtraction of the photon count rate observed on the detector with zero bias voltage $\dot{c}_{D,ref}$, from the photon count rate with non-zero bias voltage $\dot{c}_{D,raw}$.

Figure 8.1a) shows the detected resonant fluorescence signal as a function of the applied bias voltage U_B for excitation laser wavelengths of $\lambda_L = 797.000\ 00(21)$ nm, $797.337\ 30(21)$ nm, $797.625\ 40(21)$ nm, and $798.000\ 00(21)$ nm⁽⁵⁾. The excitation power is $P_L = 120$ nW is well below saturation, as shown in section 8.1.2. For each wavelength, the polarization optics and beam position is corrected for chromatic aberrations to achieve an optimal signal-to-noise ratio⁽⁶⁾.

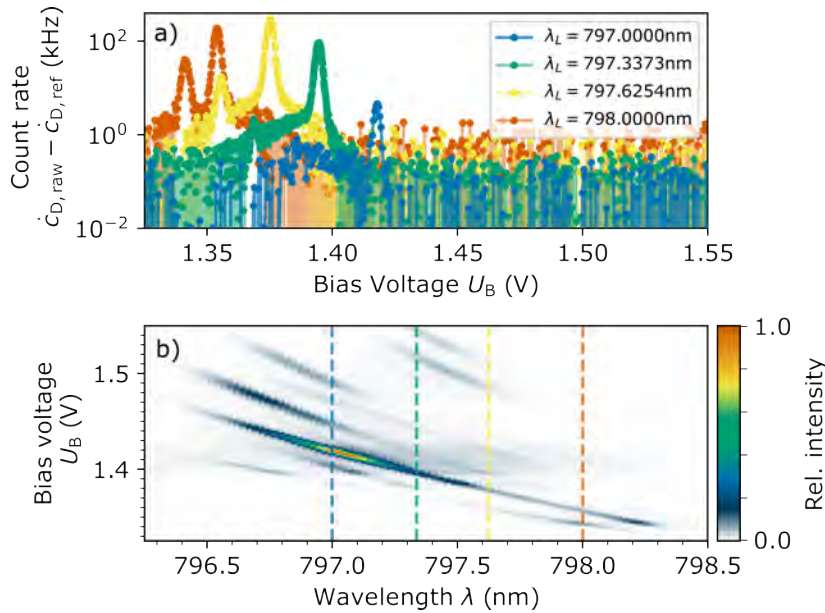


Figure 8.1: a) Resonant fluorescent spectra for continuous wave excitation probed with excitation laser wavelengths of $\lambda_L = 797.000\ 00(21)$ nm, $\lambda_L = 797.337\ 30(21)$ nm, $\lambda_L = 797.625\ 40(21)$ nm, $\lambda_L = 798.000\ 00(21)$ nm. For excitation wavelengths of 100 pm above or below the probed wavelengths, no fluorescence is observable within the bias voltage interval between 1.325 V and 1.55 V. For these spectra, the bias voltage was sampled in a randomized order. The difference in the background count noise is attributable to mechanical drifts of the excitation laser during data acquisition. b) Zoom into the frequency-voltage map obtained by quasi-resonant excitation of figure 7.7. The dashed lines indicate the wavelengths probed for resonant excitation, as shown in figure a).

Two charge states show resonant photoluminescence under continuous wave excitation, which both can be identified with charge states observed under quasi-resonant excitation shown in figure 8.1b). As for quasi-resonant excitation, the

(5) The difference in bias voltage sampling resolutions among the data sets lead to varying total acquisition duration resulting in differing signal-to-noise ratios.

(6) Most important is the laser background suppression by cross-polarization of the excitation laser and the accepted polarization of the photodetection.

charge state with higher resonance energy (higher bias voltages) is brighter. For ease of reference, the higher (lower) energy state is referred to in the following as $|X_h\rangle$ ($|X_l\rangle$)⁽⁷⁾. Based on the available data, the corresponding charge states are not deducible. However, comparing the spectra with comparable spectra in literature [27] suggests an identification as neutral exciton $|X_l\rangle = |X^0\rangle$ and positive trion $|X_h\rangle = |X^+\rangle$.

As observed under quasi-resonant excitation, discussed in section 7.3, the two charge states differ in their Stark tuning strength. The identical shift in wavelength corresponds to a higher bias voltage shift for the higher frequency state $|X_h\rangle$.

For the charge state $|X_h\rangle$, the photoluminescence rate is high for an excitation wavelength around a charge plateau center near $\lambda_L = 797.625\ 40(21)$ nm. At the edges of the plateau, the photoluminescence rate drops rapidly. Towards short wavelengths, at $\lambda_L = 797.000\ 00(21)$ nm the photoemission rate has dropped by a factor 100 from its maximum. No photoluminescence signal can be observed for excitation wavelengths 100 pm shorter or longer than those shown in figure 8.1a). The width of the charge state plateau exceeds 1 nm and is comparable to values reported in the literature [27] for comparable platforms. As shown in figure 8.1b), a significantly wider charge plateau appears in quasi-resonant excitation, which is attributable to higher energy continuum states not populated by resonant excitation.

For the charge state $|X_l\rangle$, the photoluminescence rate is high for an excitation wavelength plateau centered near $\lambda_L = 798.000\ 00(21)$ nm. The lower wavelength edge of the charge plateau appears to be between $\lambda_L = 797.337\ 30(21)$ nm and $\lambda_L = 797.000\ 00(21)$ nm. The sampled excitation wavelengths suggest a shorter charge plateau for the charge state $|X_l\rangle$. However, nanophotonic device limitations (such as non-uniform transmission and other dispersive effects of the waveguide, mode adapter, and grating coupler) may mask parts of the charge plateau.

8.1.2 Description as Two-Level-Systems

Characterizing the QD's photoluminescence under variation of the excitation laser's frequency and power gives access to the spectral line shape without power broadening and power tuning effects. Instead of sweeping the laser frequency, a sweep of the bias voltage provides the same information using an accurate DC-stark-tuning calibration. This way, the chromatic aberrations of the optical setup and dispersion of the polarization filtering setup do not cause systematic errors. Once aligned, the signal-to-noise ratio remains optimal apart from slow mechanical random drifts.

The smallest linewidth is observable near or at the charge-plateau centers [27] in the absence of co-tunneling interaction with the Fermi-reservoir [132]. Therefore, both charge states' properties are investigated near the centers of the charge plateau around $U_B = 1.375$ V and $U_B = 1.342$ V. For supplementary discussion of the model and the data-evaluation method, see appendix A.VIII.

(7) Cf. the two peaks in the red curve in figure 8.1a).

High Energy Charge State $|X_h\rangle$ Characterization

Figure 8.2 shows the photo-detection rate $\dot{C}_{D,raw}$ under resonant excitation of the charge state $|X_h\rangle$ with an excitation laser wavelength of $\lambda_L = 797.625\,40(21)$ nm as a function of the square root of excitation power P_L and as a function of the bias voltage U_B .

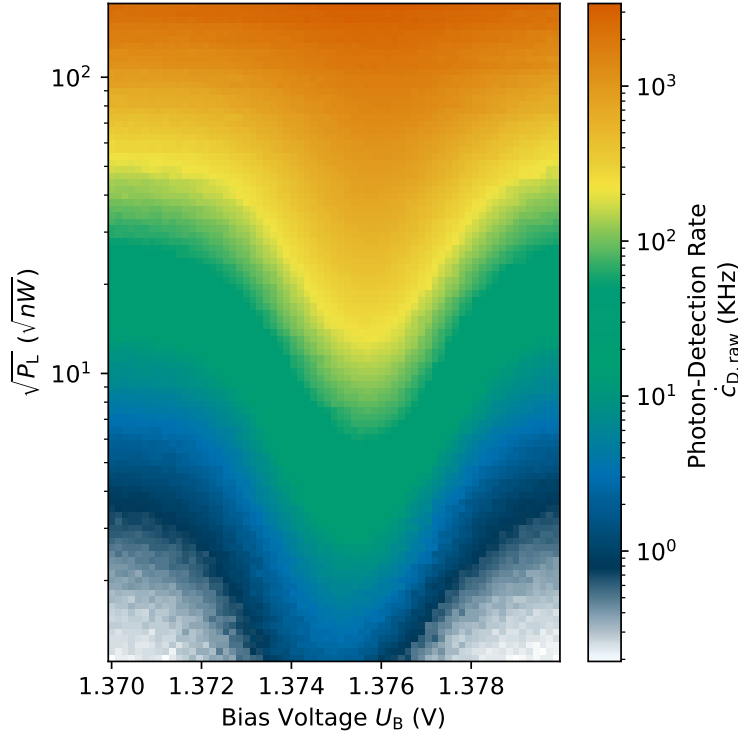


Figure 8.2: Photoluminescence detection rate under continuous wave excitation. Experimental settings $\lambda_L = 797.625\,40(21)$ nm, integration time $t_i = 1$ s. The dark detector's dark count rate limits the signal-to-noise ratio for the very lowest excitation powers. At the highest excitation powers, the excitation saturates, and the spectral line disappears in the laser background noise.

The excitation-laser background is negligible for low excitation power, and the detector dark count rate limits the signal-to-noise ratio. For increasing excitation power, the scattered light from the laser leads to a significant background. For the highest probed excitation powers, the emission saturates, and the spectral line disappears in the laser background noise.

The spectrum of each excitation laser power P_L is modeled as a two-level system. The model and data evaluation details are discussed in appendix A.VIII, and examples of line-fits are displayed in figure 8.3. Figure 8.4 displays the extracted linewidth Δf_{FWHM} , the photo-emission rate on the detector γ_D , and the power-induced frequency tuning Δf_{P_L} as a function of the excitation laser power P_L .

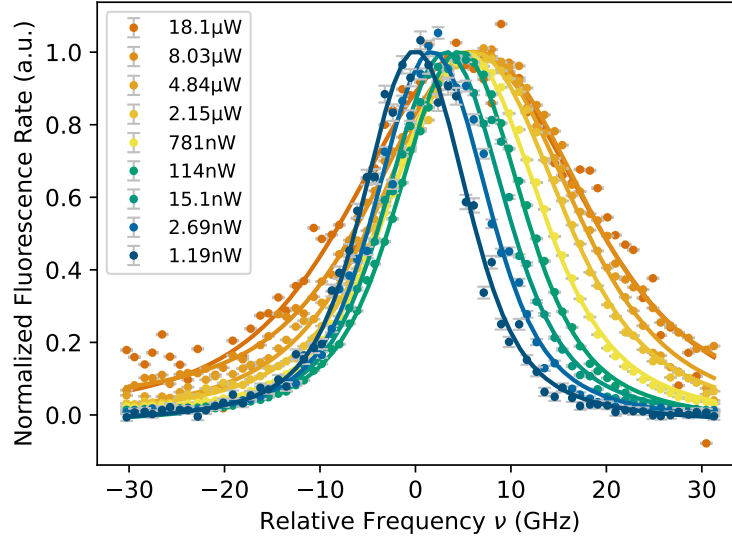


Figure 8.3: Examples of background subtracted normalized photoluminescence detection rate for various powers P_L , and two-level-system line fits. The model and data evaluation details are discussed in appendix A.VIII.

The background-subtracted photoluminescence rate, displayed in figure 8.4b), is well described by a two-level system model. The model fit obtains a saturation power $P_S = 934(27)$ nW and saturation photo emission rate $\gamma_S = 7.99(20)$ MHz.

The extracted linewidth, displayed in figure 8.4a), shows only a slight relative increase within the experiment's excitation power range. A two-level-system model can not explain the observed power dependence. In the limit of a low excitation powers ($\sqrt{P_L} < 2 \text{ nW}^{1/2}$), the power-average linewidth is $\Delta f_{\text{FWHM}}/2\pi = 12.1(9)$ GHz. Only 4.1(10) GHz of which are associated with a Lorentzian line shape, and most of the linewidth is associated with a Gaussian line shape, i.e., inflicted by spectral diffusion (see appendix A.VIII). By assuming the lifetime limited linewidth of $\Gamma/2\pi = 198.0(4)$ MHz (see section 7.4) and only pure dephasing determining the width of the Lorentzian line shape, the pure dephasing rate estimate is $\Gamma_{\text{dp}}/2\pi = 1.9(5)$ GHz. In figure 8.4a), the linewidth's power dependence, as expected from the photoluminescence rate fit, is shown for the assumption of no spectral diffusion. Under this assumption, the effect of power-broadening is only comparable with the observable linewidth at or above the saturation power. Indeed, the slight increase in the observable linewidth by power broadening matches the expectations qualitatively.

In conclusion, spectral diffusion is the dominant linewidth-broadening mechanism. Yet, the homogenous broadening from pure dephasing is significant, as suggested by the Hanbury Brown and Twiss experiments presented in section 7.4.2. The contribution of the power broadening mechanism is negligible until reaching the saturation power. The signal-to-noise ratio is relatively low compared with the

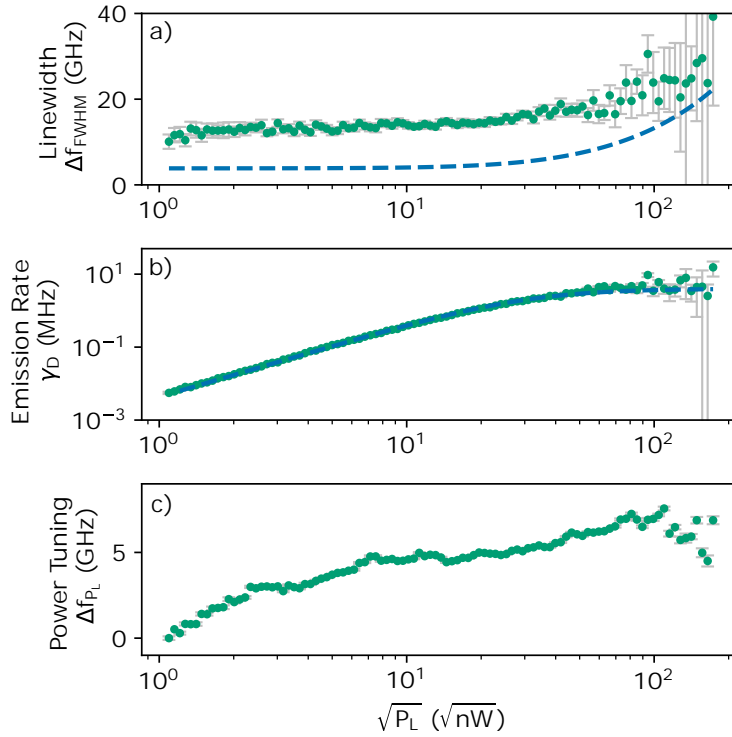


Figure 8.4: Two-level system parameters extracted from the power- and bias voltage scan of the high-energy state $|X_h\rangle$. a) the linewidth Δf_{FWHM} , b) the (detected) photo-emission rate γ_D , and c) the frequency tuning Δf_{PL} of the QD

literature [27, 28], which is likely attributed to the magnitude of spectral diffusion randomly driving the QD in and out of resonance with the narrow-band laser. A fine structure splitting, assuming a neutral exciton as the charge state, cannot be resolved. This can have several reasons. One reason may be a fine structure splitting well below the QD linewidth, i.e. $\Delta_{\text{FSS}}/2\pi < 12.1(9)$ GHz. Another reason may be the individual coupling of the two optical dipoles to the guided mode of the waveguide. The line defect photonic crystal waveguide has points of high linear polarization where only one dipole couples significantly to the guided mode while the other dipole is suppressed. Lastly, it cannot be excluded that at least one dipole moment is partially aligned out of the plane and does not couple to the waveguide mode. It has been shown that droplet-etched GaAs QDs are inherently low in strain [27, 117]. Moreover, low amounts of axial stress, as potentially inflicted by the nanofabrication process [233, 306], can flip the natural quantization axis of a QD [117].

Like in similar platforms power tuning, beyond the two-level-system model's expectations are observable (displayed in figure 8.4c)), and may be explainable by the alternation of surface charge environment [307–311].

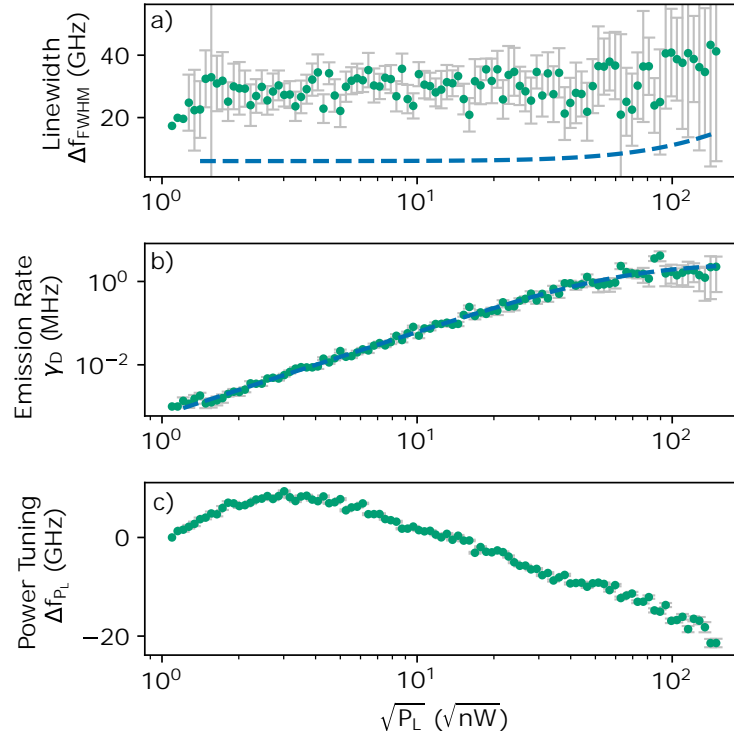


Figure 8.5: Two-level system parameters extracted from the power- and bias voltage scan of the high energy state $|X_1\rangle$. a) the linewidth Δf_{FWHM} , b) the (detected) photo-emission rate γ_D , and c) the frequency tuning Δf_{P_L} of the QD

Low Energy Charge State $|X_1\rangle$ Characterization

Figure 8.5 shows the two-level-system parameters obtained by resonant excitation of the low energy charge state $|X_1\rangle$ with an excitation laser wavelength $\lambda_L = 798$ nm. The data evaluation is analogous to the high energy state $|X_h\rangle$, and raw data is discussed in the appendix A.VIII.

Line-fitting obtains a significantly higher saturation power $P_S = 4.2(6)$ μW but slightly lower saturation photoemission rate $\gamma_S = 5.2(8)$ MHz compared to the high energy charge state $|X_h\rangle$. An even stronger spectral diffusion can partly explain the higher saturation power and lower signal-to-noise ratio. The slightly lower saturation photoluminescence rate observed may be explained by the non-ideal transmission of the photonic waveguide.

Within the full excitation power range of the data set, the linewidth extracted shows no significant increase. In the limit of low excitation amplitude ($\sqrt{P_L} < 2$ $\text{nW}^{1/2}$) the average linewidth is $\Delta f_{\text{FWHM}}/2\pi = 25(5)$ GHz. The Lorentzian contribution is insignificant, while strong spectral diffusion dominates the line width (see appendix A.VIII). The linewidth expected from the parameters extracted from the brightness fit is displayed in figure 8.5a), with the assumption of no spectral

diffusion. The induced power-broadening is negligible for all excitation powers below or near the saturation power.

8.2 PHONON-SIDEBAND-RESOLVED SPECTROSCOPY

The linewidths of both charge states $|X_1\rangle$ and $|X_n\rangle$ exceed the transform limit significantly and are dominated by spectral diffusion. The origin of spectral diffusion is electric noise in the environment around the QD caused by charge fluctuations on the surface [307–311], by bias voltage-driven tunneling of charge carriers through the semiconductor heterojunction, or by the voltage noise on the gate. The lower-voltage charge state $|X_1\rangle$ shows, however, more pronounced spectral diffusion despite the lower current in the diode, and the voltage noise is well below a limiting level (see section A.VIII). Thus, only surface charge effects and inelastic phonon-scattering may explain the observable linewidths and the pure dephasing.

Pure dephasing, mainly caused by phonons [186, 187], is suppressed by cooling down the QD to close to zero absolute temperature [186–189]. Therefore, the observed linewidths question the sufficient cooling of the phonon-bath. Utilizing the shape of the thermally smeared Fermi distribution of the charge plateau is an accurate method for temperature sensing [152]. However, without a thorough characterization of the photonic device's transmission and a high-resolution map of the resonant frequency and the bias voltage, the Fermi distribution cannot be utilized. Observing the temperature-induced resonance frequency shift turned out to be insufficient to estimate the sample temperature, as demonstrated in section A.IX. Instead, to overcome the dependency of independent temperature measurement, the shape of the well-understood, temperature-dependent phonon-sideband is used [312]. Unlike the resonance frequency shift, which asymptotically approaches a zero-kelvin value, the phonon-sideband spectrum is expected to change most drastically at temperatures below approximately 10 K. This section presents phonon-bath temperature measurements by phonon-sideband-resolved spectroscopy and reveals insufficient thermalization of the sample to limit the linewidth by phonon-scattering.

Modelling the Phonon-Sideband Spectrum

Next to excited- to ground-state transitions into the zero-phonon-line (ZPL), transitions into the phonon-sideband (PSB) occur even at absolute zero temperature [188, 313]. Therefore, phonon-scattering always induces a small amount of dephasing and ultimately limits the indistinguishability of emitted photons [190, 312, 314]. The ratio of transitions into the ZPL and PSB scales with the Franck-Condon factor B_{FC} . The magnitude of the Frank-Condon factor depends on both QD size and phonon-bath temperature. Consequently, the PSB's spectrum can serve as a temperature measurement of the phonon bath. Here, we employ a simplified model of non-Markovian phonon interaction [312] to estimate the temperature of a QD.

Considering a QD as a two-level system of ground state $|0\rangle$ and excited state $|X\rangle$ of energy $\hbar\omega_X$. The QD is located in a photonic crystal waveguide and coupled to a

phononic environment which yields the Hamiltonian:

$$\mathcal{H} = \hbar\omega_X |X\rangle \langle X| + \mathcal{H}_{\text{int}}^{\text{pht}} + \mathcal{H}_{\text{int}}^{\text{phn}} + \mathcal{H}_{\text{env}}^{\text{pht}} + \mathcal{H}_{\text{env}}^{\text{phn}}, \quad (8.1)$$

where the term $\mathcal{H}_{\text{int}}^{\text{pht}}$ ($\mathcal{H}_{\text{int}}^{\text{phn}}$) describes the QD interaction with the photonic (phononic) environment and $\mathcal{H}_{\text{env}}^{\text{pht}}$ ($\mathcal{H}_{\text{env}}^{\text{phn}}$) describes the free evolution of the photonic (phonon) environments. Among various possible phonon-interactions deformation potential by coupling by longitudinal acoustic (LA) phonons is assumed [186, 315, 316]. The phonon environment is described by

$$\mathcal{H}_{\text{env}}^{\text{phn}} = \hbar \sum_{\mathbf{k}} v_{\mathbf{k}} b_{\mathbf{k}}^{\dagger} b_{\mathbf{k}} \quad (8.2)$$

and the phonon interaction term is described by

$$\mathcal{H}_{\text{int}}^{\text{phn}} = \hbar |X\rangle \langle X| \sum_{\mathbf{k}} g_{\mathbf{k}} (b_{\mathbf{k}}^{\dagger} + b_{\mathbf{k}}), \quad (8.3)$$

where $g_{\mathbf{k}}$ is the coupling strength between the QD and the phonon mode of wavevector \mathbf{k} , frequency $v_{\mathbf{k}}$ and $b_{\mathbf{k}}^{\dagger}$ ($b_{\mathbf{k}}$) is the phonon creation (annihilation) operator of the phonon mode with wavevector \mathbf{k} . The phonons' interaction with the QD can be fully characterized by the phonon spectral density [312]. Droplet epitaxy grown GaAs QDs are well approximated as spherically symmetric QD [26, 317] such that a harmonic confinement potential is assumed, and the phonon spectral density written as [318]:

$$J_{\text{phn}}(\nu) = \alpha \nu^3 \exp\left(-\frac{\nu^2}{\xi^2}\right), \quad (8.4)$$

where α is the an effective phonon coupling parameter, and ξ is the phonon cut-off frequency. The phonon cut-off frequency is given by

$$\xi = \frac{\sqrt{2}v_{\text{LA}}}{d_{\text{QD}}}, \quad (8.5)$$

where v_{LA} is the speed of sounds and d_{QD} the QD size. The photonic environment is described by

$$\mathcal{H}_{\text{env}}^{\text{pht}} = \hbar \sum_{\mu, l} \omega_{\mu, l} c_{\mu, l}^{\dagger} c_{\mu, l} \quad (8.6)$$

and the photonic interaction term is described by

$$\mathcal{H}_{\text{int}}^{\text{pht}} = \hbar \sum_{\mu, l} \left(f_{\mu, l} \sigma c_{\mu, l}^{\dagger} + f_{\mu, l}^* \sigma^{\dagger} c_{\mu, l} \right), \quad (8.7)$$

where $\sigma = |0\rangle \langle X|$, $c_{\mu, l}^{\dagger}$ ($c_{\mu, l}$) is the creation (annihilation) operator of guided ($\mu = \text{guided}$) or non-guided modes, ($\mu = \text{lost}$) of mode index l and with eigenfrequency

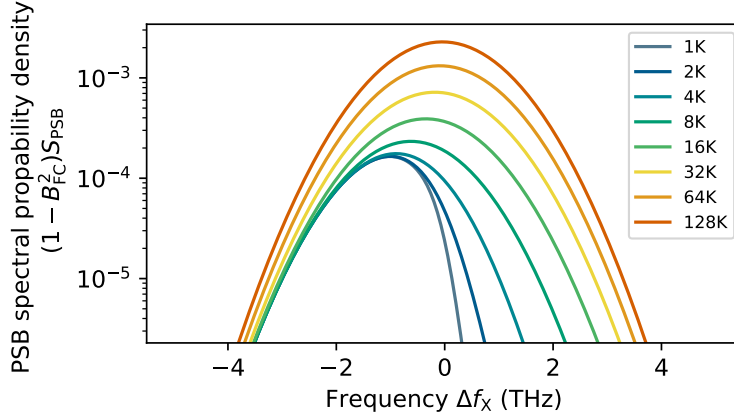


Figure 8.6: Spectral probability density for phonon sideband emission $(1 - B_{\text{FC}}^2)S_{\text{PSB}}$ as a function of the photo-emission frequency relative to resonance $\Delta f_X = f - f_X$ emission for various temperatures T . The parameters are those obtained from the evaluation of the experimental data, shown in figure 8.7.

$\omega_{\mu,l}$. For guided modes, the wavenumber k constitutes the mode index l . The QD's coupling strength $f_{\mu,l}$ with the photonic environment is assumed to be constant for guided and non-guided modes accounting for a flat spectral density as expected for the fast-light region of a broad-band waveguide mode [5].

Non-Markovian phonon interaction theory based on unitary polaron transformation [312] derives the Frank-Condon factor

$$B_{\text{FC}} = \exp\left(-\frac{1}{2} \int_0^\infty dv \frac{J_{ph}}{v^2} \coth\left(\frac{\hbar v}{2k_B T}\right)\right) \quad (8.8)$$

and the guided (lost) photonic spectra S_{guided} (S_{lost}). The guided photonic spectrum is further separable into the emission into the ZPL $S_{\text{ZPL}}(\omega)$ and the emission into the PSB $S_{\text{PSB}}(\omega)$ under the assumption of a field transformation by a uniform Green's function corresponding to an unfiltered collection of emission into the fast-light region of the guided mode of a waveguide [312]:

$$S_{\text{guided}}(\omega) = B_{\text{FC}}^2 S_{\text{ZPL}}(\omega) + (1 - B_{\text{FC}}^2) S_{\text{PSB}}(\omega), \quad (8.9)$$

where B_{FC}^2 and $1 - B_{\text{FC}}^2$ are the probabilities of the exciton decay into the ZPL and PSB. The PSB forms an asymmetric, broad profile around the Lorentzian ZPL of

$$S_{\text{PSB}}(\omega) = S_0(\omega - \omega_X) \exp\left(-\frac{(\omega - \omega_X)^2}{\xi^2}\right) \left(\coth\left(\frac{\hbar(\omega - \omega_X)}{2k_B T}\right) - 1\right), \quad (8.10)$$

where $S_0 = \int_0^\infty d\omega S_{\text{PSB}}(\omega) = 1$.

Figure 8.6 shows the spectral probability density for emission into the PSB $(1 - B_{\text{FC}}^2)S_{\text{PSB}}$ as a function of the photo-emission frequency relative to resonance $\Delta f_X =$

$f - f_X$ for various temperatures. The spectrum is highly asymmetric in the low-temperature regime, below $T = 8$ K. The PSB spectrum contains S_{PSB} mainly photons with smaller frequency than the ZPL center frequency ω_X . The phonon-bath is barely populated, and mainly Stokes processes occur. At $T = 8$ K, the phonon-bath population rises rapidly with increasing temperatures, and anti-Stokes processes are likely to occur along with Stokes processes. The PSB emission spectrum S_{PSB} becomes increasingly symmetric. For high temperatures above $T = 32$ K, the PSB S_{PSB} approximates a Gaussian shape since Stokes and anti-Stokes processes are similar in probability.

In the high-temperature regime, a temperature increase is associated with an increased probability of both processes, while the spectral distribution S_{PSB} itself does not change. In the low-temperature regime, the PSB reveals a QD's temperature by its asymmetric shape. In the higher temperature regime, the emission probability into the PSB ($1 - B_{\text{FC}}^2$) and ZPL reveals the QD's temperature.

Phonon Bath Temperature Estimation

For determining the phonon-sideband spectra, a narrow-band resonant continuous wave laser in out-of-plane configuration drives the QD's charge state $|X_h\rangle$. By choice of an excitation power well below saturation ($P_L = 0.056(16)I_S$), power-broadening and evanescent coupling of the excitation field into the guided mode of the photonic crystal waveguide are avoided. The excitation laser is cross-polarized with the collection from the shallow-etch grating coupler. The collected light is routed to a spectrometer without any spectral filtering, but excitation laser rejection by polarization filtering (see appendix A.IV). The spectrometer's signal is acquired by averaging over 10 spectra, where the CCD camera is exposed for 10 s for each acquisition. For each signal acquisition with resonant voltage bias ($U_B = 1.3755$ V) an off-resonant background signal ($U_B = 0$ V) is acquired to subtract the residual laser background. The emission spectra for cryostat sample-mount platform temperatures of $T_{\text{SMP}} = 7$ K, 11 K, 16 K, and 21 K are shown in figure 8.7.

The background-subtracted signal is modeled as the convolution of the detector's instrument response function (IRF) and the QD emission into the PSB and the ZPL with a residual constant optical background I_{bgr} . A Levenberg–Marquardt non-linear least-square fit is performed simultaneously on all datasets. The model for the detected spectra $c_D(\omega)$ is:

$$c_D(\omega) = c_{D,0} \left(\left((1 - B_{\text{FC}}^2) S_{\text{PSB}} + B_{\text{FC}}^2 S_{\text{ZPL}} \right) \otimes S_{\text{IRF}} \right) (\omega) + c_{D,\text{bgr}}, \quad (8.11)$$

where

$$S_{\text{ZPL}} = \frac{1}{2\pi} \frac{\gamma}{(\omega - \omega_X)^2 + \gamma^2/4}, \quad (8.12)$$

and where $c_{D,0}$ describes the brightness, and $c_{D,\text{bgr}}$ describes a residual background. The cut-off frequency ξ and the phonon-coupling strength α are shared system

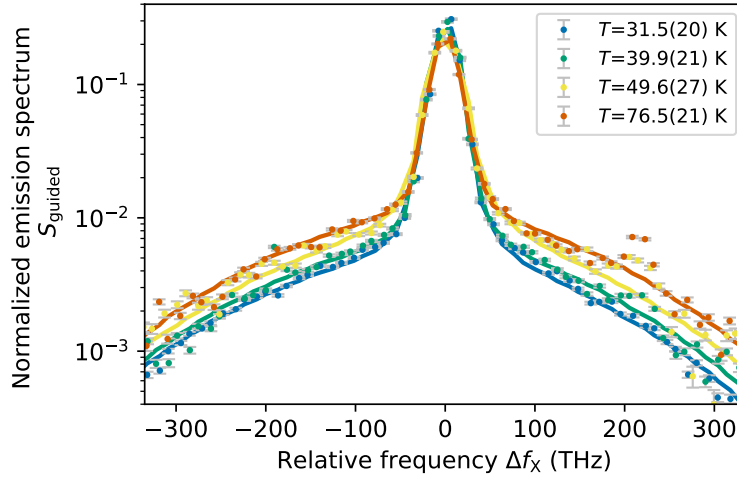


Figure 8.7: Phonon-sideband-resolving Spectra, re-normalized by their total emission rate for a sample mount temperature of $T_{\text{SMP}} = 7$ K, $T_{\text{SMP}} = 11$ K, $T_{\text{SMP}} = 16$ K and $T_{\text{SMP}} = 21$ K and fits. The fit results are summarized in table 8.1. The spectrum of the lowest temperature shows a significant asymmetry owed to a lower probability of a Stokes process than an anti-Stokes process. The spectrum of the highest temperature is within the signal-to-noise ratio fully symmetric.

parameters among the data sets, while the phonon-bath temperature T (and hence the Frank-Condon coefficient B_{FC}) are individual for each dataset.

Temperature estimation by the PSB spectrum and the Frank-Condon factor is sensitive to the PSB's shape and the emission ratio into the ZPL and PSB. As such, the method is insensitive to the QD's decay rate γ and also insensitive to the line shape due to the significantly wider spectrometer's instrument response function S_{IRF} (characterized by a narrow band laser, see appendix A.IV). For data evaluation, the QD's decay rate is fixed to the rate determined at a sample mount platform temperature of $T_{\text{SMP}} = 7$ K, discussed in section 8.1. The spectral diffusion and homogeneous broadening of the QD are neglected⁽⁸⁾.

Best fit is achieved with the temperature-independent parameters of a phonon coupling strength of $\alpha = 4\pi^2 0.022(6)$ ps² and cut-off frequency of $\xi/2\pi = 227(8)$ GHz, $c_{\text{D,bgr}} = 0.72(16)$ Hz. The final noise level is limited by the CCD camera's dark count noise and cosmic rays exciting the CCD camera. The fit residual of fitting all datasets is $\chi_{\text{res}}^2 = 112$ is limited by the spectrometer's camera exposure to cosmic rays during the exposure time. The non-zero optical background $c_{\text{D,bgr}}$ may reflect the proximity of the other charge state's photon sideband (see section 8.1).

The parameters are in the range of typical experimental values for comparable platforms in literature [8, 137, 187, 319–321]. The comparable low phonon cut-off

(8) Taking the spectral diffusion and homogeneous broadening increases the uncertainty of the phonon bath temperature and Frank-Condon coefficient slightly but does not significantly affects their estimate. This is owed to the resolution limit instrument response function.

Sample Mount Temperature T_{SMP}	Parameter	Value
7 K	T	31.5(20) K
7 K	$\omega_X/2\pi$	375.848 20(29) THz
7 K	B_{FC}	0.93(3)
7 K	$\dot{c}_{\text{D},0}$	19.05(26) kHz
11 K	T	39.9(21) K
11 K	$\omega_X/2\pi$	375.8485(4) THz
11 K	B_{FC}	0.91(3)
11 K	$\dot{c}_{\text{D},0}$	11.58(18) kHz
16 K	T	49.6(27) K
16 K	$\omega_X/2\pi$	375.819 19(28) THz
16 K	B_{FC}	0.89(5)
16 K	$\dot{c}_{\text{D},0}$	4.97(11) kHz
21 K	T	76.5(21) K
21 K	$\omega_X/2\pi$	375.795 82(23) THz
21 K	B_{FC}	0.83(7)
21 K	$\dot{c}_{\text{D},0}$	6.59(11) kHz

Table 8.1: Sample mount temperature dependent parameters obtained by Levenberg–Marquardt non-linear least-square fit of the phonon-sideband resolving spectra as shown in figure 8.7.

frequency ξ reflects the large confinement length scale of QDs, attributed to the droplet epitaxy growth method. However, the offsets between the sample mount platform temperature measured and the temperature derived by the fit are more than 24 K. This may be explained by exposure to thermal radiation from the microscope objective, which is thermally anchored to the cryostats housing at room temperature. The QD is located in a thin semiconductor membrane of limited thermal conductance, which cannot dissipate the heat intake from the microscope objective’s thermal radiation it is exposed to.

The fraction of emission into the ZPL as a function of the system temperature as derived from the fit is displayed in figure 8.8. While the highest achieved ZPL emission fraction is $B_{\text{FC}}^2(T = 31.5(20) \text{ K}) = 0.858(28)$, the model predicts improvements for typical cryogenic temperatures $B_{\text{FC}}^2(T = 4.2 \text{ K}) = 0.970(7)$. The expected fraction of emission into the ZPL at low temperatures agrees with the value reported with a similar platform 96 % [8] well.

Although the elevated system temperature explains a strong line-broadening by phonon-induced dephasing [186,187], it cannot fully explain the strong homogeneous broadening as observed and derived in section 8.1. If and to what extent the low homogeneous broadening decreases along with phonon-induced dephasing depends on the underlying mechanism and is not predictable based on the experimental data [322,323].

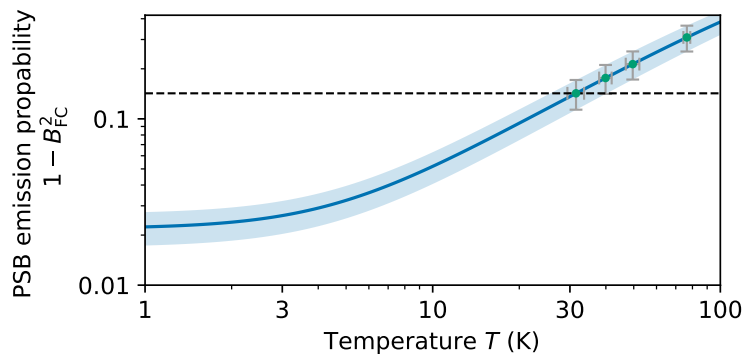


Figure 8.8: Zero-phonon-line contributions of the emission spectra for various temperatures according to the fit results of figure 8.1.

* * *

In this chapter, a droplet-etched GaAs quantum dot integrated into a line defect photonic crystal waveguide was characterized by resonant excitation using high-resolution spectroscopy. Phonon-sideband-resolved spectroscopy revealed a high phonon-bath temperature limiting the quantum dots in their linewidth and pure dephasing rate. In the next chapter, the quality of this quantum dot as a single-photon source is evaluated using time-resolved and coherent spectroscopy under resonant excitation.

DROPLET-ETCHED GaAs QUANTUM DOTS IN PLANAR PHOTONIC DEVICES AS SINGLE PHOTON SOURCE

For the application in scalable quantum networks, quantum dots must (i) allow coherent manipulation, (ii) provide pure photoemission of single photons, and (iii) show high indistinguishability of subsequent emitted single photons. This chapter successfully demonstrates the operation of a droplet-etched GaAs quantum dots in a planar photonic device as a single photon source at elevated temperatures. Its high-temperature characterization provides insight into the platform's potential performance at low temperatures.

For the application as a single photon source in scalable quantum networks, a QD must allow coherent state manipulation and provide streams of pure and indistinguishability single photons [2, 7, 12]. In the previous chapter, phonon-side-band-resolved spectroscopy reveals a high phonon-bath temperature of $T = 31.5(20)$ K. At such elevated temperatures, the phonon-induced pure dephasing exceeds the optical decay rate and limits the performance of a QD as a single photon source [187–189]. This chapter demonstrates the operation of a tunable droplet-etched GaAs QD embedded in a planar photonic device as a source of pure single photons at elevated temperatures. The high-temperature characterization provides insight into the platform's potential performance as a single photon source at low temperatures.

In this chapter, the ability of optical state manipulation, the single-photon purity, and the indistinguishability of consequent emitted photons of a QD are probed by time-resolved and coherent spectroscopy under resonant excitation. The QD is

embedded in a line defect photonic crystal waveguide⁽ⁱ⁾ of an ultra-thin semiconductor p-i-n heterojunction. The photonic properties of the device are described in section 6.4. The QD's lifetime is discussed in section 7.4, and the linewidth, pure dephasing, and the phonon sideband spectrum are discussed in chapter 8 for the operation at the same bias voltage of 1.375 V. The QD's lifetime-limited linewidth of $\Gamma/2\pi = 198.0(4)$ MHz is drastically smaller than the linewidth obtained from resonance fluorescence spectroscopy of $\Delta f_{\text{FWHM}}/2\pi = 12.1(10)$ GHz. Partially, the broadening is attributed to the high temperature and associated phonon-induced pure dephasing.

For the characterization as a single photon source, a pulsed resonant laser with a center wavelength of $\lambda_L \approx 797.63$ nm, and with a pulse repetition rate $t_{\text{rep}} \approx 80$ MHz drives the QD after passing a pulse-stretcher. After the pulse stretcher, the initial 6.8 ps laser pulse is spectrally compressed to a pulse width of ≈ 22 ps. The QD is excited using out-of-plane optical modes, and its photoemission into the guided mode of the waveguide is collected. The cross-polarized excitation laser is filtered by a set of two linear polarizers and fiber-coupled. The light is detected by avalanche photodetectors. The optical setup is described in detail in appendix A.IV

9.1 COHERENT STATE MANIPULATION

Coherent manipulation of a QD's state is essential to its application in quantum information processing. Low temperatures are necessary to limit decoherence driven by phonon-induced dephasing [188, 189]. However, coherent state manipulation can be demonstrated even at elevated temperatures [324].

(i) QD2 in the photonic crystal waveguide $W1_{206,36}^{(3,5)}$ of sample B15459 – A (see appendix A.II).

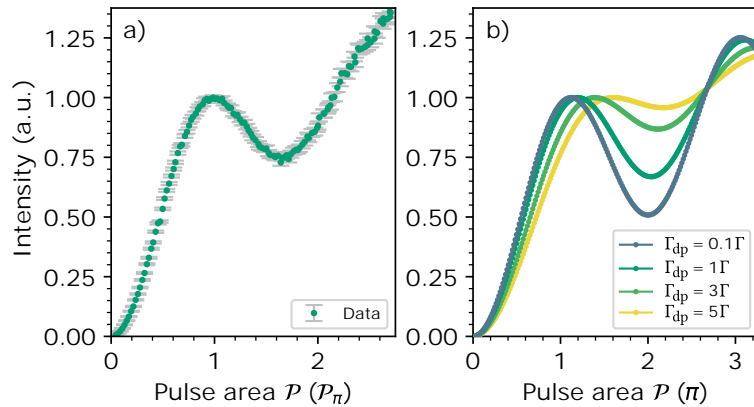


Figure 9.1: a) Intensity of an optically driven Rabi oscillation of the state $|X_h\rangle$ of QD2 as a function of the pulse area \mathcal{P} . The time-averaged count rate for a π -pulse ($\mathcal{P} = \mathcal{P}_\pi$) is approximately 191 kHz. b) Numerical prediction of the time-averaged intensity for a Rabi-oscillation for a two-level-system under the assumption of a decay rate of $\gamma = 1/T_1 = 1.2442 \text{ ns}^{-1}$, a laser pulse length of 20 ps, and a Gaussian spectral diffusion with a width of $\Delta f_{\text{FWHM}}^{\text{SD}} = 10\Gamma$ for various dephasing rates Γ_{dp} .

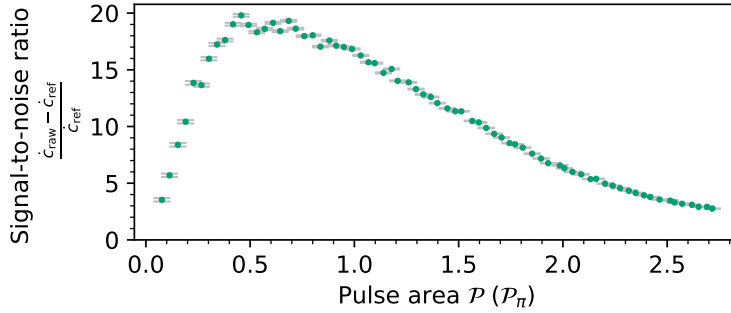


Figure 9.2: Signal-to-noise ratio of an optically driven Rabi oscillation of the state $|X_h\rangle$ of QD2 as a function of the pulse area \mathcal{P} .

Figure 9.1a) shows optically driven Rabi oscillation of the state $|X_h\rangle$ of QD2 as a function of the pulse area \mathcal{P} . The state is excited by pulsed resonant excitation with varying power. The raw photoemission signal \hat{c}_{raw} is background subtracted by a reference measurement \hat{c}_{ref} without a bias voltage, and hence no QD emission.

The pulse area corresponding to a full π -rotation is $\mathcal{P}_\pi = 536(25)$ nW (see appendix A.X). Figure 9.1b) shows a numerical prediction of the time-averaged intensity for a Rabi-oscillation for a two-level-system for various dephasing rates γ_{dp} , and assuming the lifetime T_1 and Gaussian spectral diffusion from the prior characterization of the QD. A qualitative comparison of the simulated and measured intensity confirms a strong spectral diffusion and a pure dephasing rate comparable to the decay rate $\gamma_{\text{dp}} \geq \gamma$. Acoustic phonons are the principal source of the pure dephasing, responsible for the intensity damping of the Rabi rotations. The magnitude of damping agrees qualitatively with observation on similar platforms at comparable temperatures [325, 326]. Additionally to the damping, the Rabi oscillation exhibits a pronounced inclination. Numerically, such an inclination can only be explained by substantial spectral diffusion that exceeds the optical decay rate. A qualitative similarity is obtained for a Gaussian spectral diffusion with a width of $\Delta f_{\text{FWHM}}^{\text{SD}} \approx 10\Gamma$.

The signal-to-noise ratio is shown in figure 9.2. Since the laser background increases with the excitation power, the optimal signal-to-noise ratio is reached around $\mathcal{P}_{\text{opt}} \approx \frac{\mathcal{P}_\pi}{2}$.

9.2 SINGLE PHOTON PURITY

The single-photon purity is a measure of the relative contribution of the single-photon state to the QD emission [6]. A QD emission is probed with a Hanbury Brown and Twiss experiment analogous to the experiment in section 7.4, but utilizing a pulsed resonant excitation laser. A pulsed excitation scheme reduces the dependence of the detector time jitter, provides better insight into the optical background, and

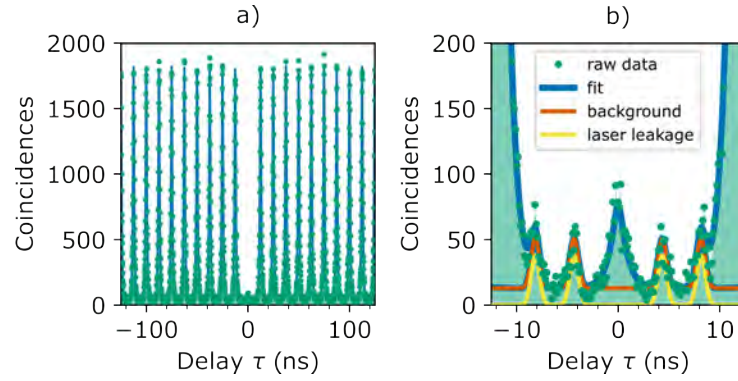


Figure 9.3: Autocorrelation histogram of a Hanbury Brown and Twiss experiment under pulsed resonant excitation. a) Close-to-zero delay region of the first pulses (green) and the fit-result (blue). b) Zoom into the zero-delay region, showing the contribution of the total background (red) and the excitation laser leakage (yellow) obtained from the fit result.

provides better sensitivity for close to accurate single-photon sources. Leakage of the pulsed excitation laser into the detector can be distinguishable from a constant background of other sources, and the zero-delay region of interest is well separated from regions where an ideal single photon source bunches.

Figure 9.3a) shows the spectrally unfiltered autocorrelation histogram obtained by excitation with $\pi/2$ -pulse for optimal signal-to-noise ratio⁽²⁾ with a total integration time of $t_i = 1$ h at a bias voltage of $U_B = 1.375$ V. The single photon purity is extracted from the background corrected pulse areas of zero-delay peak \mathcal{A}_0 relative to the side peaks \mathcal{A}_∞ by:

$$\Phi = \frac{\mathcal{A}_0}{\mathcal{A}_\infty}. \quad (9.1)$$

Both pulse areas are obtained from curve fitting a model of the autocorrelation function to the time-bin histogram. The fitting modes takes small peaks caused by excitation laser leakage, a constant optical background, blinking, and the detector time-jitter into account. The model and data evaluation is discussed in appendix A.VII.3. The short time delay region of the autocorrelation function obtained from a Levenberg–Marquardt non-linear least-square is displayed in figure 9.3. Figure 9.4 displays the pulse areas (background-corrected and normalized) for time delays up to $|\tau| = 25 \mu\text{s}$.

The fit yields a single photon purity of $\Phi = 3.46(22)$ %. The single-photon purity estimate is exceeds the noise level significantly, as shown in figure 9.3b), and is likely limited by the high temperature of the sample. Elevated temperatures can allow for phonon-assisted tunneling and thermal occupation of higher-order states [286]. The area of the non-coincident photodetection peaks, shown in figure 9.4b), reveals low blinking probability in a timescale exceeding $10 \mu\text{s}$. Assuming a telegraph-like

(2) C.f. figure 9.1.

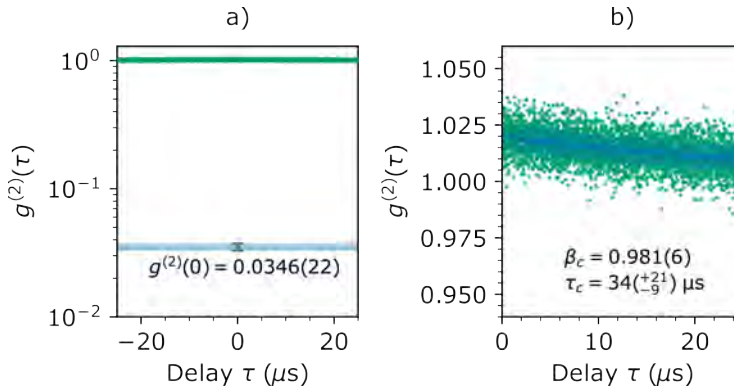


Figure 9.4: Autocorrelation function $g^{(2)}(\tau)$ (background corrected normalized time-bin histogram pulse areas) for long photodetection event time delay $\tau \leq 25 \mu\text{s}$. Figure a) displays the antibunching of the time-bin-histogram peak corresponding to coincident photodetection $\tau = 0$ and the non-coincident photodetection peaks at delays of integer multiples of the laser repetition rate $t_{\text{rep}} \approx 12.5 \text{ ns}$. The blue area highlights the antibunching estimate $g^{(2)}(0)$ and its confidence interval. Figure b) displays a zoom into the area of the non-coincident photodetection peaks, revealing low blinking probability in a timescale exceeding $10 \mu\text{s}$. The blue line corresponds to a fit and its confidence interval.

blinking⁽³⁾, the relative fraction of time the QD is in resonance with the laser is $\beta_c = 0.981(6)$ and the blinking time constant is $\tau_c = 34(+21/-9) \mu\text{s}$. Both, the blinking probability near unity and the blinking time constant exceeding the μs time-scale well, in stark contrast to the observations under continuous-wave excitation⁽⁴⁾. This can be explained by the increased spectral width of the pulsed laser⁽⁵⁾ compared to the continuous wave laser, which results in a lower sensitivity to μs time-scale spectral diffusion.

9.3 TWO-PHOTON INTERFERENCE

For many protocols in a quantum network, the stream of single photons emitted by a QD must contain indistinguishable photons. The indistinguishability of photons emitted by the QD is measured through a Hong-Ou-Mandel (HOM) experiment [327] based on an unbalanced Mach-Zehner-interferometer (MZI). The visibility of the interference defines the photons' indistinguishability.

For indistinguishability characterization of the QDs, the pulsed resonant laser with repetition rate t_{rep} is again employed. One arm of the MZI is longer, where the length difference corresponding to a delay of $\tau = t_{\text{rep}}$. Two subsequently emitted photons from subsequent laser pulses interfere at the MZI's second beam splitter in the same temporal mode. The output modes of the beam splitter are detected and time tagged. The temporal second-order cross-correlation of the two detectors is sensitive to the mode overlap between two of the two photons on the beam splitter.

(3) See appendix A.VII.3.

(4) See section 7.4.

(5) See appendix A.IV.1 for the excitation pulse-stretcher setup.

The input-output relation of the input modes $a_1(t)$, $a_2(t)$ and output modes $a_3(t)$, $a_4(t)$ of the beam splitter reads:

$$a_1^\dagger(t)a_2^\dagger(t)|0,0\rangle_{1,2} \rightarrow \frac{i}{2} \left(a_3^\dagger(t)a_3^\dagger(t) + a_4^\dagger(t)a_4^\dagger(t) \right) |0,0\rangle_{3,4} \quad (9.2)$$

In a HOM experiment, with two input photons $|1,1\rangle_{1,2}$ on the beam splitter in the same time bin, the only possible output states are with equal probability $|2,0\rangle_{3,4}$ or $|0,2\rangle_{3,4}$. In this case, second-order cross-correlation of the two detectors will never show coincidences at zero time delay τ between the two detectors. However, in the general case of the photons being partially indistinguishable, the interference visibility will be non-ideal. The beam splitter output state $|1,1\rangle_{3,4}$ occupation number has a non-zero expectation value. In this case, the second-order cross-correlation of the two detectors shows coincidences at zero time delay $\tau = 0$ proportional to the visibility of interference. Therefore, the second-order cross-correlation of the two detectors provides insight into the repeatability (coherence) of generating two indistinguishable photons [94].

At temporal coincidence $\tau = 0$, the cross-correlation of the two detectors is sensitive to spectral, spatial, and temporal overlap and the polarization of the two photons. Temporal and spatial overlap, as well as collinear polarization, is achievable by sub-lifetime excitation laser pulses and careful alignment of the interferometer. In this case, the HOM experiment probes the spectral indistinguishability between the two subsequently emitted photons. In the case of non-zero pure dephasing the second-order cross-correlation feature at the temporal coincidence region ($\tau \sim 0$) is [328]:

$$H(\tau) = \exp(-\gamma|\tau|) \left(1 - \exp(-2|\tau|\gamma_{\text{dp}}) \right), \quad (9.3)$$

where $H(\tau)$ is normalized for the radiative decay rate. The expected temporal interference pattern is shown in figure 9.5.

As shown in figure 9.5, the visibility of the temporal interference pattern is most sensitive in the regime of low dephasing rates $\gamma_{\text{dp}} < \gamma$. For high dephasing rates $\gamma_{\text{dp}} \geq \gamma$, the temporal interference pattern differs from the pattern of fully distinguishable photons only in a very small time region $\tau \ll 1/\gamma$ significantly.

The HOM interferometer employed to measure the indistinguishability of the QD is further described in section A.XI. By using the polarization control of one arm of the interferometer, the photons in the interferometer either have collinear or transverse polarization. The configuration of transverse polarization serves as a reference for the visibility of collinear polarization, representing the limit of maximally distinguishable photons.

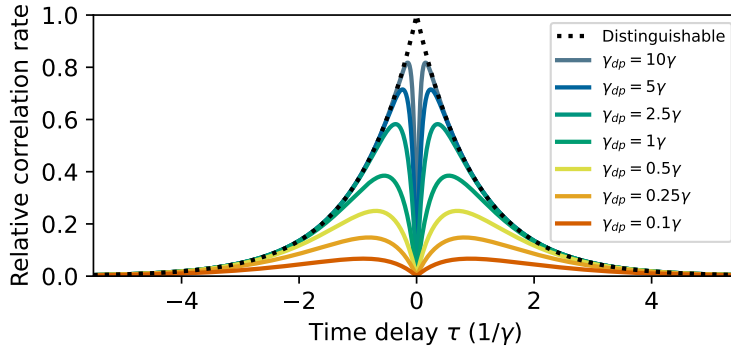


Figure 9.5: Time-resolved interference pattern relative to the radiative decay rate γ for pairs of partially indistinguishable photons after equation 9.3 for various dephasing rates assuming ideal temporal overlap, absence of spectral diffusion, and collinear polarization.

Spectrally Unfiltered Hong-Ou-Mandel Interference

The QD characterized in chapter 8⁽⁶⁾ is excited by the resonant pulsed laser passing through a pulse stretcher (see section A.IV.1) with a sub- π -pulse power ($P_L = 0.63/P_\pi$) for optimal signal-to-noise ratio. The spectrally unfiltered photo-emission is time-tagged on both detectors⁽⁷⁾. The second-order cross-correlation feature of the photodetection time-bin-histogram at the temporal coincidence region is displayed in figure 9.6.

The indistinguishability \mathcal{I} is measured as the HOM visibility,

$$\mathcal{I} = \frac{\mathcal{A}_\perp - \mathcal{A}_\parallel}{\mathcal{A}_\parallel}, \quad (9.4)$$

where \mathcal{A}_\perp (\mathcal{A}_\parallel) denotes the pulse area of the orthogonal (collinear) configuration. For details on the modeling and curve fitting method, see section A.XI.

Despite the a ZPL emission fraction of $B_{FC}^2 = 0.858(28)$, no significant indistinguishability is obtained: $\mathcal{I} = 0.007(11)$.

Without spectral filtering, emission into the phonon-sidebands and pure dephasing limit the indistinguishability. Pure dephasing is a fast process in the ps timescale [186, 187]. Hence, within the laser repetition rate (ns timescale), pure dephasing is an inevitable process. However, by spectrally filtering to prohibit the detection of photons from the phonon-sidebands, the indistinguishability can be improved. Inhomogeneous broadening by spectral diffusion occurs in the μs time-scale [106] and is thus not expected to result in reduced indistinguishability.

(6) QD2 at a bias voltage of $U_B = 1.375$ V in the W1 waveguide $W1_{206,36}^{(3,5)}$, see appendix A.II.

(7) Picoharp pulse correlator, see section A.IV.4.

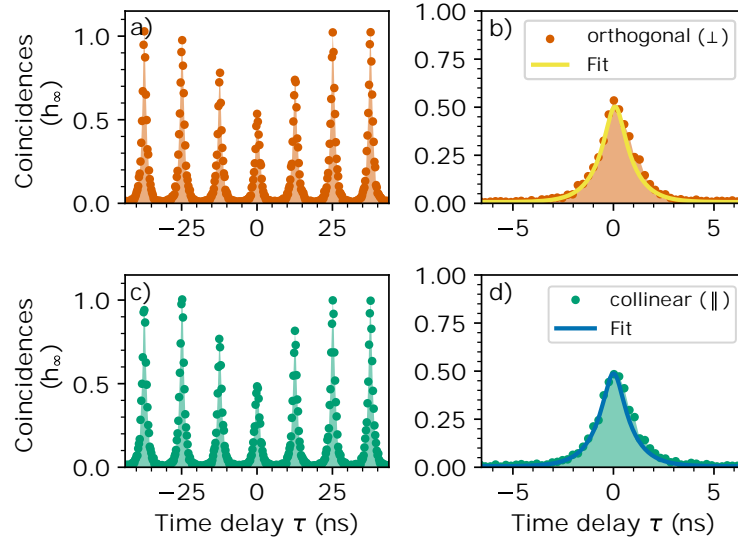


Figure 9.6: The second-order cross-correlation histograms of a spectrally unfiltered HOM experiment normalized to the bunching peaks a longer time scales where no interference occurs (see section A.XI). Figure a) and c) show the central region of the orthogonal polarized (red) and collinear (green) configuration of the interferometer. Figure b) and d) show the a zoom into the section where two subsequently emitted photons interfere. The yellow (blue) lines are fits to the orthogonal (collinear) polarized interferometer configurations.

Spectrally Filtered Hong-Ou-Mandel Interference

The poor indistinguishability caused by photons from the phonon-sidebands and the zero-phonon-line can be improved by narrow spectral filtering [285].

Figure 9.7 shows the HOM interference coincidence histograms spectrally filtered by a filter setup consisting of a volume phase holographic transmission grating and an serial etalon filter. The filter setup has a bandwidth of 1.6 GHz⁽⁸⁾, which is larger than the lifetime-limited linewidth, but about an order of magnitude smaller than the determined emission bandwidth of 12(10) GHz.

Due to the narrow filter bandwidth and the spectral filtering setup's intrinsic losses, the count rate is drastically reduced after filtering. The signal-to-noise ratio does not allow statistically significant fitting. However, the indistinguishability can be estimated directly from the ratio of integrated counts in the center peaks⁽⁹⁾ of fig. 9.7b) and 9.7d). This leads to $\mathcal{I} = 0.10(7)$, which proves some degree of indistinguishability even with no background correction from a fit.

(8) See appendix A.IV.1 for the setup.

(9) Restriction to the center region of each peak within a window of $\pm 2T_1$.

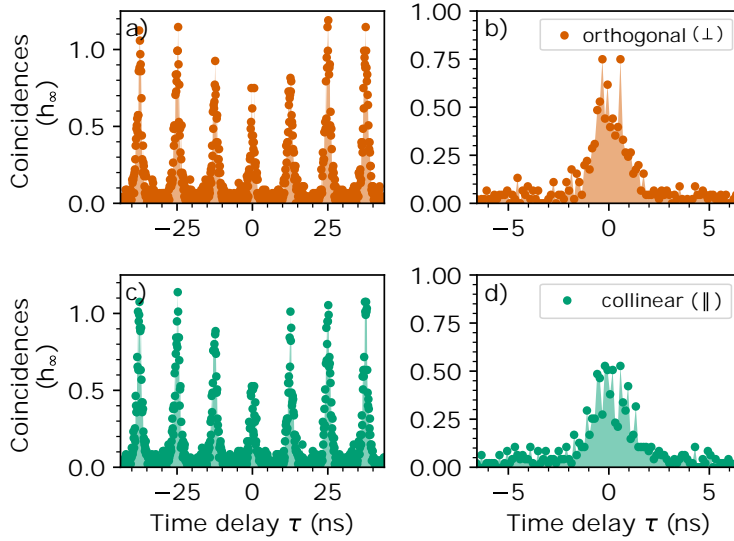


Figure 9.7: The second-order cross-correlation histograms of a spectrally filtered HOM experiment normalized to the bunching peaks a longer time scales where no interference occurs (see section A.XI). Figure a) and c) show the central region of the orthogonal polarized (red) and collinear (green) configuration of the interferometer. Figure b) and d) show the a zoom into the section where two subsequently emitted photons interfere.

Equation 9.4 provides an estimate of the indistinguishability for the case of only pure dephasing:

$$\mathcal{I}_{\text{ideal}} = \frac{\gamma}{\gamma + 2\gamma_{\text{dp}}} \quad (9.5)$$

Assuming the radiative decay rate obtained from lifetime measurements⁽¹⁰⁾ and the pure dephasing estimate from the characterization by resonant excitation⁽¹¹⁾ the estimate for the indistinguishability for the case of only pure dephasing after equation 9.5 is $\mathcal{I}_{\text{ideal}} = 0.048(21)$. In contrast, for a pure dephasing rate comparable with the life-time ($\gamma_{\text{dp}} \approx \gamma$), as indicated from the Rabi oscillations in section 9.1, the indistinguishability is estimated to $\mathcal{I}_{\text{ideal}} \approx 1/3$.

The indistinguishability remains significantly below the estimate under the assumption of pure dephasing comparable with the decay rate ($\gamma_{\text{dp}} \approx \gamma$), as indicated by the Rabi oscillation. Measurements and model descriptions of the indispensability's temperature dependence [187, 189] show a rapid drop of the indistinguishability for temperature above 10 K. At the present sample temperature of $T = 31.5(20)$ K, the thermal energy $k_{\text{B}}T$ can be sufficient to induce virtual transitions between the s and p states⁽¹²⁾. These are known to cause pure dephasing rates comparable with

(10) $\gamma = 1.2442(24) \text{ ns}^{-1}$, see section 7.4.

(11) $\Gamma_{\text{dp}}/2\pi = 12(3) \text{ GHz}$, see section 8.1.2.

(12) See section 7.2.1.

the lifetime-limited linewidth and strongly suppress the indistinguishability beyond the phonon-sideband limitations [187, 188].

The observation of a finite indistinguishability at a sample temperature of $T = 31.5(20)$ K suggests a high indistinguishability at low temperatures [187]. Yet, it remains open if the spectral diffusion reduces along with the pure dephasing towards lower temperatures.

CONCLUSION AND OUTLOOK

Conclusions and summary of the work carried out in this thesis, and an outlook towards future work for single photons from GaAs quantum dots in photonic crystal waveguides and topological waveguides for chiral light-matter interfaces.

10.1 CHIRAL LIGHT-MATTER INTERFACES WITH TOPOLOGICAL PHOTONIC CRYSTAL WAVEGUIDES

This thesis presents a numerical performance study, design, fabrication, and photonic characterization of topological photonic crystal waveguides for chiral light-matter interfaces with Quantum Dots (QDs).

Full three-dimensional finite-element quantification of conventional and topological photonic crystal waveguides as chiral emitter-photon interfaces show that topological photonic crystal waveguides are useful for efficient, on-chip chiral quantum devices. Analysis of photonic crystal waveguides to support and enhance directional interactions while suppressing subsequent backscattering losses show that the bearded-interface waveguide, a photonic analog of the Quantum Valley-Hall effect, can outperform dispersion-engineered conventional PhCWs. While all structures suffer from backscattering losses due to fabrication imperfections, these are found to be smaller at high Purcell enhancement factors for the topological bearded interface waveguide. However, these reduced losses occur because the optical mode is further away from the air-dielectric interfaces where backscattering occurs and not because of any genuine topological protection.

This thesis presents topological photonic crystal waveguides integrated into efficient nanophotonic circuits and the embedment of state-of-the-art InGaAs QDs. Scanning electron microscope images, photonic characterization, and finite-element

band calculations show that the utilization of topological PhCW for chiral light-matter interfaces is demanding on the nanofabrication capabilities. While the transmission spectrum of a bearded interface waveguide reveals decently efficient mode adapters, the illumination of the guided mode with QDs reveals low group indices and, consequently, the absence of Purcell enhancements. The fabrication of slow light resonant with InGaAs quantum dots is conditional on photonic crystal feature sizes below the limits of the employed nanofabrication method.

Outlook

Purcell enhancement of InGaAs in topological photonic crystal waveguides can be achieved by improvement of the etching selectivity using intermediate hard masks [206], and modeling and optimization of the electron-beam scattering process [207–209]. For sufficiently small feature sizes, topological waveguides for droplet-epitaxy-grown GaAs QDs can be designed, which would allow to exploit their significantly lower fine structure splitting.

The topological waveguides considered in the numerical study have yet to be optimized. By dispersion engineering, modifying the size, shape, or position of the photonic crystal holes, slow light single-mode operation away from the bulk modes [204, 243], or reduced backscattering losses are possible, allowing for the design of efficient and directional interfaces.

By designing a mode adapter that adiabatically converts the inversion-symmetric nanobeam waveguide mode to the asymmetric bearded interface waveguide mode, similar to the design for the topologically trivial glide plane waveguide [17], the transmission of the interface efficiency can be further improved. However, the successful integration of topological photonic crystal waveguides into nanophotonic circuits of the state-of-the-art InGaAs QD platform promises high-performance designs of efficient, on-chip non-reciprocal devices and scalable circuits based on topological waveguides and may enable the design of optical isolators [18], circulators [48–50] and quantum gates [19–21].

10.2 LOCAL DROPLET ETCHED GALLIUM ARSENIDE QUANTUM DOTS FOR PLANAR QUANTUM PHOTONICS

This thesis presents the photonic integration of charge and transition-energy tunable droplet-epitaxy-grown GaAs quantum dots into photonic crystal waveguides. The presented platform features all principal nanophotonic elements of a scalable quantum photonic network.

Soft-mask nanofabrication processes the semiconductor heterostructure wafer, which hosts the QDs, into a membrane with nanophotonic devices and structures for charge control of the QDs. Nanobeam waveguides route the light emitted from QDs embedded in PhCWs to high-efficiency shallow-etch grating chip-to-fiber couplers. Transmission measurements suggest a propagation loss of 20 dB/mm to 30 dB/mm, higher than in the platform of planar nanophotonics with Stranski-Krastanov InGaAs

QDs [157]. The increased loss is attributable to the nanofabrication-induced sidewall and surface roughness, the membrane's absorptive GaAs protection layers against post-process oxidation, and due to wavelength-dependent electroabsorption [272]. Line defect (W_1) PhCW with slow light near the spectral region of GaAs droplet epitaxy QDs at 795 nm are fabricated, which can enhance the light-matter interaction strength. The required small photonic crystal hole size, with 40 nm to 50 nm well below the state-of-the-art, is achieved by optimizing soft-mask nanofabrication processes for high etching selectivity in a tradeoff for increased sidewall roughness and pattern infidelity.

Above-band excitation of QDs allows for their localization on camera images with high precision and signal-to-noise ratio. However, strong background fluorescence attributable to nanofabrication-induced impurities renders only quasi-resonant and resonant excitation suitable for spectroscopy. Under quasi-resonant excitation, charge-state and stark-shift control are demonstrated, revealing large polarizabilities and a wavelength tuning close to 1 nm. Lifetime measurements show slow radiative decay and the absence of significant Purcell enhancements. The efficiency of the realized photon-emitter interface can be boosted by interfacing QDs with slow light modes of a W_1 PhCW, where a Purcell factor $F_p > 10$ could be achieved.

Resonant excitation and phonon sideband spectroscopy reveal a high phonon bath temperature ($T = 31.5(20)$ K) and associated pure dephasing comparable with the radiative decay rate, attributable to insufficient thermalization of the sample in the cryostat. Extrapolation of the phonon sideband emission estimates an emission fraction (Frank-Condon Factor) into the zero-phonon line of $B_{FC}^2 = 0.858(28)$ and predicts a further increase of ($B_{FC}^2 = 0.970(7)$) at low temperatures. Autocorrelation measurements in a Hanbury Brown and Twiss setup confirm the single-photon nature ($g^{(2)}(0) = 3.46(22)$ %) of the QDs' photoemission. The study of the autocorrelation function under pulsed and continuous-wave resonant excitation indicates strong spectral diffusion and low blinking probability in timescales up to 25 μ s.

Despite the phonon bath temperature and spectral diffusion, coherent driving of a QD in a W_1 waveguide is demonstrated. The Rabi oscillation confirms the strong spectral diffusion, significantly exceeding the optical decay rate. The electric bandstructure and the electric characterization show that the heterojunction's layout shifts the Coulomb plateaus to large forward bias voltages, resulting in high tunneling currents which contribute to charge noise effects, i.e., spectral diffusion. However, in the literature, InGaAs QDs in W_1 s in similar heterostructure layouts show less spectral diffusion. It appears that the observed spectral diffusion comes from the short distances between the relatively large QD and the semiconductor-oxide interface, inevitably resulting in spectral diffusion caused by surface charge fluctuations.

The visibility of Hong-Ou-Mandel experiments revealed low indistinguishability of consequent photons, limited by the high phonon bath temperature. The single photon purity, mutual coherence between photons created, and coherent optical

driving promises prospects for realizing deterministic sources of indistinguishable single photons.

Outlook

The next step to characterize the presented light-matter interface's performance as a deterministic source of indistinguishable single photons is the low-temperature characterization, i.e., in the absence of phonon-induced dephasing, of several QDs embedded in PhCWs. However, the presented study at elevated temperatures provides insights for designing and developing the architecture of the next-generation planar platform for GaAs droplet epitaxy QDs.

The scanning electron microscope images show that the soft-mask nanofabrication method induces a high sidewall and surface roughness, pronounced over-etching that requires pre-characterization of the fabricated feature sizes and inhibits the reliability and reproducibility of the fabrication. Resist reflow techniques [205] could be incorporated into the fabrication process to reduce the spatial resist inhomogeneity. A homogenous thickness improves fabrication reliability and decreases surface roughness, potentially reducing the intrinsic waveguide loss. Ultimately, higher etching selectivity and improved control over the fabrication process can be achieved by using intermediate hard masks [206].

An alternative approach to absorptive GaAs layers for surface layer protection may be chemical passivation by sulfur and deposition of Al_2O_3 [279]. Chemical passivation of the surface layers can also reduce surface charge noise and free carrier absorption losses [46, 270]. Selectively, etching away the p-doped layer from the surface can further reduce the free-carrier absorption and suppress the Franz-Keldysh effect of built-in fields [46]. However, the increased electroabsorption may be exploitable for realizing Franz-Keldysh effect-based high-speed, high-efficiency on-chip photodetectors [272].

As the first generation of ultra-thin membrane heterojunction for GaAs QDs, the presented heterojunction does not feature a tunnel barrier [107, 260, 281] for deterministic spin-photon interfaces with quantum dots [12]. The functionality of a tunneling barrier has been demonstrated in high performance as GaAs bulk-samples [27] but has yet to be adapted into the ultra-thin membrane layout. However, for future-generation devices, n-i-n⁺ type of heterojunction layouts [280] may provide an alternative route. An n-i-n⁺ heterojunction layout allows for high-speed tunable platforms [280] and may allow re-design of the layout within the limitations of an ultra-thin membrane free of p-doped layers.

Integrating multiple quantum dots in photonic circuits [329] paves a way towards scaling up to multiple coherent single photon sources. At the same time, the combination with QD's spin degree of freedom leads to multiphoton entanglement for large-scale quantum computations. Further interfaces between GaAs QDs and quantum memories based on Rubidium atomic ensembles [330] or Tm³⁺-doped crystals [331] shows a route to the realization of quantum networks and device-independent quantum key distribution [332, 333].



APPENDIX

A.1 SUPPORTIVE INFORMATION AND THEORY FOR THE NUMERICAL STUDY ON CHIRAL LIGHT-MATTER INTERFACES IN PHOTONIC WAVEGUIDES

This appendix is supplementary to chapter 5.

A.1.1 Photonic Crystals Parameters

All PhCWs's parameters can be re-scaled with the crystal lattice constant a . For numerical implementation, it has been set: a lattice constant of $a = 266$ nm, a membrane thickness of $h = 170$ nm, the refractive index of the high-index membrane of $n_1 = 3.4638$ and in the surrounded by vacuum of $n_2 = 1$, representing a GaAs-based platform in cryogenic conditions ($T = 4$ K) [269].

For the W₁ have a hole radius of $r/a = 0.3$ is assumed. For the GPW the proposed design parameters [17] are assumed. The center hole-to-hole distance is $d = 0.75\sqrt{3}a$. The radii r_i and outwards position shifts l_i of the first four rows of index i of air holes are $r_1/a = r_2/a = 0.35$, $r_3/a = 0.24$, $r_4/a = 0.3$, and $l_1/a = 0$, $l_2/a = \sqrt{3}/8$, $l_3/a = \sqrt{3}/10$, $l_4/a = \sqrt{3}/20$. The other rows are not shifted in position and have a hole radius identical to the fourth hole row radius r_4 . The latter is identical to a W₁'s hole radii of $r/a = 0.3$. The topological photonic insulator's unit cell (BIW and ZIW) consists of two holes of radius of $r_1/a = 0.105$ and $r_2/a = 0.235$, resembling an experimental implementation of a chiral light-matter interface [78].

A.1.2 FEM calculations settings, Bloch mode normalization, group index, and mode width calculations

Numerical finite element calculations (FEMs) are performed to determine the PhCW's Bloch modes and eigenvalues. The PhCWs are systems of mixed dielectric media for which the steady state solutions of the Maxwell equations is computed,

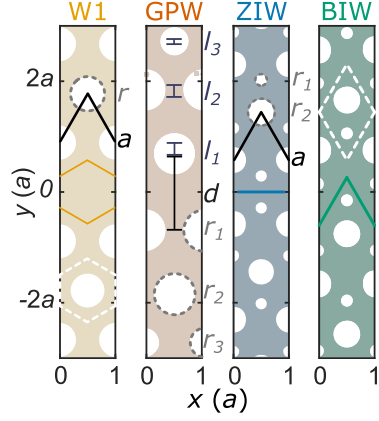


Figure A.1: Schematic of the waveguide center region of the PhCWs's supercells and their parameters for the simulations, as discussed in the text. Each photonic crystal border lines are highlighted in color. Hole radii are indicate in grey. The GPW's photonic crystal is deformed from the W1 in the PhCW's center region as discussed in the text. The deformation parameters are indicated and labeled in grey. The lattice vectors (photonic crystal's unit cells) are indicated for the W1 and the topological waveguides in a solid black (white dashed) line. The ZIW's and BIW's photonic crystals have the same unit cell and lattice vectors but their interface follows along different directions.

which resemble linear Hermitian eigenvalue problems [165], by using the commercial software COMSOL Multiphysics.

For each type of PhCW, a supercell of the one-dimensional periodic structure was studied using periodic boundary conditions (PBC). With a perfect magnetic conductor (PMC) plane, aligned with the reflection symmetry plane of the waveguides the numerical complexity is simplified limiting the study to transverse electric (TE) modes only. This takes the in-plane electric dipole moments of QEs suitable for chiral light-matter interaction [5] and TE-like mode profiles of the discussed PhCWs into account [17, 65, 165]. The simulated volume was restrained by perfectly matched layers (PML) below the membrane and each side of the PhCWs. The distance between the waveguide center and the PML below the membrane and on the sides of the PhCWs was chosen to achieve negligible mode leakage into the PML with a width of $12\sqrt{3}a$ on each side. Numerical convergence was tested sweeping the maximal element size of the mesh grid the Master's equation was solved for. This resulted in a tetrahedral mesh with a locally maximal element edge length of 1/10 of the minimal distance between any local interface of differing dielectric constants.

A right-handed Cartesian coordinate system is defined with \hat{x} being aligned with direction of propagation in the waveguide, \hat{y} pointing into the plane of the 2D photonic crystal and \hat{z} pointing out of plane, i.e., normal to the membrane.

The k -space of the PhCW has been sampled in increments of $\Delta k = 0.003 \cdot 2\pi/a$. The electric $\mathbf{e}_{n,k}(\mathbf{r})$ Bloch modes (with magnetic field $\mathbf{h}_{n,k}(\mathbf{r})$) and eigenfrequencies $\nu_{n,k} = \omega_{n,k}(k)/2\pi$ of each Bloch mode n of wavenumber k are computed. For clarity, the mode index is omitted in the following. Solutions in the light cone are omitted. The Bloch modes satisfy the normalization by:

$$\int_{\mathcal{V}_s} d\mathbf{r} \|\mathbf{e}_k(\mathbf{r})\|^2 \epsilon(\mathbf{r}) = 1, \quad (\text{A.1})$$

where $\|\mathbf{e}_k(\mathbf{r})\|$ is the norm of the electric field of the Bloch mode and $\epsilon = n^2$ is the dielectric constant. The group index for each mode $n_g(\omega_k) = c \frac{d}{d\omega} \omega_k$ is determined

using the Hellmann-Feynmann theorem [161]:

$$n_g(\omega_k) = \frac{2c(U_{e,k} + U_{h,k})}{\left| \int_{\mathcal{V}_s} d\mathbf{r} \operatorname{Re}(\mathbf{e}_k^*(\mathbf{r}) \times \mathbf{h}_k(\mathbf{r})) \right|}, \quad (\text{A.2})$$

where c is the speed of light, \mathcal{V}_s is the total super cell volume, and $U_{e,k}$ ($U_{h,k}$) is the time averaged electric (magnetic) field energy.

A characteristic mode width measure w_k is defined to be the volume integral of the electric energy density $u_{e,k}(\mathbf{r})$ (magnetic $u_{h,k}(\mathbf{r})$ density) and evaluated. The mode width measure w_k is assigned implicitly by the volume $\mathcal{V}_w = \{\mathbf{r} \in \mathcal{V}_s : -w_k < \mathbf{r} \times \hat{y} < w_k\}$ such that the time-averaged field energy inside the integration volume \mathcal{V}_w is $1/e$ of the time-averaged field in the entire supercell volume \mathcal{V}_s :

$$\int_{\mathcal{V}_w} d\mathbf{r} \frac{u_{e,k}(\mathbf{r}) + u_{h,k}(\mathbf{r})}{U_{e,k} + U_{h,k}} = \frac{1}{e}, \quad (\text{A.3})$$

where $u_{e,k}(\mathbf{r})$, $u_{h,k}(\mathbf{r})$ are the electric and magnetic field energy density and $\mathcal{V}_w = \{\mathbf{r} \in \mathcal{V}_s : -w_k < \mathbf{r} \times \hat{y} < w_k\}$ is the effective mode volume.

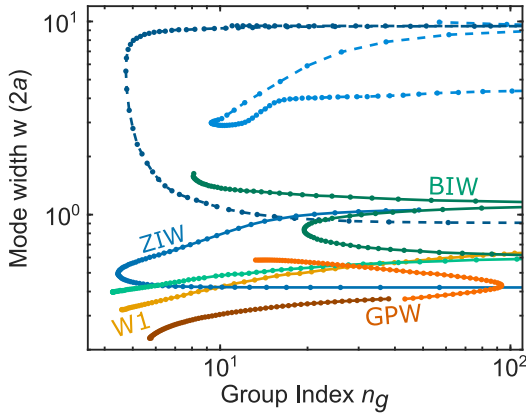


Figure A.2: Characteristic mode width w_n as a function of the group index $n_g(\omega_{n,k})$ of all band-gap modes of the BIW, ZIW and the selected modes of the GPW and W1 for comparison. The data points are connected along their individual wavenumber k . The dashed lines correspond to the modes of the ZIW which are not considered for a chiral-light interface due to their extreme mode widths.

The tight confinement of the GPW stems from the modified hole radii and position, and the modification of the space between the photonic crystals. The BIW's and ZIW's modes vary drastically in their characteristic mode width compared to topological trivial PhCWs and deviate clearly from the trend of increasing mode volume with increasing group index as observed for the W1. The GPW's lower frequency modes deviates from this trend only slightly.

A.1.3 Incoherent backscattering power-loss factor caused by structural disorder

Beyond intrinsic losses of the dielectric medium, guided modes of PhCW experience further losses, which arise from photon-scattering. In the most general case, a guided mode of a PhCW experiences out-of-plane losses (scaling with n_g) and in-plane scattering losses into bulk modes and reverse propagation modes (scaling

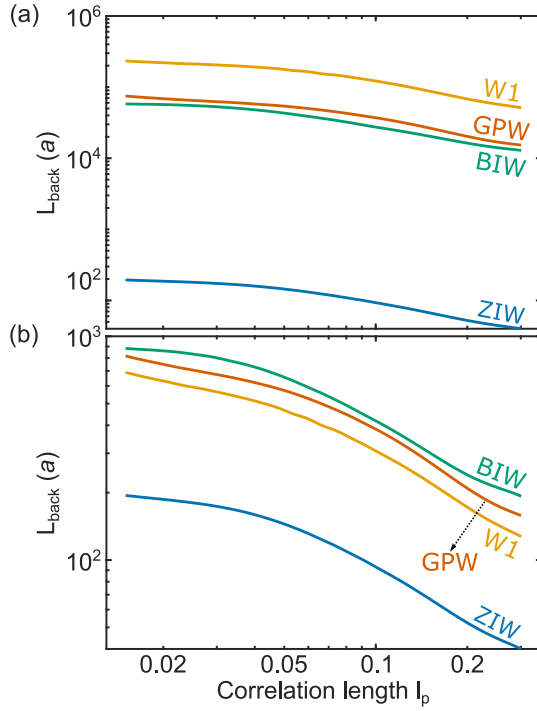


Figure A.3: Inelastic mean-free path $L_{\text{back},k} = \langle \alpha_{\text{back},k} \rangle^{-1}$ sweeping the correlation constant l_p and keeping the deformation parameter $\sigma = 3$ nm constant for chosen modes representing minimal backscattering fulfilling the requirements of: (a) providing Purcell enhancement $F = 1$ and a directionality $|D| = 0.99$ in locations being separated from hole by δ within the high-index regions of the vertical symmetry plane \mathcal{S}_c (see Appendix A.I.5) and (b) providing a Purcell enhancement $F = 10$ and providing the highest directionality D_{max} accessible for each PhCW within the same position restrictions as in (a). The inset shows a schematic of the stastical hole deformation parameters. A hole is deformed by a dent of amplitude σ over a correlation length l_p .

with n_g^2) [219]. For sufficiently large group indices, the out-of plane can be neglected. Scattering into bulk modes can be suppressed by lifting the frequency region of interest away from the bulk by choice of the lattice parameters and by photonic band engineering [204, 211, 246]. Furthermore, the single-mode operation of a PhCW can also be achieved by photonic band engineering [65, 74, 175]. Yet, in contrast to systems with broken TRS, backscattering losses in systems obeying TRS cannot be eliminated due to the guaranteed double degeneracy of the modes in forward (k) and backwards propagation ($-k$) ⁽ⁱ⁾. Consequently, backscattering between these two modes is allowed. While there are indications of a potentially exploitable advantage of topological waveguides to be less sensitive to defects of the same symmetry group as the corresponding Hamiltonian [65, 79], backscattering is assumed to be caused by isotropic fabrication induced disorder in good agreement with theory and experiment [219]. As discussed in section 5.3, the single-event backscattering regime is assumed, as is typical for relatively short waveguides [224].

The ensemble average $\langle \alpha_{\text{back}} \rangle$ of the fabrication disorder-induced single-event incoherent backscattering power loss per unit cell α_{back} can be calculated semi-analytically using the slowly varying surface approximation [219, 334]. For a short W_1 ($< 100 \mu\text{m}$) and group index of about $n_g < 22$, α_{back} is the backwards reflections loss described by the Beer-Lambert relation [221]. For higher group indices or longer

(i) In all-dielectric media light propagation is described by Maxwell's equations obeying time-reversal symmetry. In that regard the overall performance of the discussed chiral interfaces for a given directionality D is identical to a directionality $-D$.

waveguides, the Beer-Lambert relation overestimates the backwards reflections for long waveguides due to multiple-scattering. In the multiple-scattering regime the effective losses per unit cell decreases to $\alpha_{\text{back}}^{\text{eff}} = \alpha_{\text{rad}} \sqrt{1 + 2\alpha_{\text{back}}/\alpha_{\text{rad}}}$ where α_{rad} is radiative loss [221]. For our discussion, PhCWs of minimal length are assumed to form a chiral light-matter interface to achieve minimal losses. Therefore, multiple-scattering events are omitted. PhCWs as short as 10 unit cells are sufficient for high quality light-matter interfaces [223]. Out-of-plane scattering losses are neglected, taking the scaling only linear in n_g into account [221].

Furthermore, multi-mode scattering is neglected as discussed in the main text and therefore find the backscattering power loss factor per unit cell by adaption from [225] to be:

$$\begin{aligned} \alpha_{\text{back},k} &= \frac{a^2 \omega_k^2 n_g^2(\omega_k)}{4} \\ &\times \iint d\mathbf{r} d\mathbf{r}' \Delta\epsilon(\mathbf{r}) \Delta\epsilon(\mathbf{r}') \\ &\times [\mathbf{e}_k^*(\mathbf{r}) \cdot \mathbf{p}_k^*(\mathbf{r})] [\mathbf{e}_k(\mathbf{r}') \cdot \mathbf{p}_k(\mathbf{r}')] \\ &\times \exp(i2k(x - x')), \end{aligned} \quad (\text{A.4})$$

where $\Delta\epsilon(\mathbf{r})$ describes the difference of the dielectric function between the ideal and disordered structure and $\mathbf{p}_{n,k}$ is the polarization density:

$$\mathbf{p}_k(\mathbf{r}) = \left(\mathbf{e}_{k,\parallel}(\mathbf{r}) + \epsilon(\mathbf{r}) \frac{\mathbf{d}_{k,\perp}(\mathbf{r})}{\epsilon_1 \epsilon_2} \right) \delta(\mathbf{r} - \mathbf{r}'), \quad (\text{A.5})$$

where $\mathbf{e}_{k,\parallel}$ is the electric field components of the Bloch mode parallel to interfaces of changing dielectric constants $\epsilon_1 = n_1^2$ and $\epsilon_2 = n_2^2$ and $\mathbf{d}_{k,\perp}$ is perpendicular electric displacement fields. This disorder form satisfies the correct boundary conditions at the hole interface.

In-plane hole deformation of ΔR of the holes is assumed to be the dominant source of scattering in good agreement with theory and experiment [221, 234]. Thus $\Delta\epsilon(\mathbf{r})$ is only non-zero at the hole walls. With air hole indices α and the corresponding hole's Radius R_α , the change of the dielectric function is:

$$\begin{aligned} \Delta\epsilon(\mathbf{r}) &= (\epsilon_2 - \epsilon_1) \Theta\left(\frac{h}{2} - |z|\right) \sum_{\alpha} \Delta R(\tilde{\phi}(\boldsymbol{\rho}, \boldsymbol{\rho}_\alpha)) \\ &\times \delta(R_\alpha - |\boldsymbol{\rho} - \boldsymbol{\rho}_\alpha|), \end{aligned} \quad (\text{A.6})$$

where $\boldsymbol{\rho}, \boldsymbol{\rho}_\alpha$ are the in-plane vectors to \mathbf{r} and the hole center position of hole α , and where $\tilde{\phi}$ is the angular coordinate of the position \mathbf{r} in the cylindrical coordinate system centered in the hole α , so that

$$\tilde{\phi}(\boldsymbol{\rho}, \boldsymbol{\rho}_\alpha) = \arctan\left(\frac{\boldsymbol{\rho} \sin(\phi) - \boldsymbol{\rho}_\alpha \sin(\phi_\alpha)}{\boldsymbol{\rho} \cos(\phi) - \boldsymbol{\rho}_\alpha \cos(\phi_\alpha)}\right). \quad (\text{A.7})$$

Disorder between different air holes α_i and α_j are assumed to be uncorrelated for $i \neq j$ but to be perfectly correlated within each air hole in the cylindrical axis direction. This assumption takes the statistical functions determined by imaging of photonic crystal slabs into account [227]. The disorder correlation between two points of the sidewall is

$$\begin{aligned} \left\langle \Delta R(\tilde{\phi}) \Delta R(\tilde{\phi}') \right\rangle &= \sigma^2 \exp\left(\frac{-R_\alpha |\tilde{\phi} - \tilde{\phi}'|}{l_p}\right) \\ &\times \delta(\alpha, \alpha'). \end{aligned} \quad (\text{A.8})$$

Thus, the ensemble averaged incoherent disorder-induced backwards scattering power loss per unit cell in the single-scattering event approximation omitting multi-mode scattering is then:

$$\begin{aligned} \langle \alpha_{\text{back},k} \rangle &= \sum_{\alpha} \frac{a^2 \omega_k^2 n_g^2(\omega_k) \sigma^2}{4} (\epsilon_2 - \epsilon_1)^2 \\ &\times \iint d\mathbf{r} d\mathbf{r}' \Theta\left(\frac{h}{2} - |\mathbf{z}|\right) \Theta\left(\frac{h}{2} - |\mathbf{z}'|\right) \\ &\times \delta(R_\alpha - |\boldsymbol{\rho} - \boldsymbol{\rho}_\alpha|) \\ &\times [\mathbf{e}_k^*(\mathbf{r}) \cdot \mathbf{p}_k^*(\mathbf{r})] [\mathbf{e}_k(\mathbf{r}') \cdot \mathbf{p}_k(\mathbf{r}')] \\ &\times \exp\left(\frac{-R_\alpha |\tilde{\phi} - \tilde{\phi}'|}{l_p} + i2k(x - x')\right). \end{aligned} \quad (\text{A.9})$$

This formalism recovers the approximate backscattering scaling quadratic in the group index. However, the backscattering is highly dependent on the PhCW's morphology by means of the intensity profile at the air-hole walls, and the Bloch modes change as a function of frequency and k [224]. Mode profiles with high field strengths at a large number of holes show high backscattering losses. Similarly, small holes are associated with larger backscattering losses due to the R_α/l_p -term, as they occur in the third row of holes in the GPW and the throughout the BIW's and the ZIW's photonic crystals.

While all WG scale quadratically in σ the effect of l_p is non trivial, depending on the hole-sizes and the field amplitude at the air-hole interfaces. However, the influence of the backscattering parameters seems to be low and affects all PhCWs similarly as shown in figure A.I.3 where the inelastic mean-free path $L_{\text{back},k} = \langle \alpha_{\text{back},k} \rangle^{-1}$ is shown. Thus, the choice of the correlation length and the deformation strength do not influence the choice of the waveguide topology significantly.

A.I.4 Backscattering and Purcell enhancement scaling in the group index

Upon re-normalization of the Purcell enhancement and of the mean free path by their inverse explicit group index dependence, the significance of the dispersion

of the mode profiles and their polarization is revealed. Variations in the mode dependence of the re-normalized enhancement (mean free path) are observed to vary up to a factor 4 (20) throughout the full k -space outside the light cone. For identical group index the implicit group index dependence is taken into account. Still, variations in the mode profile dependence of the re-normalized enhancement (mean free path) are found and vary up to a factor 4 (9). The mode profile dependence of both properties does not correlate among different PhCW and their relative dependence is highly dispersive.

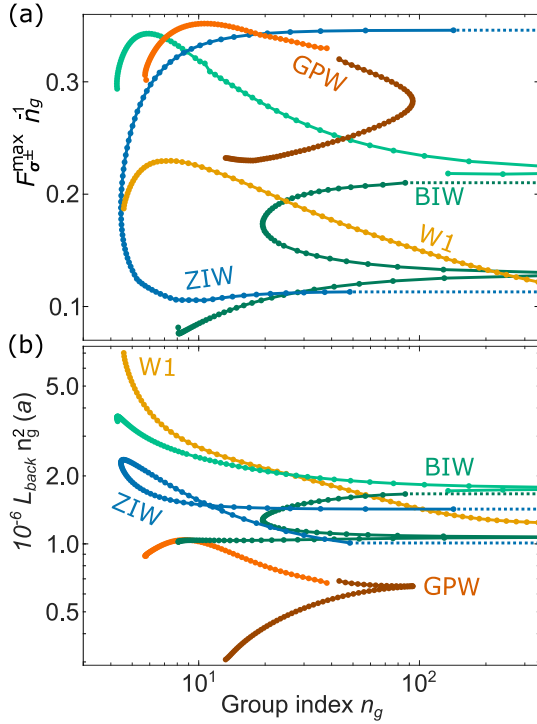


Figure A.4: (a) Re-normalized maximal Purcell enhancement $F_{\sigma_{\pm},k}^{\max}/n_g$ within the high-index regions of the vertical symmetry plane \mathcal{S}_c (see Appendix A.1.5) and (b) re-normalized mean free path $L_{\text{back},k} n_g^2$. The solid lines connect modes along the wavenumber k while the dashed lines indicate regions of divergence. The non-trivial dispersion of the re-normalized Purcell enhancement and the re-normalized mean free path indicate the significance of the dispersion of the mode profiles and their polarization.

A.1.5 Areas of Purcell enhancement and directionality

In order to compare the PhCWs' performances as quantum emitter based chiral light-matter interfaces, the maximal propagation length $L_{\text{back},n,k}$ is compared under free choice of the mode and free choice of wavenumber k , for which a non-zero area of a minimal directionality D and Purcell enhancement F can be obtained. The free choice of wavenumber k and mode n means to tune the PhCW optimally to resonance with the QE by tuning the lattice parameters⁽²⁾. However, for a realistic platform, two more restrictions of QE positioning are taken into account. State-of-the art fabrication techniques only allow for placing QE only at certain minimal distance

(2) For photonic crystals there is no fundamental constant with the dimension of length since the master equation in dielectric media is scale invariant. A quantum emitter can be brought in resonance with a mode of wavenumber k by scaling the lattice constant a .

δ_{\min} from any air-hole wall interface and only with a certain positioning accuracy δ_{acc} .

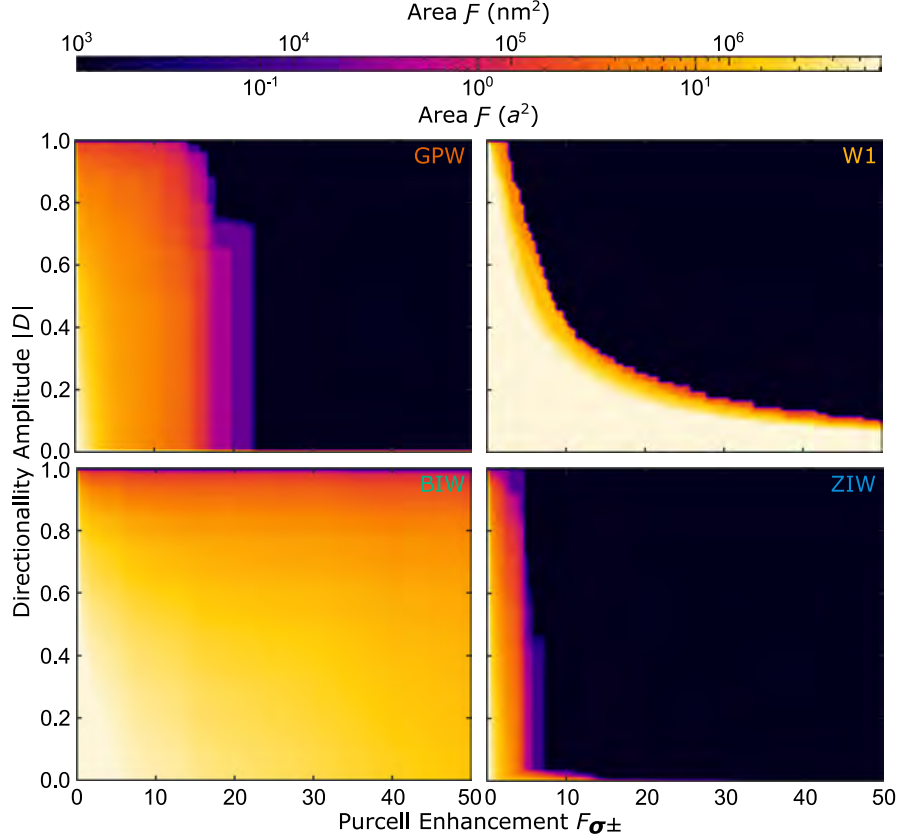


Figure A.5: Maximal area \mathcal{F} of all modes for minimal directionality amplitude $|D|$ and minimal Purcell enhancements P in the high index material area given by \mathcal{S}_{\min} , not limiting the associated group index or backscattering losses.

Experimentally, the minimum air hole distance has been estimated for near-infrared InGaAs QDs to be about $\delta_{\min} = 30$ nm [233]. This restriction of positioning QDs is taken mathematically into account by only considering points in the manifold \mathcal{S}_{\min} , defined as all points of the symmetry plane of the high index material \mathcal{S}_c that have a minimal distance δ_{\min} to any air hole:

$$\mathcal{S}_{\min}(\delta_{\min}) = \{ \mathbf{r} \in \mathcal{S}_c : \| \boldsymbol{\rho} - \boldsymbol{\rho}_\alpha \| \geq R_\alpha + \delta_{\min} \}, \quad (\text{A.10})$$

where \mathcal{S}_c is the high index material region of the PhCWs vertical symmetry plane of the supercell, and $\boldsymbol{\rho}$ ($\boldsymbol{\rho}_\alpha$) is the in-plane vector to \mathbf{r} (the center of hole with index α).

The area $A_k(|D|, F, \delta_{\min})$ of a minimal directionality $D_k(\mathbf{r}) > |D|$ and Purcell enhancement $F_{\sigma_{\pm},k}(\mathbf{r}) > F$ per supercell considering the QD positioning restriction

given by δ_{\min} is:

$$\begin{aligned}
 A_k(|D|, F, \delta_{\min}) &= \int_{S(\delta_{\min})} d\mathbf{r} \\
 &\times \Theta(F_{\sigma_{\pm},k}(\mathbf{r}) - F) \\
 &\times \Theta(D_k(\mathbf{r}) - |D|),
 \end{aligned} \tag{A.11}$$

where Θ is the Heaviside step function.

In figure A.5 shows the maximal areas $A_k(|D|, F, \delta_{\min})$ for a Purcell enhancement F and Directionality D under free choice of the mode and the wavenumber k .

$$\mathcal{F} = \max_k \{A_k(|D|, F, \delta_{\min})\}. \tag{A.12}$$

The W_1 to shows large areas for high Purcell enhancements but due to its predominately linear polarization throughout the k -space, it does not allow for Purcell enhancements and high directionality for $F > 3$. The ZIW is very similar to the W_1 in this regard, although the areas A are for all pairs D, F at least an order of magnitude smaller. The GPW and BIW seem to be similar. However, for areas as of $|D| > 0.9$ ($|D| < 0.9$) the GPW (BIW) offers more area for most pairs D, F . The BIW is the only PhCW allowing for QE interfaces with significant directionality and the highest Purcell enhancement of $F > 20$.

The QE positioning accuracy δ_{acc} is taken into account by only considering areas $A_k(|D|, F, \delta_{\min})$ large enough to place a QD within the minimum area $A_{\min}(\delta_{\text{acc}}) = \pi\delta_{\text{acc}}^2$. The precision of placing a InGaAs QD in a photonic structure is estimated to be about $\delta_{\text{acc}} = 40$ nm [233].

Taking both fabrication limitations into account, the maximal propagation length $L_{\text{back}}^{\max}(F, |D|)$ under free choice of the wavenumber k and free choice of the mode is assessed for which there is an area $A_k(|D|, F, \delta_{\min}) > A_{\min}(\delta_{\text{acc}})$ of a minimal directionality amplitude $D_k(\mathbf{r}) > |D|$ and minimal Purcell enhancement $F_{\sigma_{\pm},k}(\mathbf{r}) > F$ and satisfying the QE positioning limitations into account as:

$$\begin{aligned}
 L_{\text{back}}^{\max}(|D|, F, \delta_{\min}, \delta_{\text{acc}}) &= \\
 &\max_k \{L_{\text{back},k} : \\
 &A_k(|D|, F, \delta_{\min}) > A_{\min}(\delta_{\text{acc}})\}.
 \end{aligned} \tag{A.13}$$

The conditional maximal propagation length $L_{\text{back}}^{\max}(|D|, F, \delta_{\min}, \delta_{\text{acc}})$ in is displayed in figure 5.4.

A.1.6 Modes for highest photon number rates

The modes for maximal photon number rate $\Phi_{L/R}/Y_{L/R}^0$ are for a directionality $|D| = 0.99$ and minimal losses as a function of the Purcell enhancement F are highlighted in figure A.1.6. The discreet sampling of the k -space allows only for

discreet evaluation of the optimal mode with optical enhancement to loss-ratio. Particularly, for high enhancements involving high group indices, the finite sampling of the k -space limits the resolution of the optimal enhancement to loss ratio.

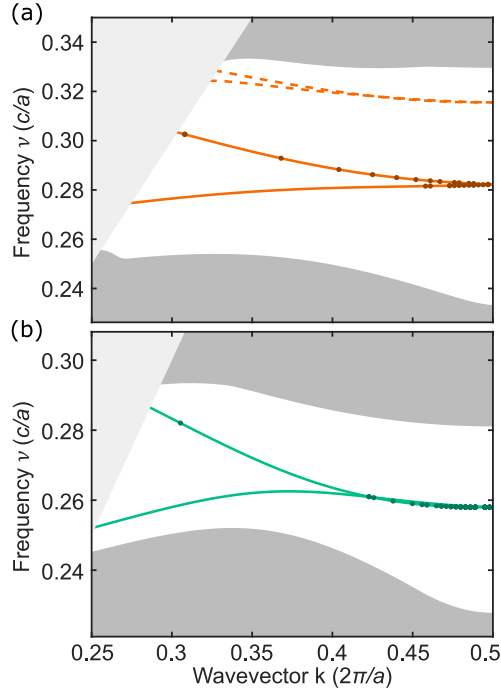


Figure A.6: Band diagram of the (a) GPW and (b) BIW showing only the light cone, the bulk bands and the relevant modes for which the photon number rate $\Phi_{L/R}/\gamma_{L/R}^0$ is maximal, desiring a directionality of $|D| = 0.99$ and minimal losses. Each point shown corresponds to a different optimal Purcell enhancement.

For increasing enhancement desired, the group index increases monotonously. When increasing the enhancements for the BIW the wavenumber k monotonously increases as well. For the BIW only modes of the upper band are optimal. In the case of the GPW the upper band shows less losses for the same group index compared to the lower band. However, the lower bands exceeds the upper bands maximal group index and thus its maximal accessible enhancement. Consequently, modes of the lower band with high losses are to be utilized above a certain desired Purcell enhancement.

A.II WAFERS, SAMPLES AND FABRICATION RECIPE

This appendix provides supplementary information about the wafer layouts, sample layouts and the fabrication recipes.

Wafer B15280 - with Droplet-Epitaxy-Grown GaAs QDs

Material	Thickness (nm)	Doping (cm ³)
GaAs	4	$N_p = 10^{19}$
Al _{0.15} Ga _{0.85} As	16	$N_p = 10^{19}$
Al _{0.15} Ga _{0.85} As	5	$N_p = 10^{18}$
Al _{0.15} Ga _{0.85} As	50	intrinsic
GaAs	0.94	intrinsic
AlAs	0.33	intrinsic
Al _{0.15} Ga _{0.85} As	15	intrinsic
Al _{0.15} Ga _{0.85} As	13	intrinsic
Al _{0.15} Ga _{0.85} As	5	intrinsic
Al _{0.15} Ga _{0.85} As	25	$N_n = 10^{18}$
Al _{0.15} Ga _{0.85} As	15	$N_n = 10^{19}$
Al _{0.15} Ga _{0.85} As	6	intrinsic
GaAs	3.18	intrinsic
GaAs	0.56	intrinsic
GaAs	0.28	intrinsic
Al _{0.75} Ga _{0.25} As	25	intrinsic
AlAs	0.28	intrinsic
GaAs/Al _{0.75} Ga _{0.25} As/AlAs	36x(0.28/24.58/0.14)	intrinsic
GaAs	0.14	intrinsic
Al _{0.75} Ga _{0.25} As	25	intrinsic
GaAs	4	intrinsic
Al _{0.15} Ga _{0.85} As	53	intrinsic
AlAs	67	intrinsic
AlAs/Al _{0.15} Ga _{0.85} As	14x(67/57)	intrinsic
Al _{0.15} Ga _{0.85} As	57	intrinsic
GaAs/AlAs	16x(1.3/2.8)	intrinsic
GaAs	100	intrinsic
GaAs	Substrate	intrinsic

Table A.1: Wafer B15459 growth layout. Based on a (100) GaAs wafer. The red (blue) highlighted layers are the p-doped (n-doped) layers. The etching- and filling layer is highlighted in green. The yellow layer is the GaAs capping layer on the membrane face towards the substrate.

Wafer B15459 - with Droplet-Epitaxy-Grown GaAs QDs

Material	Thickness (nm)	Doping (cm ³)
GaAs	4	$N_p = 8 \cdot 10^{18}$
Al _{0.15} Ga _{0.85} As	20	$N_p = 8 \cdot 10^8$
Al _{0.15} Ga _{0.85} As	5	$N_p = 1.7 \cdot 10^{18}$
Al _{0.15} Ga _{0.85} As	2	intrinsic
Al _{0.34} Ga _{0.66} As	49	intrinsic
GaAs	1.8	intrinsic
AlAs	0.37	intrinsic
Al _{0.34} Ga _{0.66} As	13	intrinsic
Al _{0.15} Ga _{0.85} As	20	intrinsic
Al _{0.15} Ga _{0.85} As	25	$N_n = 2 \cdot 10^{18}$
Al _{0.15} Ga _{0.85} As	15	$N_n = 8 \cdot 10^{18}$
Al _{0.15} Ga _{0.85} As	6	intrinsic
GaAs	4	intrinsic
Al _{0.75} Ga _{0.25} As	950	intrinsic
GaAs	4	intrinsic
Al _{0.15} Ga _{0.85} As	53	intrinsic
AlAs	67	intrinsic
AlAs	67	intrinsic
Al _{0.33} Ga _{0.67} As/AlAs (14x)	57/67	intrinsic
Al _{0.15} Ga _{0.85} As	57	intrinsic
GaAs	1.27	intrinsic
GaAs/AlAs (16x)	1.27/2.8	intrinsic
GaAs (10x)	1.27	intrinsic

Table A.2: Wafer B15280 growth layout. Based on a (100) GaAs wafer. The red (blue) highlighted layers are the p-doped (n-doped) layers. The etching- and filling layer is highlighted in green. The yellow layer is the GaAs capping layer on the membrane face towards the substrate.

A.II.1 Wafers Layouts

This section provides the relevant wafer layouts.

Wafer B14769 - with Stranski-Krastanov InGaAs QDs

Material	Thickness (nm)
GaAs	77
InAs	-
GaAs	2.8
GaAs	78.2

Table A.3: Wafer B14769 growth layout.

A.II.2 Sample Layouts

This section provides supplementary information about the sample layouts.

Sample B15459-A

Figure A.7 is a schematic of the electron beam write fields and the electronic connections of sample B15459A.

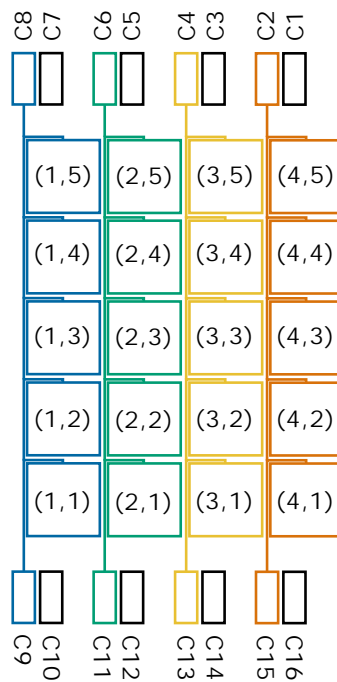


Figure A.7: Schematic overview of the electrical contacts of the electron-beam writing fields of sample B15459-A. The writing fields are labeled in the format (x, y) , where x is the column, and y is the row. All writing fields of each column share two pairs of electronic connections. The electronic connections are noted in the format C_x , where x is the index. Colored squares denote the positive electronic connectors of a column, whereas black squares denote negative electronic connectors. Example: Write field $(3, 5)$ is electronic connected by the contact pairs $C_3 + C_4$ and $C_{13} + C_{14}$, where C_3 and C_{14} are negative electronic connectors. Only one contact pair is contacted by wire-bonding.

Table A.4 gives an overview of the photonic devices in each write field.

Devices	Column 1:	Column 2:	Column 3:	Column 4:	Column 5:
Row 5:	W1 _A	W1 _A	W1 _A	W1 _A	W1 _A
Row 4:	NB	NB	NB	NB	NB
Row 3:	GPW	GPW	GPW	GPW	GPW
Row 5:	W1 _B	W1 _B	W1 _B	W1 _B	W1 _B
Row 1:	SSW1	SSW1	SSW1	SSW1	CoCW

Table A.4: Overview of the photonic devices in each electron-beam writing field on sample B15459A. W1_A and W1_B are W1-type PhCWs of different parameter sets. CoCW refers to concentric nanobeam waveguides. Column 5 is not electrically contacted with any gate.

W1 waveguides are labeled by $W1_{a,r}^{(x,y)}$, where (x, y) identifies the writing field, and a, r provide the photonic lattice parameters of lattice constant a and hole radii r . In the rows of index 5 are W1 with the lattice parameters of set A arranged as shown in table A.5.

r, a (nm)	Column 1:	Column 2:	Column 3:	Column 4:	Column 5:
Row 1	36,203	36,204	36,206	36,208	36,210
Row 2	35,203	35,204	35,206	35,208	35,210
Row 3	34,203	34,204	34,206	34,208	34,210
Row 4	33,203	33,204	33,206	33,208	33,210
Row 5	32,203	32,204	32,206	32,208	32,210
Row 6	31,203	31,204	31,206	31,208	31,210
Row 7	30,203	30,204	30,206	30,208	30,210
Row 8	29,203	29,204	29,206	29,208	29,210
Row 9	28,203	28,204	28,206	28,208	28,210

Table A.5: Look-up table for the parameters of W1 waveguides of parameter set A (W1_A) and their position in a write field. Devices are referred to as $W1_{a,r}^{(x,y)}$. The first index in this table is the hole radius r in nm, the second the lattice constant a in nm.

A.II.3 Nanofabrication Recipes

This section provides supplementary information about the nanofabrication recipes.

Recipe of Sample B15459-A and Sample B15280-C

Step 1 - Chip Preparation

- Cleave a ≈ 10 mmx10 mm GaAs chip.
- 2 min sonication in acetone.
- Flush by IPA and nitrogen.

Step 2 - MESA layer

- Spin-coat CSAR9 at 4000 RPM for 1 min
- Bake on hot plate at 185°C for 1 min. The final thickness is around 220 nm.
- Electron beam (Ebeam) exposure with Elionix F125. Settings: current 60 nA. , dose 220 $\mu\text{C}/\text{cm}^2$, pitch 40.
- Develop in n-amylacetate at room temperature for 1 min. Rinse 10 s in IPA. Nitrogen blow dry.
- RIE etching in BCl_3/Ar (5:10). RF power 43 W, 20mTorr. Time depends on the etch depth. Approximately 110 nm deep of GaAs, which can be monitored with end-point detection (around 1 and 1/4 period).
- Strip residual resist in hot NMP (70°C) for 10 min, room temperature NMP for 2 min, rinse in IPA and nitrogen blow dry.
- Measure the etch depth with the profilometer.

Step 3 - n-type contacts

- Dehydrate sample at 185°C on a hot plate for 5 min.
- Spin-coat CSAR13 at 2000 RPM for 1 min (recipe 2 in spinner).
- Bake on hot plate at 185°C for 1 min.
- Ebeam exposure with Elionix F125 Settings: current 20 nA, dose 250 $\mu\text{C}/\text{cm}^2$, pitch 20.
- Develop in n-amylacetate at room temperature for 1 min. Rinse 10 s in IPA. Nitrogen blow dry.
- Descum in oxygen plasma (100 W, 1 min).
- Deoxidation $\text{H}_3\text{PO}_4:\text{H}_2\text{O}$ (1:5) for 2 min. Rinse 1 min in MQ water. Nitrogen blow dry.
- Evaporate Ni/Ge/Au/Ni/Au n-type contact to GaAs (5/40/60/27/150 nm) using the e-gun.
- Lift-off in 1,3-dioxolane for 5 min. Sonicate for 1 min at 80 kHz at 50 % of the power. Then repeat this again (1,3-dioxolane for 5 min and sonication for 1 min).

- Finally flush in IPA and blow dry.
- Rapid thermal anneal at 420°C.

Step 4 - p-type contacts

- Dehydrate sample at 185°C on a hot plate for 5 min.
- Spin-coat CSAR13 at 2000 RPM for 1 min.
- Bake on hot plate at 185°C for 1 min.
- Ebeam exposure with Elionix F125. Settings: current 5 nA, dose 250 $\mu\text{C}/\text{cm}^2$, pitch 10.
- Develop in n-amylacetate at room temperature for 1 min. Rinse 10 s in IPA. Nitrogen blow dry.
- Descum in oxygen plasma (100 W, 1 min).
- Deoxidation $\text{H}_3\text{PO}_4:\text{H}_2\text{O}$ (1:20) for 2 min. Rinse 1 min in MQ water.
- Evaporate Cr/Au p-type contact to GaAs (50/150 nm) using the e-gun.
- Lift-off in 1,3-dioxolane for 5 min. Sonicate for 1 min at 80 kHz at 50 % of the power. Then repeat this again (1,3-dioxolane for 5 min and sonication for 1 min). Finally flush in IPA and blow dry.
- No need to anneal. Test impedance and sheet resistance.

Step 5 - Shallow Etch Gratings

- Dehydrate sample at 185°C on a hot plate for 5 min.
- Spin-coat CSAR9 at 4000 RPM for 1 min.
- Bake on hot plate at 185°C for 1 min.
- Ebeam exposure with Elionix F125. Settings: current 1 nA, dose 250 $\mu\text{C}/\text{cm}^2$, pitch 4
- Develop in n-amylacetate at -5°C (prepare cold plate in advance for at least 40 min) for 40 s. Rinse 20 s in IPA. Nitrogen blow dry.
- RIE etching in BCl_3/Ar (5 : 10). RF power 43 W, 20 mTorr. Time depends on the etch depth. Approximately 90 nm deep of GaAs, which can be monitored with end-point detection (around 1 period).
- Strip residual resist in hot NMP (70°C) for 10 min, room temperature NMP for 2 min, rinse in IPA and nitrogen blow dry.
- Measure the etch depth with the profilometer.

Step 6 - Photonic Devices

- Dehydrate sample at 185°C on a hot plate for 5 min.
- Spin-coat ZEP at 3500 RPM for 1 min (recipe 2 in spinner). The thickness should be around 400 nm.
- Bake on hot plate at 185°C for 5 min.

- Ebeam exposure with Elionix F125 (Suggested settings for waveguides: current 1 nA, dose PhC: $450 \mu\text{C}/\text{cm}^2$, pitch 4. For PhC: current 1 nA, dose $310 \mu\text{C}/\text{cm}^2$, pitch 4.)
- Develop in n-amylacetate at -5°C (prepare cold plate in advance for at least 40 min) for 1 min. Rinse 10 s in IPA. Nitrogen blow dry.
- ICP etching in $\text{BCl}_3/\text{Cl}_2/\text{Ar}$ (3:4:25). RF power 43 W, ICP power 300, 4.7 mTorr, ended by end-point detector. The etching time is around 50 s, while the etch depth in EPD is ≈ 270 nm by simulation but 249 nm is measured.
- Strip residual resist in hot NMP 70°C for 10 min, room temperature NMP for 2 min, rinse in IPA and nitrogen blow dry.

Step 7- Hydrogen Fluoride Etching

- Put the chip in plastic boat, wet etch in 5 % HF for 45 s, and rinse in MQ water for 10 s/1.5 min/3.5 min/1.5 min. Then clean in H_2O_2 for 1 min and MQ water for 10 s/1.5 min/3.5 min/5 min. Finally in $\text{H}_3\text{PO}_4:\text{H}_2\text{O}$ (5 : 50) for 1 min and MQ water for 10 s/1.5 min/3.5 min/5 min
- Put the boat in a medium-sized plastic beaker with 10 mL MQ water. Hold it by tweezers and pour in IPA from the beaker sidewall gently
- Transfer the boat to 4 more beakers of IPA (3 min each) and remove the boat in the second beaker
- Move the sample in the critical point dryer holder filled with IPA. Load in the CPD and dry with recipe *MemsTest2* (≈ 2 h).

A.II.4 Electric Properties

This section provides supplementary information about the electric properties of sample B15459-A.

Charge State Identification

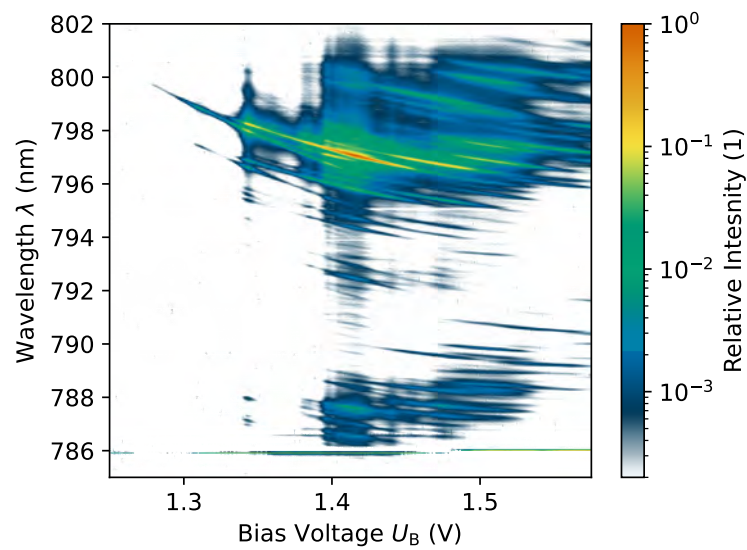


Figure A.8: The photoluminescence emitted by QD2 as a function of the gate voltage U_B (positive gate voltage indicates a forward bias) under quasi-resonant excitation ($\lambda_L = 784.85$ nm) in a logarithmic color map. The wavelength is resolved by a spectrometer and the intensity measured on a CCD-camera. The emission spectrum shows several plateaus corresponding to different charge states of the quantum dot. The spectrally shifted parallel transitions (copies) can be observed.

Diode Properties

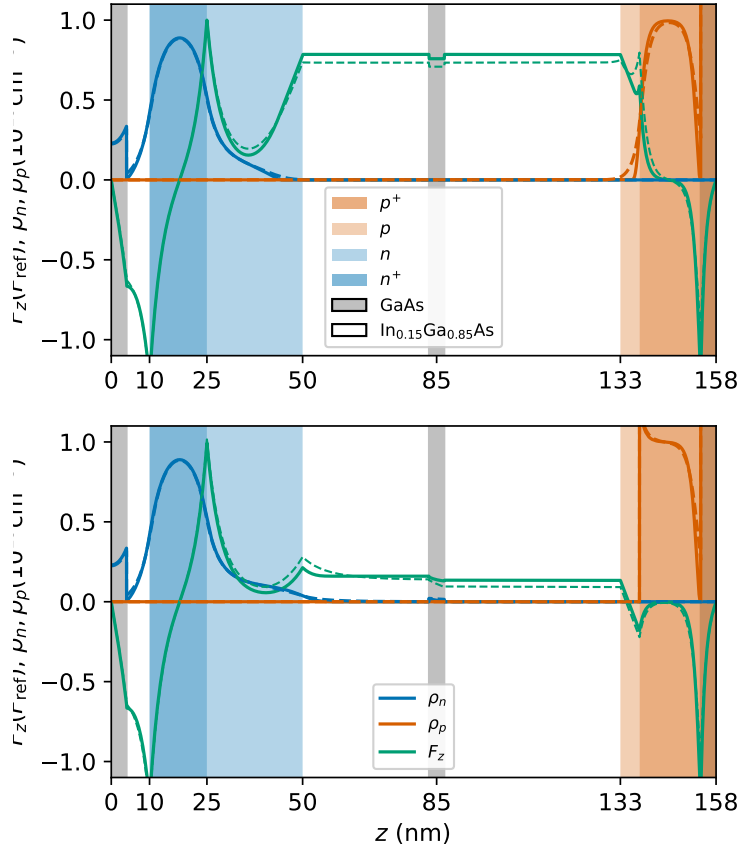


Figure A.9: Electric fields F_z (solid green line), donor number density ρ_n (solid blue line), and acceptor density ρ_p (solid red line) of wafer B15459, calculated using a one-dimensional Poisson equation solver, assuming perfect ohmic contacts to the p-type and n-type layers for a bias voltage of a) $U_B = 0$ V and b) $T = U_B = 1.4$ V at $T = 30$ K. GaAs layers are shaded as gray and $\text{Al}_{0.15}\text{Ga}_{0.85}\text{As}$ layers are shaded as white backgrounds. Overlaid colored shading indicates the doping levels with acceptors (red) and donors (blue).

DC-Stark Tuning

The depletion length of a p - n junction is described by [335]:

$$x_n = \sqrt{\frac{2\epsilon_0\epsilon_r N_a}{q} \frac{1}{N_d N_a + N_d}} U_0, \quad (\text{A.14})$$

and

$$x_p = \sqrt{\frac{2\epsilon_0\epsilon_r N_d}{q} \frac{1}{N_a N_a + N_d} U_0}, \quad (\text{A.15})$$

where ϵ_r (ϵ_0) is the relative dielectric (vacuum) permittivity, q is the electron charge, N_d (N_a) is the donor (acceptor) charge density, and U_0 is the built-in voltage. Taking the width of the intrinsic layer where $d_i = 83$ nm (excluding the deposited GaAs and AlAs for QD formation), the bias voltage U_B , and the thermal mobility of the charge carriers near the edges of the depletion region into account, the depletion region width of a p - i - n junction is [335]:

$$d_{dl} = d_i + \sqrt{\frac{2\epsilon_0\epsilon_r}{q} \frac{N_d + N_a}{N_d + N_a} \left(U_0 - U_B - \frac{2k_B T}{q} \right)}, \quad (\text{A.16})$$

where T is the temperature and k_B is the Boltzmann constant. The electric field F_D in the intrinsic layer is then in first order approximation:

$$F_D = \frac{U_0 - U_B}{d_{dl}(U_B)}. \quad (\text{A.17})$$

Figure A.10 shows the electric field F_D and depletion width d_{dl} as function of the applied bias voltage U_B for various temperatures T .

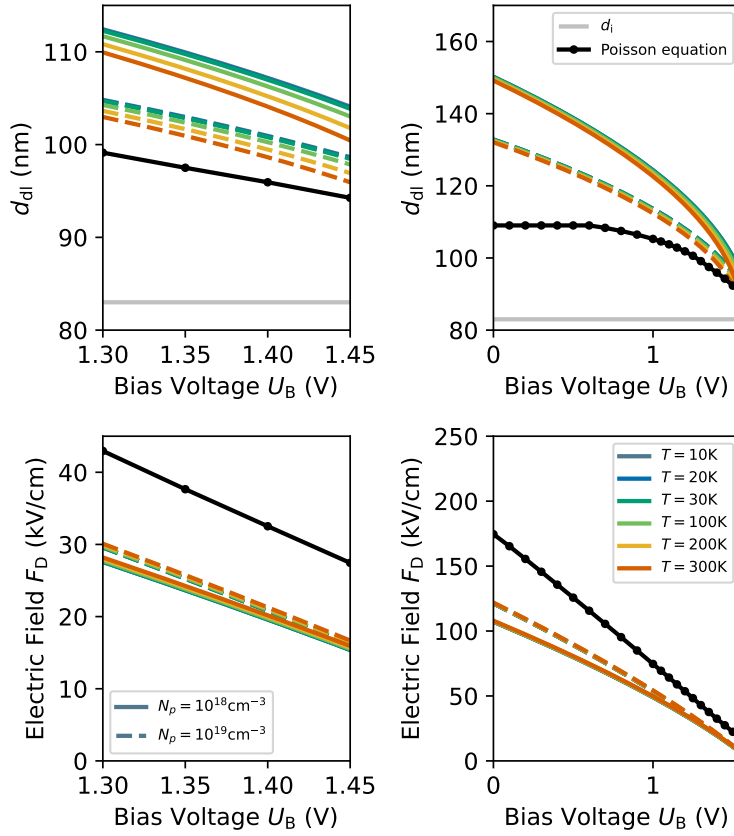


Figure A.10: Electric field F_D (colored lines) and depletion width d_{dl} (colored lines) as function of the applied bias voltage U_B for various temperatures T . The color represents the temperature T . Solid lines assume the doping levels next to the intrinsic layers ($N_p, N_a = 1 \times 10^{18} \text{ cm}^{-2}$), the dashed lines assume the highly-doped p -layer $N_p = 1 \times 10^{19} \text{ cm}^{-2}$. The solid-black line represent numerical calculations using a one-dimensional Poisson equation solver of the full heterojunction layout, assuming perfect ohmic contacts and neglecting Fermi-level pinning.

A.III CHARACTERIZATION OF TOPOLOGICAL PHOTONIC WAVEGUIDES

This appendix is supplementary to chapter 4.

Effectiveness of the Mode Adapters

Figure A.11 shows the transmission of devices with bearded-type and zig-zag-type interfaces with and without a mode adapter.

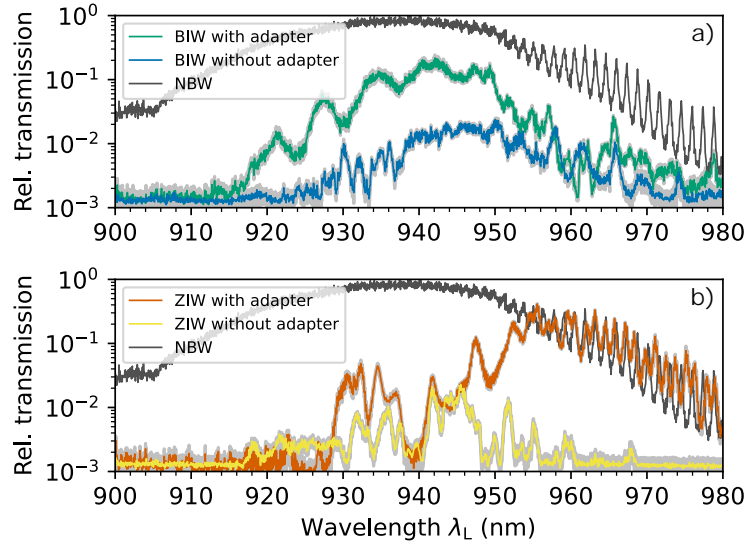


Figure A.11: Laser transmission of five photonic devices. Figure a) shows the transmission of devices with a bearded-type of interface with (without) a mode adapter in green (blue). The black transmission spectrum is the reference nanobeam waveguide device (NBW). Figure b) shows the transmission of devices with a zig-zag-type of interface with (without) a mode adapter in green (blue). The photonic crystal parameters are $a = 280$ nm, $r_s = 35$ nm, and $r_c = 55$ nm.

Group Index Estimation with Quantum Dots

Figure A.12 shows the transmission of a NBW as a photonic reference device (narrow-band laser, detected with an avalanche photodetector) and the photoluminescence signal from QDs as a white-light source (excited with p -shell excitation with a power of $P_L = 300$ μ W, detected with a spectrometer).

For long wavelengths, $\lambda_L > 950$ nm, the SEG fiber-to-chip coupler has a finite reflectivity [162] and the transmission spectrum shows characteristic Farby-Pérot fringes. Both illumination methods of the NBW's guided mode reveal the same set of fringes.

The group index of the reference device calculated from the device length of $L = 73.132$ μ m and the free spectral range $\Delta\lambda_{\text{FSR}}$ is shown in figure A.13.

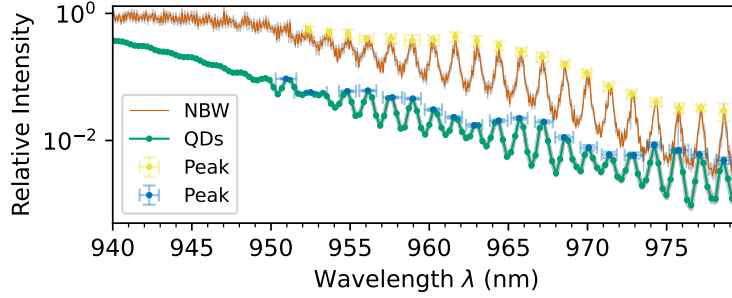


Figure A.12: Transmission of NBW reference device probed with a single mode laser (red) its Farby-Pérot fringes (yellow) and the photoluminescence signal from QDs as a white-light source (green) and its Farby-Pérot fringes (blue). Both spectra are normalized to their intensity maximum.

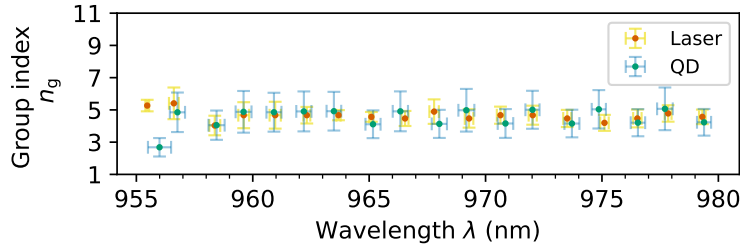


Figure A.13: The group index of the reference device calculated from the device length of $L = 73.132 \mu\text{m}$ and the free spectral range $\Delta\lambda_{\text{FSR}}$ for both illumination methods. The transmission of the laser provides the group index estimates shown in red. The QD photoluminescence estimates the group index shown in green.

The group index estimates are within the expectation values [157, 165]. The estimates of both illumination methods agree with their uncertainties.

Group Index Estimation with Quantum Dots for the BIW

The signal-to-noise ratio is limited due to the imperfect mode adapters of the bearded-type topological PhCW and the lower quantum efficiency of the spectrometer. The photoluminescence data are filtered using a digital Butterworth filter [336] of 3rd order, with a cutoff wavelength of 1 nm (≈ 5 pixels of the spectrometer's CCD camera). Figure A.14 shows the transmission of the BIW waveguide and the QD photoemission emission into the guided mode as a white light source with and without the Butterworth filtering.

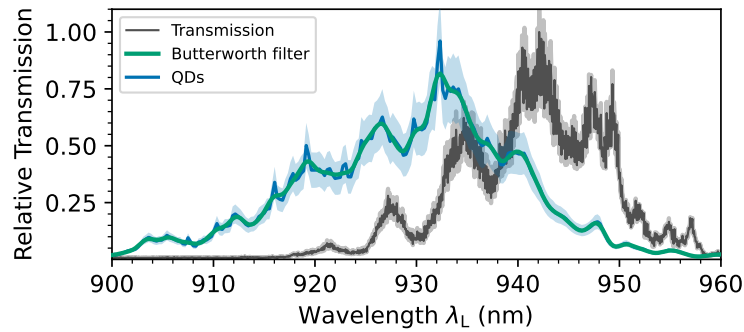


Figure A.14: Transmission of the BIW waveguide (dark gray) and the QD photoemission emission into the guided mode as white light source with (green) and without (blue) the Butterworth filtering.

The transmission spectra are normalized to their individual intensity maximum. For long wavelengths ($\lambda_L > 950$ nm), the laser transmission spectrum shows fringes from the SEG fiber-to-chip coupler. The photoluminescence spectra from the quantum dots show the same long-periodicity fringes for shorter wavelengths ($\lambda_L < 950$ nm) as the laser transmission spectrum. These are attributed due to reflection at the mode adapters of the PhCWs. The Butterworth filter rejects high-frequency modulation of the spectrum, allowing to resolve the Farby-Pérot fringes caused by the mode adapters more clearly.

The group index of the BIW interface is evaluated for two devices featuring two different PhCW lengths of $L_1 = 13.02 \mu\text{m}$ and $L_2 = 23.10 \mu\text{m}$. The free spectral range is expected to scale with the device's length. The fringes of the spectrum are evaluated in the spectral range of $905 \text{ nm} < \lambda < 950 \text{ nm}$. In this wavelength range, the fiber-to-chip coupler has negligible reflection, and the signal-to-noise ratio is optimal. The positions of the maxima are read off, and the half-width-half-maximum width is estimated as the uncertainty of the position.

Figure A.15 shows the evaluated maxima for the BIW waveguide.

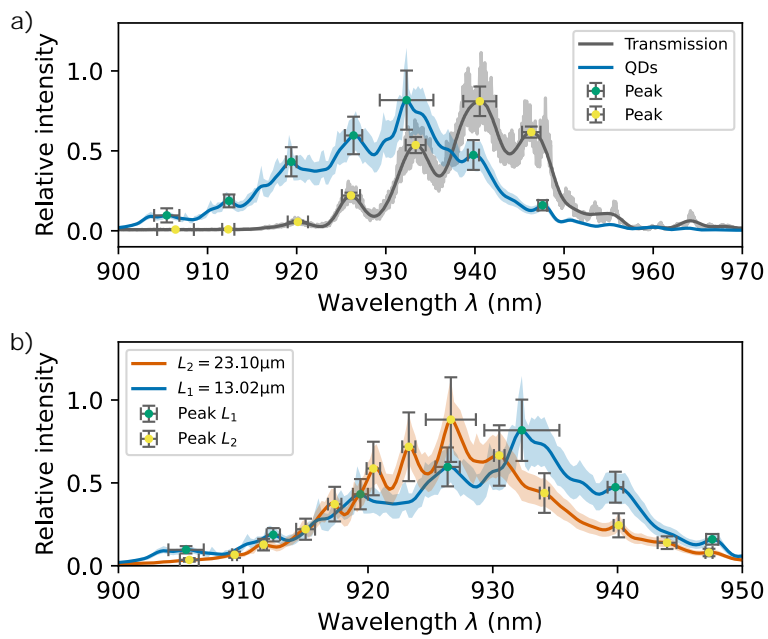


Figure A.15: Transmission of the BIW waveguide and evaluated fringe maxima. Figure a) shows the outcome of the evaluation method on the laser transmission spectrum (gray) and the QD spectrum (blue). Figure b) shows the maxima for the BIW of both lengths $L_1 = 13.02 \mu\text{m}$ and $L_2 = 23.10 \mu\text{m}$. The free spectral range scales inverse with the PhCW length.

A.IV EXPERIMENTAL SETUPS AND EQUIPMENT

This appendix describes the setups, equipment and instruments for the characterization of photonic circuits supplementary to chapter 6 and the characterization of GaAs QDs in chapter 7, 8, and 9.

A.IV.1 Optical Setup

This section describes the optical setups.

Optical Setup for Sample Access

The sample is placed into a close-cycle cryostat⁽³⁾ on top of linear nanopositioners⁽⁴⁾ (X, Y, Z). The cryostat has optical access through a fixed microscope objective⁽⁵⁾, mounted on the cryostat's housing. A schematic of the optical setup to access the sample located in the cryostat is shown in figure A.16.

Input

The excitation laser can be connected to one of the three input fiber ports. The coupler (FP_1) is chosen to fill the back focal plane of the objective, which then focuses the laser to a diffraction-limited laser spot on the sample (to focus maximal power onto a single QD). The second out-coupler (FP_2) is mode-matched to the SEG fiber-to-chip couplers on the sample. The third out-coupler (FP_3) is used to focus the green laser diode to a diffraction-limited laser spot or for co-illumination with the HeNe laser. The input paths of the two outcouplers FP_1 and FP_2 are combined with a polarizing beam splitter (FP_2). Their shared path is split with a 50:50 beam splitter, where the reflection is used for power monitoring with a photodiode PM_1 . The photodiode's signal is fed back to a variable microelectromechanical-based fiber-optic attenuator for power control and stabilization with a PID regulator (1 kHz bandwidth). This input path has a set of motorized half and quarter-wave plates for precise control of the input (HWP_4, QWP_1) polarization. A neutral density filter in the input path (F_1) allows for lower excitation powers on the sample without compromising the signal-to-noise level of the power monitoring photodiode.

The path of the third out-coupler features the same power control setup (with the photodiode PM_2). All three input paths are combined with a dichroic mirror (DM_1). The beam splitter BS_3 ($R = 0.9, T = 0.1$) combines the input and collection paths, where the input path is transmitted towards the microscope objective.

(3) Montana Cryostation; Model 4200-109; Serial number 4200-1290.

(4) Attocube ANPx101/RES and ANPz101/Res.

(5) Olympus LCPLN100XIR, NA = 0.85.

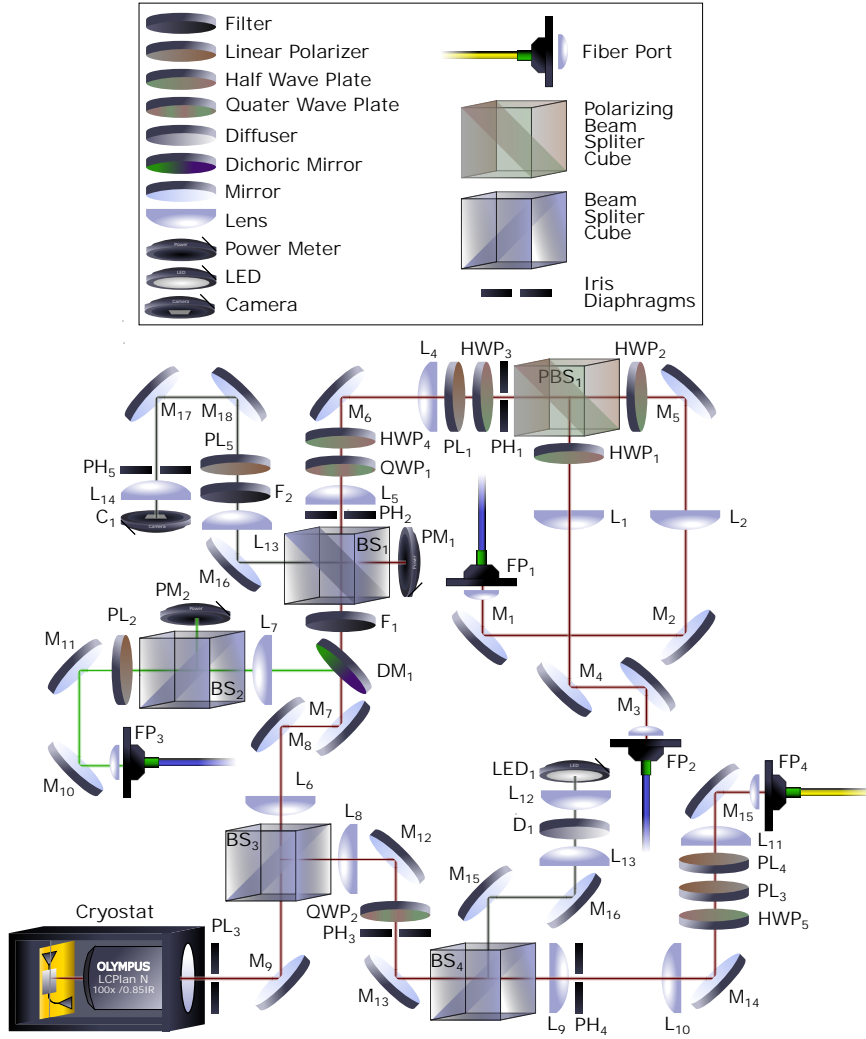


Figure A.16: The optical access to the sample located in a the cryostat. The fiber ports FP_1 , FP_2 and FP_3 are the input ports, featuring polarization-maintaining single-mode fibers. The input ports are combined by the polarizing beam splitter PBS_1 and the dichoric mirror DM_1 . The fiber port FP_4 is the collection port, featuring a single-mode fiber. The beam splitter BS_3 ($R = 0.9, T = 0.1$) separates the input and collection paths. The CMOS camera C_1 images the sample which can be illuminated with an infrared LED (LED_1). Laser input powers are monitored with the photodiodes PM_1 and PM_2 . The lens pairs (L_1, L_4) , (L_2, L_4) , and (L_{10}, L_{11}) adjust the beam diameters. Other lenses belong to the $4f$ imaging system.

Output

The output from a shallow etched grating chip-to-fiber coupler is collected through the microscope objective and reflected at the beam splitter BS_3 . A set of waveplates (HWP_5 , QWP_2) compensates for any rotation of the polarization along the out-coupling path. For resonant excitation experiments, a set of linear polarizers (PL_3 , PL_4) is utilized to suppress the excitation laser.

Camera

An infrared light (LED_1) illuminates the sample for white light imaging. The corresponding beam splitter, a 50:50 beam splitter with a flip-mount (BS_4), is removed from the collection path when performing experiments. The camera path, separated at the beam splitter (BS_1), features a color filter and a linear polarizer for the suppression of the laser.

Optical Filtering Setup

The beam is expanded to a diameter of 20 mm with two lenses (L_1, L_2), which approximately matches the optical clearance of the transmission grating. A schematic of the optical filtering setup is shown in figure A.17. The first-order diffraction is

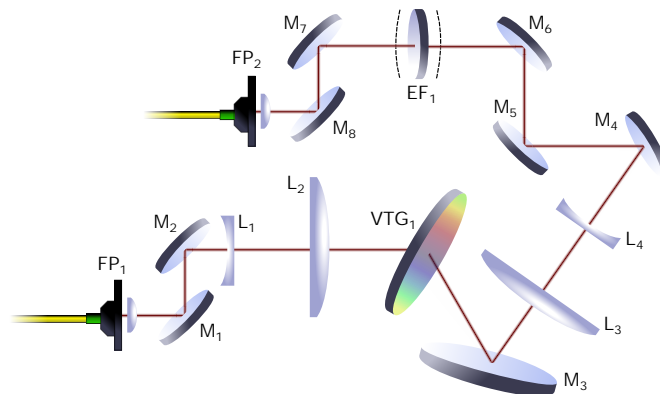


Figure A.17: Optical filtering setup with Volume Phase Holographic Transmission Grating (VTG_1) and an Etalon Filter EF_1 .

passing an solid silica Etalon filter with coated end faces as second stage and fiber coupled. The transmission through the grating is shown in figure A.18. The Etalon is tuned and stabilized with a Peltier element.

Volume phase holographic transmission gratings VTG_1 specifications:

- Manufacturer: Wasatch Photonics
- Part number: HD1650780.8-30x6B
- Wavelength range: 700 - 850 nm
- Center wavelength: 780.8 nm

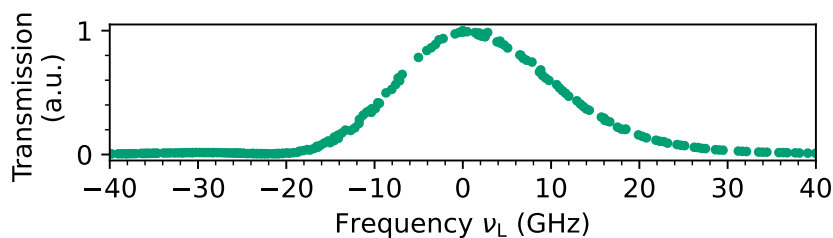


Figure A.18: Transmission scan through the filter setup without the Etalon filter, the center wavelength is 797.3 nm. The full-width-half-maximum width of the transmission peak is ≈ 20.34 GHz. Without the Etalon filter, the rejection of wavelength components takes place when the collimated beam is fiber-coupled. The peak transmission (fiber-to-fiber) is $\approx 42\%$. Credit for the data acquisition to Hanna Salamon.

- Line density: 1650/mm
- 1st Order diffraction efficiency: $> 70\%$ for 750 - 810 nm

Etalon Filter EF₁ specifications:

- Manufacturer: LightMachinery Inc.
- Part number: OP-7423-1686-2
- Wavelength range: 700 - 850 nm
- Finesse: 30 (measured)
- FSR: 2/cm (specified)
- Bandwidth 1.6 GHz at 795 nm (calculated)
- Transmission: 77 % at 795 nm (measured)

Pulse-Stretcher Setup

The bandwidth of a pulse from the Ti:Sapphire pulse is compressed in frequency by stretching it in the time domain. The 6.8 ps wide laser pulse is dispersed using a diffraction grating, using a standard 1200 lines/mm blazed diffraction grating, optimized to diffract primarily into the first order with a dispersion of 0.75 ns/mrad. A schematic of the pulse-stretcher setup is shown in figure A.19.

The beam is expanded to a diameter of 25 mm with two lenses (L_1, L_2), which approximately matches the area of the grating. The large beam diameter ensures higher spatial resolution between different frequency components in the Fourier plane when imaging the reflected beam. The dispersed beam is imaged using a large focal length lens ($L_3, f = 750$ mm) which focuses it onto a mirror (M_7). A tunable width mechanical slit placed in front of the mirror transmits a fraction of the spectral bandwidth in the pulse. The spatial dispersion of the back-reflected bandwidth-modified pulse is reversed when passing the grating again. This is important in order to avoid a chirp from the different optical path lengths of the frequency components.

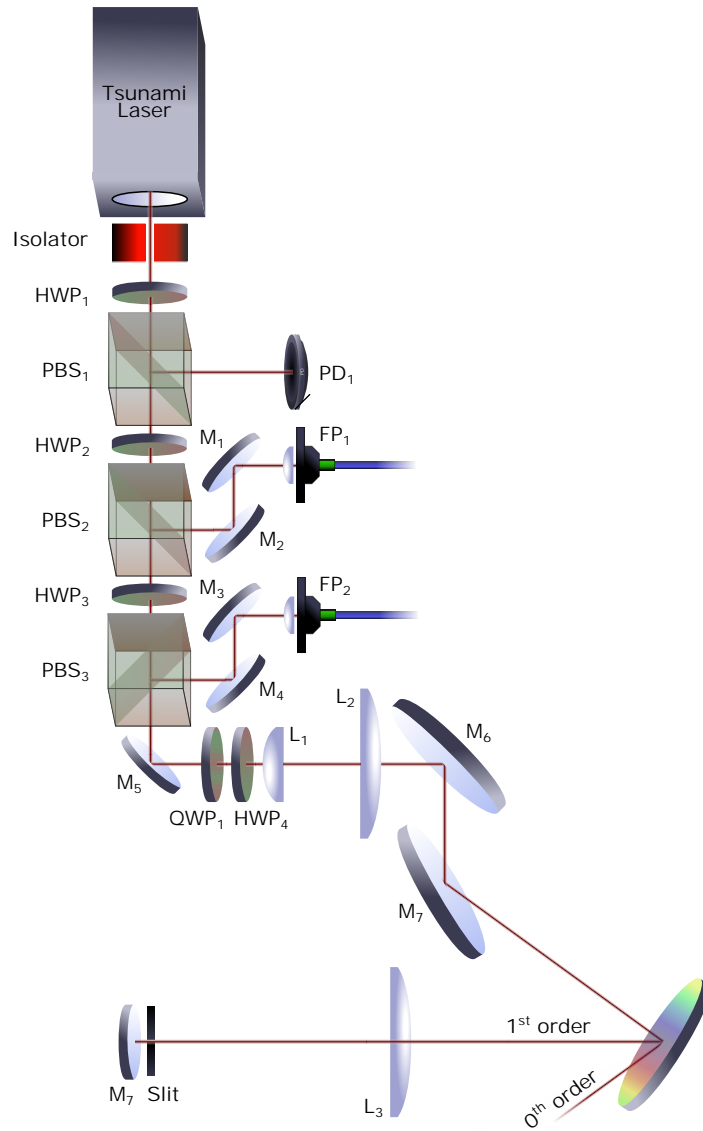


Figure A.19: Pulse-stretcher setup for the Ti:Sapphire laser. After passing the isolator, the beam is split (PBS_1) for exposure of the trigger diode (PD_1). The transmitted beam is split for fiber coupling unmodified laser pulses (FP_1) and feeding the pulse-stretcher setup, discussed in the main text.

The output can be separated from the input by using a polarizing beam splitter (PBS₃) and fiber-coupled (FP₂). A polarization control stage of a set of quarter and half waveplates (QWP₁,HWP₄) accounts for the polarization sensitivity of blazed gratings and for efficient out-coupling.

The slit width is adjustable with a micrometer screw, determining the resulting laser pulse bandwidth. The maximum possible bandwidth compression is ≈ 20 GHz.

A.IV.2 Detectors

This section specifies and describes all relevant detectors.

Spectrometer

- Manufacturer: Andor Technology
- Model: SR500B1
- Serial number: SR-0541

The installed grating has a line density of 1200/mm and 300 nm blaze with 60 pm nominal resolution. The nominal efficiency is $\approx 23\%$ at 780 nm. The spectrometer is calibrated with the DLPro laser and the wavemeter's readings with 6 different wavelengths between 780 nm and 810 nm. Fitting a Gaussian as the instrument's response function yields 60.4(7) pm as FWHM linewidth with a goodness of fit of $\chi^2_{\text{res}} = 5.2$.

Avalanche Photo Diode Detectors

- Manufacturer: Excelitas Technologies Inc.
- Model: SPCM-AQRH-14-FC
- Serial number: 27190 and 27191

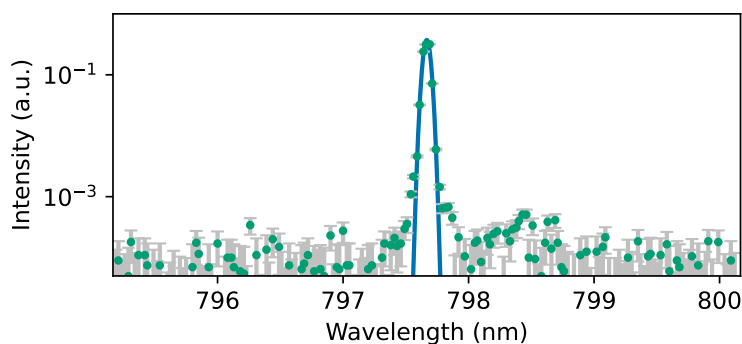


Figure A.20: Instrument's response function of the spectrometer illuminated by the DLPro narrow-band continuous-wave laser.

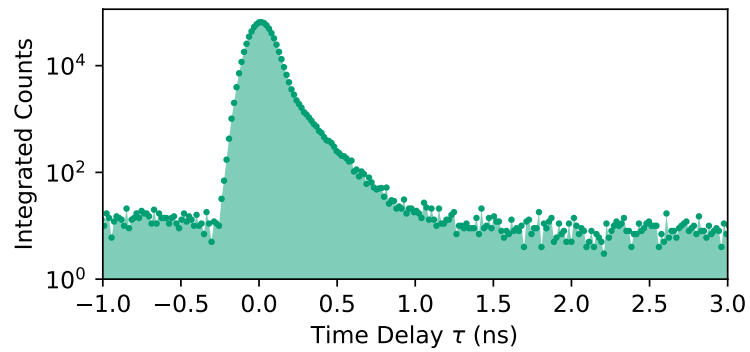


Figure A.21: Time-bin histogram of a 6.8 ps pulse from the Tsunami Ti:Sapphire laser, detected with APD₁. The instrument's response function describes a peak with full-width-half-maximum ≈ 320 ps. To the left, the function shows super-exponential decay. To the right, the function shows a slow exponential decay with $\tau_{1/e} \approx 720$ ps, compatible with the device specifications.

- Specified photon timing resolution: 350 ps
- Dead time: 24 ns
- Dark count rate: 100 Hz

A.IV.3 Light Sources

This section specifies and describes all light sources.

Tsunami - Pulsed Ti:Sapphire Laser

Pump Laser:

- Manufacturer: Spectra-Physics
- Model: Millennia eV105
- Serial number: 10498

Trigger Diode:

- Manufacturer: PicoQuant GmbH
- Model: TDA200
- Serial number: 932009

The pulse-stretcher is described in section [A.IV.1](#).

DLPro Laser

The DLPro laser is utilized for photonic characterization and QD excitation by quasi-resonant, phonon-sideband, and resonant excitation. The frequency is locked using a wavemeter and stabilized by active regulation of the Piezo's voltage (10 MHz > regulation error).

- Manufacturer: Toptica
- Model: DLC DL pro
- Wavelength tuning range: 760 nm - 805 nm
- Linewidth (5 μ s integration time): <100 kHz

HeNe Laser

For short wavelength quasi-resonant excitation.

- Manufacturer: Uniphase
- Model: 1135P
- Serial Number: 1277109
- Wavelength: 632.80 nm

Green Diode Laser

For above band excitation.

- Type: Diode-Pumped Solid State laser (Nd:YVO₄ and KTP crystals pumped by an 808 nm laser diode)

- Manufacturer: Thorlabs Inc.
- Product Number: DJ532-10
- Wavelength 532 nm

Super-Continuum Laser

- Manufacturer: NKT Photonics)
- Model: SuperK EXTREME

A.IV.4 Other Devices

This section specifies uncategorized devices relevant for this thesis.

CMOS Camera

- Manufacturer: Thorlabs
- Model: CS165CU
- Quantum Efficiency: 30 % (30 %) for the red (blue, green) channel at 800 nm.

The camera pixel resolution is 47.82(23) nm. The conversion factor is derived by comparing pixel positions with a high resolution scanning electron microscope image. The uncertainty estimate stems from the imprecision of mapping the cameras discrete pixels onto the scanning electron microscope image.

Wavemeter

- Manufacturer: HighFinesse
- Model: WS7
- Serial number: 4011

Time-Related Single Photon Counting (TCSPC) Module

- Manufacturer: PicoQuant
- Model: PicoHarp 300 (PH-300)
- Timing precision: 8.5 ps
- T2 mode time resolution: 4.0 ps

A.V PHOTONIC CHARACTERIZATION OF CONCENTRIC WAVEGUIDES

This appendix is supplementary to chapter 6.

A.V.1 Cocentric Waveguide Transmission

The transmission spectra of the concentric waveguides are discussed in the main text.

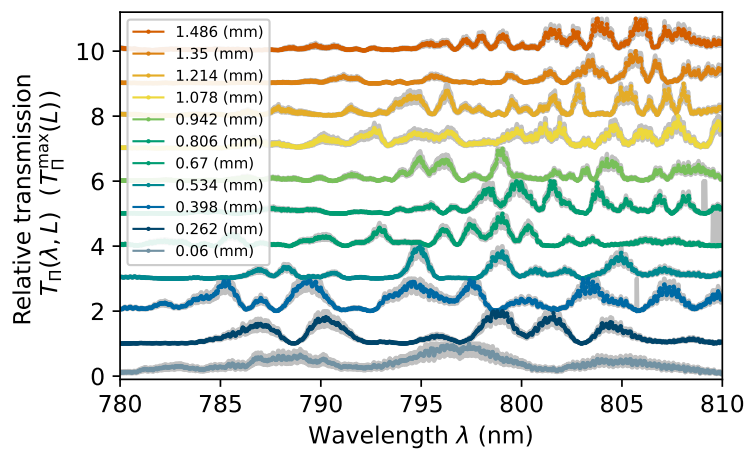


Figure A.22: Transmission spectra of concentric waveguides of various lengths. The individual spectra are normalized to their transmission maximum.

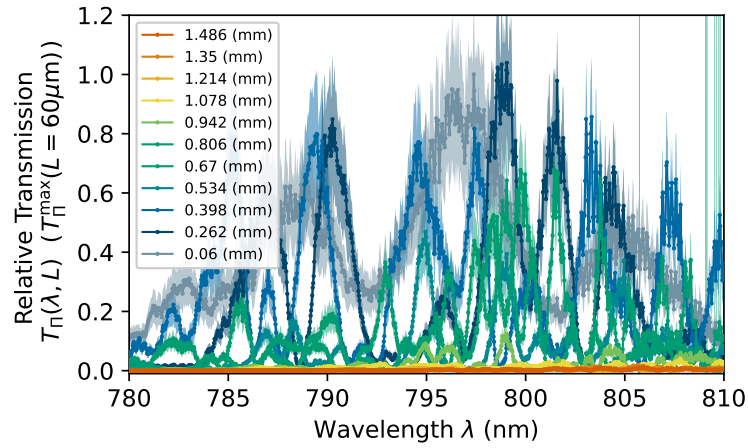


Figure A.23: Transmission spectra of concentric waveguides of various lengths. The individual spectra are normalized to the transmission maximum of the shortest waveguide ($L = 60 \mu\text{m}$).

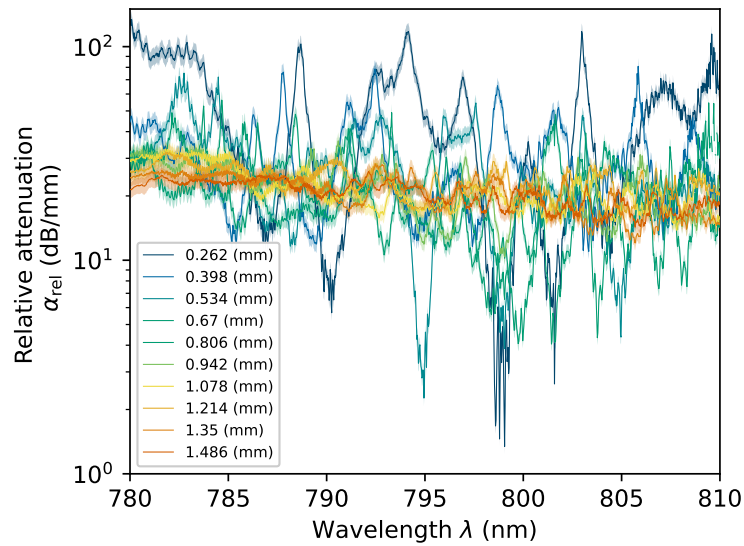


Figure A.24: Attenuation spectra of concentric waveguides of various lengths, relative to the transmission of the shortest waveguide ($L = 60 \mu\text{m}$).

A.VI ELECTRONICS

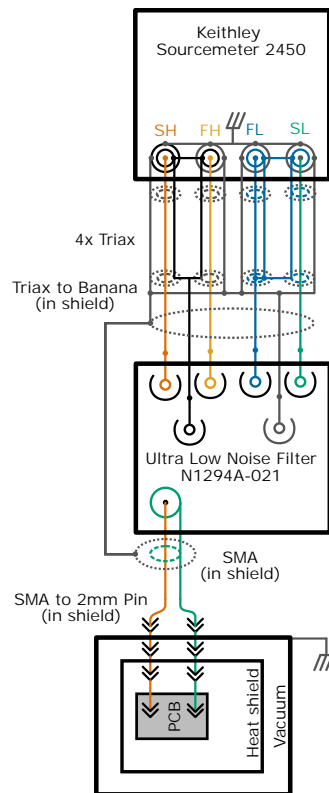


Figure A.25: Schematic of the the source measure unit (SMU) and the electronic wiring for controlling the bias voltage U_B and voltage-current characterization of the p-i-n junction. Only one column of the sample is connected to the SMU while the others are terminated by a $50\ \Omega$ resistor directly after the vacuum-feed-through (not shown).

Figure A.25 shows the source measure unit (SMU) and the electronic wiring for controlling the bias voltage U_B and voltage-current characterization of the p-i-n junction. Only one column of the sample (compare figure A.7) is connected to the SMU while the others are terminated by a $50\ \Omega$ resistor directly after the vacuum-feed-through. Inside the cryostat thermally anchored twisted-pairs of magnin wires with diameter of $127\ \mu\text{m}$ connect the vacuum feed-through terminal with the printed circuit board which hosts the sample. The wires each have about $8\ \Omega$ at 300 K.

Source meter unit:

- Manufacturer: Keithley
- Model: 2450 SourceMeter
- Serial Number: 04330921

A.VII TIME RESOLVED SPECTROSCOPY

A.VII.1 Life Time Measurements

The time-bin histogram of photodetection events $C(\tau)$ is modeled by a single exponential decay with an radiative decay time constant T_1 and a constant optical background C_{bgr} :

$$C(\tau) = C_0 \exp\left(-\frac{(\tau - \tau_0)}{T_1}\right) \otimes C_{\text{IRF}} + C_{\text{bgr}}, \quad (\text{A.18})$$

where \otimes denotes the convolution with the normalized instrument response function (IRF) C_{IRF} of the photodetector (APD₁, see figure A.21 in section A.IV.2).

The lifetime is measured for two excitation powers of $P_L = 60 \text{ pW}$ and $P_L = 240 \text{ pW}$, well below the QDs saturation power. For the data evaluation, the first time-bins within the full-width-half-maximum width of the IRF are omitted. The time-bin histograms, the fit of equation A.18 and the corresponding residuals are shown in figure A.26.

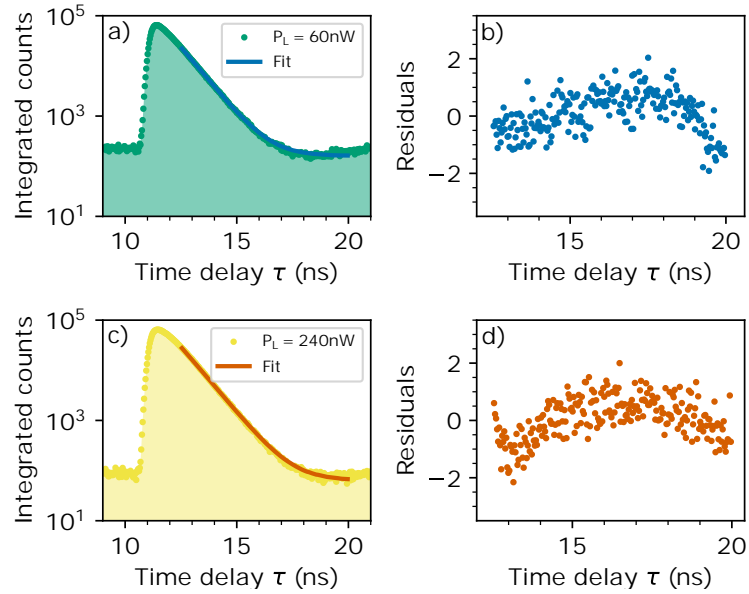


Figure A.26: The time-bin histogram and fits of the lifetime measurements for two excitation powers of a) $P_L = 60 \text{ pW}$ and c) $P_L = 240 \text{ pW}$. Figure b) and d) show the corresponding residuals.

For the lower excitation laser power the parameter estimates are: $T_1 = 818.7(13) \text{ ps}$, $C_0 = 7.074(24) \cdot 10^4$, and $C_{\text{bgr}} = 1.440(21) \cdot 10^2$ ($\chi_{\text{red}}^2 = 2.85$). For the higher excitation power the parameters are: $T_1 = 803.7(16) \text{ ns}$, $C_0 = 8.36(3) \cdot 10^4$, and $C_{\text{bgr}} = 3.68(19)$ ($\chi_{\text{red}}^2 = 2.02$). The lifetimes of the radiative decay slightly differ. The discrepancy can be explained by the non-homogenous optical background. The background is caused by laser leakage directly from the laser setup of the Tsunami laser into the detector,

invariant under variation of the laser excitation power into the cryostat. A significant feature of the laser leakage is observable around $\tau = 20$ ns. The measurement with the higher-power, with about 1/4 shorter data acquisition time, shows about a 1/4 of the optical background near $\tau = 20$ ns. The residual plots in figure A.26 indicate the background significance to the data fit and its acquisition time dependence. The life-time limited linewidth estimate from the higher power measurement (with lower background sensitivity) is $\Gamma = \frac{\gamma}{2\pi} = 198.0(4)$ MHz.

A.VII.2 Continuous-Wave Hanbury-Brown-Twiss Experiment

The autocorrelation function for a quantum dot under coherent resonant continuous-wave excitation is [94, 295]

$$g^{(2)}(\tau) = 1 + \alpha(\tau - \tau_0) (g_0 - 1), \quad (\text{A.19})$$

where g_0 describes the anti-bunching at zero time delay $\tau = \tau_0$, and $\alpha(\tau)$ describes the time evolution by:

$$\alpha(\tau) = \exp(-\eta\tau) \text{Re} \left(\cos(\mu\tau) + \frac{\eta}{\mu} \sin(\mu\tau) \right). \quad (\text{A.20})$$

The functions μ and η determine the time evolution and coherent features by

$$\mu = 2\pi \sqrt{\Omega^2 - (\gamma - 2\gamma_{\text{dp}})/4^2 + i}, \quad (\text{A.21})$$

and

$$\eta = 2\pi(3\gamma + 2\gamma_{\text{dp}})/4, \quad (\text{A.22})$$

where Ω is the optical driving strength, γ is the decay rate, and γ_{dp} is the pure dephasing rate.

Blinking into Dark States and Detector Time-Jitter

The auto-correlation histograms show pronounced bunching at short time delays, particularly for excitation laser powers. The bunching indicates the probability of a higher photon detection event at short time delays than for uncorrelated photons ($\tau \rightarrow \infty$). This is attributable to the presence of telegraph-type noise [300, 337] associated with the population of the QD blinking from a bright state into dark states, a charged state, or impurities outside the quantum dot [296, 297]. In the dark state, the QD transition is transparent to the laser for short timescales. The interaction between the two-level system and the dark states and the involved timescales depend on the physical mechanism responsible for the noise. The autocorrelation function in the presence of telegraph-type of noise can be phenomenologically described by [185, 300]:

$$g_{\text{TN}}^{(2)}(\tau) = g^{(2)}(\tau) \left(1 + \frac{1 - \beta_c}{\beta_c} \exp\left(\frac{-|\tau|}{\tau_c}\right) \right), \quad (\text{A.23})$$

where β_c corresponds to the fraction of time in which the QD is in the bright state, and τ_c is the blinking time constant. Taking the finite time-jitter σ and the signal delay difference τ_0 of the two detectors into account, the autocorrelation function becomes:

$$g_{\text{jitter}}^{(2)}(\tau) = g_{\text{TN}}^{(2)}(\tau) \otimes \frac{1}{\sigma\sqrt{2\pi}} \exp\left(-\frac{\tau^2}{2\sigma^2}\right). \quad (\text{A.24})$$

Data Evaluation

The auto-correlation histograms are normalized for each excitation laser power by adding a normalization constant as free parameters to equation A.24. The histograms are least-square curve fitted with the Levenberg–Marquardt algorithm the optical decay rate $\gamma = 1/T_1$ from section A.VII.1, and the detector time-jitter σ of the APD detectors from section A.IV.2.

The fit of the autocorrelation histograms of the fit of the lowest six excitation powers is displayed in figure A.27 as a function of the excitation laser power P_L . The fitting parameters are summarized in figure A.28. The goodness of fit is $1.02 < \chi_{\text{red}}^2 < 1.57$. The parameter estimation uncertainties are dominated by the low time resolution of the detectors. The detector time resolution and the high pure dephasing rate inhibits resolving coherent features of the autocorrelation function and a significant assessment of the Rabi-frequency's power dependence.

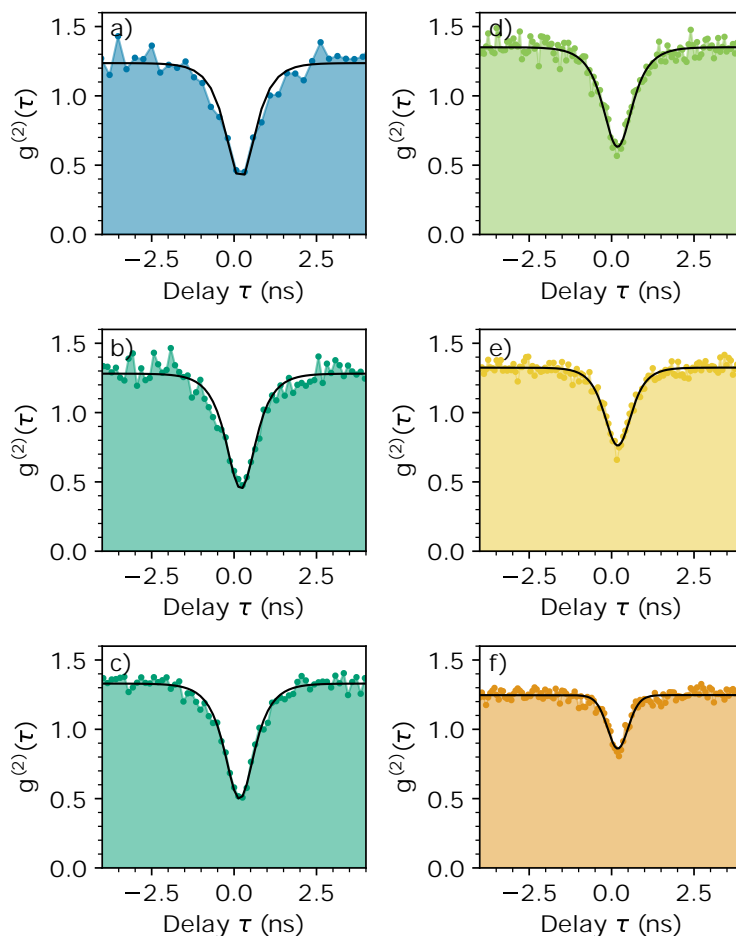


Figure A.27: Near zero time delay regions of the autocorrelation histograms and least-square curve fits with the Levenberg–Marquardt algorithm of equation A.24 ($N = 1$) for an excitation laser power of a) 7.5 nW, b) 15 nW, c) 30 n watt, d) 60 nW, e) 120 nW, and f) 240 nW.

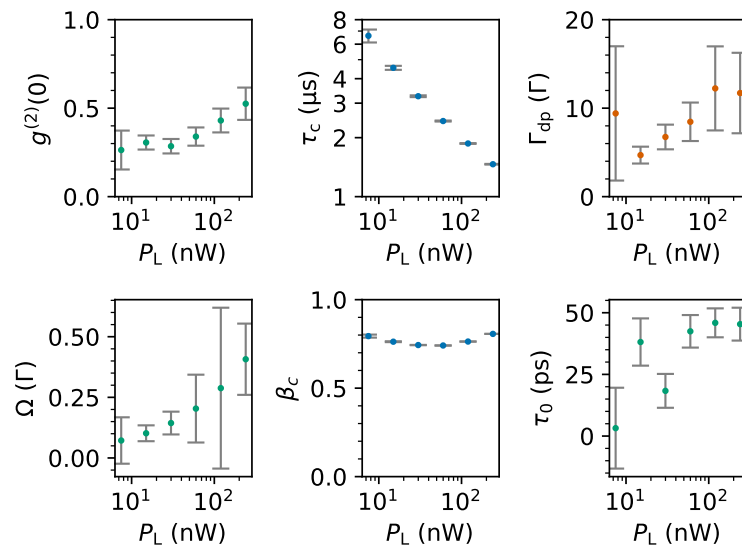


Figure A.28: Fitting parameters of the autocorrelation histograms of figure A.27 by equation A.24.

A.VII.3 Pulsed Hanbury-Brown-Twiss Experiment

For periodic pulsed excitation, the second-order cross-correlation time-bin histogram of the two detectors of a Hanbury-Brown-Twiss experiment consists of isolated peaks separated by the laser pulse repetition rate t_{rep} . The peaks are uncorrelated, except for the peak of temporally coinciding photodetection at the two detectors. The number of photodetection events in a peak of index n can be expressed as:

$$\mathcal{G}_n = \begin{cases} \mathcal{G}_0 & \text{if } n = 0 \\ \mathcal{G}_\infty & \text{otherwise,} \end{cases} \quad (\text{A.25})$$

where $n = 0$ corresponds to the peak of temporal coincidence of photodetection at the time delay $\tau = \tau_0$. In the presence of telegraph-type noise, the peak height of the time-bin histogram can phenomenologically be described by [185, 300]:

$$\mathcal{G}_n = \begin{cases} \mathcal{G}_0 \frac{1}{\beta_c} & \text{if } n = 0 \\ \mathcal{G}_\infty \left(1 + \frac{1-\beta_c}{\beta_c} \exp\left(\frac{-|nt_{\text{rep}}-\tau_0|}{\tau_c}\right) \right) & \text{otherwise,} \end{cases} \quad (\text{A.26})$$

where β_c corresponds to the fraction of time the QD is in the bright state, and τ_c is the blinking time constant. Re-normalization of equation A.26 by the number of photodetection events of uncorrelated peaks \mathcal{G}_∞ yields the autocorrelation function for pulsed excitation:

$$g^{(2)}(\tau) = \begin{cases} \frac{\mathcal{G}_0}{\beta_c \mathcal{G}_\infty} & \text{if } n = 0 \\ 1 + \frac{1-\beta_c}{\beta_c} \exp\left(\frac{-|nt_{\text{rep}}-\tau_0|}{\tau_c}\right) & \text{otherwise,} \end{cases} \quad (\text{A.27})$$

where $g^{(2)}(\tau = \tau_0) = \frac{\mathcal{G}_0}{\beta_c \mathcal{G}_\infty}$ is the single-photon purity.

Data Evaluation

The time-bin histogram of the Hanbury-Brown-Twiss experiment under pulsed excitation is evaluated in two steps. In the first step, the center region of the histogram corresponding to the peaks of index $n \in [-50, 50]$ (approximately ± 625 ns), where no significant blinking can be detected, is evaluated. By modeling and curve fitting, the temporal shape of the time-bin histogram, the number of photodetection events corresponding to the peak of coincidence \mathcal{G}_0 , the detectors time delay offset τ_0 , the laser pulse repetition rate t_{rep} , and the background counts g_{bgr} are determined. Taking the finite lifetime of the QD's excited state T_1 into account, the time-bin histogram peaks \mathcal{G}_n of index n are:

$$\mathcal{G}_n(\tau) = \begin{cases} g_0 \exp\left(-\frac{|\tau-\tau_0|}{T_1}\right) + g_{\text{bgr}} & \text{if } n = 0 \\ g_\infty \exp\left(-\frac{|\tau-n t_{\text{rep}}-\tau_0|}{T_1}\right) & \text{otherwise,} \end{cases} \quad (\text{A.28})$$

where g_0 is the peak height of the peak at zero time delay $\tau = \tau_0$, g_∞ is the peak height of uncorrelated photons at the n th side peak at a time delay $\tau = n\tau_{\text{rep}} + \tau_0$, T_1 is the QD's lifetime. The time-bin histogram shows additional peaks from laser leakage into the signal detection path. The laser leakages dress each of the histogram's peaks with an additional peak on each side. With finite laser leakage the time-bin histogram model of A.28 becomes

$$\mathcal{G}_{n,L}(\tau) = \begin{cases} g_0 \exp\left(-\frac{|\tau - \tau_0|}{T_1}\right) + \xi_L(\tau - \tau_0 \pm \tau_{0,L}) & \text{if } n = 0 \\ g_\infty \exp\left(-\frac{|\tau - n\tau_{\text{rep}} - \tau_0|}{T_1}\right) + \xi_L(\tau - n\tau_{\text{rep}} - \tau_0 \pm \tau_{0,L}) & \text{otherwise,} \end{cases} \quad (\text{A.29})$$

where $\xi_L(\tau)$ approximates the laser's pulse intensity profile [338] by

$$\xi_L(\tau) = g_L \text{sech}\left(1.76 \frac{|\tau|}{\Delta_L}\right), \quad (\text{A.30})$$

where g_L is the peak intensity and Δ_L is the full width at half maximum of the intensity profile. Taking the finite detector time-jitter σ and a constant background g_{bgr} into account, the final model of the time-bin histogram is:

$$G_{\text{jitter}}^{(2)}(\tau) = \left(\sum_{n=-N_{\text{sp}}}^{N_{\text{sp}}} \mathcal{G}_{n,L}(\tau) \right) \otimes \frac{1}{\sigma\sqrt{2\pi}} \exp\left(-\frac{\tau^2}{2(\sqrt{2}\sigma)^2}\right) + g_{\text{bgr}}. \quad (\text{A.31})$$

The fit of equations A.31 by least-square curve fitting with the Levenberg–Marquardt algorithm is shown in figure A.29. The obtained parameter estimations are shown in table A.6, and the residuals are shown in figure A.30.

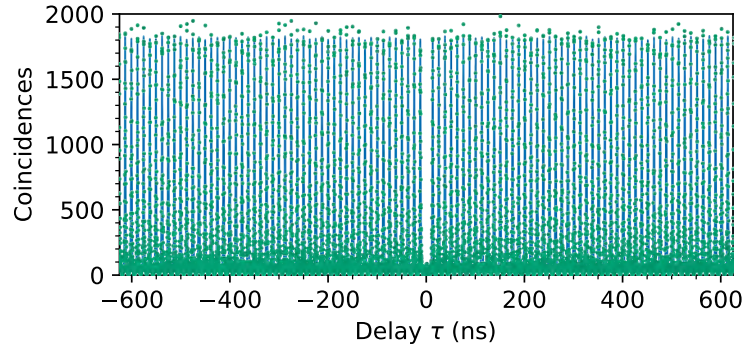


Figure A.29: The time-bin histogram and fit of the autocorrelation function of equation A.31 assuming $\beta_c = 1$. Goodness of fit: $\chi_{\text{red}}^2 = 1.46$ over 9765 data points.

In the second step, the pulse repetition rate and pulse shape estimates are used to determine the background-corrected number of photodetection events of all peaks

Parameter	Value
g_0	$80(4) \times 10^2$
g_∞	$2.324(4) \times 10^3$
T_1	$3.917(39) \times 10^2$ ps
τ_0	$2.3(7) \times 10^1$ ps
τ_{rep}	$1.249\,944\,5(24) \times 10^1$ ns
σ	$2.643(21) \times 10^2$ ps
g_{bgr}	$1.291(14) \times 10^1$
g_L	$5.51(14) \times 10^1$
$\tau_{0,L}$	$4.342(4)$ ns
Δ_L	$19.3(7)$ ps

Table A.6: Multi-peak fit results ($N_{\text{sp}} = 50$) of the data shown in figure 9.3 with the model given by equation A.31.

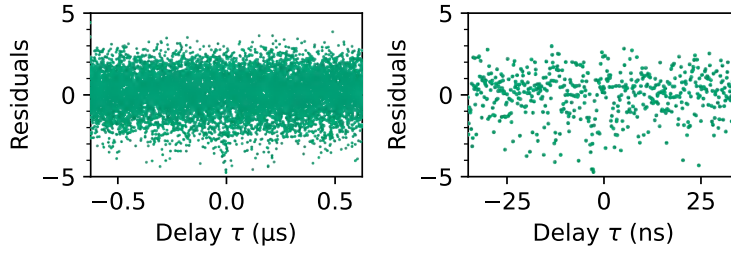


Figure A.30: Autocorrelation fit (equation A.31) residuals of the fit shown in figure A.29. The goodness of fit is $\chi_{\text{red}}^2 = 1.46$

in the full time-bin histogram width of $\pm 50 \mu\text{s}$. The blinking parameters β_c , and τ_c are determined, taking all peaks in the $50 \mu\text{s}$ time-bin histogram into account. The background-corrected photodetection events in the temporal region of $\pm 3T_1$ around the center of each peak are determined, and the blinking parameters are extracted by least-square curve fitting of equation A.27 with the Levenberg–Marquardt algorithm. The fit yields $\beta_c = 0.981(6)$ and $\tau_c = 34(13) \mu\text{s}$ with a goodness of fit of $\chi_{\text{red}}^2 = 1.21$.

Single-Photon Purity Estimation

The background-corrected central peak area \mathcal{G}_0 and the uncorrelated peak area \mathcal{G}_∞ are obtained from

$$\mathcal{G}_{0/\infty} = \int_{-\tau_{\text{rep}}/2}^{-\tau_{\text{rep}}/2} d\tau \frac{g_{0/\infty}}{\beta_c} \exp\left(-\frac{|\tau|}{T_1}\right) \otimes \frac{1}{\sigma\sqrt{2\pi}} \exp\left(-\frac{\tau^2}{2(\sqrt{2}\sigma)^2}\right). \quad (\text{A.32})$$

The integrals are calculated numerically by trapezoidal rule based on the parameter estimation in table A.6. The error on the peak area is estimated numerically by

propagating the statistical errors σ_{x_i} of all fitted parameters x_i in table A.6 via the covariance matrix $cov(x_i, x_j)$ of the fit:

$$\sigma_{\mathcal{G}_{0/\infty}}^2 = \sum_i \sum_j \frac{\partial \mathcal{G}_{0/\infty}}{\partial x_i} \frac{\partial \mathcal{G}_{0/\infty}}{\partial x_j} cov(x_i, x_j), \quad (\text{A.33})$$

where the partial derivative $\frac{\partial \mathcal{G}_{0/\infty}}{\partial x_i}$ is approximately:

$$\frac{\partial \mathcal{G}_{0/\infty}}{\partial x_i} \approx \frac{\Delta \mathcal{G}_{0/\infty}}{\Delta x_i} = \frac{\mathcal{G}_{0/\infty}(x_i + \sigma_{x_i}) - \mathcal{G}_{0/\infty}(x_i)}{\sigma_{x_i}}. \quad (\text{A.34})$$

The single photon purity, is

$$g^{(2)}(0) = \frac{\mathcal{G}_0}{\beta_c \mathcal{G}_\infty} = 0.0346(22). \quad (\text{A.35})$$

A.VIII EXPERIMENTAL DETAILS FOR CONTINUOUS-WAVE RESONANCE FLUORESCENCE

This section is supplementary to chapter 8.

Data Acquisition

Experimentally, the photoluminescence signal is extracted from the photo-detection rate on the detector $\dot{c}_{\text{D,raw}}^{(i,j)} = \dot{c}_{\text{D,raw}}^{(i,j)}(U_{\text{B}} = U_i, P_{\text{L}} = P_j)$ of every bias voltage U_i and power P_j combination, sampled for $t_{\text{int}} = 1$ s. For each sample, $\dot{c}_{\text{D,raw}}^{(i,j)}$ the laser background $\dot{c}_{\text{D,ref}}^{(i,j)} = \dot{c}_{\text{D,ref}}^{(i,j)}(U_{\text{B}} = 0 \text{ V}, P_{\text{L}} = P_j)$ is estimated by turning the QD out of resonance. The laser background-corrected fluorescence rate is then estimated by

$$Y_{\text{D}}^{(i,j)} = \dot{c}_{\text{D,raw}}^{(i,j)} - \dot{c}_{\text{D,ref}}^{(i,j)} \quad (\text{A.36})$$

A.VIII.1 Resonant fluorescence of $|X_h\rangle$

The background corrected photoluminescence rate for resonant excitation of the state $|X_h\rangle$ is shown in figure A.31.

The mathematical model is described in chapter 3. However, the spectra shown in figure 8.1 already indicate deviations from the expectation of Voigt profiles due to an approximately 30 mV wide feature. This feature is comparatively low in amplitude but shows excitation wavelength dependencies. For an excitation wavelength of $\lambda_{\text{L}} = 797.337\ 30(2)$ nm the broad feature is asymmetric with brighter fluorescence for blue-detuned excitation (lower bias voltage) as expected for a phonon-sideband excitation mechanism at low temperatures [339]. However, for $\lambda_{\text{L}} = 797.000\ 00(2)$ nm it is still well visible while the QD's line has lost most of its intensity. Without further study, the mechanism behind this feature cannot be understood. However, for the characterization of the lineshape near the centers of the charge-plateaus ($\lambda_{\text{L}} \geq 797.625\ 40(2)$ nm), this feature is relatively small and can be modeled as a constant background the due to its symmetry.

To translate the bias voltage U_{B} into the corresponding frequency scale, the voltage sweep of the emission spectrum under p -shell excitation shown in figure 7.3 is reused. A voltage-to-DC-Stark-frequency-shift conversion function is obtained by performing a quadratic fit, shown in figure A.32.

At $U_{\text{B}} = 1.375$ V, the DC-stark tuning strength is μ_{DCS} defined as resonant frequency shift Δf_{DCS} per bias voltage change ΔU_{B} can be interpolated with $\mu_{\text{DCS}} = 6.457(5)$ GHz/mV. The voltage-to-frequency conversion function is completed by taking the resonant excitation laser frequency for the bias voltage $U_{\text{B}} = 1.375$ V into account, as measured by the Wavemeter. This limits the absolute frequency conversion error to the QD linewidth.

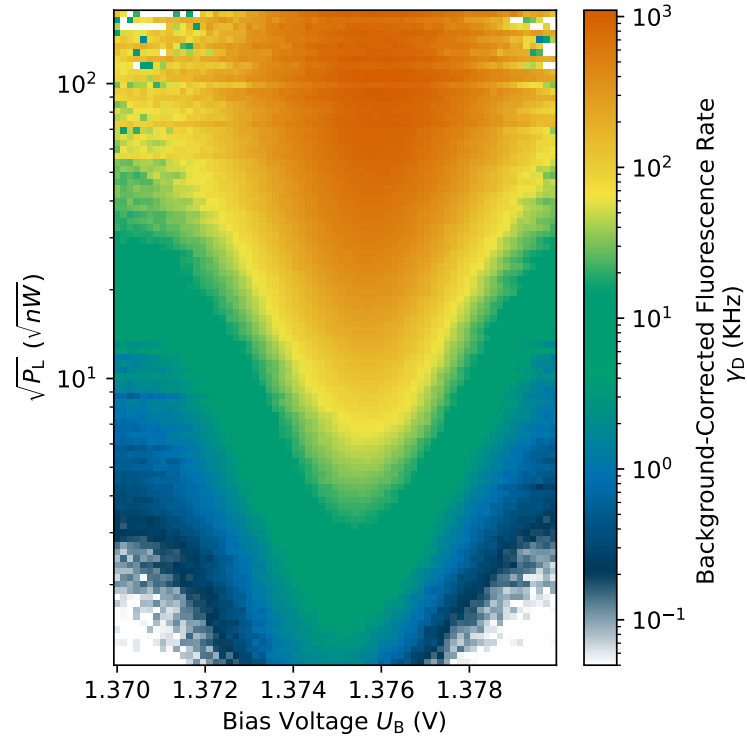


Figure A.31: Background corrected photoluminescence rate as function of excitation laser amplitudes \sqrt{P} and the bias voltage (U_B). The excitation wavelength is $\lambda_L = 797.625\ 40(2)$ nm and the integration time $t_i = 1$ s.

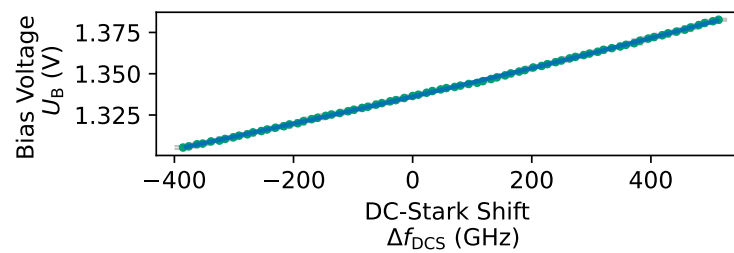


Figure A.32: Voltage-to-DC-Stark-frequency-shift conversion function relative to the resonance frequency at ($U_B = 1.375$ V) obtained from the evaluation of the voltage sweep of the emission spectrum under p -shell. The blue line is a quadratic fit.

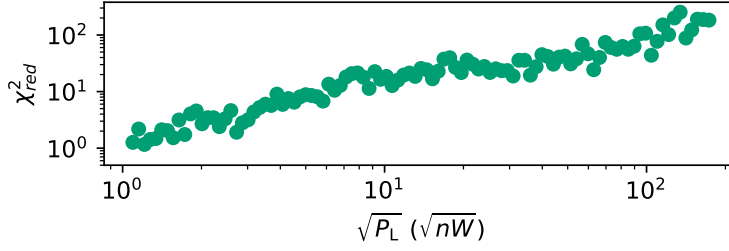


Figure A.33: Fit residuals of figure 8.4 b). Discussion in the main text.

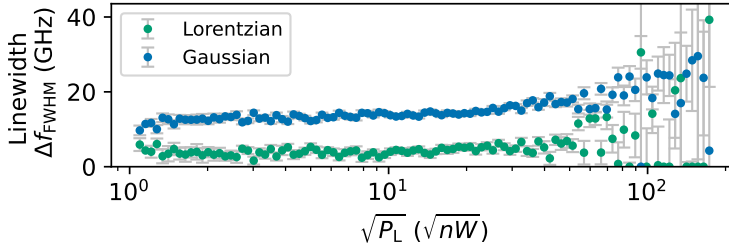


Figure A.34: Gaussian and Lorentzian linewidth contributions to the fit in figure 8.4 b), reflecting the contribution of inhomogeneous broadening. Discussion in the main text.

Electronic Noise in Resonance Fluorescence Experiments

This section discusses the electronic source measure unit readings during the experiment shown in figure 8.2. The electronic setup is described further in section A.VIII. The voltage and current are sampled 10 times for every voltage and power setting (U_i, P_j) . Figure A.35 shows the mean voltage offset $U_{B,off}$ defined as the pointwise difference of the set voltage $U_{B,set}^{(i,j)}$ and the voltage read back $U_{B,read}^{(i,j)}$ at the low noise filter:

$$U_{B,off} = U_{B,set} - U_{B,read} \quad (\text{A.37})$$

where (i, j) denotes the voltage setting of index i and power setting of index j . The steps seen in the voltage offset $U_{B,off}$ along the voltage axis reflect the resolution limit of the voltage source. All values are within a $30 \mu\text{V}$ peak-peak range ⁽⁶⁾. A voltage resolution of $30 \mu\text{V}$ is equivalent to a DC-stark shift of the QDs resonance frequency of approximately 186 MHz (see section 7.3). A voltage resolution of $30 \mu\text{V}$ may limit a linewidth estimation of a near-transform limited QD with similar lifetimes (see section 7.4). However, the linewidths observed are more than an order of magnitude larger than the voltage resolution limitation. Figure A.36 shows the standard deviation $\sigma_{U_{B,off}}$ of the 10 samples of the voltage offset $U_{B,off}$. The standard

(6) Equivalent to $2.2 \cdot 10^{-5}$ relative voltage setting error

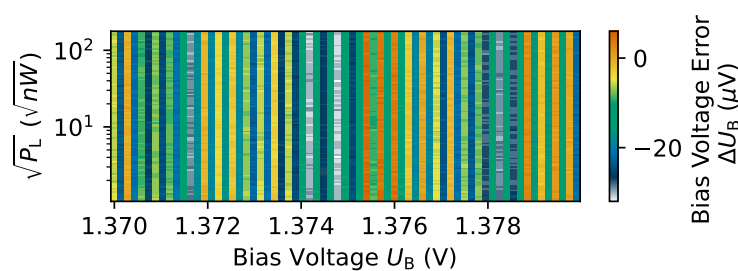


Figure A.35: Mean voltage offset $U_{B,\text{off}}$ (10 samples) of the resonant excitation voltage-power scan shown in figure 8.2.

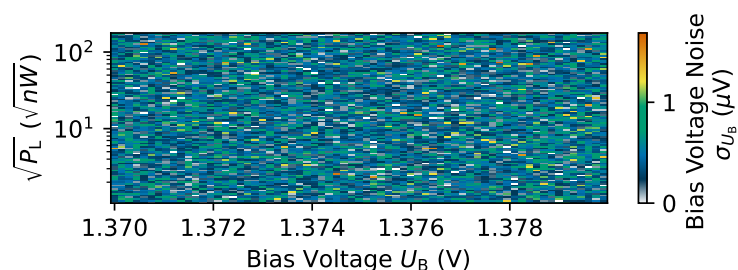


Figure A.36: Standard deviation of the voltage offset $\sigma_{U_{B,\text{off}}}$ (10 samples) of the resonant excitation voltage-power scan shown in figure 8.2.

deviation of the voltage offset is below $2\ \mu\text{V}$. The voltage fluctuations are 3 orders of magnitude too small to cause voltage noise-induced spectral diffusion comparable with the observable broadening of Gaussian lineshape. The laser-induced electrical current readings $I_{\text{ind}}^{(i,j)}$, defined as the electrical currents readings $I_{\text{raw}}^{(i,j)}$ relative to the electrical current with the excitation laser off $I_{\text{dark}}^{(i)}$

$$I_{\text{ind}}^{(i,j)} = I_{\text{raw}}^{(i,j)} - I_{\text{dark}}^{(i)} \quad (\text{A.38})$$

is shown in figure A.37. By increasing the laser power, no significant increase in the electrical current is observable. The fluctuations of the electrical currents are of the same order as the standard deviation of the electrical current measurements of each voltage and power setting $\sigma_{I_{\text{raw}}}^{(i,j)}$.

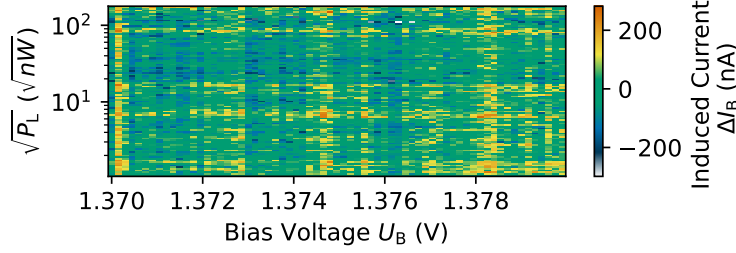


Figure A.37: Mean laser-induced electrical current $I_{\text{ind}}^{(i,j)}$ (10 samples) of the resonant excitation voltage-power scan shown in figure 8.2.

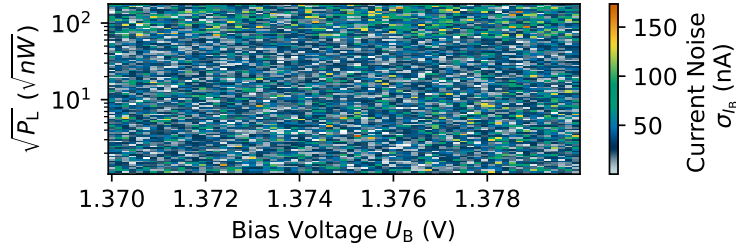


Figure A.38: Standard deviation of the electrical current readings $\sigma_{I_{\text{raw}}}^{(i,j)}$ (10 samples) of the resonant excitation voltage-power scan shown in figure 8.2.

A.VIII.2 Resonant fluorescence of $|X_l\rangle$

The raw photoluminescence rate for resonant excitation of the state $|X_l\rangle$ is shown in figure A.39.

The data evaluation is analogous to the abovementioned state $|X_h\rangle$. The background corrected photoluminescence rate for resonant excitation of the state $|X_l\rangle$ is shown in figure A.40.

To translate the bias voltage U_B into the corresponding frequency scale, the voltage sweep of the emission spectrum under p -shell excitation shown in figure 7.3 is reused, analogous to the approach described for the evaluation of the high-energy state above. A voltage-to-DC-Stark-frequency-shift conversion function is obtained by performing a quadratic fit, shown in figure A.41.

At $U_B = 1.342$ V, the DC-stark tuning strength is μ_{DCS} defined as resonant frequency shift Δf_{DCS} per bias voltage change ΔU_B can be interpolated with $\mu_{\text{DCS}} = 11.62(4)$ GHz/mV.

A full voltage-to-frequency conversion function is obtained by taking the resonant excitation laser frequency for the bias voltage $U_B = 1.342$ V into account, as measured by the Wavemeter.

Examples of Voigt-line profile fits are shown in figure A.42.

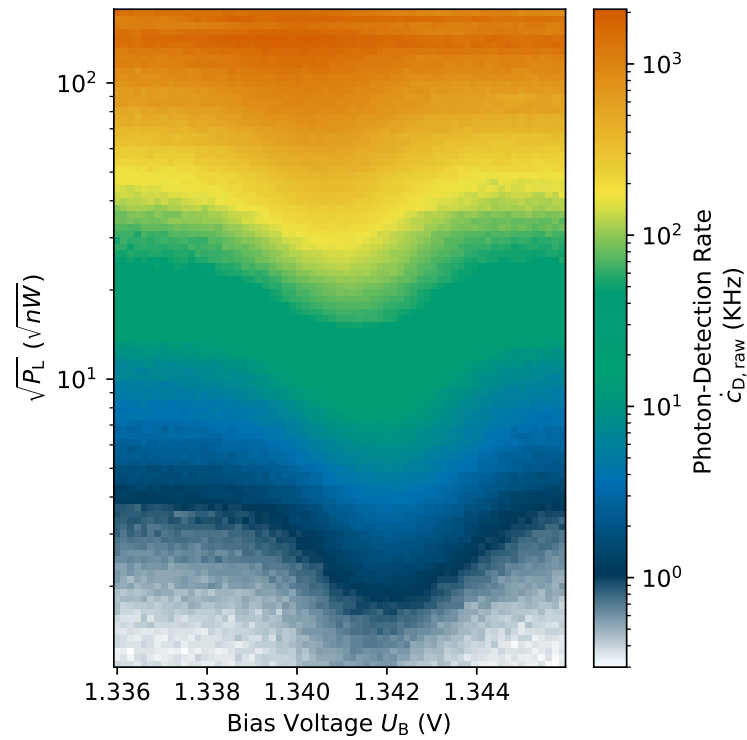


Figure A.39: Raw photoluminescence rate as function of excitation laser amplitudes \sqrt{P} and the bias voltage (U_B). The excitation wavelength is $\lambda_L = 797.625\ 40(2)$ nm and an the integration time $t_i = 1$ s.

The fit residuals of figure 8.5 b) are shown in figure A.43 and the Gaussian and Lorentzian linewidth contributions are shown in figure A.44. Both are discussed in the main text.

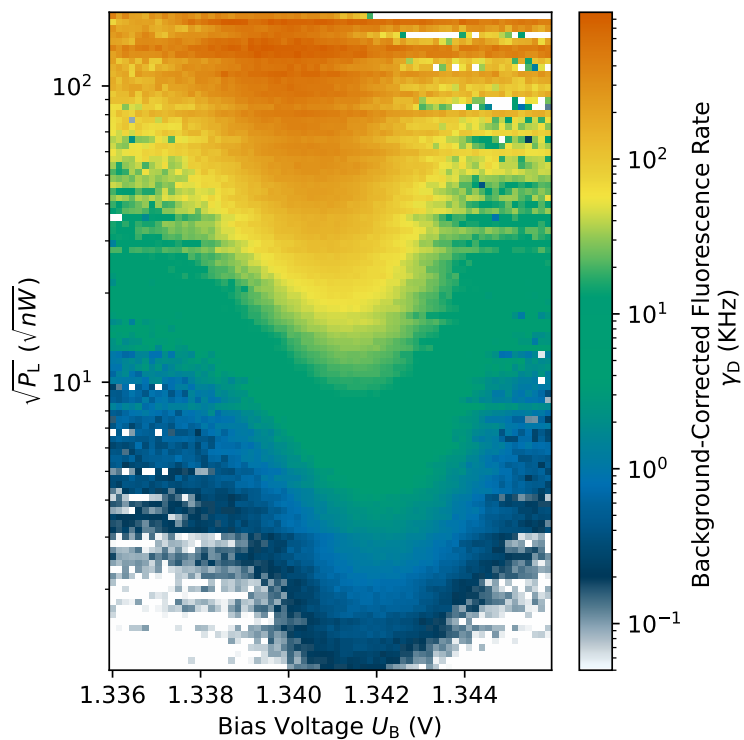


Figure A.40: Background corrected photoluminescence rate as function of excitation laser amplitudes \sqrt{P} and the bias voltage (U_B). The excitation wavelength is $\lambda_L = 797.625\,40(2)$ nm and an the integration time $t_i = 1$ s.

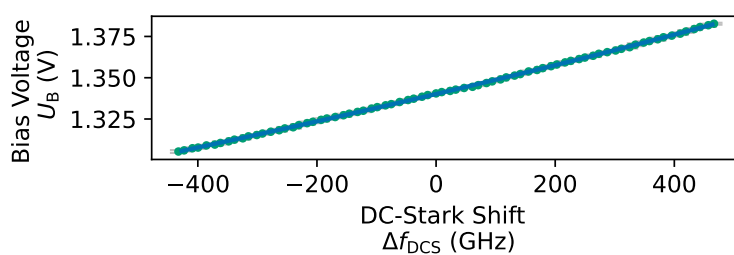


Figure A.41: Voltage-to-DC-Stark-frequency-shift conversion function relative to the resonance frequency at ($U_B = 1.342$ V) obtained from evaluation of the voltage sweep of the emission spectrum under p -shell. The blue line is a quadratic fit.

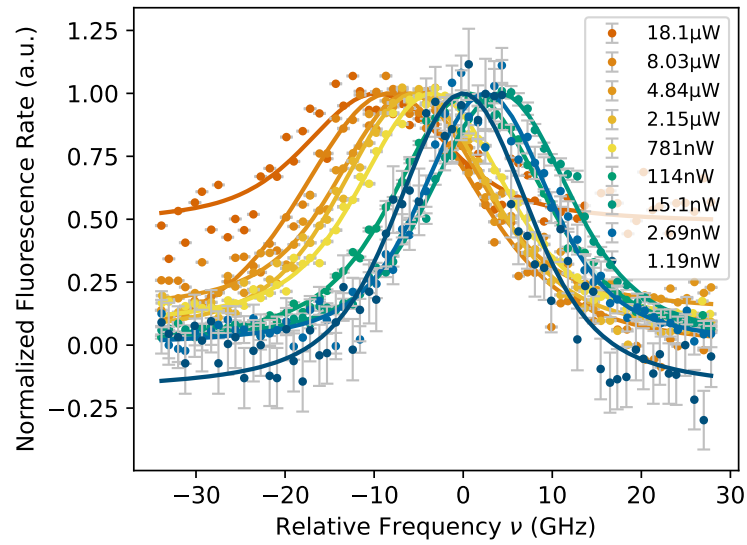


Figure A.42: Examples of background-subtracted normalized photoluminescence rate for various powers and their line fits.

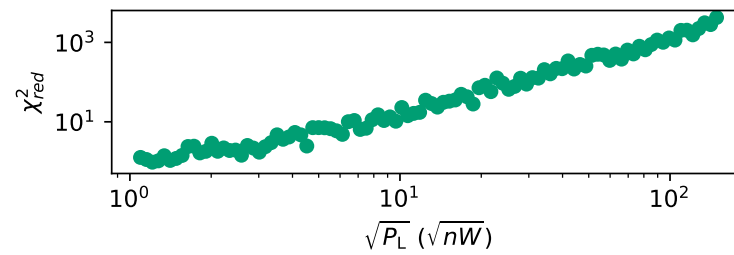


Figure A.43: Fit residuals of figure 8.5 b). Discussion in the main text.

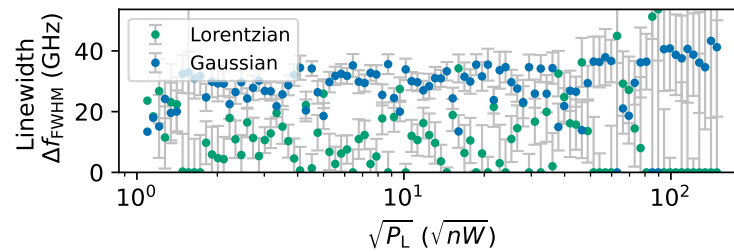


Figure A.44: Gaussian and Lorentzian linewidth contributions to the fit in figure 8.5 b), reflecting the contribution of inhomogeneous broadening. Discussion in the main text.

A.IX BAND GAP TEMPERATURE TUNING

Figure A.45 shows the shift of the resonance frequency of QD2 in the W_1 waveguide $W_{1,260,35}^{(3,5)}$ as a function of the cryostat's sample stage thermometer temperature reading for various sample stage temperatures between $T_{\text{SMP}} = 5.2$ K and $T_{\text{SMP}} = 34$ K.

The data is obtained with the spectrometer using sub-saturation quasi-resonant excitation and fitting for each temperature a Voigt profile to extract the resonance frequency. At low temperatures, the spectrometer resolution is limiting, while a reduced signal-to-noise ratio is limiting for higher temperatures.

In figure A.45 two predictions of the temperature-induced resonance frequency shift, based on the band gap tuning, are shown. The dashed line assumes literature parameters for bulk material, i.e. without doping and nanostructuring [340]. The dashed line assumes parameters for a comparable platform of InGaAs quantum dots in a PhCW [184].

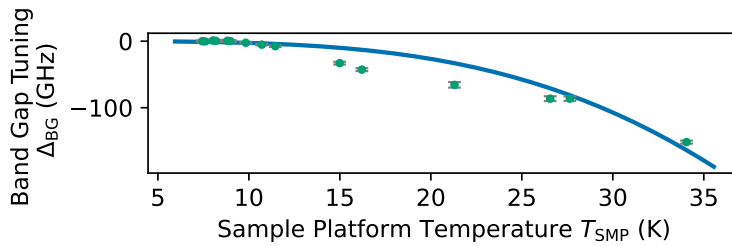


Figure A.45: shift of the resonance frequency of QD2 in the W_1 waveguide $W_{1,260,35}^{(3,5)}$ as a function of the cryostat's sample stage thermometer temperature reading T_{SMP} . The solid line shows a prediction based on a measurement of a similar platform [184] and the dashed line a prediction based on parameters found for bulk material, i.e. without doping and nanostructuring [340].

Both models, along with a general fit of Varshni's law [341] fail to describe the experimental data, even when allowing for a free temperature offset between the system and the sample stage thermometer. This shows that in contrast to bulk samples [342], a temperature estimation of the phonon bath of this sample based on the band gap tuning is not feasible. Both an accurate model for the given nanostructure and the model for the non-trivial temperature variation between the sample thermometer and the sample need to be included. However, in the cryostat in which the experiments were performed in, the temperature variation between the sample and thermometer might be particularly high since the cryostat's microscope is not thermally anchored to the heat shield, and the sample may be exposed to high thermal radiation.

A.X π -PULSE CHARACTERIZATION

The power of a π -pulse is estimated by performing a phenomenological quadratic fit at the first maximum in the photoluminescence.

$$y = a_{\text{Rabi},\pi}x^2 + b_{\text{Rabi},\pi}x + c_{\text{Rabi},\pi}, \quad (\text{A.39})$$

where $x = \sqrt{P_L}$ is the square root of the excitation laser power on the sample.

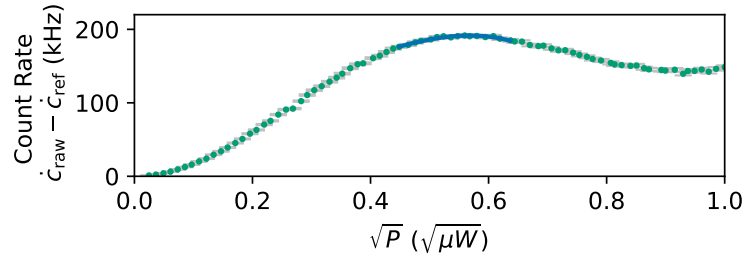


Figure A.46: Quadratic fit on the photoluminescence as function of the excitation laser power on the sample.

The fit yields $a_{\text{Rabi},\pi} = -1.025(70)$, $b_{\text{Rabi},\pi} = 660(40)$, and $c_{\text{Rabi},\pi} = 84(6)$ with a fit goodness of $\chi_{\text{red}}^2 = 1.86$.

A.XI HONG–OU–MANDEL INTERFEROMETRY

This section is supplementary to chapter 9.

Experimental Setup

Figure A.47 shows a schematic of the Hong–Ou–Mandel interferometer. The input polarization is adjusted for transmission through the first polarizing beam splitter PBS_1 with a stress-induced birefringence polarization controller. The polarizing beam splitter PBS_1 transforms unwanted polarization fluctuations in the input to count rate fluctuations which otherwise would cause a drop in visibility. The first half wave plate HWP_1 balances the interferometer via PBS_2 . The second half-wave plate HWP_2 is motorized to allow for a change between the polarization configuration for two-photon interference (collinear polarization) and reference (transverse polarization) measurement. The mirror pair M_1 and M_2 (M_3 and M_4) fiber couple the input into the port FP_2 (FP_3). Mirror M_4 is mounted on a Piezo and allows for the characterization of the interferometer’s visibility with a continuous wave laser as input.

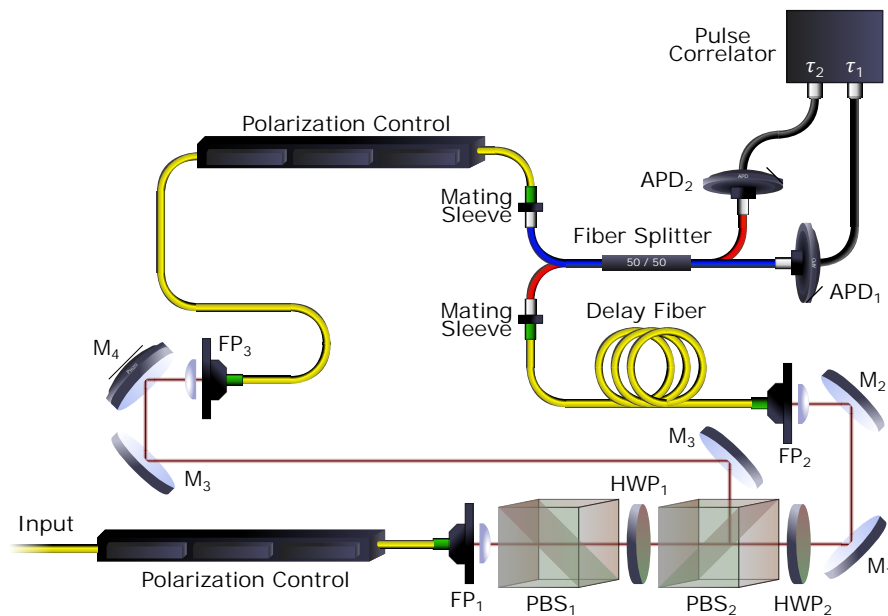


Figure A.47: Schematic of the Hong–Ou–Mandel interferometer setup. A legend can be found in figure A.16.

A second polarization controller in the path of fiber port FP_3 ensures collinear polarization of both interferometer’s arms. The delay fiber in the arm of fiber port FP_2 , in combination with a linear translation stage, matches the repetition rate of the pulsed laser with the propagation time difference of the two arms of the interferometer. Consequently, the two paths are coupled into a balanced fiber

beam splitter. The fiber beam splitter's outputs are connected to the fiber-coupled avalanche photodiode detectors APD₁ and APD₂. The detectors' signals are time-tagged with a pulse correlator.

The path difference of the interferometer is aligned with the pulsed laser⁽⁷⁾ directly coupled into the input. The temporal overlap is verified by the insertion of the pulsed excitation laser, which has a full-width half-maximum pulse width of approximately 6.8 ps which is much shorter than the lifetime of a quantum dot. The precision is limited by the pulse correlator's time resolution of 4 ps and the pulse laser's pulse width of approximately 6.8 ps full-width half maximum. The setup's polarization controllers are aligned with a continuous wave laser and laser frequency modulation. When inserting a narrow-band continuous wave laser⁽⁸⁾ the interferometer's visibility exceeds 99 % in the collinear configuration and below 1 % in the transverse configuration with stability in the timescale of several hours.

A.XI.1 Modeling and Evaluation

This section provides further details about the model and the data evaluation method of the Hong–Ou–Mandel interferometry (HOM) of section 9.3.

For periodic pulsed excitation, the region of temporal coincidence $\tau = t_0$ the second-order cross-correlation time-bin histogram of the two detectors of a HOM experiment is⁽⁹⁾ for collinear polarization (\parallel) and non-zero pure-dephasing ($\gamma_{\text{dp}} > 0$) [91, 328]:

$$H_{0,\parallel}(\tau) = h_0 \exp\left(-\frac{|\tau - t_0|}{T_1}\right) \left(1 - \exp\left(-2\gamma_{\text{dp}}|\tau - t_0|\right)\right), \quad (\text{A.40})$$

where T_1 is the quantum dot's lifetime, and h_0 is a normalization for the radiative decay rate and the histogram's integration time. For transverse-polarization of (\perp) the two consequent emitted photons do not interfere and the second-order cross-correlation time-bin histogram of the two detectors in the region of temporal coincidence is:

$$H_{0,\perp}(\tau) = h_0 \exp\left(-\frac{|\tau - t_0|}{T_1}\right). \quad (\text{A.41})$$

For uncorrelated photons, i.e., photons that are not from consequent laser pulses, the second-order cross-correlation time-bin histogram is

$$H_{\infty}(\tau, t_c) = h_{\infty} \exp\left(-\frac{|\tau - t_c|}{T_1}\right), \quad (\text{A.42})$$

where $h_{\infty} = 2h_0$ [328], and t_c is the center of the time-bin histogram peak. The first time-bin histogram peak on each side of the central peak of coinciding photodetection events (index $n = \pm 1$) are separated in the analysis, as they are partially

(7) Tsunami, see section A.IV.3.

(8) DL Pro, see section A.IV.3.

(9) Assuming ideal spectral, spatial, and temporal overlap.

correlated [285] and differ in their amplitude $h_{\pm 1} \neq h_{\infty}$. The function for the n th-peak of the second-order cross-correlation the time-bin histogram peaks is then:

$$H_n^{(\perp/\parallel)}(\tau) = \begin{cases} H_{0,\perp/\parallel}(\tau - t_0) & \text{if } n = 0, \\ h_1 \exp\left(-\frac{|\tau - t_0 - nt_{\text{rep}}|}{T_1}\right) & \text{if } n = \pm 1, \\ H_{\infty}(\tau, t_c = t_0 - nt_{\text{rep}}), & \text{otherwise,} \end{cases} \quad (\text{A.43})$$

where t_{rep} is the laser repetition rate. Taking the detectors time jitter σ and a constant background h_{bgr} into account, the model function for the polarization configuration \perp/\parallel finally is:

$$H^{(\perp/\parallel)}(\tau) = \sum_{n=-N_{\text{sp}}}^{N_{\text{sp}}} H_n^{(\perp/\parallel)}(\tau) \otimes \frac{1}{\sigma\sqrt{2\pi}} \exp\left(-\frac{\tau^2}{2(\sqrt{2}\sigma)^2}\right) + h_{\text{bgr}}, \quad (\text{A.44})$$

where \otimes denotes a convolution. To obtain the normalization constants h_{∞} and h_0 , the second-order cross-correlation the time-bin histogram peaks of index n until an index of $\pm N_{\text{sp}}$ are evaluated for both polarization configurations (\parallel/\perp).

Data Evaluation of Spectrally Unfiltered HOM Experiment

The outcome of a multi-peak least-square curve fitting with the Levenberg–Marquardt algorithm of the model given by equation A.44, including the peaks up to index $N_{\text{sp}} = 10$, is summarized in table A.7 for the data-sets of transverse (\perp) and collinear polarization (\parallel).

The pure dephasing rate is $\gamma_{dp} = 78_{-37}^{+116}$ GHz. The imprecision of the pure dephasing estimate reflects the HOM experiment's insensitivity in the presence of pure dephasing comparable with the optical decay rate. The heights of h_{∞} for each polarization configuration allow normalizing and comparing the central peak area \mathcal{A}_{\parallel} and \mathcal{A}_{\perp} .

The background corrected collinear- (transverse-) polarized center peak area \mathcal{A}_{\parallel} (\mathcal{A}_{\perp}) is calculated numerically by trapezoidal rule from the background-corrected fit functions. The error on the peak area is estimated numerically by propagating the statistical errors σ_{x_i} of all fitted parameters x_i in table A.7, γ_{dp} , and H_0 via the covariance matrix $\text{cov}(x_i, x_j)$ of the fit:

$$\sigma_{\mathcal{A}_{\parallel/\perp}}^2 = \sum_i \sum_j \frac{\partial \mathcal{A}_{\parallel/\perp}}{\partial x_i} \frac{\partial \mathcal{A}_{\parallel/\perp}}{\partial x_j} \text{cov}(x_i, x_j), \quad (\text{A.45})$$

where the partial derivative $\frac{\partial \mathcal{A}_{\parallel/\perp}}{\partial x_i}$ is approximately:

$$\frac{\partial \mathcal{A}_{\parallel/\perp}}{\partial x_i} \approx \frac{\Delta \mathcal{A}_{\parallel/\perp}}{\Delta x_i} = \frac{\mathcal{A}_{\parallel/\perp}(x_i + \sigma_{x_i}) - \mathcal{A}_{\parallel/\perp}(x_i)}{\sigma_{x_i}}. \quad (\text{A.46})$$

Configuration	Parameter	Value
⊥	h_∞	$1.968(14) \times 10^3$
∥	h_∞	$1.967(14) \times 10^3$
⊥	h_1	$1.507(20) \times 10^3$
∥	h_1	$1.529(22) \times 10^3$
⊥	h_{bgr}	7.8(3)
∥	h_{bgr}	7.8(3)
⊥	t_0	2(3) ps
∥	t_0	-4(3) ps
⊥	t_{rep}	12.5001(6) ns
∥	t_{rep}	12.4992(6) ns
⊥	T_1	794(5) ps
∥	T_1	800(5) ps
⊥	σ	228(11) ps
∥	σ	219(12) ps

Table A.7: Multi-peak fit results of the far-off peaks of the data shown in figure 9.6 with the model given by equation A.44. The symbol ⊥ denotes the transverse polarization configuration while ∥ denotes the collinear polarization configuration.

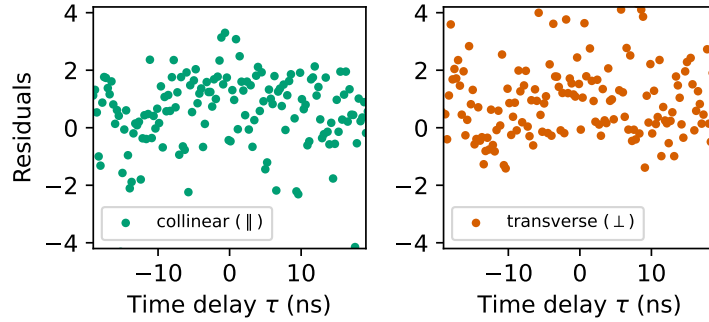


Figure A.48: Residuals of the center regions of a multi-peak least-square curve fitting with the Levenberg–Marquardt algorithm of the data shown in figure 9.6 with the model given by equation A.44 for both data-sets (transverse and collinear polarization) with the fit parameters in table A.7.

The re-normalized center peak areas are finally $\mathcal{A}_\perp = 0.500(7)h_\infty$ and $\mathcal{A}_\parallel = 0.496(10)h_\infty$. The over all fit-quality for the transverse polarized (collinear polarized) configuration is $\chi_{\text{red}}^2 = 1.68$ ($\chi_{\text{red}}^2 = 1.64$). The residuals of both fits for the center region is shown in figure A.48.

LIST OF FIGURES

- Fig. 2.1 Figure a) shows a scanning tunneling microscope image of a Stranski-Krastanov InGaAs QD, grown on GaAs. Image from [87]. Figure b) shows schematics of the growth process of droplet-epitaxy grown GaAs QDs, adapted from [88]: (i) Al is deposited under low arsenic pressure, forming droplets on the surface of the AlGaAs substrate; (ii) dissolution of As from the substrate and concurrent (iii) diffusion of Al into the substrate; (iv) high in-plane symmetry nanoholes etched into the AlGaAs substrate; (v) overgrown with GaAs; (vi) capping with AlGaAs. Figures c) and d) show the cross-section and top view of an AFM image of a droplet-epitaxy-grown GaAs QD. These images are from [40]. In figure c), the color scale reflects the local surface inclination (white for flat areas and black for maximal inclination). The aspect ratio is set to 17 to highlight the shape of the etched hole. 6
- Fig. 2.2 Schematics of the structural properties of Stranski-Krastanov-grown InGaAs QDs and droplet-epitaxy grown GaAs QDs. The confinement potentials, where dark, neutral, and bright gray indicate AlGaAs, GaAs, and InAs are shown in figure a) for Stranski-Krastanov-grown InGaAs QDs and b) for droplet-epitaxy grown GaAs QDs. Schematics of the electron and hole wave functions are shaded blue and red oval. The wave functions along the growth axis \hat{z} are shown in figure c) for Stranski-Krastanov-grown InGaAs QDs and d) for droplet-epitaxy grown GaAs QDs. For Stranski-Krastanov QDs, the electron and hole wavefunctions have a significant offset in their center of mass, due to an asymmetric confinement potential a pyramidal shape [112]. In contrast to unstrained GaAs QDs, the materials intermix significantly during growth, leading to strain that varies throughout the QD. 8

- Fig. 2.3 The lowest-energy confined states in QDs and their transitions. The full (empty) circles indicate the electron (hole) configuration in the conduction (valence) band s shells of the QD. The pseudospin states are discussed in the main text. The biexciton decays to one of the two bright exciton states by emission of a horizontally (H , green) or vertically (V , yellow) polarized photon. The negative (positive) trion decays to a single electron (hole) by emission of circularly polarized light with the helicity depending on the total electric charge state. Furthermore, spin-flip processes (dashed arrows) couple bright and dark excitons. Non-radiative processes (gray arrows) are generally present and can for some transitions be dominant [115,123,125]. Here, only the non-radiative decays of the bright excitons are indicated explicitly. The ordering of the states in the figure follows the occupancy, while the emission energies of the radiative excitonic complexes depend not only on the occupancy but also on confinement, correlation effects and manipulation Zeeman- and Stark-effect [5]. Figure adapted from [5]. 11
- Fig. 2.4 Examples of excitonic level schemes in QDs of relevance for quantum-optics experiments. (a) Fundamental three-level optical transition scheme of a single bright exciton, here $|X_b\rangle$, that can emit a photon by decaying radiatively to the ground state $|g\rangle$. Also non-radiative decay processes and coupling to the corresponding dark exciton state $|X_d\rangle$ through spin-flip processes may occur. The dark state can also re-combine nonradiatively. This level scheme leads to a biexponential decay of the emitted intensity. Figure adapted from [5]. 12
- Fig. 3.1 Schematic of a planar nanophotonic device often investigated in this thesis. A QD (green dot) embedded in the guided mode region of a line-defect (W_1) photonic crystal waveguide, emits photons into the guided mode. The emitted photons are routed in-plane by nanobeam waveguides (NBWs) towards shallow-etch grating (SEG) chip-to-fiber couplers, where they are scattered quasi-orthogonal out of plane. The photons are collected by a microscope objective and fiber coupled by free-space optics. The devices are aligned to the crystallographic axes of the membrane, such that the dipole orientations are oriented along with x and y . In chapter 4, topological photonic crystal waveguides in place of the W_1 waveguide are investigated. 18

- Fig. 3.2 The excited state population ρ_{ee} of the steady state solutions of the Maxwell-Bloch equations for continuous-wave excitation for various pure dephasing rate Γ_{dp} . a) The dependence of the laser frequency detuning $\Delta = \omega_L - \omega_0$ for weak excitation $\Omega \ll \Gamma$, showing a Lorentzian lineshape. b) The Rabi frequency area dependence Ω^2 (normalized excitation intensity) of the steady state solutions for zero detuning ($\Delta = 0$). 27
- Fig. 3.3 The saturation parameter S and the full-width-half-maximum linewidth (FWHM) Δ_{FWHM} of the steady state solutions of the Maxwell-Bloch equations for continuous-wave excitation for various pure dephasing rate Γ_{dp} for zero detuning ($\Delta = 0$). a) The saturation parameter S as a function of the Rabi frequency area Ω^2 . b) The FWHM linewidth Δ_{FWHM} as function of the saturation parameter. 28
- Fig. 4.1 Schematic of a topological photonic insulator and crystal waveguides based on a photonic Quantum Valley-Hall effect analogon. Figure a) shows three unit cells (with lattice constants a_1, a_1) of a photonic insulator of non-trivial Valley-Chern number. The inversion symmetry of the unit cells is broken due to non-identical circular hole radii within the unit cell. Figure b) shows non-identical equilateral triangles as an alternative for elements in the unit cell. Figure c) shows the unit cell of a shamrock pattern, consisting of three overlapping holes of radii r_s , and a single circular hole of radius r_c . The photonic topological insulators' configuration as a bearded-type interface and zig-zag-type interfaces are shown in Figures d) and e). Three unit cells of each distinct photonic topological insulator (blue/green) are highlighted in black, whereas the interface is highlighted in red. The one-dimensional supercell of the waveguides is highlighted in yellow. The zig-zag-type interface features an inversion symmetry at the interface. The bearded-type interface has a glide-plane-like symmetry [17]. 33
- Fig. 4.2 Schematic of a BIW device with mode adapter to a nanobeam waveguide (NBW) [75]. The two distinct photonic topological insulators are highlighted in blue and green, and their interface is highlighted as a solid red line. Two solid black lines and blue/green shading marks a single supercell of the one-dimensional waveguide. For mode adaptation to a NBW, the first row of shamrocks is removed in the adapter section (over eight supercell columns), highlighted in red. The NBW routes the guided mode to shallow etch grating (SEG) fiber-to-chip couplers [162]. 34

- Fig. 4.3 Scanning electron microscope images of a photonic device with a topological PhCW. Figure a) shows a bird-eye image of a full photonic device. The device consists of two polarizing SEG fiber-to-chip couplers (shown in b), NBWs to connect the couplers with mode adapters (shown in c), and a topological PhCW. Figures d) and e) show a zoom into the topological interface of a bearded and a zig-zag-type. The interface is highlighted as a dashed red line, and a unit cell of each distinct topological insulator is highlighted in blue and green. 35
- Fig. 4.4 Schematic of the optical setup. The sample is installed in the cryostat. All free-space optics and the microscope objective are mounted onto an open-loop X - Y stage to characterize and compare different photonic devices without requiring optical realignment. Polarizing beam splitters (PBS), half-wave plates (HWP), and quarter-wave plates (QWP) control the input polarization and filter the excitation laser from the collected signal. The optical collection and photonic characterization input path match the output mode diameter from an SEG fiber-to-chip coupler. 36
- Fig. 4.5 Laser transmission of three photonic devices. Green (red) shows the transmission of a device with a $L \approx 13 \mu\text{m}$ long topological PhCW section based on a bearded-type (zig-zag-type) interface. The photonic crystal parameters are $a = 280 \text{ nm}$, $r_s = 35 \text{ nm}$, and $r_c = 55 \text{ nm}$. Blue shows the transmission of the photonic reference device where the topological waveguide section is replaced with a nanobeam waveguide (NBW). The transmission of the topological PhCW is normalized to the maximal transmission of the NBW. The gray shades indicate the uncertainty of the transmission measurements based on photon counting statistics. The NBW shows characteristic fringes for long wavelengths, which are attributable to reflections at the interface of the NBW to the SEG fiber-to-chip couplers [162]. 37
- Fig. 4.6 a) The low-pass filtered photoluminescence spectra of two devices with a BIW length of $L_1 = 13.02 \mu\text{m}$ (blue) and $L_2 = 23.10 \mu\text{m}$ (yellow) and their fringes (green and red), probed by illumination with QDs as an internal probe. The shaded areas represent the statistical uncertainties of the spectrometer signal. b) Group index of the BIW of length $L_1 = 13.02 \mu\text{m}$ (green) and $L_2 = 23.10 \mu\text{m}$ (red) determined with the photoluminescence of embedded quantum dots as internal light probe and the prediction of finite-element (FEM) calculations based on scanning electron microscope images of the unit cell (black). The wavelength uncertainties represent the half-width-half-maximum fringe width. The device parameters $a = 280 \text{ nm}$, $r_s = 35 \text{ nm}$, and $r_c = 55 \text{ nm}$. 39

- Fig. 4.7 Scanning electron microscope image of a unit cell of a photonic topological photonic insulator of $a = 280$ nm, $r_s = 35$ nm, and $r_c = 55$ nm. The blue line marks the unit cell border. The green area indicates the pattern of the electron-beam lithography soft mask. Due to feature sizes below the resolution limit of the soft mask fabrication method, the shamrocks emerge similar to the pattern of blunt triangles. The circular hole and the shamrocks experience significant over-etching and visible random deformation. 40
- Fig. 4.8 Band diagram (a) and dispersion of the group index (b) of the BIW and ZIW from FEM calculations based on the scanning electron microscope image of the PhCW. The lattice constant is $a = 280$ nm. Dark gray areas indicate bulk modes. The light gray area indicates the light cone. The light yellow shading indicates the bandgap. Red indicates the ZIW mode. Blue and green indicate the two modes of the BIW. 41
- Fig. 5.1 (a) Schematic of a chiral light-matter interface utilizing an edge mode between two topological photonic insulators (dark and bright green). The field norm for the guided edge-mode is shown (yellow to red) and an embedded quantum emitter indicated. The quantum emitter's transition dipoles are left- or right-handed circular (σ_{\pm}), resulting in directional emission (left and right as shown in the inset) when it is placed at a position where the polarization of the guided mode is circular. The white-dashed line highlights a single supercell of the waveguide. (b) Schematics of the supercells of the glide-plane waveguide (GPW), line-defect waveguide (W_1), bearded-type interface waveguide (BIW), and zig-zag-type interface waveguide (ZIW) with the interface or center of each waveguide highlighted with a dashed line. 44
- Fig. 5.2 a) Photonic band diagram of the GPW (orange) and W_1 (yellow) waveguides. Shaded regions correspond to the bulk modes of the GPW (brown) and W_1 (yellow), while the grey region represents the light cone. The solid and dashed curves represent guided modes that are considered or excluded in this work, as discussed in the main text. Insets show exemplary mode profiles at $n_g \approx 15$. (b) Same as (a) but for topological BIW (green) and ZIW (blue) waveguides, noting that both topological waveguides share the same bulk modes. (c) Group index of the guided modes denoted by solid curves in (a) and (b) as a function of frequency for all four structures, with circles representing the modes whose profiles are shown above. The band-edges are indicated by a dotted line. 47

- Fig. 5.3 a) Mode maps of the directional Purcell factor $F_{\sigma_{\pm},k}(\mathbf{r})$ and directionality $D_k(\mathbf{r})$ for a unit cell of each PhCW, taken at $n_g \approx 15$ as shown in figure 5.2c). b) Maximal $F_{\sigma_{\pm},k}^{\max}$ for each mode as a function of frequency, with dashed curves representing the divergence predicted in the slow-light regions. c) Corresponding backscattering length $L_{\text{back},n,k}$ in units of the lattice constant a as a function of frequency. Note that both the backscattering losses and interaction enhancement diverge as the group index diverges. The band-edges are indicated by dotted lines, where the group index of all PhCWs except for the GPW diverge. Dashed lines indicate group-index divergences of the band-edge. Circles in b) and c) represent the modes whose profiles are shown in a). 49
- Fig. 5.4 A summary of PhCW parameters for use as practical quantum chiral-light matter interfaces. Maps of the maximal achievable propagation length (in units of the lattice constant a) as a function of the minimum desired directionality or Purcell Enhancement factor (structure marked in each panel). This combination of D and F must be found in an area $A \geq A_{\min}$, which is sufficiently distant δ_{\min} from a hole, as sketched in the inset of the first panel and explained in the main text. The bright grey area indicates the area A as an example for the W_1 , while the dark and black areas indicate the excluded regions given by δ_{\min} . Insets in the W_1 and ZIW panels show line cuts showing the propagation length as a function of F for $|D| = 0.5$ and $|D| = 0.99$, respectively (cuts taken along the white dashed lines). 52
- Fig. 5.5 Calculated delectable photon flux, in units of the homogeneous decay rate, as a function of the Purcell enhancement for a quantum emitter χ chirally coupled to a PhCW as shown in the inset to a) [22]. The photon rate is shown for (a) short, 10-unit cell structures and b), the more typical 100-unit cell waveguides in solid circles resolution limited by the k -space sampling, which are labeled as an example for the BIW for the data points of highest Purcell enhancements, (cf. appendix A.I.6). The dashed lines represent a guide to the eye, while the solid curves represent a sub-optimal positioning of the QE. In both a) and b), the performance of all 4 structures is shown, with the topological BIW supporting the highest-rate operation. This is true both for the shorter systems, where losses are low in all cases, as well as for the longer structures, where the high n_g (enhancement) operation is limited by the scattering. 54

- Fig. 6.1 Band structure of the heterojunction, calculated using a one-dimensional Poisson equation solver, assuming perfect ohmic contacts to the p-type and n-type layers for a bias voltage of a) $U_B = 0\text{ V}$ and b) $T = U_B = 1.4\text{ V}$ at 30 K. GaAs layers are shaded as gray and $\text{Al}_{15}\text{Ga}_{0.85}\text{As}$ layers are shaded as white backgrounds. Overlaid colored shading indicates the doping levels with acceptors (red) and donors (blue). The black lines indicate the calculated conduction and valence band. In a more realistic scenario, the waveguide surfaces have been exposed to air and have oxidized [251]. 58
- Fig. 6.2 Schematic cross-section of the planar quantum photonics platform of GaAs droplet epitaxy QDs. The sample is processed out of a wafer on top of which a distributed Bragg mirror (DBR), a sacrificial layer (shaded light-gray), and the semiconductor heterojunction are grown. The junction is made out of $\text{Al}_{15}\text{Ga}_{0.85}\text{As}$ (shaded white), and its lowest and uppermost layers are made out of GaAs (shaded dark gray). Blue and red shaded overlays indicate the donor and acceptor levels in the heterojunction. The centered intrinsic layer hosts the QDs. The sacrificial layer is removed chemically to suspend nanophotonic structures above the DBR. Nanophotonic devices are formed by etching into the heterojunction. The top and back-gate are electrically contacted from the surface. 59
- Fig. 6.3 Scanning Electron Microscope of a nanobeam waveguide (NBW) with shallow etch grating (SEG) couplers with embedded GaAs droplet epitaxy QDs. Figure a) shows one of the two SEG couplers for coupling light into the waveguide mode and collecting the light from the waveguide mode. Figure b) shows a zoom into a NBW section with high resolution. Figure c) shows a tether supporting the NBW in its suspension. Figure d) shows the entire device. 61
- Fig. 6.4 Scanning Electron Microscope of a nanophotonic device consisting of a line-defect photonic crystal waveguide (W_1 PhCW) of fast and slow light, mode tapers, and nanobeam waveguides (NBWs) that route light from the PhCW's guided mode to SEG couplers (sample B15459-A). Figure a) shows the waveguide center of the W_1 PhCW in the slow-light section. Figure b) shows the mode adapter from the W_1 PhCW to the NBW. Figure c) shows a zoom into a single hole of the photonic crystals of approximately 53 nm radius. The image is blurred due to the drift of the sample during the image acquisition. Figure d) shows the entire device. 62

- Fig. 6.5 The radius of the etched holes on the surface post fabrication r_s as a function of the radius on the electron beam exposure mask r_m (sample B15459-A). Each data point is the average and standard deviation of the characterization of 3 holes of a photonic crystal. While the hole radius on the surface varied little between photonic crystals of the same parameters, holes with a radius $r_s < 40$ nm did not etch through the heterojunction reliably. The dashed blue line is the identity function and resembles the absence of over-etching. 63
- Fig. 6.6 The current-voltage characteristic of the p-i-n heterojunction after nanofabrication in cryogenic conditions. Figure a) shows the absolute current of the heterojunction, where the green (blue) indicates forward (backward) currents. The dashed line indicates the source-meters systematic error specifications, and the area shaded in gray indicates the statistical error of 30 samples. Figure b) shows a fit, as discussed in the text. Figure c) shows the current-voltage characteristic at 300 K (green) for comparison with cryogenic conditions (blue). Figure d) shows the current-voltage characteristic through two separate back gate contacts (green) and a fit (blue). 65
- Fig. 6.7 Schematic of the optical setup. The sample is installed in the cryostat on top of nanopositioners (XYZ). Linear polarizers (LP), half-wave plates (HWP), and quarter-wave plates (QWP) control the input polarization and filter the excitation laser from the collected signal. The optical collection path is matched to the output mode diameter from a shallow etched grating. 67
- Fig. 6.8 Figure a) shows the CMOS camera image of a nanophotonic device of two shallow etch grating (SEG) couplers linked by a nanobeam waveguide (NBW). A laser with $\lambda_L = 795$ nm is injected into the coupler on the top right. The input coupler appears bright due to the direct reflection of the laser on the grating. The injected light is transmitted to the other coupler on the left. The light at the output coupler is of comparable brightness to the light reflected from the input port. Figure b) shows a scanning electron microscope image of the same device. 68
- Fig. 6.9 Relative laser transmission through a NBW for injection of a laser ($\lambda_L = 795$ nm) and as a function of the half-wave and quarter-wave-plate angles ϕ_{HWP} , ϕ_{QWP} controlling the input laser polarization. 70

- Fig. 6.10 A set of concentric devices consisting of two fiber-to-chip couplers and NBWs of various lengths between $L_0 = 60 \mu\text{m}$ and $L_{10} = 1.486 \text{ mm}$. The gratings are placed at a fixed relative position from each other to avoid re-aligning the position and angle of laser injection and collection beams. The couplers' relative orientation enables laser-background filtering by cross-polarizing the injected laser at the input port and the collected light at the output port. 70
- Fig. 6.11 Examples of the devices transmission $T_{\Pi, \text{concentric}}(L, \lambda)$ relative to the shortest waveguide of $L = 60 \mu\text{m}$. The devices are probed by injection of a super-continuum laser. The emission band is filtered to the spectral range of 750 nm to 850 nm. The transmission spectra is measured with a spectrometer. The input-path and collection-path are aligned by an initial alignment with the narrow band laser at $\lambda = 795 \text{ nm}$. The transmission spectra are normalized by the spectral power-density of the continuum laser obtained by the direct exposure of the spectrometer. The shaded areas indicate the uncertainty of 3 standard deviations. 71
- Fig. 6.12 Waveguide attenuation from the FKE of the electric fields inside the heterojunction of light transmitted in a $42.2 \mu\text{m}$ long NBW as a function of the applied bias voltage U_B probed with laser wavelengths of $\lambda_L = 785 \text{ nm}$, $\lambda_L = 795 \text{ nm}$ and $\lambda_L = 805 \text{ nm}$. The attenuation is estimated from the waveguide transmissions for a bias voltage of $U_B = 1.5 \text{ V}$. 73
- Fig. 6.13 Scanning Electron Microscope of nanophotonic devices (sample B15459-A). The device in figure a) consists of a W_1 PhCW section, a mode taper, and NBWs that route light from the PhCW's guided mode to SEG couplers. Figure b) shows a reference device of identical dimensions but where the PhCW is replaced with a nanobeam section. 74
- Fig. 6.14 The transmission of W_1 PhCW test devices of various lattice constants a and hole radii r and a NBW reference (fabricated on wafer B15280). The hole radii refer to the radius on the electron-beam-resist mask. The hole radius over-etching of these test devices is approximately 5 nm. The reference NBW reference is the normalized transmission envelope of the averaged transmission spectrum 4 reference devices. 76

- Fig. 6.15 Relative transmission of two devices of sample B15459-A with identical waveguide length with a narrow-band diode laser and photo-detection with an avalanche photodiode. Blue shows the device's transmission where a nanobeam links two fiber-to-chip couplers, as shown in figure 6.8. Green shows the transmission of a device with a intermediate W1 PhCW waveguide section, like the device shown in figure 6.4. The W1 waveguide consists of holes with a electron-beam mask radius of $r_m = 35$ nm and an etched hole radius of approximately $r_s \approx 45$ nm. The photonic crystal lattice constant is $a = 206$ nm. The red area indicates the wavelength region of the QDs examined in this device in chapter 7, 8, and 9. 77
- Fig. 7.1 Schematic of the optical setup. The sample is installed in the cryostat on top of nanopositioners (XYZ). A dichroic mirror combines the input paths for above-band-excitation (532 nm and 632.8 nm), the path for quasi-resonant excitation, and the path matched with the shallow-etch-grating coupler mode diameter. Linear polarizers (LP), half-wave plates (HWP), and quarter-wave plates (QWP) control the input polarization and filter the excitation laser from the collected signal and from the CMOS camera image. The camera image path can be equipped with a filter. The optical collection path is matched to the output mode diameter from a shallow etched grating. 80
- Fig. 7.2 Camera images of a non-structured section of sample B15459-A under excitation with a wavelength of $\lambda_L = 632.8$ nm. The camera image is filtered by a 750 nm long-pass filter. The integration time is 5 s, and the excitation power of approximately $P_L \approx 500$ nW. Figure a) shows the image for a bias voltage of $U_B = 0$ V. No QDs are visible, and the fluorescence of impurities on the surface of the sample can be seen. Figure b) shows the same area for a bias voltage of $U_B = 1.5$ V. QDs are clearly visible not only at the center of the near-aberration limited laser focus spot, but also micrometers away from the focus spot. 81
- Fig. 7.3 Scanning electron microscope images of a) the mode adapter b) the waveguide center of a W1 PhCW showing typical nanofabrication-induced impurities. The sidewalls of deep trenches show wrapping by μm -sized flakes (Green arrows in figure a). Both the surface of the substrate and the surface of the membrane show nm-sized randomly scattered particles. 82

- Fig. 7.4 Camera images of the sample B15459-A near the W_1 waveguide $W_{260,35}^{(3,5)}$ (see appendix A.II) under excitation with a wavelength of $\lambda_L = 632.8$ nm. The laser spot is centered in the microscope objective. The integration time is 5 s, and the excitation power of approximately $P_L \approx 2.5$ μ W. The camera image is filtered by a 800 ± 5 nm long-pass filter. Figure a) shows the image for a bias voltage of $U_B = 0$ V. Figure b) shows the same area for a bias voltage of $U_B = 1.5$ V and is background-subtracted. The area where the laser spot saturated the camera has been removed from the image (white area). See discussion in the main text. 83
- Fig. 7.5 a) Zoom onto a single QD in the camera image in figure 7.4. b) Levenberg–Marquardt non-linear least-square fit of a single Airy disc pattern and a homogeneous background. 85
- Fig. 7.6 Excitation-emission fluorescence map of QD1 for a bias voltage of $U_B = 1.4$ V as a function of the excitation laser’s wavelength λ_L from 760 nm to 785.5 nm. 86
- Fig. 7.7 The photoluminescence emitted by QD2 as a function of the gate voltage U_B (positive gate voltage indicates a forward bias) under quasi-resonant excitation ($\lambda_L = 784.85$ nm). The wavelength is resolved by a spectrometer, and the intensity is measured on a CCD camera. The emission spectrum shows several plateaus corresponding to different charge states of the quantum dot (lines labeled with numbers). The charge states are discussed in the main text. The spectrally shifted parallel transitions (copies) can be observed (unlabeled lines). 87
- Fig. 7.8 Photoluminescence energy E_{PL} as a function of electric field F extracted from the data shown in figure 7.7. 89
- Fig. 7.9 Time-bin histogram of a lifetime measurement of QD2 under pulsed resonant excitation with a power of $P_L = 240$ nW, displayed in green. The blue line represents the fit to a single exponential decay convolved with the instrument’s response function (IRF). 90
- Fig. 7.10 Autocorrelation histogram of a Hanbury Brown and Twiss experiment under continuous wave excitation for various excitation laser power P_L settings. The integration time for each excitation power is $t_i = 1$ h. Figure a) shows a close-up of the close-to-zero delay region. For increasing excitation power at zero time-delay, the autocorrelation histogram transitions from pronounced anti-bunching to bunching. Figure b) shows the long delay-time autocorrelation histogram. The QD shows strong blinking in the μ s timescale. 91

- Fig. 7.11 The fraction of time in which the QD is in the bright state β_c , and the blinking time constant τ_c of the autocorrelation function g_2 for the lowest six excitation laser power P_L settings. 93
- Fig. 8.1 a) Resonant fluorescent spectra for continuous wave excitation probed with excitation laser wavelengths of $\lambda_L = 797.000\ 00(21)$ nm, $\lambda_L = 797.337\ 30(21)$ nm, $\lambda_L = 797.625\ 40(21)$ nm, $\lambda_L = 798.000\ 00(21)$ nm. For excitation wavelengths of 100 pm above or below the probed wavelengths, no fluorescence is observable within the bias voltage interval between 1.325 V and 1.55 V. For these spectra, the bias voltage was sampled in a randomized order. The difference in the background count noise is attributable to mechanical drifts of the excitation laser during data acquisition. b) Zoom into the frequency-voltage map obtained by quasi-resonant excitation of figure 7.7. The dashed lines indicate the wavelengths probed for resonant excitation, as shown in figure a). 97
- Fig. 8.2 Photoluminescence detection rate under continuous wave excitation. Experimental settings $\lambda_L = 797.625\ 40(21)$ nm, integration time $t_i = 1$ s. The dark detector's dark count rate limits the signal-to-noise ratio for the very lowest excitation powers. At the highest excitation powers, the excitation saturates, and the spectral line disappears in the laser background noise. 99
- Fig. 8.3 Examples of background subtracted normalized photoluminescence detection rate for various powers P_L , and two-level-system line fits. The model and data evaluation details are discussed in appendix A.VIII. 100
- Fig. 8.4 Two-level system parameters extracted from the power- and bias voltage scan of the high-energy state $|X_h\rangle$. a) the linewidth Δf_{FWHM} , b) the (detected) photo-emission rate γ_D , and c) the frequency tuning Δf_{P_L} of the QD 101
- Fig. 8.5 Two-level system parameters extracted from the power- and bias voltage scan of the high energy state $|X_l\rangle$. a) the linewidth Δf_{FWHM} , b) the (detected) photo-emission rate γ_D , and c) the frequency tuning Δf_{P_L} of the QD 102
- Fig. 8.6 Spectral probability density for phonon sideband emission $(1 - B_{\text{FC}}^2)S_{\text{PSB}}$ as a function of the photo-emission frequency relative to resonance $\Delta f_X = f - f_X$ emission for various temperatures T . The parameters are those obtained from the evaluation of the experimental data, shown in figure 8.7. 105

- Fig. 8.7 Phonon-sideband-resolving Spectra, re-normalized by their total emission rate for a sample mount temperature of $T_{\text{SMP}} = 7$ K, $T_{\text{SMP}} = 11$ K, $T_{\text{SMP}} = 16$ K and $T_{\text{SMP}} = 21$ K and fits. The fit results are summarized in table 8.1. The spectrum of the lowest temperature shows a significant asymmetry owed to a lower probability of a Stokes process than an anti-Stokes process. The spectrum of the highest temperature is within the signal-to-noise ratio fully symmetric. 107
- Fig. 8.8 Zero-phonon-line contributions of the emission spectra for various temperatures according to the fit results of figure 8.1. 109
- Fig. 9.1 a) Intensity of an optically driven Rabi oscillation of the state $|X_h\rangle$ of QD2 as a function of the pulse area \mathcal{P} . The time-averaged count rate for a π -pulse ($\mathcal{P} = \mathcal{P}_\pi$) is approximately 191 kHz. b) Numerical prediction of the time-averaged intensity for a Rabi-oscillation for a two-level-system under the assumption of a decay rate of $\gamma = 1/T_1 = 1.2442 \text{ ns}^{-1}$, a laser pulse length of 20 ps, and a Gaussian spectral diffusion with a width of $\Delta f_{\text{FWHM}}^{\text{SD}} = 10\Gamma$ for various dephasing rates Γ_{dp} . 112
- Fig. 9.2 Signal-to-noise ratio of an optically driven Rabi oscillation of the state $|X_h\rangle$ of QD2 as a function of the pulse area \mathcal{P} . 113
- Fig. 9.3 Autocorrelation histogram of a Hanbury Brown and Twiss experiment under pulsed resonant excitation. a) Close-to-zero delay region of the first pulses (green) and the fit-result (blue). b) Zoom into the zero-delay region, showing the contribution of the total background (red) and the excitation laser leakage (yellow) obtained from the fit result. 114
- Fig. 9.4 Autocorrelation function $g^2(\tau)$ (background corrected normalized time-bin histogram pulse areas) for long photodetection event time delay $\tau \leq 25 \mu\text{s}$. Figure a) displays the antibunching of the time-bin-histogram peak corresponding to coincident photodetection $\tau = 0$ and the non-coincident photodetection peaks at delays of integer multiples of the laser repetition rate $t_{\text{rep}} \approx 12.5 \text{ ns}$. The blue area highlights the antibunching estimate $g^2(0)$ and its confidence interval. Figure b) displays a zoom into the area of the non-coincident photodetection peaks, revealing low blinking probability in a timescale exceeding $10 \mu\text{s}$. The blue line corresponds to a fit and its confidence interval. 115
- Fig. 9.5 Time-resolved interference pattern relative to the radiative decay rate γ for pairs of partially indistinguishable photons after equation 9.3 for various dephasing rates assuming ideal temporal overlap, absence of spectral diffusion, and collinear polarization. 117

- Fig. 9.6 The second-order cross-correlation histograms of a spectrally unfiltered HOM experiment normalized to the bunching peaks a longer time scales where no interference occurs (see section A.XI). Figure a) and c) show the central region of the orthogonal polarized (red) and collinear (green) configuration of the interferometer. Figure b) and d) show the a zoom into the section where two subsequently emitted photons interfere. The yellow (blue) lines are fits to the orthogonal (collinear) polarized interferometer configurations. 118
- Fig. 9.7 The second-order cross-correlation histograms of a spectrally filtered HOM experiment normalized to the bunching peaks a longer time scales where no interference occurs (see section A.XI). Figure a) and c) show the central region of the orthogonal polarized (red) and collinear (green) configuration of the interferometer. Figure b) and d) show the a zoom into the section where two subsequently emitted photons interfere. 119
- Fig. A.1 Schematic of the waveguide center region of the PhCWs's super-cells and their parameters for the simulations, as discussed in the text. Each photonic crystal border lines are highlighted in color. Hole radii are indicate in grey. The GPW's photonic crystal is deformed from the W_1 in the PhCW's center region as discussed in the text. The deformation parameters are indicated and labeled in grey. The lattice vectors (photonic crystal's unit cells) are indicated for the W_1 and the topological waveguides in a solid black (white dashed) line. The ZIW's and BIW's photonic crystals have the same unit cell and lattice vectors but their interface follows along different directions. 126
- Fig. A.2 Characteristic mode width w_n as a function of the group index $n_g(\omega_{n,k})$ of all band-gap modes of the BIW, ZIW and the selected modes of the GPW and W_1 for comparison. The data points are connected along their individual wavenumber k . The dashed lines correspond to the modes of the ZIW which are not considered for a chiral-light interface due to their extreme mode widths. 127

- Fig. A.3 Inelastic mean-free path $L_{\text{back},k} = \langle \alpha_{\text{back},k} \rangle^{-1}$ sweeping the correlation constant l_p and keeping the deformation parameter $\sigma = 3$ nm constant for chosen modes representing minimal backscattering fullfilling the requirements of: (a) providing Purcell enhancement $F = 1$ and a directionality $|D| = 0.99$ in locations being separated from hole by δ within the high-index regions of the vertical symmetry plane \mathcal{S}_c (see Appendix A.1.5) and (b) providing a Purcell enhancement $F = 10$ and providing the highest directionality D_{max} accessible for each PhCW within the same position restrictions as in (a). The inset shows a schematic of the stastical hole deformation parameters. A hole is deformed by a dent of amplitude σ over a correlation length l_p . 128
- Fig. A.4 (a) Re-normalized maximal Purcell enhancement $F_{\sigma_{\pm,k}}^{\text{max}}/n_g$ within the high-index regions of the vertical symmetry plane \mathcal{S}_c (see Appendix A.1.5) and (b) re-normalized mean free path $L_{\text{back},k}n_g^2$. The solid lines connect modes along the wavenumber k while the dashed lines indicate regions of divergence. The non-trivial dispersion of the re-normalized Purcell enhancement and the re-normalized mean free path indicate the significance of the dispersion of the mode profiles and their polarization. 131
- Fig. A.5 Maximal area \mathcal{F} of all modes for minimal directionality amplitude $|D|$ and minimal Purcell enhancements P in the high index material area given by \mathcal{S}_{min} , not limiting the associated group index or backscattering losses. 132
- Fig. A.6 Band diagram of the (a) GPW and (b) BIW showing only the light cone, the bulk bands and the relevant modes for which the photon number rate $\Phi_{L/R}/\gamma_{L/R}^0$ is maximal, desiring a directionality of $|D| = 0.99$ and minimal losses. Each point shown corresponds to a different optimal Purcell enhancement. 134
- Fig. A.7 Schematic overview of the electrical contacts of the electron-beam writing fields of sample B15459-A. The writing fields are labeled in the format (x, y) , where x is the column, and y is the row. All writing fields of each column share two pairs of electronic connections. The electronic connections are noted in the format Cx , where x is the index. Colored squares denote the positive electronic connectors of a column, whereas black squares denote negative electronic connectors. Example: Write field $(3, 5)$ is electronic connected by the contact pairs $C3 + C4$ and $C13 + C14$, where $C3$ and $C14$ are negative electronic connectors. Only one contact pair is contacted by wire-bonding. 137

- Fig. A.8 The photoluminescence emitted by QD2 as a function of the gate voltage U_B (positive gate voltage indicates a forward bias) under quasi-resonant excitation ($\lambda_L = 784.85$ nm) in a logarithmic color map. The wavelength is resolved by a spectrometer and the intensity measured on a CCD-camera. The emission spectrum shows several plateaus corresponding to different charge states of the quantum dot. The spectrally shifted parallel transitions (copies) can be observed. 142
- Fig. A.9 Electric fields F_z (solid green line), donor number density ρ_n (solid blue line), and acceptor density ρ_p (solid red line) of wafer B15459, calculated using a one-dimensional Poisson equation solver, assuming perfect ohmic contacts to the p-type and n-type layers for a bias voltage of a) $U_B = 0$ V and b) $T = U_B = 1.4$ V at $T = 30$ K. GaAs layers are shaded as gray and $\text{Al}_{15}\text{Ga}_{0.85}\text{As}$ layers are shaded as white backgrounds. Overlaid colored shading indicates the doping levels with acceptors (red) and donors (blue). 143
- Fig. A.10 Electric field F_D (colored lines) and depletion width d_{dl} (colored lines) as function of the applied bias voltage U_B for various temperatures T . The color represents the temperature T . Solid lines assume the doping levels next to the intrinsic layers ($N_p, N_a = 1 \times 10^{18} \text{ cm}^{-2}$), the dashed lines assume the highly-doped p-layer $N_p = 1 \times 10^{19} \text{ cm}^{-2}$. The solid-black line represent numerical calculations using a one-dimensional Poisson equation solver of the full heterojunction layout, assuming perfect ohmic contacts and neglecting Fermi-level pinning. 145
- Fig. A.11 Laser transmission of five photonic devices. Figure a) shows the transmission of devices with a bearded-type of interface with (without) a mode adapter in green (blue). The black transmission spectrum is the reference nanobeam waveguide device (NBW). Figure b) shows the transmission of devices with a zig-zag-type of interface with (without) a mode adapter in green (blue). The photonic crystal parameters are $a = 280$ nm, $r_s = 35$ nm, and $r_c = 55$ nm. 146
- Fig. A.12 Transmission of NBW reference device probed with a single mode laser (red) its Farby-Pérot fringes (yellow) and the photoluminescence signal from QDs as a white-light source (green) and its Farby-Pérot fringes (blue). Both spectra are normalized to their intensity maximum. 147
- Fig. A.13 The group index of the reference device calculated from the device length of $L = 73.132 \mu\text{m}$ and the free spectral range $\Delta\lambda_{\text{FSR}}$ for both illumination methods. The transmission of the laser provides the group index estimates shown in red. The QD photoluminescence estimates the group index shown in green. 147

- Fig. A.14 Transmission of the BIW waveguide (dark gray) and the QD photoemission emission into the guided mode as white light source with (green) and without (blue) the Butterworth filtering. 148
- Fig. A.15 Transmission of the BIW waveguide and evaluated fringe maxima. Figure a) shows the outcome of the evaluation method on the laser transmission spectrum (gray) and the QD spectrum (blue). Figure b) shows the maxima for the BIW of both lengths $L_1 = 13.02 \mu\text{m}$ and $L_2 = 23.10 \mu\text{m}$. The free spectral range scales inverse with the PhCW length. 149
- Fig. A.16 The optical access to the sample located in a the cryostat. The fiber ports FP_1 FP_2 and FP_3 are the input ports, featuring polarization-maintaining single-mode fibers. The input ports are combined by the polarizing beam splitter PBS_1 and the dichoric mirror DM_1 . The fiber port FP_4 is the collection port, featuring a single-mode fiber. The beam splitter BS_3 ($R = 0.9, T = 0.1$) separates the input and collection paths. The CMOS camera C_1 images the sample which can be illuminated with an infrared LED (LED_1). Laser input powers are monitored with the photodiodes PM_1 and PM_2 . The lens pairs (L_1, L_4) , (L_2, L_4) , and (L_{10}, L_{11}) adjust the beam diameters. Other lenses belong to the $4f$ imaging system. 151
- Fig. A.17 Optical filtering setup with Volume Phase Holographic Transmission Grating (VTG_1) and an Etalon Filter EF_1 . 152
- Fig. A.18 Transmission scan through the filter setup without the Etalon filter, the center wavelength is 797.3 nm. The full-width-half-maximum width of the transmission peak is ≈ 20.34 GHz. Without the Etalon filter, the rejection of wavelength components takes place when the collimated beam is fiber-coupled. The peak transmission (fiber-to-fiber) is $\approx 42\%$. Credit for the data acquisition to Hanna Salamon. 153
- Fig. A.19 Pulse-stretcher setup for the Ti:Sapphire laser. After passing the isolator, the beam is split (PBS_1) for exposure of the trigger diode (PD_1). The transmitted beam is split for fiber coupling unmodified laser pulses (FP_1) and feeding the pulse-stretcher setup, discussed in the main text. 154
- Fig. A.20 Instrument's response function of the spectrometer illuminated by the DLPro narrow-band continuous-wave laser. 155
- Fig. A.21 Time-bin histogram of a 6.8 ps pulse from the Tsunami Ti:Sapphire laser, detected with APD_1 . The instrument's response function describes a peak with full-width-half-maximum ≈ 320 ps. To the left, the function shows super-exponential decay. To the right, the function shows a slow exponential decay with $\tau_{1/e} \approx 720$ ps, compatible with the device specifications. 156

- Fig. A.22 Transmission spectra of concentric waveguides of various lengths. The individual spectra are normalized to their transmission maximum. 159
- Fig. A.23 Transmission spectra of concentric waveguides of various lengths. The individual spectra are normalized to the transmission maximum of the shortest waveguide ($L = 60 \mu\text{m}$). 160
- Fig. A.24 Attenuation spectra of concentric waveguides of various lengths, relative to the transmission of the shortest waveguide ($L = 60 \mu\text{m}$). 160
- Fig. A.25 Schematic of the the source measure unit (SMU) and the electronic wiring for controlling the bias voltage U_B and voltage-current characterization of the p-i-n junction. Only one column of the sample is connected to the SMU while the others are terminated by a 50Ω resistor directly after the vacuum-feed-through (not shown). 161
- Fig. A.26 The time-bin histogram and fits of the lifetime measurements for two excitation powers of a) $P_L = 60 \text{ pW}$ and c) $P_L = 240 \text{ pW}$. Figure b) and d) show the corresponding residuals. 162
- Fig. A.27 Near zero time delay regions of the autocorrelation histograms and least-square curve fits with the Levenberg–Marquardt algorithm of equation A.24 ($N = 1$) for an excitation laser power of a) 7.5 nW , b) 15 nW , c) 30 nW , d) 60 nW , e) 120 nW , and f) 240 nW . 165
- Fig. A.28 Fitting parameters of the autocorrelation histograms of figure A.27 by equation A.24. 166
- Fig. A.29 The time-bin histogram and fit of the autocorrelation function of equation A.31 assuming $\beta_c = 1$. Goodness of fit: $\chi_{\text{red}}^2 = 1.46$ over 9765 data points. 168
- Fig. A.30 Autocorrelation fit (equation A.31) residuals of the fit shown in figure A.29. The goodness of fit is $\chi_{\text{red}}^2 = 1.46$ 169
- Fig. A.31 Background corrected photoluminescence rate as function of excitation laser amplitudes \sqrt{P} and the bias voltage (U_B). The excitation wavelength is $\lambda_L = 797.62540(2) \text{ nm}$ and an the integration time $t_i = 1 \text{ s}$. 172
- Fig. A.32 Voltage-to-DC-Stark-frequency-shift conversion function relative to the resonance frequency at ($U_B = 1.375 \text{ V}$ obtained from the evaluation of the voltage sweep of the emission spectrum under p -shell. The blue line is a quadratic fit. 172
- Fig. A.33 Fit residuals of figure 8.4 b). Discussion in the main text. 173
- Fig. A.34 Gaussian and Lorentzian linewidth contributions to the fit in figure 8.4 b), reflecting the contribution of inhomogeneous broadening. Discussion in the main text. 173
- Fig. A.35 Mean voltage offset $U_{B,\text{off}}$ (10 samples) of the resonant excitation voltage-power scan shown in figure 8.2. 174

- Fig. A.36 Standard deviation of the voltage offset $\sigma_{U_{B,\text{off}}}$ (10 samples) of the resonant excitation voltage-power scan shown in figure 8.2. 174
- Fig. A.37 Mean laser-induced electrical current $I_{\text{ind}}^{(i,j)}$ (10 samples) of the resonant excitation voltage-power scan shown in figure 8.2. 175
- Fig. A.38 Standard deviation of the electrical current readings $\sigma_{I_{\text{raw}}^{(i,j)}}$ (10 samples) of the resonant excitation voltage-power scan shown in figure 8.2. 175
- Fig. A.39 Raw photoluminescence rate as function of excitation laser amplitudes \sqrt{P} and the bias voltage (U_B). The excitation wavelength is $\lambda_L = 797.625\ 40(2)$ nm and an the integration time $t_i = 1$ s. 176
- Fig. A.40 Background corrected photoluminescence rate as function of excitation laser amplitudes \sqrt{P} and the bias voltage (U_B). The excitation wavelength is $\lambda_L = 797.625\ 40(2)$ nm and an the integration time $t_i = 1$ s. 177
- Fig. A.41 Voltage-to-DC-Stark-frequency-shift conversion function relative to the resonance frequency at ($U_B = 1.342$ V obtained from evaluation of the voltage sweep of the emission spectrum under p -shell. The blue line is a quadratic fit. 177
- Fig. A.42 Examples of background-subtracted normalized photoluminescence rate for various powers and their line fits. 178
- Fig. A.43 Fit residuals of figure 8.5 b). Discussion in the main text. 178
- Fig. A.44 Gaussian and Lorentzian linewidth contributions to the fit in figure 8.5 b), reflecting the contribution of inhomogeneous broadening. Discussion in the main text. 178
- Fig. A.45 shift of the resonance frequency of QD2 in the W1 waveguide $W1_{260,35}^{(3,5)}$ as a function of the cryostat's sample stage thermometer temperature reading T_{SMP} . The solid line shows a prediction based on a measurement of a similar platform [184] and the dashed line a prediction based on parameters found for bulk material, i.e. without doping and nanostructuring [340]. 179
- Fig. A.46 Quadratic fit on the photoluminescence as function of the excitation laser power on the sample. 180
- Fig. A.47 Schematic of the Hong–Ou–Mandel interferometer setup. A legend can be found in figure A.16. 181
- Fig. A.48 Residuals of the center regions of a multi-peak least-square curve fitting with the Levenberg–Marquardt algorithm of the data shown in figure 9.6 with the model given by equation A.44 for both data-sets (transverse and collinear polarization) with the fit parameters in table A.7. 184

LIST OF TABLES

- 5.1 Purcell factors $F_{\sigma_{\pm}}^{\max}$ and mean-free paths L_{back} for the highlighted modes with a group index of $n_g = 15$. 49
- 7.1 The DC stark tuning parameters of equation 7.4 obtained from Levenberg–Marquardt non-linear least-square fits of the extracted photoluminescence energies in figure 7.8 for both charge states $|X_h\rangle$ and $|X_l\rangle$. Goodness of fit $\chi_{\text{red}}^2 = 1.55$ for $|X_h\rangle$, $\chi_{\text{red}}^2 = 2.54$ for $|X_l\rangle$. 89
- 8.1 Sample mount temperature dependent parameters obtained by Levenberg–Marquardt non-linear least-square fit of the phonon-sideband resolving spectra as shown in figure 8.7. 108
- A.1 Wafer B15459 growth layout. Based on a (100) GaAs wafer. The red (blue) highlighted layers are the p-doped (n-doped) layers. The etching- and filling layer is highlighted in green. The yellow layer is the GaAs capping layer on the membrane face towards the substrate. 135
- A.2 Wafer B15280 growth layout. Based on a (100) GaAs wafer. The red (blue) highlighted layers are the p-doped (n-doped) layers. The etching- and filling layer is highlighted in green. The yellow layer is the GaAs capping layer on the membrane face towards the substrate. 136
- A.3 Wafer B14769 growth layout. 137
- A.4 Overview of the photonic devices in each electron-beam writing field on sample B15459A. $W1_A$ and $W1_B$ are W1-type PhCWs of different parameter sets. CoCW refers to concentric nanobeam waveguides. Column 5 is not electrically contacted with any gate. 138
- A.5 Look-up table for the parameters of W1 waveguides of parameter set A ($W1_A$) and their position in a write field. Devices are referred to as $W1_{a,r}^{(x,y)}$. The first index in this table is the hole radius r in nm, the second the lattice constant a in nm. 138
- A.6 Multi-peak fit results ($N_{\text{sp}} = 50$) of the data shown in figure 9.3 with the model given by equation A.31. 169

- A.7 Multi-peak fit results of the far-off peaks of the data shown in figure 9.6 with the model given by equation A.44. The symbol \perp denotes the transverse polarization configuration while \parallel denotes the collinear polarization configuration. 184

BIBLIOGRAPHY

- [1] N. V. Hauff, H. Le Jeannic, P. Lodahl, S. Hughes, and N. Rotenberg, “Chiral quantum optics in broken-symmetry and topological photonic crystal waveguides,” *Physical Review Research*, vol. 4, no. 2, p. 023082, 2022.
- [2] R. Uppu, L. Midolo, X. Zhou, J. Carolan, and P. Lodahl, “Quantum-dot-based deterministic photon–emitter interfaces for scalable photonic quantum technology,” *Nature nanotechnology*, vol. 16, no. 12, pp. 1308–1317, 2021.
- [3] J. Wang, F. Sciarrino, A. Laing, and M. G. Thompson, “Integrated photonic quantum technologies,” *Nature Photonics*, vol. 14, no. 5, pp. 273–284, 2020.
- [4] J. L. O’Brien, A. Furusawa, and J. Vučković, “Photonic quantum technologies,” *Nature Photonics*, vol. 3, no. 12, pp. 687–695, 2009.
- [5] P. Lodahl, S. Mahmoodian, and S. Stobbe, “Interfacing single photons and single quantum dots with photonic nanostructures,” *Reviews of Modern Physics*, vol. 87, no. 2, p. 347, 2015.
- [6] P. Senellart, G. Solomon, and A. White, “High-performance semiconductor quantum-dot single-photon sources,” *Nature nanotechnology*, vol. 12, no. 11, pp. 1026–1039, 2017.
- [7] R. Uppu, F. T. Pedersen, Y. Wang, C. T. Olesen, C. Papon, X. Zhou, L. Midolo, S. Scholz, A. D. Wieck, A. Ludwig, *et al.*, “Scalable integrated single-photon source,” *Science advances*, vol. 6, no. 50, p. eabc8268, 2020.
- [8] L. Zhai, G. N. Nguyen, C. Spinnler, J. Ritzmann, M. C. Löbl, A. D. Wieck, A. Ludwig, A. Javadi, and R. J. Warburton, “Quantum interference of identical photons from remote GaAs quantum dots,” *Nature Nanotechnology*, vol. 17, no. 8, pp. 829–833, 2022.
- [9] J.-P. Li, X. Gu, J. Qin, D. Wu, X. You, H. Wang, C. Schneider, S. Höfling, Y.-H. Huo, C.-Y. Lu, *et al.*, “Heralded nondestructive quantum entangling gate with single-photon sources,” *Physical Review Letters*, vol. 126, no. 14, p. 140501, 2021.
- [10] S. E. Economou, N. Lindner, and T. Rudolph, “Optically generated 2-dimensional photonic cluster state from coupled quantum dots,” *Physical review letters*, vol. 105, no. 9, p. 093601, 2010.

- [11] I. Aharonovich, D. Englund, and M. Toth, “Solid-state single-photon emitters,” *Nature photonics*, vol. 10, no. 10, pp. 631–641, 2016.
- [12] P. Lodahl, “Quantum-dot based photonic quantum networks,” *Quantum Science and Technology*, vol. 3, no. 1, p. 013001, 2017.
- [13] G. Costantini, A. Rastelli, C. Manzano, R. Songmuang, O. Schmidt, K. Kern, and H. v. Känel, “Universal shapes of self-organized semiconductor quantum dots: striking similarities between InAs/GaAs (001) and Ge/Si (001),” *Applied physics letters*, vol. 85, no. 23, pp. 5673–5675, 2004.
- [14] D. Leonard, M. Krishnamurthy, C. Reaves, S. P. DenBaars, and P. M. Petroff, “Direct formation of quantum-sized dots from uniform coherent islands of InGaAs on GaAs surfaces,” *Applied Physics Letters*, vol. 63, no. 23, pp. 3203–3205, 1993.
- [15] A. Rastelli, M. Stoffel, A. Malachias, T. Merdzhanova, G. Katsaros, K. Kern, T. H. Metzger, and O. G. Schmidt, “Three-dimensional composition profiles of single quantum dots determined by scanning-probe-microscopy-based nanotomography,” *Nano letters*, vol. 8, no. 5, pp. 1404–1409, 2008.
- [16] M. Arcari, I. Söllner, A. Javadi, S. L. Hansen, S. Mahmoodian, J. Liu, H. Thyrrestrup, E. H. Lee, J. D. Song, S. Stobbe, *et al.*, “Near-unity coupling efficiency of a quantum emitter to a photonic crystal waveguide,” *Physical review letters*, vol. 113, no. 9, p. 093603, 2014.
- [17] S. Mahmoodian, K. Prindal-Nielsen, I. Söllner, S. Stobbe, and P. Lodahl, “Engineering chiral light–matter interaction in photonic crystal waveguides with slow light,” *Optical Materials Express*, vol. 7, no. 1, pp. 43–51, 2017.
- [18] I. Söllner, S. Mahmoodian, S. L. Hansen, L. Midolo, A. Javadi, G. Kiršanskė, T. Pregnolato, H. El-Ella, E. H. Lee, J. D. Song, *et al.*, “Deterministic photon–emitter coupling in chiral photonic circuits,” *Nature nanotechnology*, vol. 10, no. 9, pp. 775–778, 2015.
- [19] I. Shomroni, S. Rosenblum, Y. Lovsky, O. Bechler, G. Guendelman, and B. Dayan, “All-optical routing of single photons by a one-atom switch controlled by a single photon,” *Science*, vol. 345, no. 6199, pp. 903–906, 2014.
- [20] F. T. Østfeldt, E. M. González-Ruiz, N. Hauff, Y. Wang, A. D. Wieck, A. Ludwig, R. Schott, L. Midolo, A. S. Sørensen, R. Uppu, *et al.*, “On-demand source of dual-rail photon pairs based on chiral interaction in a nanophotonic waveguide,” *PRX Quantum*, vol. 3, no. 2, p. 020363, 2022.
- [21] B. Schriniski, M. Lamaison, and A. S. Sørensen, “Passive quantum phase gate for photons based on three level emitters,” *Physical Review Letters*, vol. 129, no. 13, p. 130502, 2022.

- [22] S. Mahmoodian, P. Lodahl, and A. S. Sørensen, “Quantum networks with chiral-light–matter interaction in waveguides,” *Physical review letters*, vol. 117, no. 24, p. 240501, 2016.
- [23] H. Siampour, C. O’Rourke, A. J. Brash, M. N. Makhonin, R. Dost, D. J. Hallett, E. Clarke, P. K. Patil, M. S. Skolnick, and A. M. Fox, “Observation of large spontaneous emission rate enhancement of quantum dots in a broken-symmetry slow-light waveguide,” *npj Quantum Information*, vol. 9, no. 1, p. 15, 2023.
- [24] S. F. C. da Silva, G. Undeutsch, B. Lehner, S. Manna, T. M. Krieger, M. Reindl, C. Schimpf, R. Trotta, and A. Rastelli, “Gaas quantum dots grown by droplet etching epitaxy as quantum light sources,” *Applied Physics Letters*, vol. 119, no. 12, p. 120502, 2021.
- [25] M. Gurioli, Z. Wang, A. Rastelli, T. Kuroda, and S. Sanguinetti, “Droplet epitaxy of semiconductor nanostructures for quantum photonic devices,” *Nature materials*, vol. 18, no. 8, pp. 799–810, 2019.
- [26] H. G. Babin, J. Ritzmann, N. Bart, M. Schmidt, T. Kruck, L. Zhai, M. C. Löbl, G. N. Nguyen, C. Spinnler, L. Ranasinghe, *et al.*, “Charge tunable gaas quantum dots in a photonic nip diode,” *Nanomaterials*, vol. 11, no. 10, p. 2703, 2021.
- [27] L. Zhai, M. C. Löbl, G. N. Nguyen, J. Ritzmann, A. Javadi, C. Spinnler, A. D. Wieck, A. Ludwig, and R. J. Warburton, “Low-noise gaas quantum dots for quantum photonics,” *Nature communications*, vol. 11, no. 1, pp. 1–8, 2020.
- [28] E. Schöll, L. Hanschke, L. Schweickert, K. D. Zeuner, M. Reindl, S. F. Covre da Silva, T. Lettner, R. Trotta, J. J. Finley, K. Müller, *et al.*, “Resonance fluorescence of gaas quantum dots with near-unity photon indistinguishability,” *Nano letters*, vol. 19, no. 4, pp. 2404–2410, 2019.
- [29] C. Heyn, A. Stemmann, T. Köppen, C. Strelow, T. Kipp, M. Grave, S. Mendach, and W. Hansen, “Highly uniform and strain-free gaas quantum dots fabricated by filling of self-assembled nanoholes,” *Applied Physics Letters*, vol. 94, no. 18, p. 183113, 2009.
- [30] D. Huber, M. Reindl, S. F. C. Da Silva, C. Schimpf, J. Martín-Sánchez, H. Huang, G. Piredda, J. Edlinger, A. Rastelli, and R. Trotta, “Strain-tunable gaas quantum dot: A nearly dephasing-free source of entangled photon pairs on demand,” *Physical review letters*, vol. 121, no. 3, p. 033902, 2018.
- [31] J. Plumhof, V. Křápek, L. Wang, A. Schliwa, D. Bimberg, A. Rastelli, and O. Schmidt, “Experimental investigation and modeling of the fine structure splitting of neutral excitons in strain-free gaas/al x ga 1- x as quantum dots,” *Physical Review B*, vol. 81, no. 12, p. 121309, 2010.
- [32] B. Urbaszek, X. Marie, T. Amand, O. Krebs, P. Voisin, P. Maletinsky, A. Högele, and A. Imamoglu, “Nuclear spin physics in quantum dots: An optical investigation,” *Reviews of Modern Physics*, vol. 85, no. 1, p. 79, 2013.

- [33] N. Ha, T. Mano, Y.-L. Chou, Y.-N. Wu, S.-J. Cheng, J. Bocquel, P. M. Koenraad, A. Ohtake, Y. Sakuma, K. Sakoda, *et al.*, “Size-dependent line broadening in the emission spectra of single GaAs quantum dots: Impact of surface charge on spectral diffusion,” *Physical Review B*, vol. 92, no. 7, p. 075306, 2015.
- [34] A. Ulhaq, Q. Duan, E. Zallo, F. Ding, O. G. Schmidt, A. Tartakovskii, M. Skolnick, and E. A. Chekhovich, “Vanishing electron g factor and long-lived nuclear spin polarization in weakly strained nanohole-filled GaAs/AlGaAs quantum dots,” *Physical Review B*, vol. 93, no. 16, p. 165306, 2016.
- [35] E. A. Chekhovich, S. F. C. da Silva, and A. Rastelli, “Nuclear spin quantum register in an optically active semiconductor quantum dot,” *Nature Nanotechnology*, vol. 15, no. 12, pp. 999–1004, 2020.
- [36] L. Zaporski, N. Shofer, J. H. Bodey, S. Manna, G. Gillard, M. H. Appel, C. Schimpf, S. F. Covre da Silva, J. Jarman, G. Delamare, *et al.*, “Ideal refocusing of an optically active spin qubit under strong hyperfine interactions,” *Nature Nanotechnology*, pp. 1–7, 2023.
- [37] Y. Huo, A. Rastelli, and O. Schmidt, “Ultra-small excitonic fine structure splitting in highly symmetric quantum dots on GaAs (001) substrate,” *Applied Physics Letters*, vol. 102, no. 15, p. 152105, 2013.
- [38] J. Liu, R. Su, Y. Wei, B. Yao, S. F. C. da Silva, Y. Yu, J. Iles-Smith, K. Srinivasan, A. Rastelli, J. Li, *et al.*, “A solid-state source of strongly entangled photon pairs with high brightness and indistinguishability,” *Nature nanotechnology*, vol. 14, no. 6, pp. 586–593, 2019.
- [39] H. Wang, H. Hu, T.-H. Chung, J. Qin, X. Yang, J.-P. Li, R.-Z. Liu, H.-S. Zhong, Y.-M. He, X. Ding, *et al.*, “On-demand semiconductor source of entangled photons which simultaneously has high fidelity, efficiency, and indistinguishability,” *Physical review letters*, vol. 122, no. 11, p. 113602, 2019.
- [40] D. Huber, M. Reindl, Y. Huo, H. Huang, J. S. Wildmann, O. G. Schmidt, A. Rastelli, and R. Trotta, “Highly indistinguishable and strongly entangled photons from symmetric GaAs quantum dots,” *Nature communications*, vol. 8, no. 1, p. 15506, 2017.
- [41] C. Schimpf, M. Reindl, F. Basso Basset, K. D. Jöns, R. Trotta, and A. Rastelli, “Quantum dots as potential sources of strongly entangled photons: Perspectives and challenges for applications in quantum networks,” *Applied Physics Letters*, vol. 118, no. 10, p. 100502, 2021.
- [42] P. G. Kwiat, K. Mattle, H. Weinfurter, A. Zeilinger, A. V. Sergienko, and Y. Shih, “New high-intensity source of polarization-entangled photon pairs,” *Physical Review Letters*, vol. 75, no. 24, p. 4337, 1995.
- [43] K. Tiurev, M. H. Appel, P. L. Mirambell, M. B. Lauritzen, A. Tiranov, P. Lodahl, and A. S. Sørensen, “High-fidelity multiphoton-entangled cluster state with

- solid-state quantum emitters in photonic nanostructures,” *Physical Review A*, vol. 105, no. 3, p. L030601, 2022.
- [44] P. Lodahl, S. Mahmoodian, S. Stobbe, A. Rauschenbeutel, P. Schneeweiss, J. Volz, H. Pichler, and P. Zoller, “Chiral quantum optics,” *Nature*, vol. 541, no. 7638, pp. 473–480, 2017.
- [45] T. Lettner, K. D. Zeuner, E. Schoöll, H. Huang, S. Scharmer, S. F. C. da Silva, S. Gyger, L. Schweickert, A. Rastelli, K. D. Jöns, *et al.*, “Gaas quantum dot in a parabolic microcavity tuned to 87rb d1,” *ACS photonics*, vol. 7, no. 1, pp. 29–35, 2019.
- [46] L. Midolo, T. Pregolato, G. Kiršanskè, and S. Stobbe, “Soft-mask fabrication of gallium arsenide nanomembranes for integrated quantum photonics,” *Nanotechnology*, vol. 26, no. 48, p. 484002, 2015.
- [47] K. Stannigel, P. Rabl, and P. Zoller, “Driven-dissipative preparation of entangled states in cascaded quantum-optical networks,” *New Journal of Physics*, vol. 14, no. 6, p. 063014, 2012.
- [48] K. Xia, G. Lu, G. Lin, Y. Cheng, Y. Niu, S. Gong, J. Twamley, *et al.*, “Reversible nonmagnetic single-photon isolation using unbalanced quantum coupling,” *Physical Review A*, vol. 90, no. 4, p. 043802, 2014.
- [49] C. Sayrin, C. Junge, R. Mitsch, B. Albrecht, D. O’Shea, P. Schneeweiss, J. Volz, and A. Rauschenbeutel, “Nanophotonic optical isolator controlled by the internal state of cold atoms,” *Physical Review X*, vol. 5, no. 4, p. 041036, 2015.
- [50] M. Scheucher, A. Hilico, E. Will, J. Volz, and A. Rauschenbeutel, “Quantum optical circulator controlled by a single chirally coupled atom,” *Science*, vol. 354, no. 6319, pp. 1577–1580, 2016.
- [51] A. B. Young, A. C. T. Thijssen, D. M. Beggs, P. Androvitsaneas, L. Kuipers, J. G. Rarity, S. Hughes, and R. Oulton, “Polarization engineering in photonic crystal waveguides for spin-photon entanglers,” *Phys. Rev. Lett.*, vol. 115, p. 153901, Oct 2015.
- [52] C. P. Dietrich, A. Fiore, M. G. Thompson, M. Kamp, and S. Höfling, “Gaas integrated quantum photonics: Towards compact and multi-functional quantum photonic integrated circuits,” *Laser & Photonics Reviews*, vol. 10, no. 6, pp. 870–894, 2016.
- [53] X.-L. Qi and S.-C. Zhang, “Topological insulators and superconductors,” *Reviews of Modern Physics*, vol. 83, no. 4, p. 1057, 2011.
- [54] M. Z. Hasan and C. L. Kane, “Colloquium: topological insulators,” *Reviews of modern physics*, vol. 82, no. 4, p. 3045, 2010.
- [55] B. Bradlyn, L. Elcoro, J. Cano, M. Vergniory, Z. Wang, C. Felser, M. Aroyo, and B. A. Bernevig, “Topological quantum chemistry,” *Nature*, vol. 547, no. 7663, pp. 298–305, 2017.

- [56] L. Lu, J. D. Joannopoulos, and M. Soljačić, “Topological photonics,” *Nature photonics*, vol. 8, no. 11, pp. 821–829, 2014.
- [57] T. Ozawa, H. M. Price, A. Amo, N. Goldman, M. Hafezi, L. Lu, M. C. Rechtsman, D. Schuster, J. Simon, O. Zilberberg, *et al.*, “Topological photonics,” *Reviews of Modern Physics*, vol. 91, no. 1, p. 015006, 2019.
- [58] A. B. Khanikaev and G. Shvets, “Two-dimensional topological photonics,” *Nature photonics*, vol. 11, no. 12, pp. 763–773, 2017.
- [59] A. B. Khanikaev, S. H. Mousavi, W.-K. Tse, M. Kargarian, A. H. MacDonald, and G. Shvets, “Photonic topological insulators,” *Nature materials*, vol. 12, no. 3, pp. 233–239, 2013.
- [60] S. Raghu and F. D. M. Haldane, “Analogues of quantum-hall-effect edge states in photonic crystals,” *Physical Review A*, vol. 78, no. 3, p. 033834, 2008.
- [61] M. Hafezi, E. A. Demler, M. D. Lukin, and J. M. Taylor, “Robust optical delay lines with topological protection,” *Nature Physics*, vol. 7, p. 907–912, Aug 2011.
- [62] Z. Wang, Y. Chong, J. D. Joannopoulos, and M. Soljačić, “Observation of unidirectional backscattering-immune topological electromagnetic states,” *Nature*, vol. 461, no. 7265, pp. 772–775, 2009.
- [63] F. D. M. Haldane and S. Raghu, “Possible realization of directional optical waveguides in photonic crystals with broken time-reversal symmetry,” *Phys. Rev. Lett.*, vol. 100, p. 013904, Jan 2008.
- [64] S. A. Skirlo, L. Lu, and M. Soljac, “Multimode one-way waveguides of large chern numbers,” *Phys. Rev. Lett.*, vol. 113, p. 113904, Sep 2014.
- [65] X.-T. He, E.-T. Liang, J.-J. Yuan, H.-Y. Qiu, X.-D. Chen, F.-L. Zhao, and J.-W. Dong, “A silicon-on-insulator slab for topological valley transport,” *Nature communications*, vol. 10, no. 1, pp. 1–9, 2019.
- [66] J. Li, R.-L. Chu, J. K. Jain, and S.-Q. Shen, “Topological anderson insulator,” *Physical review letters*, vol. 102, no. 13, p. 136806, 2009.
- [67] F. Gao, H. Xue, Z. Yang, K. Lai, Y. Yu, X. Lin, Y. Chong, G. Shvets, and B. Zhang, “Topologically protected refraction of robust kink states in valley photonic crystals,” *Nature Physics*, vol. 14, no. 2, pp. 140–144, 2018.
- [68] T. Ma and G. Shvets, “All-si valley-hall photonic topological insulator,” *New Journal of Physics*, vol. 18, no. 2, p. 025012, 2016.
- [69] J.-W. Dong, X.-D. Chen, H. Zhu, Y. Wang, and X. Zhang, “Valley photonic crystals for control of spin and topology,” *Nature materials*, vol. 16, no. 3, pp. 298–302, 2017.
- [70] X.-D. Chen, F.-L. Zhao, M. Chen, and J.-W. Dong, “Valley-contrasting physics in all-dielectric photonic crystals: Orbital angular momentum and topological propagation,” *Physical Review B*, vol. 96, no. 2, p. 020202, 2017.

- [71] X. Wu, Y. Meng, J. Tian, Y. Huang, H. Xiang, D. Han, and W. Wen, “Direct observation of valley-polarized topological edge states in designer surface plasmon crystals,” *Nature communications*, vol. 8, no. 1, p. 1304, 2017.
- [72] L. Ye, Y. Yang, Z. Hong Hang, C. Qiu, and Z. Liu, “Observation of valley-selective microwave transport in photonic crystals,” *Applied Physics Letters*, vol. 111, no. 25, p. 251107, 2017.
- [73] S. Barik, A. Karasahin, C. Flower, T. Cai, H. Miyake, W. DeGottardi, M. Hafezi, and E. Waks, “A topological quantum optics interface,” *Science*, vol. 359, no. 6376, pp. 666–668, 2018.
- [74] T. Yamaguchi, Y. Ota, R. Katsumi, K. Watanabe, S. Ishida, A. Osada, Y. Arakawa, and S. Iwamoto, “Gaas valley photonic crystal waveguide with light-emitting inas quantum dots,” *Applied Physics Express*, vol. 12, no. 6, p. 062005, 2019.
- [75] M. I. Shalae, W. Walasik, A. Tsukernik, Y. Xu, and N. M. Litchinitser, “Robust topologically protected transport in photonic crystals at telecommunication wavelengths,” *Nature nanotechnology*, vol. 14, no. 1, pp. 31–34, 2019.
- [76] M. Hafezi, S. Mittal, J. Fan, A. Migdall, and J. Taylor, “Imaging topological edge states in silicon photonics,” *Nature Photonics*, vol. 7, no. 12, pp. 1001–1005, 2013.
- [77] S. Barik, A. Karasahin, S. Mittal, E. Waks, and M. Hafezi, “Chiral quantum optics using a topological resonator,” *Physical Review B*, vol. 101, no. 20, p. 205303, 2020.
- [78] M. J. Mehrabad, A. P. Foster, R. Dost, E. Clarke, P. K. Patil, A. M. Fox, M. S. Skolnick, and L. R. Wilson, “Chiral topological photonics with an embedded quantum emitter,” *Optica*, vol. 7, no. 12, pp. 1690–1696, 2020.
- [79] M. Saba, S. Wong, M. Elman, S. S. Oh, and O. Hess, “Nature of topological protection in photonic spin and valley hall insulators,” *Phys. Rev. B*, vol. 101, p. 054307, Feb 2020.
- [80] N. Tomm, A. Javadi, N. O. Antoniadis, D. Najer, M. C. Löbl, A. R. Korsch, R. Schott, S. R. Valentin, A. D. Wieck, A. Ludwig, *et al.*, “A bright and fast source of coherent single photons,” *Nature Nanotechnology*, vol. 16, no. 4, pp. 399–403, 2021.
- [81] X. Ding, Y. He, Z.-C. Duan, N. Gregersen, M.-C. Chen, S. Unsleber, S. Maier, C. Schneider, M. Kamp, S. Höfling, *et al.*, “On-demand single photons with high extraction efficiency and near-unity indistinguishability from a resonantly driven quantum dot in a micropillar,” *Physical review letters*, vol. 116, no. 2, p. 020401, 2016.
- [82] N. Somaschi, V. Giesz, L. De Santis, J. Lored, M. P. Almeida, G. Hornecker, S. L. Portalupi, T. Grange, C. Anton, J. Demory, *et al.*, “Near-optimal single-photon sources in the solid state,” *Nature Photonics*, vol. 10, no. 5, pp. 340–345, 2016.

- [83] F. Liu, A. J. Brash, J. O'Hara, L. M. Martins, C. L. Phillips, R. J. Coles, B. Royall, E. Clarke, C. Bentham, N. Prtljaga, *et al.*, "High purcell factor generation of indistinguishable on-chip single photons," *Nature nanotechnology*, vol. 13, no. 9, pp. 835–840, 2018.
- [84] H. Wang, Y.-M. He, T.-H. Chung, H. Hu, Y. Yu, S. Chen, X. Ding, M.-C. Chen, J. Qin, X. Yang, *et al.*, "Towards optimal single-photon sources from polarized microcavities," *Nature Photonics*, vol. 13, no. 11, pp. 770–775, 2019.
- [85] W. Gao, P. Fallahi, E. Togan, J. Miguel-Sánchez, and A. Imamoglu, "Observation of entanglement between a quantum dot spin and a single photon," *Nature*, vol. 491, no. 7424, pp. 426–430, 2012.
- [86] R. Stockill, M. Stanley, L. Huthmacher, E. Clarke, M. Hugues, A. Miller, C. Matthiesen, C. Le Gall, and M. Atatüre, "Phase-tuned entangled state generation between distant spin qubits," *Physical review letters*, vol. 119, no. 1, p. 010503, 2017.
- [87] J. Marquez, L. Geelhaar, and K. Jacobi, "Atomically resolved structure of inas quantum dots," *Applied Physics Letters*, vol. 78, no. 16, pp. 2309–2311, 2001.
- [88] R. Keil, M. Zopf, Y. Chen, B. Höfer, J. Zhang, F. Ding, and O. G. Schmidt, "Solid-state ensemble of highly entangled photon sources at rubidium atomic transitions," *Nature communications*, vol. 8, no. 1, p. 15501, 2017.
- [89] E. Peter, P. Senellart, D. Martrou, A. Lemaître, J. Hours, J. Gérard, and J. Bloch, "Exciton-photon strong-coupling regime for a single quantum dot embedded in a microcavity," *Physical review letters*, vol. 95, no. 6, p. 067401, 2005.
- [90] G. Kiršanskė, H. Thyrrstrup, R. S. Daveau, C. L. Dreeßen, T. Pregnolato, L. Midolo, P. Tighineanu, A. Javadi, S. Stobbe, R. Schott, *et al.*, "Indistinguishable and efficient single photons from a quantum dot in a planar nanobeam waveguide," *Physical Review B*, vol. 96, no. 16, p. 165306, 2017.
- [91] K. H. Madsen, S. Ates, J. Liu, A. Javadi, S. M. Albrecht, I. Yeo, S. Stobbe, and P. Lodahl, "Efficient out-coupling of high-purity single photons from a coherent quantum dot in a photonic-crystal cavity," *Phys. Rev. B*, vol. 90, p. 155303, Oct 2014.
- [92] A. V. Kuhlmann, J. H. Prechtel, J. Houel, A. Ludwig, D. Reuter, A. D. Wieck, and R. J. Warburton, "Transform-limited single photons from a single quantum dot," *Nature communications*, vol. 6, no. 1, pp. 1–6, 2015.
- [93] F. T. Pedersen, Y. Wang, C. T. Olesen, S. Scholz, A. D. Wieck, A. Ludwig, M. C. LObl, R. J. Warburton, L. Midolo, R. Uppu, *et al.*, "Near transform-limited quantum dot linewidths in a broadband photonic crystal waveguide," *ACS Photonics*, vol. 7, no. 9, pp. 2343–2349, 2020.

- [94] C. Santori, D. Fattal, J. Vučković, G. S. Solomon, and Y. Yamamoto, “Indistinguishable photons from a single-photon device,” *nature*, vol. 419, no. 6907, pp. 594–597, 2002.
- [95] R. Stockill, C. Le Gall, C. Matthiesen, L. Huthmacher, E. Clarke, M. Hugues, and M. Atatüre, “Quantum dot spin coherence governed by a strained nuclear environment,” *Nature communications*, vol. 7, no. 1, pp. 1–7, 2016.
- [96] N. Sangouard, C. Simon, H. De Riedmatten, and N. Gisin, “Quantum repeaters based on atomic ensembles and linear optics,” *Reviews of Modern Physics*, vol. 83, no. 1, p. 33, 2011.
- [97] T. Mano, M. Abbarchi, T. Kuroda, C. Mastrandrea, A. Vinattieri, S. Sanguinetti, K. Sakoda, and M. Gurioli, “Ultra-narrow emission from single gaas self-assembled quantum dots grown by droplet epitaxy,” *Nanotechnology*, vol. 20, no. 39, p. 395601, 2009.
- [98] Z. M. Wang, B. Liang, K. Sablon, and G. Salamo, “Nanoholes fabricated by self-assembled gallium nanodrive on gaas (100),” *Applied physics letters*, vol. 90, no. 11, p. 113120, 2007.
- [99] M. Hosseini, B. M. Sparkes, G. Campbell, P. K. Lam, and B. C. Buchler, “High efficiency coherent optical memory with warm rubidium vapour,” *Nature communications*, vol. 2, no. 1, pp. 1–5, 2011.
- [100] F. Basso Basset, S. Bietti, M. Reindl, L. Esposito, A. Fedorov, D. Huber, A. Rastelli, E. Bonera, R. Trotta, and S. Sanguinetti, “High-yield fabrication of entangled photon emitters for hybrid quantum networking using high-temperature droplet epitaxy,” *Nano letters*, vol. 18, no. 1, pp. 505–512, 2018.
- [101] M. Muller, S. Bounouar, K. Jons, M. Glasl, and P. Michler, “On-demand generation of indistinguishable polarization-entangled photon pairs. nat. photonics 8, 224–228 (2014),” 2013.
- [102] P. Mooney, “Deep donor levels (dx centers) in iii-v semiconductors,” *Journal of Applied Physics*, vol. 67, no. 3, pp. R1–R26, 1990.
- [103] L. Schweickert, K. D. Jöns, K. D. Zeuner, S. F. Covre da Silva, H. Huang, T. Lettner, M. Reindl, J. Zichi, R. Trotta, A. Rastelli, *et al.*, “On-demand generation of background-free single photons from a solid-state source,” *Applied Physics Letters*, vol. 112, no. 9, p. 093106, 2018.
- [104] E. Chekhovich, M. Makhonin, A. Tartakovskii, A. Yacoby, H. Bluhm, K. Nowack, and L. Vandersypen, “Nuclear spin effects in semiconductor quantum dots,” *Nature materials*, vol. 12, no. 6, pp. 494–504, 2013.
- [105] D. Gangloff, G. Ethier-Majcher, C. Lang, E. Denning, J. Bodey, D. Jackson, E. Clarke, M. Hugues, C. Le Gall, and M. Atatüre, “Quantum interface of an electron and a nuclear ensemble,” *Science*, vol. 364, no. 6435, pp. 62–66, 2019.

- [106] A. V. Kuhlmann, J. Houel, A. Ludwig, L. Greuter, D. Reuter, A. D. Wieck, M. Poggio, and R. J. Warburton, “Charge noise and spin noise in a semiconductor quantum device,” *Nature Physics*, vol. 9, no. 9, pp. 570–575, 2013.
- [107] R. B. Patel, A. J. Bennett, I. Farrer, C. A. Nicoll, D. A. Ritchie, and A. J. Shields, “Two-photon interference of the emission from electrically tunable remote quantum dots,” *Nature photonics*, vol. 4, no. 9, pp. 632–635, 2010.
- [108] D. Najer, I. Söllner, P. Sekatski, V. Dolique, M. C. Löbl, D. Riedel, R. Schott, S. Starosielec, S. R. Valentin, A. D. Wieck, *et al.*, “A gated quantum dot strongly coupled to an optical microcavity,” *Nature*, vol. 575, no. 7784, pp. 622–627, 2019.
- [109] I. Schwartz, D. Cogan, E. R. Schmidgall, Y. Don, L. Gantz, O. Kenneth, N. H. Lindner, and D. Gershoni, “Deterministic generation of a cluster state of entangled photons,” *Science*, vol. 354, no. 6311, pp. 434–437, 2016.
- [110] S. M. Girvin and K. Yang, *Modern condensed matter physics*. Cambridge University Press, 2019.
- [111] Y. Peter and M. Cardona, *Fundamentals of semiconductors: physics and materials properties*. Springer Science & Business Media, 2010.
- [112] H. Eisele, A. Lenz, R. Heitz, R. Timm, M. Dähne, Y. Temko, T. Suzuki, and K. Jacobi, “Change of inas/gaas quantum dot shape and composition during capping,” *Journal of Applied Physics*, vol. 104, no. 12, p. 124301, 2008.
- [113] T. Belhadj, T. Amand, A. Kunold, C.-M. Simon, T. Kuroda, M. Abbarchi, T. Mano, K. Sakoda, S. Kunz, X. Marie, *et al.*, “Impact of heavy hole-light hole coupling on optical selection rules in gaas quantum dots,” *Applied Physics Letters*, vol. 97, no. 5, p. 051111, 2010.
- [114] G. Bester, S. Nair, and A. Zunger, “Pseudopotential calculation of the excitonic fine structure of million-atom self-assembled in 1-x ga x a s/g a a s quantum dots,” *Physical Review B*, vol. 67, no. 16, p. 161306, 2003.
- [115] Y. Huo, B. Witek, S. Kumar, J. Cardenas, J. Zhang, N. Akopian, R. Singh, E. Zallo, R. Grifone, D. Kriegner, *et al.*, “A light-hole exciton in a quantum dot,” *Nature Physics*, vol. 10, no. 1, pp. 46–51, 2014.
- [116] M. Vidal, M. Durnev, L. Bouet, T. Amand, M. Glazov, E. Ivchenko, P. Zhou, G. Wang, T. Mano, T. Kuroda, *et al.*, “Hyperfine coupling of hole and nuclear spins in symmetric (111)-grown gaas quantum dots,” *Physical Review B*, vol. 94, no. 12, p. 121302, 2016.
- [117] X. Yuan, F. Weyhausen-Brinkmann, J. Martín-Sánchez, G. Piredda, V. Křápek, Y. Huo, H. Huang, C. Schimpf, O. G. Schmidt, J. Edlinger, *et al.*, “Uniaxial stress flips the natural quantization axis of a quantum dot for integrated quantum photonics,” *Nature communications*, vol. 9, no. 1, p. 3058, 2018.

- [118] J. Johansen, S. Stobbe, I. S. Nikolaev, T. Lund-Hansen, P. T. Kristensen, J. M. Hvam, W. L. Vos, and P. Lodahl, "Size dependence of the wavefunction of self-assembled inas quantum dots from time-resolved optical measurements," *Physical Review B*, vol. 77, no. 7, p. 073303, 2008.
- [119] S. M. Sze, Y. Li, and K. K. Ng, *Physics of semiconductor devices*. John Wiley & sons, 2021.
- [120] I. Vurgaftman, J. á. Meyer, and L. á. Ram-Mohan, "Band parameters for iii-v compound semiconductors and their alloys," *Journal of applied physics*, vol. 89, no. 11, pp. 5815–5875, 2001.
- [121] M. Bayer, G. Ortner, O. Stern, A. Kuther, A. Gorbunov, A. Forchel, P. Hawrylak, S. Fafard, K. Hinzer, T. Reinecke, *et al.*, "Fine structure of neutral and charged excitons in self-assembled in (ga) as/(al) gaas quantum dots," *Physical Review B*, vol. 65, no. 19, p. 195315, 2002.
- [122] R. Seguin, A. Schliwa, S. Rodt, K. Pötschke, U. Pohl, and D. Bimberg, "Size-dependent fine-structure splitting in self-organized inas/gaas quantum dots," *Physical review letters*, vol. 95, no. 25, p. 257402, 2005.
- [123] E. Poem, Y. Kodriano, C. Tradonsky, N. Lindner, B. Gerardot, P. Petroff, and D. Gershoni, "Accessing the dark exciton with light," *Nature physics*, vol. 6, no. 12, pp. 993–997, 2010.
- [124] Y. Huo, V. Křápek, A. Rastelli, and O. Schmidt, "Volume dependence of excitonic fine structure splitting in geometrically similar quantum dots," *Physical Review B*, vol. 90, no. 4, p. 041304, 2014.
- [125] J. Johansen, B. Julsgaard, S. Stobbe, J. M. Hvam, and P. Lodahl, "Probing long-lived dark excitons in self-assembled quantum dots," *Physical Review B*, vol. 81, no. 8, p. 081304, 2010.
- [126] G. Juska, V. Dimastrodonato, L. O. Mereni, A. Gocalinska, and E. Pelucchi, "Towards quantum-dot arrays of entangled photon emitters," *Nature Photonics*, vol. 7, no. 7, pp. 527–531, 2013.
- [127] T. Kuroda, T. Mano, N. Ha, H. Nakajima, H. Kumano, B. Urbaszek, M. Jo, M. Abbarchi, Y. Sakuma, K. Sakoda, *et al.*, "Symmetric quantum dots as efficient sources of highly entangled photons: Violation of bell's inequality without spectral and temporal filtering," *Physical Review B*, vol. 88, no. 4, p. 041306, 2013.
- [128] A. Bennett, y. M. Pooley, n. R. Stevenson, M. Ward, R. Patel, A. B. de La Giroday, N. Sköld, I. Farrer, C. Nicoll, D. Ritchie, *et al.*, "Electric-field-induced coherent coupling of the exciton states in a single quantum dot," *Nature Physics*, vol. 6, no. 12, pp. 947–950, 2010.
- [129] R. J. Warburton, "Single spins in self-assembled quantum dots," *Nature materials*, vol. 12, no. 6, pp. 483–493, 2013.

- [130] K. Roszak, V. M. Axt, T. Kuhn, and P. Machnikowski, "Erratum: exciton spin decay in quantum dots to bright and dark states [phys. rev. b 76, 195324 (2007)]," *Physical Review B*, vol. 77, no. 24, p. 249905, 2008.
- [131] Y.-H. Liao, J. I. Climente, and S.-J. Cheng, "Dominant channels of exciton spin relaxation in photoexcited self-assembled (in, ga) as quantum dots," *Physical Review B*, vol. 83, no. 16, p. 165317, 2011.
- [132] J. Smith, P. Dalgarno, R. Warburton, A. Govorov, K. Karrai, B. Gerardot, and P. Petroff, "Voltage control of the spin dynamics of an exciton in a semiconductor quantum dot," *Physical review letters*, vol. 94, no. 19, p. 197402, 2005.
- [133] H. Thyrrestrup, L. Sapienza, and P. Lodahl, "Extraction of the β -factor for single quantum dots coupled to a photonic crystal waveguide," *Applied Physics Letters*, vol. 96, no. 23, p. 231106, 2010.
- [134] A. Javadi, S. Mahmoodian, I. Söllner, and P. Lodahl, "Numerical modeling of the coupling efficiency of single quantum emitters in photonic-crystal waveguides," *JOSA B*, vol. 35, no. 3, pp. 514–522, 2018.
- [135] C. Hopfmann, N. L. Sharma, W. Nie, R. Keil, F. Ding, and O. G. Schmidt, "Heralded preparation of spin qubits in droplet-etched gaas quantum dots using quasiresonant excitation," *Phys. Rev. B*, vol. 104, p. 075301, Aug 2021.
- [136] M. Reindl, J. H. Weber, D. Huber, C. Schimpf, S. F. C. da Silva, S. L. Portalupi, R. Trotta, P. Michler, and A. Rastelli, "Highly indistinguishable single photons from incoherently excited quantum dots," *Physical Review B*, vol. 100, no. 15, p. 155420, 2019.
- [137] J. Yan, C. Chen, X.-D. Zhang, Y.-T. Wang, H.-G. Babin, A. D. Wieck, A. Ludwig, Y. Meng, X. Hu, H. Duan, *et al.*, "Coherent control of a high-orbital hole in a semiconductor quantum dot with near-unity fidelity," *arXiv preprint arXiv:2212.10749*, 2022.
- [138] P. Borri, W. Langbein, S. Schneider, U. Woggon, R. L. Sellin, D. Ouyang, and D. Bimberg, "Ultralong dephasing time in ingaas quantum dots," *Physical Review Letters*, vol. 87, no. 15, p. 157401, 2001.
- [139] L. Chu, M. Arzberger, G. Böhm, and G. Abstreiter, "Influence of growth conditions on the photoluminescence of self-assembled inas/gaas quantum dots," *Journal of Applied Physics*, vol. 85, no. 4, pp. 2355–2362, 1999.
- [140] A. Kurzmann, A. Ludwig, A. D. Wieck, A. Lorke, and M. Geller, "Auger recombination in self-assembled quantum dots: quenching and broadening of the charged exciton transition," *Nano letters*, vol. 16, no. 5, pp. 3367–3372, 2016.
- [141] T. Karin, X. Linpeng, A. K. Rai, A. Ludwig, A. D. Wieck, and K.-M. C. Fu, "Optical visualization of radiative recombination at partial dislocations in gaas," in *2016 IEEE 43rd Photovoltaic Specialists Conference (PVSC)*, pp. 1989–1992, IEEE, 2016.

- [142] P. Tighineanu, R. Daveau, E. H. Lee, J. D. Song, S. Stobbe, and P. Lodahl, “Decay dynamics and exciton localization in large GaAs quantum dots grown by droplet epitaxy,” *Phys. Rev. B*, vol. 88, p. 155320, Oct 2013.
- [143] B. U. Lehner, T. Seidelmann, G. Undeutsch, C. Schimpf, S. Manna, M. Gawelczyk, S. F. Covre da Silva, X. Yuan, S. Stroj, D. E. Reiter, *et al.*, “Beyond the four-level model: Dark and hot states in quantum dots degrade photonic entanglement,” *Nano Letters*, vol. 23, no. 4, pp. 1409–1415, 2023.
- [144] D. Huber, B. U. Lehner, D. Csontosová, M. Reindl, S. Schuler, S. F. Covre da Silva, P. Klenovský, and A. Rastelli, “Single-particle-picture breakdown in laterally weakly confining GaAs quantum dots,” *Phys. Rev. B*, vol. 100, p. 235425, Dec 2019.
- [145] X. Yuan, S. F. C. da Silva, D. Csontosova, H. Huang, C. Schimpf, M. Reindl, J. Lu, Z. Ni, A. Rastelli, and P. Klenovsky, “GaAs quantum dots under quasi-uniaxial stress: experiment and theory,” *arXiv preprint arXiv:2210.06999*, 2022.
- [146] S. Stobbe, T. Schlereth, S. Höfling, A. Forchel, J. M. Hvam, and P. Lodahl, “Large quantum dots with small oscillator strength,” *Physical Review B*, vol. 82, no. 23, p. 233302, 2010.
- [147] S. Stobbe, J. Johansen, P. T. Kristensen, J. M. Hvam, and P. Lodahl, “Frequency dependence of the radiative decay rate of excitons in self-assembled quantum dots: Experiment and theory,” *Physical Review B*, vol. 80, no. 15, p. 155307, 2009.
- [148] P. Tighineanu, A. S. Sørensen, S. Stobbe, and P. Lodahl, “Unraveling the mesoscopic character of quantum dots in nanophotonics,” *Physical review letters*, vol. 114, no. 24, p. 247401, 2015.
- [149] X.-L. Chu, T. Pregolato, R. Schott, A. D. Wieck, A. Ludwig, N. Rotenberg, and P. Lodahl, “Lifetimes and quantum efficiencies of quantum dots deterministically positioned in photonic-crystal waveguides,” *Advanced Quantum Technologies*, vol. 3, no. 11, p. 2000026, 2020.
- [150] M. Reindl, J. H. Weber, D. Huber, C. Schimpf, S. F. Covre da Silva, S. L. Portalupi, R. Trotta, P. Michler, and A. Rastelli, “Highly indistinguishable single photons from incoherently excited quantum dots,” *Phys. Rev. B*, vol. 100, p. 155420, Oct 2019.
- [151] R. J. Warburton, C. Schäfflein, D. Haft, F. Bickel, A. Lorke, K. Karrai, J. M. Garcia, W. Schoenfeld, and P. M. Petroff, “Optical emission from a charge-tunable quantum ring,” *Nature*, vol. 405, no. 6789, pp. 926–929, 2000.
- [152] M. C. Löbl, I. Söllner, A. Javadi, T. Pregolato, R. Schott, L. Midolo, A. V. Kuhlmann, S. Stobbe, A. D. Wieck, P. Lodahl, *et al.*, “Narrow optical linewidths and spin pumping on charge-tunable close-to-surface self-assembled quantum dots in an ultrathin diode,” *Physical Review B*, vol. 96, no. 16, p. 165440, 2017.

- [153] J. Q. Grim, A. S. Bracker, M. Zhalalutdinov, S. G. Carter, A. C. Kozen, M. Kim, C. S. Kim, J. T. Mlack, M. Yakes, B. Lee, *et al.*, “Scalable in operando strain tuning in nanophotonic waveguides enabling three-quantum-dot superradiance,” *Nature materials*, vol. 18, no. 9, pp. 963–969, 2019.
- [154] G. Wen, J. Lin, H. Jiang, and Z. Chen, “Quantum-confined stark effects in semiconductor quantum dots,” *Physical Review B*, vol. 52, no. 8, p. 5913, 1995.
- [155] S. Gyger, J. Zichi, L. Schweickert, A. W. Elshaari, S. Steinhauer, S. F. Covre da Silva, A. Rastelli, V. Zwiller, K. D. Jöns, and C. Errando-Herranz, “Reconfigurable photonics with on-chip single-photon detectors,” *Nature communications*, vol. 12, no. 1, p. 1408, 2021.
- [156] C. Bentham, I. Itskevich, R. Coles, B. Royall, E. Clarke, J. O’Hara, N. Prtljaga, A. Fox, M. Skolnick, and L. Wilson, “On-chip electrically controlled routing of photons from a single quantum dot,” *Applied Physics Letters*, vol. 106, no. 22, p. 221101, 2015.
- [157] L. Midolo, S. L. Hansen, W. Zhang, C. Papon, R. Schott, A. Ludwig, A. D. Wieck, P. Lodahl, and S. Stobbe, “Electro-optic routing of photons from a single quantum dot in photonic integrated circuits,” *Optics Express*, vol. 25, no. 26, pp. 33514–33526, 2017.
- [158] C. Papon, X. Zhou, H. Thyrrerstrup, Z. Liu, S. Stobbe, R. Schott, A. D. Wieck, A. Ludwig, P. Lodahl, and L. Midolo, “Nanomechanical single-photon routing,” *Optica*, vol. 6, no. 4, pp. 524–530, 2019.
- [159] J. Shin, Y.-C. Chang, and N. Dagli, “0.3 v drive voltage ga as/ al ga as substrate removed mach–zehnder intensity modulators,” *Applied Physics Letters*, vol. 92, no. 20, p. 201103, 2008.
- [160] R. Uppu, H. T. Eriksen, H. Thyrrerstrup, A. D. Uğurlu, Y. Wang, S. Scholz, A. D. Wieck, A. Ludwig, M. C. Löbl, R. J. Warburton, *et al.*, “On-chip deterministic operation of quantum dots in dual-mode waveguides for a plug-and-play single-photon source,” *Nature communications*, vol. 11, no. 1, p. 3782, 2020.
- [161] J. D. Joannopoulos, S. G. Johnson, J. N. Winn, and R. D. Meade, “Molding the flow of light,” *Princeton Univ. Press, Princeton, NJ [ua]*, 2008.
- [162] X. Zhou, I. Kulkova, T. Lund-Hansen, S. L. Hansen, P. Lodahl, and L. Midolo, “High-efficiency shallow-etched grating on gaas membranes for quantum photonic applications,” *Applied Physics Letters*, vol. 113, no. 25, p. 251103, 2018.
- [163] T. D. Ladd, F. Jelezko, R. Laflamme, Y. Nakamura, C. Monroe, and J. L. O’Brien, “Quantum computers,” *Nature*, vol. 464, no. 7285, pp. 45–53, 2010.
- [164] G. Roelkens, D. Vermeulen, F. Van Laere, S. Selvaraja, S. Scheerlinck, D. Tailaert, W. Bogaerts, P. Dumon, D. Van Thourhout, and R. Baets, “Bridging the gap between nanophotonic waveguide circuits and single mode optical fibers

- using diffractive grating structures,” *Journal of nanoscience and nanotechnology*, vol. 10, no. 3, pp. 1551–1562, 2010.
- [165] J. D. Joannopoulos, P. R. Villeneuve, and S. Fan, “Photonic crystals,” *Solid State Communications*, vol. 102, no. 2-3, pp. 165–173, 1997.
- [166] S. Molesky, Z. Lin, A. Y. Piggott, W. Jin, J. Vucković, and A. W. Rodriguez, “Inverse design in nanophotonics,” *Nature Photonics*, vol. 12, no. 11, pp. 659–670, 2018.
- [167] S. Hughes, L. Ramunno, J. F. Young, and J. Sipe, “Extrinsic optical scattering loss in photonic crystal waveguides: role of fabrication disorder and photon group velocity,” *Physical review letters*, vol. 94, no. 3, p. 033903, 2005.
- [168] J. Von Bergmann and H. Von Bergmann, “Foucault pendulum through basic geometry,” *American Journal of Physics*, vol. 75, no. 10, pp. 888–892, 2007.
- [169] A. Tomita and R. Y. Chiao, “Observation of berry’s topological phase by use of an optical fiber,” *Physical review letters*, vol. 57, no. 8, p. 937, 1986.
- [170] Z. Wang, Y. D. Chong, J. D. Joannopoulos, and M. Soljac, “Reflection-free one-way edge modes in a gyromagnetic photonic crystal,” *Phys. Rev. Lett.*, vol. 100, p. 013905, Jan 2008.
- [171] K. Fang, Z. Yu, and S. Fan, “Realizing effective magnetic field for photons by controlling the phase of dynamic modulation,” *Nature photonics*, vol. 6, no. 11, pp. 782–787, 2012.
- [172] L. Lu, L. Fu, J. D. Joannopoulos, and M. Soljac, “Weyl points and line nodes in gyroid photonic crystals,” *Nature photonics*, vol. 7, no. 4, pp. 294–299, 2013.
- [173] A. Tiranov, V. Angelopoulou, C. J. van Diepen, B. Schirnski, O. A. D. Sandberg, Y. Wang, L. Midolo, S. Scholz, A. D. Wieck, A. Ludwig, *et al.*, “Collective super- and subradiant dynamics between distant optical quantum emitters,” *Science*, vol. 379, no. 6630, pp. 389–393, 2023.
- [174] M. J. Collins, F. Zhang, R. Bojko, L. Chrostowski, and M. C. Rechtsman, “Integrated optical dirac physics via inversion symmetry breaking,” *Physical Review A*, vol. 94, no. 6, p. 063827, 2016.
- [175] E. Sauer, J. P. Vasco, and S. Hughes, “Theory of intrinsic propagation losses in topological edge states of planar photonic crystals,” *Phys. Rev. Research*, vol. 2, p. 043109, Oct 2020.
- [176] M. Shalaev, W. Walasik, and N. M. Litchinitser, “Experimental demonstration of valley-hall topological photonic crystal at telecommunication wavelengths,” in *CLEO: QELS_Fundamental Science*, pp. FM4Q–3, Optical Society of America, 2018.

- [177] H. Yoshimi, T. Yamaguchi, R. Katsumi, Y. Ota, Y. Arakawa, and S. Iwamoto, “Experimental demonstration of topological slow light waveguides in valley photonic crystals,” *Optics Express*, vol. 29, no. 9, pp. 13441–13450, 2021.
- [178] D. A. Steck, “Quantum and atom optics,” 2007.
- [179] P. Meystre and M. Sargent, *Elements of quantum optics*. Springer Science & Business Media, 2007.
- [180] S. M. Barnett, B. Huttner, R. Loudon, and R. Matloob, “Decay of excited atoms in absorbing dielectrics,” *Journal of Physics B: Atomic, Molecular and Optical Physics*, vol. 29, no. 16, p. 3763, 1996.
- [181] E. M. Purcell, “Spontaneous emission probabilities at radio frequencies,” in *Confined Electrons and Photons*, pp. 839–839, Springer, 1995.
- [182] S. Hughes, “Enhanced single-photon emission from quantum dots in photonic crystal waveguides and nanocavities,” *Optics letters*, vol. 29, no. 22, pp. 2659–2661, 2004.
- [183] B. Le Feber, N. Rotenberg, and L. Kuipers, “Nanophotonic control of circular dipole emission,” *Nature communications*, vol. 6, no. 1, pp. 1–6, 2015.
- [184] H. Thyrestrup, G. Kiršanskė, H. Le Jeannic, T. Pregolato, L. Zhai, L. Raahauge, L. Midolo, N. Rotenberg, A. Javadi, R. Schott, *et al.*, “Quantum optics with near-lifetime-limited quantum-dot transitions in a nanophotonic waveguide,” *Nano letters*, vol. 18, no. 3, pp. 1801–1806, 2018.
- [185] J.-P. Jahn, M. Munsch, L. Béguin, A. V. Kuhlmann, M. Renggli, Y. Huo, F. Ding, R. Trotta, M. Reindl, O. G. Schmidt, *et al.*, “An artificial rb atom in a semiconductor with lifetime-limited linewidth,” *Physical Review B*, vol. 92, no. 24, p. 245439, 2015.
- [186] B. Krummheuer, V. M. Axt, and T. Kuhn, “Theory of pure dephasing and the resulting absorption line shape in semiconductor quantum dots,” *Physical Review B*, vol. 65, no. 19, p. 195313, 2002.
- [187] A. Reigue, J. Iles-Smith, F. Lux, L. Monniello, M. Bernard, F. Margailan, A. Lemaitre, A. Martinez, D. P. S. McCutcheon, J. Mørk, R. Hosten, and V. Voliotis, “Probing electron-phonon interaction through two-photon interference in resonantly driven semiconductor quantum dots,” *Phys. Rev. Lett.*, vol. 118, p. 233602, Jun 2017.
- [188] E. V. Denning, J. Iles-Smith, N. Gregersen, and J. Mork, “Phonon effects in quantum dot single-photon sources,” *Optical Materials Express*, vol. 10, no. 1, pp. 222–239, 2020.
- [189] C. Gustin and S. Hughes, “Influence of electron-phonon scattering for an on-demand quantum dot single-photon source using cavity-assisted adiabatic passage,” *Phys. Rev. B*, vol. 96, p. 085305, Aug 2017.

- [190] P. Tighineanu, C. L. Dreeßen, C. Flindt, P. Lodahl, and A. S. Sørensen, “Phonon decoherence of quantum dots in photonic structures: Broadening of the zero-phonon line and the role of dimensionality,” *Physical Review Letters*, vol. 120, no. 25, p. 257401, 2018.
- [191] C. L. Dreeßen, C. Ouellet-Plamondon, P. Tighineanu, X. Zhou, L. Midolo, A. S. Sørensen, and P. Lodahl, “Suppressing phonon decoherence of high performance single-photon sources in nanophotonic waveguides,” *Quantum Science and Technology*, vol. 4, no. 1, p. 015003, 2018.
- [192] F. D. M. Haldane, “Nobel lecture: Topological quantum matter,” *Rev. Mod. Phys.*, vol. 89, p. 040502, Oct 2017.
- [193] S. Barik, A. Karasahin, S. Mittal, E. Waks, and M. Hafezi, “Chiral quantum optics using a topological resonator,” *Phys. Rev. B*, vol. 101, p. 205303, May 2020.
- [194] S. Arora, T. Bauer, R. Barczyk, E. Verhagen, and L. Kuipers, “Direct quantification of topological protection in symmetry-protected photonic edge states at telecom wavelengths,” *Light: Science & Applications*, vol. 10, no. 1, pp. 1–7, 2021.
- [195] Y. Plotnik, M. C. Rechtsman, D. Song, M. Heinrich, J. M. Zeuner, S. Nolte, Y. Lumer, N. Malkova, J. Xu, A. Szameit, *et al.*, “Observation of unconventional edge states in ‘photonic graphene’,” *Nature materials*, vol. 13, no. 1, pp. 57–62, 2014.
- [196] Y. Chen, Z. Lan, Z. Su, and J. Zhu, “Inverse design of photonic and phononic topological insulators: a review,” *Nanophotonics*, vol. 11, no. 19, pp. 4347–4362, 2022.
- [197] W.-S. Ruan, X.-T. He, F.-L. Zhao, and J.-W. Dong, “Analysis of unidirectional coupling in topological valley photonic crystal waveguides,” *Journal of Light-wave Technology*, vol. 39, no. 4, pp. 889–895, 2020.
- [198] G. He, Y. Qin, Q. Wang, M. Li, and C. Cai, “Multi-band acoustic topological insulator based on valley hall effect,” *Journal of Superconductivity and Novel Magnetism*, vol. 36, no. 1, pp. 163–170, 2023.
- [199] O. Florez, G. Arregui, M. Albrechtsen, R. Ng, J. Gomis-Bresco, S. Stobbe, C. Sotomayor-Torres, and P. D. García, “Engineering nanoscale hypersonic phonon transport,” *Nature Nanotechnology*, vol. 17, no. 9, pp. 947–951, 2022.
- [200] R. C. Ng, P. Nizet, D. Navarro-Urrios, G. Arregui, M. Albrechtsen, P. D. García, S. Stobbe, C. M. Sotomayor-Torres, and G. Madiot, “Intermodulation of optical frequency combs in a multimode optomechanical system,” *Preprint*, 2022.
- [201] E. Hecht, *Optics, 5e*. Addison-Wesley, 2002.

- [202] C. M. Patil, G. Arregui, M. Mechlenborg, X. Zhou, H. Alaeian, P. D. García, and S. Stobbe, "Observation of slow light in glide-symmetric photonic-crystal waveguides," *Optics Express*, vol. 30, no. 8, pp. 12565–12575, 2022.
- [203] K. Kuruma, H. Yoshimi, Y. Ota, R. Katsumi, M. Kakuda, Y. Arakawa, and S. Iwamoto, "Topologically-protected single-photon sources with topological slow light photonic crystal waveguides," *Laser & Photonics Reviews*, vol. 16, no. 8, p. 2200077, 2022.
- [204] E. Nussbaum, N. Rotenberg, and S. Hughes, "Optimizing the chiral purcell factor for unidirectional single-photon emitters in topological photonic crystal waveguides using inverse design," *Physical Review A*, vol. 106, no. 3, p. 033514, 2022.
- [205] R. Benevides, M. Ménard, G. S. Wiederhecker, and T. P. M. Alegre, "Ar/cl 2 etching of gaas optomechanical microdisks fabricated with positive electroresist," *Optical Materials Express*, vol. 10, no. 1, pp. 57–67, 2020.
- [206] I. P. González, L. E. Muñoz Camuñez, A. G. Taboada, C. Robles Urdiales, J. M. Ripalda Cobián, and P. A. Postigo Resa, "Fabrication of high quality factor gaas/inassb photonic crystal microcavities by inductively coupled plasma etching and fast wet etching," *Journal of Vacuum Science & Technology B, Nanotechnology and Microelectronics: Materials, Processing, Measurement, and Phenomena*, vol. 32, no. 1, p. 011204, 2014.
- [207] T. Figueiro, M. Saib, J.-H. Tortai, and P. Schiavone, "Psf calibration patterns selection based on sensitivity analysis," *Microelectronic engineering*, vol. 112, pp. 282–286, 2013.
- [208] C.-H. Liu, P. C. Ng, Y.-T. Shen, S.-W. Chien, and K.-Y. Tsai, "Impacts of point spread function accuracy on patterning prediction and proximity effect correction in low-voltage electron-beam-direct-write lithography," *Journal of Vacuum Science & Technology B, Nanotechnology and Microelectronics: Materials, Processing, Measurement, and Phenomena*, vol. 31, no. 2, p. 021605, 2013.
- [209] R. Wüest, P. Strasser, M. Jungo, F. Robin, D. Erni, and H. Jäckel, "An efficient proximity-effect correction method for electron-beam patterning of photonic-crystal devices," *Microelectronic Engineering*, vol. 67, pp. 182–188, 2003.
- [210] C. Anker Rosiek, G. Arregui, A. Vladimirova, M. Albrechtsen, B. Vosoughi Lahijani, R. Ellebæk Christiansen, and S. Stobbe, "Observation of strong backscattering in valley-Hall photonic topological interface modes," *arXiv e-prints*, p. arXiv:2206.11741, June 2022.
- [211] E. Nussbaum, E. Sauer, and S. Hughes, "Inverse design of broadband and lossless topological photonic crystal waveguide modes," *Optics Letters*, vol. 46, no. 7, pp. 1732–1735, 2021.

- [212] B. Orazbayev and R. Fleury, “Quantitative robustness analysis of topological edge modes in c6 and valley-hall metamaterial waveguides,” *Nanophotonics*, vol. 8, no. 8, pp. 1433–1441, 2019.
- [213] G. Arregui, J. Gomis-Bresco, C. M. Sotomayor-Torres, and P. D. Garcia, “Quantifying the robustness of topological slow light,” *Phys. Rev. Lett.*, vol. 126, p. 027403, Jan 2021.
- [214] M. I. Shalaev, W. Walasik, and N. M. Litchinitser, “Optically tunable topological photonic crystal,” *Optica*, vol. 6, no. 7, pp. 839–844, 2019.
- [215] A. Blanco-Redondo, B. Bell, D. Oren, B. J. Eggleton, and M. Segev, “Topological protection of biphoton states,” *Science*, vol. 362, no. 6414, pp. 568–571, 2018.
- [216] J. Jin, X. Yin, L. Ni, M. Soljačić, B. Zhen, and C. Peng, “Topologically enabled ultrahigh-q guided resonances robust to out-of-plane scattering,” *Nature*, vol. 574, no. 7779, pp. 501–504, 2019.
- [217] S. Schulz, L. O’Faolain, D. M. Beggs, T. P. White, A. Melloni, and T. F. Krauss, “Dispersion engineered slow light in photonic crystals: a comparison,” *Journal of Optics*, vol. 12, no. 10, p. 104004, 2010.
- [218] M. Arcari, I. Söllner, A. Javadi, S. Lindskov Hansen, S. Mahmoodian, J. Liu, H. Thyrrestrup, E. H. Lee, J. D. Song, S. Stobbe, and P. Lodahl, “Near-unity coupling efficiency of a quantum emitter to a photonic crystal waveguide,” *Phys. Rev. Lett.*, vol. 113, p. 093603, Aug 2014.
- [219] S. Hughes, L. Ramunno, J. F. Young, and J. E. Sipe, “Extrinsic optical scattering loss in photonic crystal waveguides: Role of fabrication disorder and photon group velocity,” *Phys. Rev. Lett.*, vol. 94, p. 033903, Jan 2005.
- [220] Z. F. Ezawa, *Quantum Hall effects: Field theoretical approach and related topics*. World Scientific Publishing Company, 2008.
- [221] E. Kuramochi, M. Notomi, S. Hughes, A. Shinya, T. Watanabe, and L. Ramunno, “Disorder-induced scattering loss of line-defect waveguides in photonic crystal slabs,” *Phys. Rev. B*, vol. 72, p. 161318, Oct 2005.
- [222] N. Mann, A. Javadi, P. García, P. Lodahl, and S. Hughes, “Theory and experiments of disorder-induced resonance shifts and mode-edge broadening in deliberately disordered photonic crystal waveguides,” *Physical Review A*, vol. 92, no. 2, p. 023849, 2015.
- [223] V. M. Rao and S. Hughes, “Single quantum dot spontaneous emission in a finite-size photonic crystal waveguide: proposal for an efficient “on chip” single photon gun,” *Physical review letters*, vol. 99, no. 19, p. 193901, 2007.
- [224] M. Patterson, S. Hughes, S. Schulz, D. M. Beggs, T. P. White, L. O’Faolain, and T. F. Krauss, “Disorder-induced incoherent scattering losses in photonic crystal waveguides: Bloch mode reshaping, multiple scattering, and breakdown of the beer-lambert law,” *Phys. Rev. B*, vol. 80, p. 195305, Nov 2009.

- [225] M. Patterson and S. Hughes, “Interplay between disorder-induced scattering and local field effects in photonic crystal waveguides,” *Phys. Rev. B*, vol. 81, p. 245321, Jun 2010.
- [226] A. Parini, P. Hamel, A. De Rossi, S. Combri , Y. Gottesman, R. Gabet, A. Talneau, Y. Jaou n, G. Vadal , *et al.*, “Time-wavelength reflectance maps of photonic crystal waveguides: a new view on disorder-induced scattering,” *Journal of lightwave technology*, vol. 26, no. 23, pp. 3794–3802, 2008.
- [227] M. Skorobogatiy, G. B gin, and A. Talneau, “Statistical analysis of geometrical imperfections from the images of 2d photonic crystals,” *Optics express*, vol. 13, no. 7, pp. 2487–2502, 2005.
- [228] B. Gmeiner, A. Maser, T. Utikal, S. G tzinger, and V. Sandoghdar, “Spectroscopy and microscopy of single molecules in nanoscopic channels: spectral behavior vs. confinement depth,” *Physical Chemistry Chemical Physics*, vol. 18, no. 29, pp. 19588–19594, 2016.
- [229] S. Liu, K. Srinivasan, and J. Liu, “Nanoscale positioning approaches for integrating single solid-state quantum emitters with photonic nanostructures,” *Laser & Photonics Reviews*, p. 2100223, 2021.
- [230] Y. Romach, C. Mueller, T. Uden, L. J. Rogers, T. Isoda, K. M. Itoh, M. Markham, A. Stacey, J. Meijer, S. Pezzagna, B. Naydenov, L. P. McGuinness, N. Bar-Gill, and F. Jelezko, “Spectroscopy of surface-induced noise using shallow spins in diamond,” *Phys. Rev. Lett.*, vol. 114, p. 017601, Jan 2015.
- [231] P. Schnauber, J. Schall, S. Bounouar, T. H hne, S.-I. Park, G.-H. Ryu, T. Heindel, S. Burger, J.-D. Song, S. Rodt, *et al.*, “Deterministic integration of quantum dots into on-chip multimode interference beamsplitters using in situ electron beam lithography,” *Nano Letters*, vol. 18, no. 4, pp. 2336–2342, 2018.
- [232] M. Gschrey, R. Schmidt, J.-H. Schulze, A. Strittmatter, S. Rodt, and S. Reitzenstein, “Resolution and alignment accuracy of low-temperature in situ electron beam lithography for nanophotonic device fabrication,” *Journal of Vacuum Science & Technology B, Nanotechnology and Microelectronics: Materials, Processing, Measurement, and Phenomena*, vol. 33, no. 2, p. 021603, 2015.
- [233] T. Pregolato, X.-L. Chu, T. Schr der, R. Schott, A. D. Wieck, A. Ludwig, P. Lodahl, and N. Rotenberg, “Deterministic positioning of nanophotonic waveguides around single self-assembled quantum dots,” *APL Photonics*, vol. 5, no. 8, p. 086101, 2020.
- [234] M. Patterson, S. Hughes, S. Combri , N.-V.-Q. Tran, A. De Rossi, R. Gabet, and Y. Jaou n, “Disorder-induced coherent scattering in slow-light photonic crystal waveguides,” *Physical review letters*, vol. 102, no. 25, p. 253903, 2009.

- [235] Y. Yang, H. Jiang, and Z. H. Hang, “Topological valley transport in two-dimensional honeycomb photonic crystals,” *Scientific reports*, vol. 8, no. 1, pp. 1–7, 2018.
- [236] M. Jalali Mehrabad, A. Foster, R. Dost, E. Clarke, P. Patil, I. Farrer, J. Heffernan, M. Skolnick, and L. Wilson, “A semiconductor topological photonic ring resonator,” *Applied Physics Letters*, vol. 116, no. 6, p. 061102, 2020.
- [237] M. C. Rechtsman, J. M. Zeuner, Y. Plotnik, Y. Lumer, D. Podolsky, F. Dreisow, S. Nolte, M. Segev, and A. Szameit, “Photonic floquet topological insulators,” *Nature*, vol. 496, no. 7444, pp. 196–200, 2013.
- [238] D. E. Chang, V. Vuletić, and M. D. Lukin, “Quantum nonlinear optics—photon by photon,” *Nature Photonics*, vol. 8, no. 9, pp. 685–694, 2014.
- [239] T. Volz, A. Reinhard, M. Winger, A. Badolato, K. J. Hennessy, E. L. Hu, and A. Imamoglu, “Ultrafast all-optical switching by single photons,” *Nature Photonics*, vol. 6, no. 9, pp. 605–609, 2012.
- [240] A. Javadi, I. Söllner, M. Arcari, S. L. Hansen, L. Midolo, S. Mahmoodian, G. Kiršanskė, T. Pregolato, E. Lee, J. Song, *et al.*, “Single-photon non-linear optics with a quantum dot in a waveguide,” *Nature communications*, vol. 6, no. 1, pp. 1–5, 2015.
- [241] A. B. Young, A. Thijssen, D. M. Beggs, P. Androvitsaneas, L. Kuipers, J. G. Rarity, S. Hughes, and R. Oulton, “Polarization engineering in photonic crystal waveguides for spin-photon entanglers,” *Physical review letters*, vol. 115, no. 15, p. 153901, 2015.
- [242] K. Koshino, S. Ishizaka, and Y. Nakamura, “Deterministic photon-photon swap gate using a λ system,” *Physical Review A*, vol. 82, no. 1, p. 010301, 2010.
- [243] R. E. Christiansen, F. Wang, O. Sigmund, and S. Stobbe, “Designing photonic topological insulators with quantum-spin-hall edge states using topology optimization,” *Nanophotonics*, vol. 8, no. 8, pp. 1363–1369, 2019.
- [244] J. S. Jensen and O. Sigmund, “Topology optimization for nano-photonics,” *Laser & Photonics Reviews*, vol. 5, no. 2, pp. 308–321, 2011.
- [245] T. Baba and D. Mori, “Slow light engineering in photonic crystals,” *Journal of Physics D: Applied Physics*, vol. 40, no. 9, p. 2659, 2007.
- [246] Y. Chen, F. Meng, Y. Kivshar, B. Jia, and X. Huang, “Inverse design of higher-order photonic topological insulators,” *Physical Review Research*, vol. 2, no. 2, p. 023115, 2020.
- [247] A. Laucht, F. Hofbauer, N. Hauke, J. Angele, S. Stobbe, M. Kaniber, G. Böhm, P. Lodahl, M. Amann, and J. Finley, “Electrical control of spontaneous emission and strong coupling for a single quantum dot,” *New Journal of Physics*, vol. 11, no. 2, p. 023034, 2009.

- [248] P. Lochner, A. Kurzmann, R. Schott, A. D. Wieck, A. Ludwig, A. Lorke, and M. Geller, “Contrast of 83% in reflection measurements on a single quantum dot,” *Scientific Reports*, vol. 9, no. 1, p. 8817, 2019.
- [249] I.-H. Tan, G. L. Snider, L. Chang, and E. L. Hu, “A self-consistent solution of schrödinger–poisson equations using a nonuniform mesh,” *Journal of applied physics*, vol. 68, no. 8, pp. 4071–4076, 1990.
- [250] D. Colleoni, G. Miceli, and A. Pasquarello, “Fermi-level pinning through defects at gaas/oxide interfaces: A density functional study,” *Physical Review B*, vol. 92, no. 12, p. 125304, 2015.
- [251] Y. Wang, R. Uppu, X. Zhou, C. Papon, S. Scholz, A. D. Wieck, A. Ludwig, P. Lodahl, and L. Midolo, “Electroabsorption in gated gaas nanophotonic waveguides,” *Applied Physics Letters*, vol. 118, no. 13, p. 131106, 2021.
- [252] E. Munoz, E. Calleja, I. Izpura, F. Garcia, A. Romero, J. Sánchez-Rojas, A. Powell, and J. Castagne, “Techniques to minimize dx center deleterious effects in iii-v device performance,” *Journal of applied physics*, vol. 73, no. 10, pp. 4988–4997, 1993.
- [253] G. Kiršanskè, *Electrical control of excitons in semiconductor nanostructures: from quantum dots in photonic-crystal devices*. Niels Bohr Institute at the University of Copenhagen (Dissertation), 2016.
- [254] F. P. Payne and J. P. Lacey, “A theoretical analysis of scattering loss from planar optical waveguides,” *Optical and Quantum Electronics*, vol. 26, pp. 977–986, 1994.
- [255] T. G. Oyama, K. Enomoto, A. Oshima, M. Washio, S. Tagawa, *et al.*, “Electron-beam-induced decomposition mechanisms of high-sensitivity chlorinated resist zep520a,” *Applied Physics Express*, vol. 5, no. 3, p. 036501, 2012.
- [256] P. Yao, V. Manga Rao, and S. Hughes, “On-chip single photon sources using planar photonic crystals and single quantum dots,” *Laser & Photonics Reviews*, vol. 4, no. 4, pp. 499–516, 2010.
- [257] J. P. Hugonin, P. Lalanne, T. P. White, and T. F. Krauss, “Coupling into slow-mode photonic crystal waveguides,” *Opt. Lett.*, vol. 32, pp. 2638–2640, Sep 2007.
- [258] R. Faggiani, J. Yang, R. Hostein, and P. Lalanne, “Implementing structural slow light on short length scales: the photonic speed bump,” *Optica*, vol. 4, no. 4, pp. 393–399, 2017.
- [259] E. Miyai and S. Noda, “Structural dependence of coupling between a two-dimensional photonic crystal waveguide and a wire waveguide,” *JOSA B*, vol. 21, no. 1, pp. 67–72, 2004.

- [260] M. C. Löbl, I. Söllner, A. Javadi, T. Pregnolato, R. Schott, L. Midolo, A. V. Kuhlmann, S. Stobbe, A. D. Wieck, P. Lodahl, A. Ludwig, and R. J. Warburton, "Narrow optical linewidths and spin pumping on charge-tunable close-to-surface self-assembled quantum dots in an ultrathin diode," *Phys. Rev. B*, vol. 96, p. 165440, Oct 2017.
- [261] C.-T. Sah, R. N. Noyce, and W. Shockley, "Carrier generation and recombination in pn junctions and pn junction characteristics," *Proceedings of the IRE*, vol. 45, no. 9, pp. 1228–1243, 1957.
- [262] A. Ortiz-Conde, F. J. G. Sanchez, and J. Muci, "Exact analytical solutions of the forward non-ideal diode equation with series and shunt parasitic resistances," *Solid-State Electronics*, vol. 44, no. 10, pp. 1861–1864, 2000.
- [263] R. M. Corless, G. H. Gonnet, D. E. Hare, D. J. Jeffrey, and D. E. Knuth, "On the lambert w function," *Advances in Computational mathematics*, vol. 5, pp. 329–359, 1996.
- [264] L. Midolo, P. Van Veldhoven, M. Dündar, R. Nötzel, and A. Fiore, "Electromechanical wavelength tuning of double-membrane photonic crystal cavities," *Applied Physics Letters*, vol. 98, no. 21, p. 211120, 2011.
- [265] C.-X. Wang, G.-W. Yang, H.-W. Liu, Y.-H. Han, J.-F. Luo, C.-X. Gao, and G.-T. Zou, "Experimental analysis and theoretical model for anomalously high ideality factors in zno/diamond pn junction diode," *Applied Physics Letters*, vol. 84, no. 13, pp. 2427–2429, 2004.
- [266] J. M. Shah, Y.-L. Li, T. Gessmann, and E. F. Schubert, "Experimental analysis and theoretical model for anomalously high ideality factors ($n \gg 2.0$) in algan/gan pn junction diodes," *Journal of applied physics*, vol. 94, no. 4, pp. 2627–2630, 2003.
- [267] D. Lugo-Munoz, J. Muci, A. Ortiz-Conde, F. J. Garcia-Sanchez, M. De Souza, and M. A. Pavanello, "An explicit multi-exponential model for semiconductor junctions with series and shunt resistances," *Microelectronics Reliability*, vol. 51, no. 12, pp. 2044–2048, 2011.
- [268] Y. Ding, C. Peucheret, H. Ou, and K. Yvind, "Fully etched apodized grating coupler on the soi platform with 0.58 db coupling efficiency," *Optics letters*, vol. 39, no. 18, pp. 5348–5350, 2014.
- [269] S. Adachi, "Gaas, alas, and al x gai- x as: Material parameters for use in research and device applications," *Journal of Applied Physics*, vol. 58, no. 3, pp. R1–R29, 1985.
- [270] J. Callaway, "Optical absorption in an electric field," *Phys. Rev.*, vol. 134, pp. A998–A1000, May 1964.
- [271] E. Rosencher and B. Vinter, *Optoelectronics*. Cambridge University Press, 2002.

- [272] G. Stillman, C. Wolfe, C. Bozler, and J. Rossi, "Electroabsorption in gaas and its application to waveguide detectors and modulators," *Applied Physics Letters*, vol. 28, no. 9, pp. 544–546, 1976.
- [273] M. Patterson and S. Hughes, "Theory of disorder-induced coherent scattering and light localization in slow-light photonic crystal waveguides," *Journal of Optics*, vol. 12, no. 10, p. 104013, 2010.
- [274] L. Sapienza, H. Thyrrerstrup, S. Stobbe, P. D. Garcia, S. Smolka, and P. Lodahl, "Cavity quantum electrodynamics with anderson-localized modes," *Science*, vol. 327, no. 5971, pp. 1352–1355, 2010.
- [275] T. Crane, O. J. Trojak, J. P. Vasco, S. Hughes, and L. Sapienza, "Anderson localization of visible light on a nanophotonic chip," *ACS Photonics*, vol. 4, no. 9, pp. 2274–2280, 2017.
- [276] J. P. Vasco and S. Hughes, "Statistics of anderson-localized modes in disordered photonic crystal slab waveguides," *Phys. Rev. B*, vol. 95, p. 224202, Jun 2017.
- [277] D. Pinotsi, P. Fallahi, J. Miguel-Sanchez, and A. Imamoglu, "Resonant spectroscopy on charge tunable quantum dots in photonic crystal structures," *IEEE Journal of Quantum Electronics*, vol. 47, no. 11, pp. 1371–1374, 2011.
- [278] H. Singh, D. Farfurnik, Z. Luo, A. S. Bracker, S. G. Carter, and E. Waks, "Optical transparency induced by a largely purcell enhanced quantum dot in a polarization-degenerate cavity," *Nano Letters*, vol. 22, pp. 7959–7964, sep 2022.
- [279] S. Manna, H. Huang, S. F. C. da Silva, C. Schimpf, M. B. Rota, B. Lehner, M. Reindl, R. Trotta, and A. Rastelli, "Surface passivation and oxide encapsulation to improve optical properties of a single gaas quantum dot close to the surface," *Applied Surface Science*, vol. 532, p. 147360, 2020.
- [280] T. Strobel, J. Weber, M. Schmidt, L. Wagner, L. Engel, M. Jetter, A. Wieck, S. Portalupi, A. Ludwig, and P. Michler, "A unipolar quantum dot diode structure for advanced quantum light sources," *arXiv preprint arXiv:2301.03541*, 2023.
- [281] J. Houel, A. Kuhlmann, L. Greuter, F. Xue, M. Poggio, B. Gerardot, P. Dalgarno, A. Badolato, P. Petroff, A. Ludwig, *et al.*, "Probing single-charge fluctuations at a gaas/alas interface using laser spectroscopy on a nearby ingaas quantum dot," *Physical review letters*, vol. 108, no. 10, p. 107401, 2012.
- [282] E. H. Li, "Material parameters of ingaasp and inalgaas systems for use in quantum well structures at low and room temperatures," *Physica E: Low-dimensional systems and Nanostructures*, vol. 5, no. 4, pp. 215–273, 2000.
- [283] D. A. Czuplewski and L. E. Ocola, "Increased pattern transfer fidelity of zep 520a during reactive ion etching through chemical modifications by additional

- dosing of the electron beam resist,” *Journal of Vacuum Science & Technology B, Nanotechnology and Microelectronics: Materials, Processing, Measurement, and Phenomena*, vol. 29, no. 2, p. 021601, 2011.
- [284] T. Kojima, K. Kojima, T. Asano, and S. Noda, “Accurate alignment of a photonic crystal nanocavity with an embedded quantum dot based on optical microscopic photoluminescence imaging,” *Applied Physics Letters*, vol. 102, no. 1, p. 011110, 2013.
- [285] G. Kiršanskė, H. Thyrrerstrup, R. S. Daveau, C. L. Dreeßen, T. Pregolato, L. Midolo, P. Tighineanu, A. Javadi, S. Stobbe, R. Schott, A. Ludwig, A. D. Wieck, S. I. Park, J. D. Song, A. V. Kuhlmann, I. Söllner, M. C. Löbl, R. J. Warburton, and P. Lodahl, “Indistinguishable and efficient single photons from a quantum dot in a planar nanobeam waveguide,” *Phys. Rev. B*, vol. 96, p. 165306, Oct 2017.
- [286] M. C. Löbl, C. Spinnler, A. Javadi, L. Zhai, G. N. Nguyen, J. Ritzmann, L. Midolo, P. Lodahl, A. D. Wieck, A. Ludwig, *et al.*, “Radiative auger process in the single-photon limit,” *Nature nanotechnology*, vol. 15, no. 7, pp. 558–562, 2020.
- [287] K. Müller, A. Bechtold, C. Ruppert, T. Kaldewey, M. Zecherle, J. S. Wildmann, M. Bichler, H. J. Krenner, J. M. Villas-Bôas, G. Abstreiter, *et al.*, “Probing ultrafast carrier tunneling dynamics in individual quantum dots and molecules,” *Annalen der Physik*, vol. 525, no. 1-2, pp. 49–58, 2013.
- [288] N. Cade, H. Gotoh, H. Kamada, H. Nakano, and H. Okamoto, “Fine structure and magneto-optics of exciton, trion, and charged biexciton states in single inas quantum dots emitting at $1.3 \mu\text{m}$,” *Physical Review B*, vol. 73, no. 11, p. 115322, 2006.
- [289] E. C. Le Ru, J. Fack, and R. Murray, “Temperature and excitation density dependence of the photoluminescence from annealed inas/gaas quantum dots,” *Phys. Rev. B*, vol. 67, p. 245318, Jun 2003.
- [290] C. Kittel and H. Kroemer, *Thermal physics*, vol. 9690. Wiley New York, 1970.
- [291] S. Adachi, *GaAs and related materials: bulk semiconducting and superlattice properties*. World Scientific, 1994.
- [292] H. Huang, D. Csontosová, S. Manna, Y. Huo, R. Trotta, A. Rastelli, and P. Klenovský, “Electric field induced tuning of electronic correlation in weakly confining quantum dots,” *Phys. Rev. B*, vol. 104, p. 165401, Oct 2021.
- [293] P. W. Fry, I. E. Itskevich, D. J. Mowbray, M. S. Skolnick, J. J. Finley, J. A. Barker, E. P. O’Reilly, L. R. Wilson, I. A. Larkin, P. A. Maksym, M. Hopkinson, M. Al-Khafaji, J. P. R. David, A. G. Cullis, G. Hill, and J. C. Clark, “Inverted electron-hole alignment in inas-gaas self-assembled quantum dots,” *Phys. Rev. Lett.*, vol. 84, pp. 733–736, Jan 2000.

- [294] R. H. Brown and R. Q. Twiss, “Correlation between photons in two coherent beams of light,” *Nature*, vol. 177, no. 4497, pp. 27–29, 1956.
- [295] A. Muller, *Resonance fluorescence and cavity quantum electrodynamics with quantum dots*. The University of Texas at Austin (Dissertation), 2007.
- [296] M. Arcari, *Efficiency and Coherence of Quantum-Dot Single-Photon Sources*. Niels Bohr Institute at the University of Copenhagen (Dissertation), 2015.
- [297] C. Santori, D. Fattal, J. Vučković, G. S. Solomon, E. Waks, and Y. Yamamoto, “Submicrosecond correlations in photoluminescence from inas quantum dots,” *Phys. Rev. B*, vol. 69, p. 205324, May 2004.
- [298] J. Johansen, B. Julsgaard, S. Stobbe, J. M. Hvam, and P. Lodahl, “Probing long-lived dark excitons in self-assembled quantum dots,” *Phys. Rev. B*, vol. 81, p. 081304, Feb 2010.
- [299] C. Santori, M. Pelton, G. Solomon, Y. Dale, and Y. Yamamoto, “Triggered single photons from a quantum dot,” *Phys. Rev. Lett.*, vol. 86, pp. 1502–1505, Feb 2001.
- [300] S. Machlup, “Noise in semiconductors: spectrum of a two-parameter random signal,” *Journal of Applied Physics*, vol. 25, no. 3, pp. 341–343, 1954.
- [301] P. Michler, A. Imamoglu, M. Mason, P. Carson, G. Strouse, and S. Buratto, “Quantum correlation among photons from a single quantum dot at room temperature,” *Nature*, vol. 406, no. 6799, pp. 968–970, 2000.
- [302] D. Ding, M. H. Appel, A. Javadi, X. Zhou, M. C. Löbl, I. Söllner, R. Schott, C. Papon, T. Pregolato, L. Midolo, A. D. Wieck, A. Ludwig, R. J. Warburton, T. Schröder, and P. Lodahl, “Coherent optical control of a quantum-dot spin-qubit in a waveguide-based spin-photon interface,” *Phys. Rev. Appl.*, vol. 11, p. 031002, Mar 2019.
- [303] H. Le Jeannic, T. Ramos, S. F. Simonsen, T. Pregolato, Z. Liu, R. Schott, A. D. Wieck, A. Ludwig, N. Rotenberg, J. J. García-Ripoll, and P. Lodahl, “Experimental reconstruction of the few-photon nonlinear scattering matrix from a single quantum dot in a nanophotonic waveguide,” *Phys. Rev. Lett.*, vol. 126, p. 023603, Jan 2021.
- [304] A. Albo, D. Fekete, and G. Bahir, “Electronic bound states in the continuum above (ga,in)(as,n)/(al,ga)as quantum wells,” *Phys. Rev. B*, vol. 85, p. 115307, Mar 2012.
- [305] C. W. Hsu, B. Zhen, A. D. Stone, J. D. Joannopoulos, and M. Soljačić, “Bound states in the continuum,” *Nature Reviews Materials*, vol. 1, no. 9, pp. 1–13, 2016.
- [306] T. Nakaoka, T. Kakitsuka, T. Saito, S. Kako, S. Ishida, M. Nishioka, Y. Yoshikuni, and Y. Arakawa, “Strain-induced modifications of the electronic states of ingaas quantum dots embedded in bowed airbridge structures,” *Journal of applied physics*, vol. 94, no. 10, pp. 6812–6817, 2003.

- [307] J. Liu, K. Konthasinghe, M. Davanco, J. Lawall, V. Anant, V. Verma, R. Mirin, S. W. Nam, J. D. Song, B. Ma, *et al.*, “Direct observation of nanofabrication influence on the optical properties of single self-assembled inas/gaas quantum dots,” *arXiv preprint arXiv:1710.09667*, 2017.
- [308] N. Ha, T. Mano, Y.-L. Chou, Y.-N. Wu, S.-J. Cheng, J. Bocquel, P. M. Koenraad, A. Ohtake, Y. Sakuma, K. Sakoda, and T. Kuroda, “Size-dependent line broadening in the emission spectra of single gaas quantum dots: Impact of surface charge on spectral diffusion,” *Phys. Rev. B*, vol. 92, p. 075306, Aug 2015.
- [309] C. Wang, A. Badolato, I. Wilson-Rae, P. Petroff, E. Hu, J. Urayama, and A. Imamoğlu, “Optical properties of single inas quantum dots in close proximity to surfaces,” *Applied physics letters*, vol. 85, no. 16, pp. 3423–3425, 2004.
- [310] J. Liu, K. Konthasinghe, M. Davanço, J. Lawall, V. Anant, V. Verma, R. Mirin, S. W. Nam, J. D. Song, B. Ma, Z. S. Chen, H. Q. Ni, Z. C. Niu, and K. Srinivasan, “Single self-assembled InAs/GaAs quantum dots in photonic nanostructures: The role of nanofabrication,” *Phys. Rev. Appl.*, vol. 9, p. 064019, Jun 2018.
- [311] J. Houel, A. V. Kuhlmann, L. Greuter, F. Xue, M. Poggio, B. D. Gerardot, P. A. Dalgarno, A. Badolato, P. M. Petroff, A. Ludwig, D. Reuter, A. D. Wieck, and R. J. Warburton, “Probing single-charge fluctuations at a GaAs/AlAs interface using laser spectroscopy on a nearby ingaas quantum dot,” *Phys. Rev. Lett.*, vol. 108, p. 107401, Mar 2012.
- [312] J. Iles-Smith, D. P. S. McCutcheon, A. Nazir, and J. Mørk, “Phonon limit to simultaneous near-unity efficiency and indistinguishability in semiconductor single photon sources,” in *Conference on Lasers and Electro-Optics*, p. FTu3E.3, Optica Publishing Group, 2017.
- [313] D. E. Reiter, T. Kuhn, and V. M. Axt, “Distinctive characteristics of carrier-phonon interactions in optically driven semiconductor quantum dots,” *Advances in Physics: X*, vol. 4, no. 1, p. 1655478, 2019.
- [314] Z. X. Koong, D. Scerri, M. Rambach, T. S. Santana, S. I. Park, J. D. Song, E. M. Gauger, and B. D. Gerardot, “Fundamental limits to coherent photon generation with solid-state atomlike transitions,” *Phys. Rev. Lett.*, vol. 123, p. 167402, Oct 2019.
- [315] P. Kaer, T. R. Nielsen, P. Lodahl, A.-P. Jauho, and J. Mørk, “Non-markovian model of photon-assisted dephasing by electron-phonon interactions in a coupled quantum-dot-cavity system,” *Phys. Rev. Lett.*, vol. 104, p. 157401, Apr 2010.
- [316] K. H. Madsen, P. Kaer, A. Kreiner-Møller, S. Stobbe, A. Nysteen, J. Mørk, and P. Lodahl, “Measuring the effective phonon density of states of a quantum dot in cavity quantum electrodynamics,” *Phys. Rev. B*, vol. 88, p. 045316, Jul 2013.

- [317] M. Bayer, A. Kuther, A. Forchel, T. Reinecke, and S. Walck, "Fine structure of excitons in self-assembled In_{0.6}Ga_{0.4}As quantum dots: Zeeman-interaction and exchange energy enhancement," *Physica E: Low-dimensional Systems and Nanostructures*, vol. 7, no. 3-4, pp. 475-478, 2000.
- [318] T. Calarco, A. Datta, P. Fedichev, E. Pazy, and P. Zoller, "Spin-based all-optical quantum computation with quantum dots: Understanding and suppressing decoherence," *Physical Review A*, vol. 68, no. 1, p. 012310, 2003.
- [319] G. Moody, M. Siemens, A. Bristow, X. Dai, D. Karaiskaj, A. Bracker, D. Gammon, and S. Cundiff, "Exciton-exciton and exciton-phonon interactions in an interfacial GaAs quantum dot ensemble," *Physical Review B*, vol. 83, no. 11, p. 115324, 2011.
- [320] J. H. Quilter, A. Brash, F. Liu, M. Glässl, A. M. Barth, V. M. Axt, A. Ramsay, M. Skolnick, and A. Fox, "Phonon-assisted population inversion of a single InGaAs/GaAs quantum dot by pulsed laser excitation," *Physical review letters*, vol. 114, no. 13, p. 137401, 2015.
- [321] A. J. Brash, J. Iles-Smith, C. L. Phillips, D. P. McCutcheon, J. O'Hara, E. Clarke, B. Royall, L. R. Wilson, J. Mørk, M. S. Skolnick, *et al.*, "Light scattering from solid-state quantum emitters: beyond the atomic picture," *Physical Review Letters*, vol. 123, no. 16, p. 167403, 2019.
- [322] W. Ouerghui, A. Melliti, M. Maaref, and J. Bloch, "Dependence on temperature of homogeneous broadening of InGaAs/InAs/GaAs quantum dot fundamental transitions," *Physica E: Low-dimensional Systems and Nanostructures*, vol. 28, no. 4, pp. 519-524, 2005.
- [323] I. Mal, D. Panda, B. Tongbram, D. Samajdar, and S. Chakrabarti, "Analytical modeling of temperature and power dependent photoluminescence (PL) spectra of InAs/GaAs quantum dots," *Journal of Applied Physics*, vol. 124, no. 14, p. 145701, 2018.
- [324] J. Förstner, C. Weber, J. Danckwerts, and A. Knorr, "Phonon-assisted damping of Rabi oscillations in semiconductor quantum dots," *Physical review letters*, vol. 91, no. 12, p. 127401, 2003.
- [325] A. J. Ramsay, A. V. Gopal, E. M. Gauger, A. Nazir, B. W. Lovett, A. M. Fox, and M. S. Skolnick, "Damping of exciton Rabi rotations by acoustic phonons in optically excited InGaAs/GaAs quantum dots," *Phys. Rev. Lett.*, vol. 104, p. 017402, Jan 2010.
- [326] A. J. Ramsay, T. M. Godden, S. J. Boyle, E. M. Gauger, A. Nazir, B. W. Lovett, A. M. Fox, and M. S. Skolnick, "Phonon-induced Rabi-frequency renormalization of optically driven single InGaAs/GaAs quantum dots," *Phys. Rev. Lett.*, vol. 105, p. 177402, Oct 2010.

- [327] C. K. Hong, Z. Y. Ou, and L. Mandel, "Measurement of subpicosecond time intervals between two photons by interference," *Phys. Rev. Lett.*, vol. 59, pp. 2044–2046, Nov 1987.
- [328] A. Kiraz, M. Atatüre, and A. Imamoglu, "Quantum-dot single-photon sources: Prospects for applications in linear optics quantum-information processing," *Physical Review A*, vol. 69, no. 3, p. 032305, 2004.
- [329] C. Papon, Y. Wang, R. Uppu, S. Scholz, A. D. Wieck, A. Ludwig, P. Lodahl, and L. Midolo, "Independent operation of two waveguide-integrated single-photon sources," *arXiv preprint arXiv:2210.09826*, 2022.
- [330] J. Wolters, G. Buser, A. Horsley, L. Béguin, A. Jöckel, J.-P. Jahn, R. J. Warburton, and P. Treutlein, "Simple atomic quantum memory suitable for semiconductor quantum dot single photons," *Phys. Rev. Lett.*, vol. 119, p. 060502, Aug 2017.
- [331] M. F. Askarani, A. Das, J. H. Davidson, G. C. Amaral, N. Sinclair, J. A. Slater, S. Marzban, C. W. Thiel, R. L. Cone, D. Oblak, and W. Tittel, "Long-lived solid-state optical memory for high-rate quantum repeaters," *Phys. Rev. Lett.*, vol. 127, p. 220502, Nov 2021.
- [332] J. Kołodyski, A. Máttar, P. Skrzypczyk, E. Woodhead, D. Cavalcanti, K. Banaszek, and A. Acín, "Device-independent quantum key distribution with single-photon sources," *Quantum*, vol. 4, p. 260, Apr. 2020.
- [333] E. M. González-Ruiz, S. K. Das, P. Lodahl, and A. S. Sørensen, "Violation of bell's inequality with quantum-dot single-photon sources," *Phys. Rev. A*, vol. 106, p. 012222, Jul 2022.
- [334] B. Wang, S. Mazoyer, J.-P. Hugonin, and P. Lalanne, "Backscattering in monomode periodic waveguides," *Physical Review B*, vol. 78, no. 24, p. 245108, 2008.
- [335] R. F. Pierret, *Semiconductor device fundamentals*. Pearson Education India, 1996.
- [336] S. Butterworth *et al.*, "On the theory of filter amplifiers," *Wireless Engineer*, vol. 7, no. 6, pp. 536–541, 1930.
- [337] D. Pegg, R. Loudon, and P. Knight, "Correlations in light emitted by three-level atoms," *Physical Review A*, vol. 33, no. 6, p. 4085, 1986.
- [338] F. Träger, *Springer handbook of lasers and optics*, vol. 2. Springer, 2012.
- [339] C. Husko, M. Wulf, S. Lefrancois, S. Combrié, G. Lehoucq, A. D. Rossi, B. J. Eggleton, and L. Kuipers, "Free-carrier-induced soliton fission unveiled by in situ measurements in nanophotonic waveguides," *Nature Communications*, vol. 7, no. 1, 2016.
- [340] K. O'donnell and X. Chen, "Temperature dependence of semiconductor band gaps," *Applied physics letters*, vol. 58, no. 25, pp. 2924–2926, 1991.

- [341] Y. P. Varshni, "Temperature dependence of the energy gap in semiconductors," *physica*, vol. 34, no. 1, pp. 149–154, 1967.
- [342] F. Basso Basset, S. Bietti, A. Tuktamyshev, S. Vichi, E. Bonera, and S. Sanguinetti, "Spectral broadening in self-assembled gas quantum dots with narrow size distribution," *Journal of Applied Physics*, vol. 126, no. 2, p. 024301, 2019.